



UNIVERSITAT DE
BARCELONA

Optimization of hydrogenated amorphous silicon for its use in different photovoltaic technologies

Álvaro Caballero Lorenzo

ADVERTIMENT. La consulta d'aquesta tesi queda condicionada a l'acceptació de les següents condicions d'ús: La difusió d'aquesta tesi per mitjà del servei TDX (www.tdx.cat) i a través del Dipòsit Digital de la UB (diposit.ub.edu) ha estat autoritzada pels titulars dels drets de propietat intel·lectual únicament per a usos privats emmarcats en activitats d'investigació i docència. No s'autoritza la seva reproducció amb finalitats de lucre ni la seva difusió i posada a disposició des d'un lloc aliè al servei TDX ni al Dipòsit Digital de la UB. No s'autoritza la presentació del seu contingut en una finestra o marc aliè a TDX o al Dipòsit Digital de la UB (framing). Aquesta reserva de drets afecta tant al resum de presentació de la tesi com als seus continguts. En la utilització o cita de parts de la tesi és obligat indicar el nom de la persona autora.

ADVERTENCIA. La consulta de esta tesis queda condicionada a la aceptación de las siguientes condiciones de uso: La difusión de esta tesis por medio del servicio TDR (www.tdx.cat) y a través del Repositorio Digital de la UB (diposit.ub.edu) ha sido autorizada por los titulares de los derechos de propiedad intelectual únicamente para usos privados enmarcados en actividades de investigación y docencia. No se autoriza su reproducción con finalidades de lucro ni su difusión y puesta a disposición desde un sitio ajeno al servicio TDR o al Repositorio Digital de la UB. No se autoriza la presentación de su contenido en una ventana o marco ajeno a TDR o al Repositorio Digital de la UB (framing). Esta reserva de derechos afecta tanto al resumen de presentación de la tesis como a sus contenidos. En la utilización o cita de partes de la tesis es obligado indicar el nombre de la persona autora.

WARNING. On having consulted this thesis you're accepting the following use conditions: Spreading this thesis by the TDX (www.tdx.cat) service and by the UB Digital Repository (diposit.ub.edu) has been authorized by the titular of the intellectual property rights only for private uses placed in investigation and teaching activities. Reproduction with lucrative aims is not authorized nor its spreading and availability from a site foreign to the TDX service or to the UB Digital Repository. Introducing its content in a window or frame foreign to the TDX service or to the UB Digital Repository is not authorized (framing). Those rights affect to the presentation summary of the thesis as well as to its contents. In the using or citation of parts of the thesis it's obliged to indicate the name of the author.



UNIVERSITAT_{DE} BARCELONA

DEPARTAMENT DE FÍSICA APLICADA

Av. Diagonal, 645, 08028 Barcelona

Optimization of hydrogenated amorphous silicon for its use in different photovoltaic technologies

Álvaro Caballero Lorenzo

Memoria presentada para optar al grado de Doctor

Barcelona, Abril de 2016



UNIVERSITAT DE BARCELONA

DEPARTAMENT DE FÍSICA APLICADA

Av. Diagonal, 645, 08028 Barcelona

Optimization of hydrogenated amorphous silicon for its use in different photovoltaic technologies

Álvaro Caballero Lorenzo

Directors: José Miguel Asensi López; Joan Bertomeu i Balaguero
Programa de doctorado: Física

Memoria para optar al grado de Doctor
Barcelona, Abril de 2016

This work was also supported by the Ministerio de Ciencia e Innovación, the Ministerio de Economía y Competitividad and the European Regional Development Fund through projects AMIC (ENE2010-21384-C04-03), INNDISOL (IPT-420000-2010-6) and HELLO (ENE2013-48629-C4-2-R).

A mis padres, Pedro y Lola.

Contents

| | |
|---|-----------|
| Abstract | 1 |
| Resumen | 5 |
| 1 Introduction | 9 |
| 1.1 The importance of renewable energies: The role of solar photovoltaic (PV) energy. | 9 |
| 1.2 Solar photovoltaic technologies | 10 |
| 1.2.1 Principle of operation of solar cells | 10 |
| 1.2.2 Use of silicon in solar cells | 12 |
| 1.2.3 Technologies involved in this thesis work | 14 |
| 1.2.3.1 Thin film silicon solar cells | 14 |
| 1.2.3.2 Thin film technologies for c-Si wafer based solar cells | 17 |
| 1.3 Hydrogenated amorphous silicon | 20 |
| 1.3.1 Advantages and drawbacks of a-Si:H | 21 |
| 1.4 Fundamentals on Plasma Enhanced Chemical Vapor Deposition (PECVD) | 23 |
| 1.5 Objectives and outlook of this thesis | 25 |
| 2 Experimental details | 29 |
| 2.1 Deposition methods | 29 |
| 2.1.1 Plasma enhanced chemical vapor deposition | 30 |
| 2.1.2 Magnetron sputtering | 36 |
| 2.1.3 Resistive thermal evaporation | 37 |
| 2.2 Pre- and post- deposition treatments | 39 |
| 2.2.1 Wafer cleaning and preparation | 40 |
| 2.2.2 Chemical etching | 40 |
| 2.2.3 Thermal annealing | 41 |

Contents

| | | |
|----------|--|-----------|
| 2.2.4 | Light induced degradation | 42 |
| 2.2.4.1 | Requirements and construction of the system | 43 |
| 2.2.4.2 | Illumination intensity and temperature calibrations | 45 |
| 2.3 | Characterization techniques | 48 |
| 2.3.1 | Thickness measurements | 48 |
| 2.3.1.1 | Confocal microscopy | 48 |
| 2.3.1.2 | Stylus profilometry | 49 |
| 2.3.1.3 | Ellipsometry | 49 |
| 2.3.2 | Optical and structural characterization | 50 |
| 2.3.2.1 | UV-VIS-NIR spectroscopy | 50 |
| 2.3.2.2 | Raman spectroscopy | 51 |
| 2.3.3 | Electrical characterization | 51 |
| 2.3.3.1 | High impedance measurements | 51 |
| 2.3.3.2 | Four point probe | 54 |
| 2.3.4 | Effective carrier lifetime and implicit V_{oc} measurements | 54 |
| 2.3.5 | Device characterization equipment | 55 |
| 2.3.5.1 | Current density-voltage characteristics | 56 |
| 2.3.5.2 | Spectral response (SR), external quantum efficiency (EQE) and internal quantum efficiency (IQE). | 60 |
| 3 | Optimization and improvements in thin film a-Si:H solar cells | 63 |
| 3.1 | Introduction | 63 |
| 3.2 | Homogeneity and area definition | 64 |
| 3.3 | Intrinsic amorphous silicon layer optimization | 67 |
| 3.3.1 | Properties optimization | 67 |
| 3.3.2 | Developed measurements | 68 |
| 3.3.2.1 | Thickness and deposition rate | 68 |
| 3.3.2.2 | Optical measurements | 69 |
| 3.3.2.3 | Electric measurements | 69 |
| 3.3.3 | Depletion series | 71 |
| 3.3.3.1 | Experimental | 71 |
| 3.3.3.2 | Results and discussion | 73 |
| 3.3.3.3 | Conclusions and future work | 78 |

| | | |
|----------|---|------------|
| 3.3.4 | Hydrogen series | 79 |
| 3.3.4.1 | Experimental | 79 |
| 3.3.4.2 | Results and discussion | 80 |
| 3.3.4.3 | Conclusions and future work | 83 |
| 3.3.5 | Temperature series | 84 |
| 3.3.5.1 | Experimental | 84 |
| 3.3.5.2 | Results and discussion | 84 |
| 3.3.5.3 | Conclusions and future work | 88 |
| 3.4 | Boron doped silicon layer optimization | 88 |
| 3.4.1 | Boron doped amorphous silicon | 89 |
| 3.4.2 | Boron doped microcrystalline silicon | 92 |
| 3.5 | Complete device optimization | 96 |
| 3.5.1 | Back reflector optimization | 96 |
| 3.5.2 | p layer thickness optimization | 99 |
| 3.6 | Improvement of V_{oc} in polymorphous silicon solar cells | 102 |
| 3.6.1 | Introduction | 102 |
| 3.6.2 | Experimental | 103 |
| 3.6.3 | Results and discussion | 105 |
| 3.6.3.1 | J - V curves in PIN samples | 105 |
| 3.6.3.2 | J - V curves in NIP samples | 107 |
| 3.6.3.3 | External quantum efficiency measurements | 108 |
| 3.6.4 | Conclusions and future work | 111 |
| 3.7 | Conclusions and perspectives | 112 |
| 4 | Light induced degradation | 115 |
| 4.1 | Introduction | 115 |
| 4.2 | Motivation: Seasonal effect found in power plants | 117 |
| 4.3 | Thickness optimization against LID | 119 |
| 4.3.1 | Experimental | 120 |
| 4.3.2 | Results analysis | 121 |
| 4.3.3 | Discussion: the role of the $\mu\tau$ product | 125 |
| 4.3.4 | Conclusions and future work | 130 |
| 4.4 | Temperature influence on seasonal effect | 131 |
| 4.4.1 | T -Solar samples | 132 |
| 4.4.1.1 | Results and discussion | 132 |
| 4.4.1.2 | Evaluation of the temperature coefficients | 134 |

Contents

| | | |
|----------|---|------------|
| 4.4.2 | UB samples | 135 |
| 4.4.2.1 | J - V curves: Results and discussion | 136 |
| 4.4.2.2 | Role of short and open circuit resistances | 140 |
| 4.4.2.3 | EQE and absorptance: Results and discus- sion | 141 |
| 4.4.2.4 | Evaluation of the temperature coefficients | 145 |
| 4.4.3 | Conclusions and further work | 146 |
| 4.5 | Conclusions and perspectives | 147 |
| 5 | Thin film passivation for advanced solar cell structures | 149 |
| 5.1 | Introduction | 149 |
| 5.1.1 | Fundamentals | 149 |
| 5.1.1.1 | Efficient light absorption | 150 |
| 5.1.1.2 | Reduction of the recombination | 152 |
| 5.2 | Motivation of the work | 154 |
| 5.2.1 | Passivation with alumina deposited by sputtering | 155 |
| 5.2.1.1 | Al_2O_3 advantages over SiN_x | 155 |
| 5.2.1.2 | Advantages of sputtering over ALD, and the need of an a-Si:H layer | 156 |
| 5.2.2 | Development of p -type emitters for n -type wafers | 157 |
| 5.3 | Results in Al_2O_3 passivation: role of an a-Si:H interlayer | 157 |
| 5.3.1 | Layer deposition and measurements | 157 |
| 5.3.2 | Discussion, conclusions and perspectives | 160 |
| 5.4 | Results in p -type hetero-emitter development | 163 |
| 5.4.1 | Indium tin oxide optimization | 163 |
| 5.4.1.1 | Optimization over glass | 164 |
| 5.4.1.2 | ITO deposited over devices | 168 |
| 5.4.1.3 | Conclusions | 173 |
| 5.4.2 | Silicon layers optimization | 174 |
| 5.4.2.1 | Deposition temperature of the p -doped layers | 174 |
| 5.4.2.2 | Silicon layers thickness optimization for the p -emitter | 176 |
| 5.4.2.3 | First trials of complete p -type emitter | 179 |
| 5.4.3 | Intrinsic a-Si:H passivating layer optimization | 182 |
| 5.4.3.1 | Carbon concentration and annealing tem- perature | 182 |

| | |
|--|------------|
| 5.4.3.2 Deposition temperature increase to avoid thermal annealing | 185 |
| 5.5 Conclusions and future work | 186 |
| 6 Conclusions and perspectives | 189 |
| Bibliography | 199 |
| List of Symbols | 227 |
| Curriculum Vitae | 237 |
| Acknowledgments | 241 |

Abstract

Hydrogenated amorphous silicon has been studied and used in photovoltaic solar cells for over fifty years. It is used as active layer in thin film technology, either in single junction, tandem or multijunction solar cells. Recently, the efficiency records for single a-Si:H cell and tandem cell with a-Si:H have been beaten, proving that there are still chances to improve the performance of technologies with a-Si:H as absorber layer. On the other hand, a-Si:H is used as complementary material in other technologies, specially heterojunction with intrinsic thin film (HIT) solar cells. The main objective of this work is to study and optimize the amorphous silicon deposited in a PECVD reactor of recent acquisition, making it suitable to be used in thin film and c-Si based solar cells.

First, the optimization of both intrinsic and doped a-Si:H single layers was developed, based on several optical and electrical properties, such as absorptance, Tauc band gap, dark conductivity, activation energy and photoconductivity. Concerning intrinsic a-Si:H to be used as active layer, series in three parameters were developed. The first series revealed a strong dependence on the depletion, showing a marked maximum on the deposition rate in the central values. This tendency was also found in the rest of the properties. This behavior comes as a result of the contribution of two mechanisms during the plasma deposition that reach equilibrium in the central values. The most suitable considered conditions were those corresponding to low depletion regimes. For the hydrogen series, an optimum point was found for a 2:1 ratio between hydrogen and silane flows in this plasma regime, and it was found that higher concentrations led to poor attachment of the layers. The temperature series proved that the temperature had less influence. Although higher temperature layers showed slightly better parameters, 200°C was considered the optimum value in order to not affect the potential open circuit voltage of the device.

Contents

p-type material (a-Si:H and μ c-Si:H) was also optimized to be used as doped layer in thin film solar cells. The series developed for *p* a-Si:H (TMB flow, temperature, pressure and CH₄ flow) led to obtaining device quality material, with a conductivity of $1.1 \cdot 10^{-5}$ S/cm, an activation energy of 0.43 eV and a band gap of 2.02 eV. For *p* μ c-Si:H, device quality material was also obtained after four optimization series (temperature, TMB flow, power and SiH₄ flow), with a conductivity of 1.32 S/cm, a band gap of 2.07 eV and a cristallinity factor of 0.596. With the optimized layers, studies over complete solar cells were developed. The front doped layer thickness and the back reflector optimizations led to increments on the short circuit current of 11% and 12% respectively, and some smaller improvements in other parameters. A working PIN a-Si:H solar cell fully deposited at the UB with an efficiency of 7.08% was obtained. This value is still low compared to the state of the art, due to lower open circuit voltage and short circuit current.

In the context of increasing the open circuit voltage of thin film solar cells, a study over polymorphous silicon solar cells in both PIN and NIP configuration has been developed in the Laboratoire de Physique des Interfaces et des Couches Minces (LPCIM), in Palaiseau. It has been proved that depositing a-Si:H buffer layers before the pm-Si:H intrinsic material produces an increase in the V_{oc} due to the formation of better interface with the existing μ c-SiO_x doped layer. On the contrary, when the a-Si:H layer is deposited over the pm-Si:H and before the μ c-SiO_x material, the performance of the cell drops dramatically, probably due to a bad growth of μ c-SiO_x over amorphous material, which results in the failure of the cell.

One of the key points to actually optimize amorphous silicon is to study the effect that light induced degradation (LID) has over it. To do so, a low cost light soaking system based in LED illumination has been designed and constructed. The inclusion of several platforms that make possible the use of different degradation temperatures allowed the development of experiments involving the seasonal effect of LID in amorphous silicon. Before the seasonal effect experiments, an optimization of the intrinsic layer thickness was developed, finding an optimal thickness of 200 nm. A simple model based on the mobility-lifetime product was used to explain the results.

To study the role of the temperature in seasonal effect, both solar cells extracted from the module production line of *T-Solar* and laboratory UB cells have been degraded varying the temperature between different stages of degradation (1000 h). The fact that all degradations were developed with the same constant illumination removes the spectral effect, so the real influence of the temperature was studied. The samples going from lower degradation temperatures to higher experienced a recovery of their properties appreciable in less than 10 hours after the switch. Conversely, samples going from higher to lower temperatures experienced a sudden drop of their properties. So, it has been proved that the final state of the parameters of the sample does not depend on the previous history of the sample, but only on the final degradation temperature.

When the temperature coefficients were calculated, it was found that for *T-Solar* samples the temperature coefficient is almost canceled by the fast temperature change coefficient provided by the manufacturer, which points that, on the field, the seasonal effect is mostly due to spectral changes. For UB cells, it was found that the coefficients for fill factor and efficiency are quite larger than those in commercial cells. This indicates that higher LID is produced in these samples.

After being studied as active layer, the a-Si:H deposited in the UB was used as part of c-Si solar cells in a series of experiments developed in collaboration with the Universitat Politècnica de Catalunya (UPC). First, the role of sputtered alumina combined with a-Si:H in passivation was studied. A very thin layer of a-Si:H was deposited over the crystalline wafer to act as intermediate layer before the alumina deposition by sputtering. This a-Si:H layer has a double function: it acts as physical barrier that protects the wafer from the ion bombardment in the sputtering process; and it also serves as a hydrogen source that contributes to the saturation of surface defects, helping passivation. The carrier lifetimes obtained with the a-Si:H layer are more than one order of magnitude higher than those without it. Furthermore, the results of passivation with alumina with *i* a-Si:H layer are promising to be used as an alternative in c-Si technologies.

Contents

Finally, some materials (*i* a-Si:H, *p* a-Si:H and *p* μ c-Si:H) deposited at the UB reactor were used to develop a *p*-type emitter on an *n*-wafer aiming to reproduce the results obtained with *n*-emitter over *p*-wafer. A reoptimization of these materials for this purpose was done, finding that raising the deposition temperature is beneficial. ITO deposited at the UB was also optimized to be the front contact substituting the one deposited at the UPC, obtaining an absolute increment of 3% in the efficiency of the devices with *n*-emitter. On the other hand, the thickness of the *p*-layers for the emitter was adjusted based on their performance in an a-Si:H solar cell. The open circuit voltage is good (0.875 V), but the absorption on the blue part of the spectrum has still to be minimized. The first trials of UB *p*-emitters showed values of the lifetimes which are still lower than expected, and limited by the passivation of the a-Si:H. A study on the influence of carbon concentration and deposition temperature in a-Si:H passivation was also developed, obtaining that including some methane in the plasma and increasing the temperature help passivation. Further experiments are needed in this field as these are the results of the first trials.

Resumen

El silicio amorfo hidrogenado (a-Si:H) ha sido estudiado y empleado en células solares fotovoltaicas durante más de cincuenta años. Es utilizado como capa activa en la tecnología de lámina delgada, ya sea en células solares independientes o como parte de células tándem o multiunión. Recientemente, los récords de eficiencia en células de a-Si:H y en células tándem que incluyen a-Si:H han sido batidos, probando que aún existe la posibilidad de mejorar el rendimiento de las tecnologías que emplean silicio amorfo como capa activa. Por otro lado, el a-Si:H es utilizado también como material complementario en otras tecnologías, especialmente en células de heterounión con capa intrínseca delgada (HIT). El objetivo principal de este trabajo es estudiar y optimizar el silicio amorfo depositado en un reactor PECVD de reciente adquisición, consiguiendo que sea adecuado para ser utilizado en células de lámina delgada y como parte de células basadas en silicio cristalino.

En primer lugar, se realizó la optimización del silicio amorfo (tanto intrínseco como dopado) en lámina delgada de modo independiente, basándose en varias propiedades ópticas y eléctricas, como absorbancia, gap entre bandas (Tauc), conductividad en oscuridad, energía de activación y fotoconductividad. En lo que al silicio amorfo empleado como capa activa se refiere, se han realizado series en tres parámetros diferentes. La primera serie reveló una importante dependencia de las propiedades con el nivel de agotamiento del silano, presentando un marcado máximo para la velocidad de depósito en los valores centrales, tendencia que se observa también en el resto de propiedades. Este comportamiento surge a consecuencia de la contribución de dos mecanismos durante el depósito asistido por plasma, que alcanzan el equilibrio en dichos valores centrales. Las condiciones más adecuadas son las correspondientes a valores bajos de agotamiento. En cuanto a la serie en flujo de hidrógeno, se encontró un punto óptimo para una relación de 2 a 1 de flujo de hidrógeno sobre flujo

Contents

de silano. Se encontró que valores más altos de dilución resultaban en una mala adhesión de las capas en el sustrato. La serie en temperatura, por su parte, reveló que la temperatura tiene una menor influencia. A pesar de que las capas a mayor temperatura mostraban parámetros ligeramente mejores, la que se seleccionó como óptima es 200°C, a fin de no reducir el valor potencial del voltaje de circuito abierto en dispositivo.

El material dopado tipo p (tanto amorfo como microcristalino) fue también optimizado para usarse como capa dopada en células solares de lámina delgada. A través de las series realizadas para el material p amorfo (flujo de TMB, temperatura, presión y flujo de metano) se obtuvo material con calidad suficiente para ser empleado en dispositivo, con una conductividad de $1,1 \cdot 10^{-5}$ S/cm, una energía de activación de 0,43 eV y un gap de 2,02 eV. Para el material p microcristalino, se obtuvo igualmente material de calidad para dispositivo a través de cuatro series (temperatura, flujo de TMB, potencia y flujo de silano), con una conductividad de 1,32 S/cm, un gap de 2,07 eV y un factor de cristalinidad de 0,596. Con las capas optimizadas, se realizaron experimentos sobre dispositivos completos. La optimización del espesor de la capa dopada frontal y del reflector posterior permitieron obtener incrementos en la corriente de cortocircuito del 11% y 12% respectivamente, y otras mejoras menores en otros parámetros. Finalmente, una célula PIN funcional fue depositada enteramente en la UB con una eficiencia del 7,08%. Este valor es aún bajo comparado con el estado del arte, debido a un voltaje en circuito abierto y una corriente de cortocircuito bajos.

En la línea de incrementar el voltaje en circuito abierto en células solares de silicio en lámina delgada, un estudio en células de silicio polimorfo (pm-Si:H) en ambas configuraciones (PIN y NIP) se realizó en el Laboratoire de Physique des Interfaces et des Couches Minces (LPCIM), en Palaiseau. Se probó que depositar una capa de a-Si:H intermedia antes de depositar el pm-Si:H produce un aumento del voltaje en circuito abierto debido a la formación de una mejor interficie con el óxido de silicio microcristalino de la capa dopada. Por el contrario, si el silicio amorfo se deposita después del material polimorfo y justo antes del óxido de silicio microcristalino, el rendimiento de la célula se ve gravemente reducido. Esto es probablemente debido a que el óxido de silicio mi-

crocristalino no crece bien sobre el silicio amorfo y por tanto la célula falla.

Uno de los puntos clave en la optimización real del silicio amorfo es estudiar cómo le afecta la degradación por iluminación (LID). Para ello, se ha diseñado y construido un dispositivo de degradación por iluminación de bajo coste basado en LEDs. La inclusión de varias plataformas cuya temperatura puede ajustarse independientemente permitió la realización de experimentos acerca del efecto estacional de la LID en el silicio amorfo. Antes de realizar experimentos sobre efecto estacional, se ha realizado una optimización del espesor de la capa intrínseca, obteniendo 200 nm como espesor óptimo. Los resultados se explicaron empleando un modelo sencillo basado en el producto entre la movilidad y el tiempo de vida de los portadores.

En el estudio del rol de la temperatura en el efecto estacional, se han realizado experimentos de degradación sobre células extraídas de la línea de producción de módulos de *T-Solar* y células de laboratorio de la UB; realizando cambios en la temperatura tras diferentes fases de degradación (1000 h). El hecho de que todas las degradaciones se realizaron con idéntica iluminación constante permite eliminar el efecto espectral y estudiar el efecto real de la temperatura. Las células que pasaron de temperaturas más bajas a más altas experimentaron una recuperación en sus propiedades en un periodo inferior a 10 horas tras el cambio. Por el contrario, las muestras que pasaron de temperaturas más altas a otras más bajas sufrieron una brusca disminución de sus propiedades. Por tanto, se ha demostrado que el estado final no depende de la historia de la célula, sino solamente de la temperatura final de degradación.

Cuando los coeficientes de temperatura fueron calculados, se encontró que el coeficiente obtenido para las células de *T-Solar* es prácticamente cancelado por el coeficiente para cambios rápidos de temperatura proporcionado por el fabricante, lo que apunta a que la mayoría de del efecto estacional en módulos operativos es causado por el efecto espectral. Por otro lado, los valores de los coeficientes obtenidos para las células de la UB son bastante mayores que los obtenidos para células comerciales, lo que sugiere la necesidad de una mayor optimización del dispositivo de la UB contra la degradación.

Contents

Tras estudiar su papel como capa activa, el silicio amorfo depositado en la UB fue empleado como parte de dispositivos de silicio cristalino (c-Si) en una serie de experimentos realizados en colaboración con la Universitat Politècnica de Catalunya (UPC). Primero, se estudió el uso de alúmina depositada por sputtering combinada con silicio amorfo en pasivación. Una capa muy delgada de silicio amorfo se depositó sobre la oblea antes de depositar la alúmina por sputtering. El silicio amorfo cumple una doble función: proporciona una barrera física que protege a la oblea del bombardeo de iones del sputtering; y sirve además como fuente de hidrógeno para la saturación de defectos en la superficie, ayudando a la pasivación. La vida media de los portadores obtenida en las muestras con silicio amorfo es más de un orden de magnitud superior a aquellas que no lo tienen. Los valores obtenidos en pasivación con alumina y a-Si:H son prometedores para su uso como alternativa a otros materiales y técnicas.

Finalmente, algunos materiales (*i* a-Si:H, *p* a-Si:H y *p* μ c-Si:H) depositados en la UB han sido empleados para desarrollar un emisor tipo *p* sobre oblea tipo *n*, intentando reproducir los resultados obtenidos con emisores tipo *n* sobre oblea *p*. Una reoptimización de los materiales para este uso fue realizada, descubriendo que aumentar la temperatura es beneficioso. También se optimizó ITO depositado en la UB para ser utilizado como contacto frontal en lugar del depositado en la UPC, obteniendo una mejora absoluta del 3% en la eficiencia en dispositivos con emisor tipo *n*. Por otro lado, el espesor de las capas del emisor tipo *p* se ajustó en función de su funcionamiento en células de silicio amorfo. El voltaje en circuito abierto presenta un buen valor (0,875 V) pero la absorción en la parte azul del espectro tiene que ser aún minimizada. Las primeras pruebas de emisores presentaron valores de tiempo de vida bajos, limitados por la pasivación del silicio amorfo. Se realizó un estudio sobre la influencia de la concentración de carbono y la temperatura de depósito en la pasivación con a-Si:H, encontrando que incluir metano en el plasma y aumentar la temperatura es beneficioso. Se requieren más experimentos en este campo, dado que esto son aún los resultados de las primeras pruebas.

1 Introduction

1.1 The importance of renewable energies: The role of solar photovoltaic (PV) energy.

The world population has experienced a tremendous growth in the last 65 years. In 1950 it was around 2.5 billion people; now it is 7.3 billion, almost three times larger. This, combined with the changes in human lifestyle, makes the energy demand greater than ever. In this scenario, the global energy consumption in 2014 was approximately 13000 Mtoe [1], and 78.3% is still produced by fossil fuels [2]. This fact is troublesome, because fossil fuels are bound to be exhausted at some point, and also because of the environmental issues associated with them, specially with CO₂ emissions [3]. The role of renewable energies in electricity production has been slightly increasing in the last 15 years, reaching 22.8% of estimated energy share of global production. Most of this production is achieved by hydropower (16.6%), being the role of solar photovoltaics (PV) 0.9% [2].

However, although the contribution of solar PV energy is still low, its role has been becoming more important in the last ten years, being the solar PV global capacity 177 GW, after its value has increased 60 times in the last 10 years. The strong global demand has produced a recovery in the solar PV industry during the last two years. It can be seen at Fig. 1.1 that the growth of the solar PV global capacity in 2013 and 2014 is as large as 38 and 39 GW respectively. This is associated to an important decrease in the cost in PV electricity during the last years [4]. The evolution in the United States can be observed in Fig. 1.2, but this tendency is extendable to all over the world. This has allowed solar energy to become more competitive against fossil fuels. However, its use has still to be encouraged as its role in the global energy market is still low.

1 Introduction

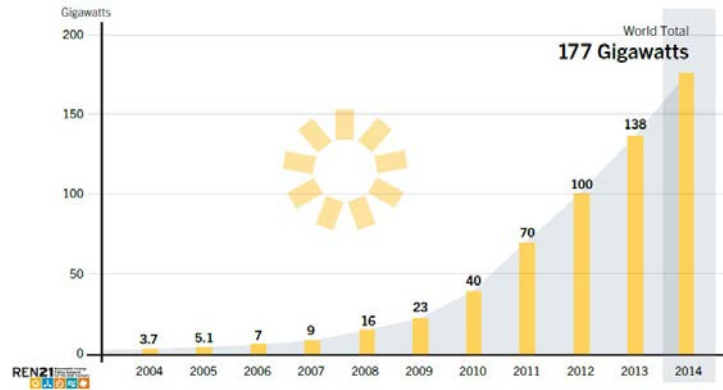


Figure 1.1: Solar PV global capacity, 2004-2014. Courtesy of REN21, 2015, *Renewables 2015 Global Status Report* (ISBN 978-3-9815934-6-4) [2].

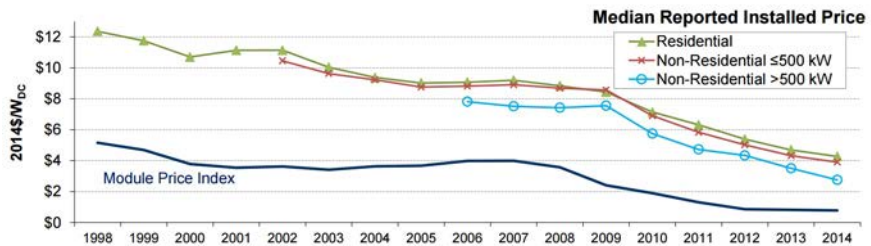


Figure 1.2: Median reported installed prices of residential and non-residential PV systems over time in the United States. This plot is extracted from SunShot Photovoltaic System Pricing Trends 2015 edition, courtesy of the National Renewable Energy Laboratory (NREL), Golden, CO. [4].

1.2 Solar photovoltaic technologies

1.2.1 Principle of operation of solar cells

PV technologies receive their name following the process that rules them, this is, photovoltaic effect. It is the phenomenon that allows a semiconductor material to convert incident light into electric current. When a photon incides over a semiconductor material, if its energy is higher than

the band gap of the material, it is absorbed and its energy is transferred to an electron, which can then escape from its normal position. The electrons jump (energetically) to the conduction band, leaving electron vacancies in the valence band (holes). If the semiconductor is somehow included in an electric circuit, the electrons can be collected as electric current. So essentially, a solar cell is a rectifying junction that favors the carrier collection by separating the electrons and the holes. This work will present a basic explanation; some bibliography can be consulted for more exhaustive explanations [5][6].

The electric behavior of a pn junction can be described using the diode equation, which relates the current density through the junction as a function of the applied voltage. For an ideal diode, this equation is as follows:

$$J = J_0(e^{(qV/\kappa T)} - 1) - J_L \quad (1.1)$$

where J_0 is the saturation density current, q is the elemental charge, κ is the Boltzmann's constant and T is the temperature. J_L is a parameter that represents the photogenerated current when the cell is under illumination. If a real diode is considered the equation is as follows:

$$J = J_0(e^{(q(V-R_s J)/n\kappa T)} - 1) + \frac{V - R_s J}{R_p} - J_L \quad (1.2)$$

Here, several effects present in the real cell are taken into account. n is an ideality factor that serves to evaluate the effect of the recombination, and R_s and R_p are the series and parallel resistances, which are related with the ohmic contacts and leak currents respectively.

There are several characteristic parameters that are used to evaluate the quality of the cell, like the short circuit current density (J_{sc}), open circuit voltage (V_{oc}) or fill factor (FF). Chapter 2, Sec. 2.3.5.1 presents a description of these parameters and the two parasitic resistances.

The typical and most simple configuration of a solar cell is a pn junction, in which one type of the layers is thinner and is called emitter and the other is quite thicker and called base or absorber, and is responsible of most of the light absorption. However, during the development of photovoltaic technologies, this structure has evolved and has been modified,

1 Introduction

and different materials have been tried on it, all aiming to increase the conversion efficiency and reduce the manufacturing costs. The specific materials and structures used in this thesis work will be presented with more detail in the next sections.

1.2.2 Use of silicon in solar cells

PV solar cells are then based on semiconductor materials that produce direct conversion of light into electricity. There are several materials and technologies that are used with this purpose. Silicon properties make it suitable for PV technology, it is very abundant (second element on the Earth's crust), economic and non-toxic. This results into the fact that the most employed technology by far is wafer-based crystalline silicon, covering an 85% of the market [7]; and also that the most developed technology is based on silicon. More accurately, monocrystalline silicon (c-Si) technology shows the highest efficiency conversion rates, of 25.6% for cells and 22.9% for modules [8]. In the first case, the technology used is Heterojunction with Intrinsic Thin layer (HIT) rear junction solar cells [9] and in the second is Passivated Emitter Rear Locally diffused (PERL) cell technology [10]. The main drawback of technologies involving c-Si is that some necessary processes like silicon purification and monocrystal wafer growth imply high manufacturing costs.

Several alternative technologies try to overcome this problem. Polycrystalline silicon (p-Si) is an interesting alternative, as p-Si wafers are cheaper to fabricate keeping a similar material. In this case, the silicon is melted and when it cools, it crystallizes forming random crystals of varying sizes. This process lowers the cost, but also the efficiency is reduced (21.25% for cells [11] and 19.2% [12] for modules). The second generation solar cells, this is thin film (TF) technologies, aimed to make the production less expensive by reducing the quantity of used material between 2 and 3 orders of magnitude, while making possible the use of large area substrates like metal, glass or even flexible plastics. Among TF technologies, the most used is cadmium telluride (CdTe) technology, which has proved itself capable of achieving module efficiencies as high as 18.6% [13]. However, it presents two main disadvantages, which are

the toxicity of Cd and the low availability of Te. This situation is also present in other thin film technologies involving materials such as Gallium Arsenide (GaAs), Cadmium Indium Gallium Selenide (CIGS) or Indium phosphide (InP).

The second most used thin film technology is based again on silicon, which allows to overcome the material issues present in other TF technologies. The drawback here is that the reached conversion efficiencies are quite low in comparison. Thin film silicon cells can present as active material hydrogenated amorphous silicon (a-Si:H) or hydrogenated microcrystalline silicon (μ c-Si:H). a-Si:H is easy and cheap to implement and has a high absorption coefficient, plus devices made of it present higher open circuit voltage (≈ 0.9 V). On the other hand, its band gap is larger (≈ 1.7 eV) and it presents light induced degradation (LID). The record efficiency in cells for a-Si:H is 10.2% [14]. μ c-Si:H is stable against LID, its band gap is 1.1 eV and it presents higher short circuit currents. On the contrary it is more difficult to deposit, its absorption coefficient is lower, its open circuit voltage in devices is lower and it can be affected by oxidation. The record efficiency for μ c-Si:H cells is 11.4% [15]. Commonly, cells made of this two materials are combined in stacks to achieve higher efficiencies in the so called multijunction or tandem technology. The record a-Si:H/ μ c-Si:H tandem cell has an efficiency of 12.7% [16], and 12.3% for the module [17].

Some other PV technologies are being used and developed in order to increase or at least maintain the efficiencies while the cost is reduced and the environmental issues are avoided. This is the third generation solar cells, which include the use of new concepts like light concentrator systems, nanostructured materials (like nanowires), up- and down- converters, hot carrier solar cells, etc. Also, new materials are being employed, like organic solar cells made of polymers, and the rising perovskite technology. Fig. 1.3 shows the evolution of the conversion efficiencies reached for different technologies. It is provided by the National Renewable Energy Laboratory (NREL) at the United States [18].

1 Introduction

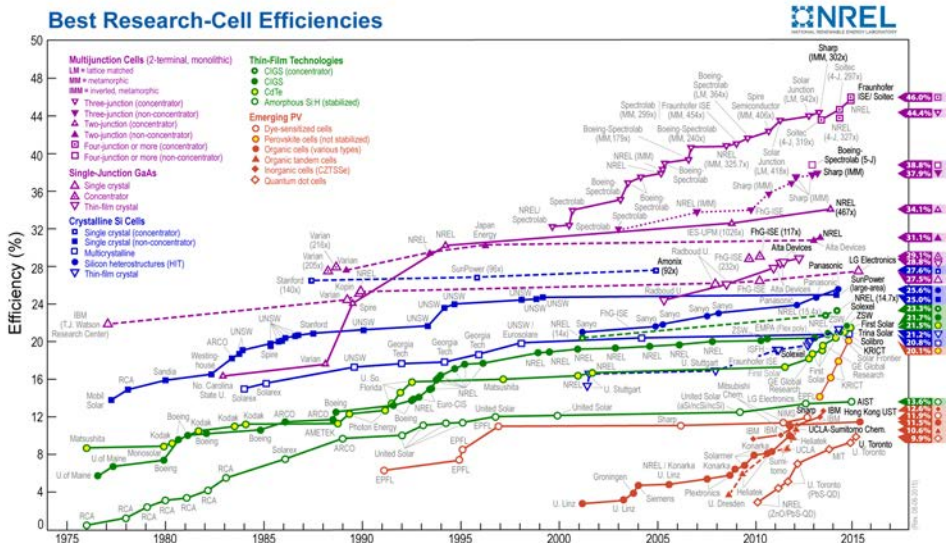


Figure 1.3: Evolution of the conversion efficiency of photovoltaic technologies. This plot is courtesy of the National Renewable Energy Laboratory (NREL), Golden, CO.

1.2.3 Technologies involved in this thesis work

Among the multiple technologies mentioned in the previous section, this thesis work is focused in the different roles of thin film silicon. The first is thin film silicon solar cells, based on *pin* junctions in which the active part is a-Si:H or μ c-Si:H (in this case, a-Si:H). The second is the role of thin films complementing c-Si wafer-based devices. These technologies are briefly explained next.

1.2.3.1 Thin film silicon solar cells

As it has been said, solar cells generate free electrons by photovoltaic effect and then collect them to create electric current. Thin film silicon technology is not an exception, but here the basic structure is a stack of thin silicon layers forming a *pin* junction (instead of a *pn* junction):

an intrinsic (non doped) a-Si:H layer between two thinner layers, one positively doped (p -type) and another negatively doped (n -type)[19]. The doped layers generate an internal electric field across the intrinsic layer [20]. When incident photons arrive at the device, if their energies are higher than the band gap, they are absorbed provoking the excitation of electrons from the valence band to the conduction band. Most of the photons that result in carrier generation are absorbed in the intrinsic layer, as it is thicker, so it is called active layer. The result is an excess of electrons on the conduction band and an excess of holes in the valence band. The internal field created by the doped layers separates the electrons and the holes, and finally they are collected by two electrodes. One of the most important issues in this devices is to avoid that the electrons and the holes cancel each other before they are collected, a process called recombination. This usually happens when the carriers can go to intermediate states in the band gap, this is, defects [21]. So, the quality of the material is critical to obtain good performance.

The light always enters through the front electrode and then crosses p -layer. The reason to do so is that, in this situation, the holes have to travel shorter distances before they can be collected, which is desirable as they have lower mobility. After, most of the light is absorbed by the intrinsic layer. The non-absorbed light at this point traverses the n -layer and reaches the back electrode. Then, a reflective layer (normally aluminum or silver) is placed at the end of the cell in order to act as electrode but also to reflect the remaining light back into the cell, providing a second chance for it to be absorbed. A Transparent Conductive Oxide (TCO) layer is deposited between the n -layer and the metal to increase the reflectivity [22]. This stack of layers after the n -layer is called back reflector (BR). With this in mind, the front electrode has to be conductive to collect the carriers, but also transparent to let the light go through it; on the other hand, the back reflector, has to present also high conductivity plus high reflectivity [23]. Transparent conductive oxides like Fluorine doped Tin Oxide ($\text{SnO}_2\text{:F}$), Indium Tin Oxide (ITO) or doped Zinc Oxide (ZnO) are commonly employed in both contacts.

Apart from the active layer material, thin film cells can be classified depending on the order of deposition of the layers. The deposition order is

1 Introduction

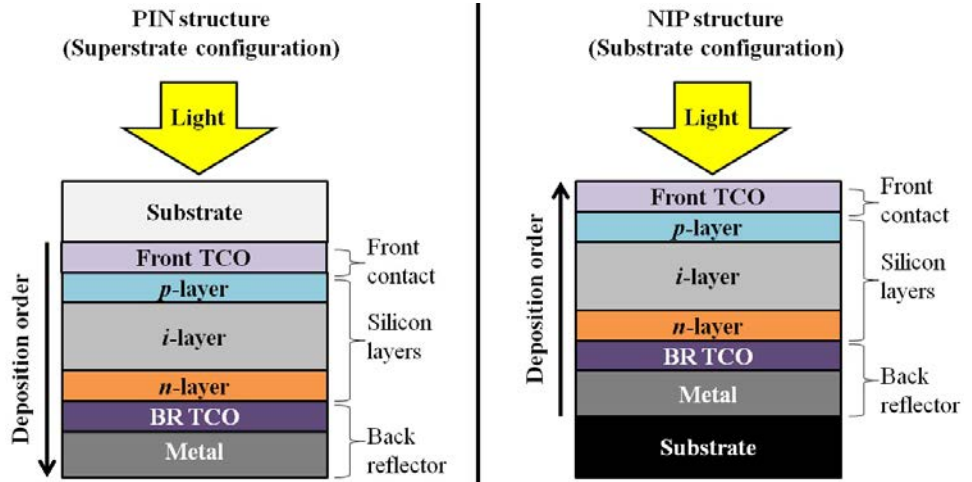


Figure 1.4: Schematic structure of a single junction silicon thin film solar cell in superstrate (left) and substrate (right) configuration. The layers are shown as flat to simplify, but they are normally textured.

important because when any layer is going to be deposited, it is necessary that the deposition process does not damage the existing material. So, depending on the deposition sequence, some processes are allowed or forbidden for different layers. In PIN structure, called superstrate configuration, the first deposited layer over the substrate is the front electrode, then the p -, i - and n - layers, and finally the back reflector. In this configuration, the light enters across the substrate, so it has to be transparent. In the NIP structure, this is substrate configuration, the first deposited layer is the rear metalization for the BR. This removes the need for the substrate of being transparent. Then, the n -, i - and p - layers are deposited, and finally, the front electrode. A scheme of a single solar cell in both configurations is shown in Fig. 1.4. The layers are pictured as flat layers, but normally they are textured in order to enhance the light path, providing higher probability of absorption [24]. This is called light-trapping, and it has been widely studied in previous group work [25][26][27].

1.2.3.2 Thin film technologies for c-Si wafer based solar cells

There are several photovoltaic technologies involving c-Si. The standard c-Si cell is a pn junction formed by diffusing phosphorous atoms in a p -type wafer to form an n -type emitter. It is also usual to diffuse aluminum to form a p^+ layer at the rear side of the cell. The front contacts are deposited or printed on top of the emitter. Several modifications have been developed in the basic c-Si solar cell structure along its history, aiming to obtain higher efficiencies.

- Screen-printed solar cells have been deposited since the 1970s. Their main advantage is the simplicity of the process. The n -dopant is thermally incorporated in the p -wafer to form the emitter. Then, the front contacts are developed forcing a metal paste (usually silver) to go through a metallic mask to develop the front grid [28]. Finally, the rear contact is also made with a metallic paste, in this case normally aluminum. The main drawback is that there are several high temperature processes involved.
- Buried contact solar cells present a configuration based on the insertion of the metal front contact into grooves made in the front side of the solar cell [29]. After the emitter is diffused, several grooves are made in the front side of the cell (either by laser or mechanically), and a second (and heavier) diffusion is made to create highly reverse-doped zones in the cell. Then, the grooves are filled with metal, finishing the contact. The rear contact is still made of thermally diffused aluminum. The main advantage over screen print solar cells is that the shading effect of the top contact is greatly reduced.
- To further reduce the shading, other configuration is the interdigitated back contact (IBC) solar cells [30]. In this configuration, both front and back contact are placed in the rear side of the cell. p and n diffusions are performed in the rear side to obtain alternated positive and negative contacts in the rear side. This configuration prevents shading losses and makes possible the interconnection with smartwire modules [31]. However, it is only useful in high quality thin wafers, or the carriers generated in the top part of the cell will recombine before reaching the electrodes.

1 Introduction

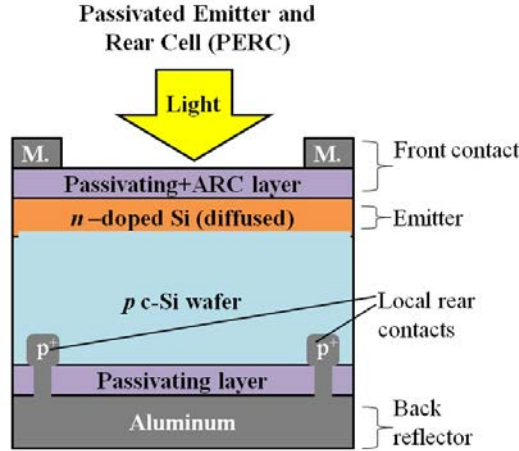


Figure 1.5: Schematic structure of a PERC silicon solar cell. In this case, a p -wafer with n -emitter is shown. The layers are shown as flat to simplify, but they are normally textured.

- One of the main problems of the previous configurations is that the recombination in the rear surface of the cell is high, as the electrode is in direct contact with the c -Si. One of the most important advances in c -Si solar cells was to reduce this effect by implementing the so called Passivated Emitter and Rear point contacted Cell (PERC) [32] configuration. In this case, both the diffused emitter and the rear side of the wafer are covered with a passivating layer, so the back contact is only contacting the c -Si on a reduced area point contact. To develop these contacts, processes like screen printing or laser fired diffusion are used. As it has been said, a variation of this structure, the Passivated Emitter Rear Locally diffused contact (PERL) solar cell technology [10] has the second highest reported efficiency. Some of the work in Chapter 5 is related to the rear part of the PERC structure, so a simple scheme is shown in Fig. 1.5.

The technologies mentioned before still share an important drawback: the need of develop the emitters by thermal diffusion, which means an important energy budget in the cell fabrication process. Silicon heterojunction solar cells are able to overcome this problem. Silicon

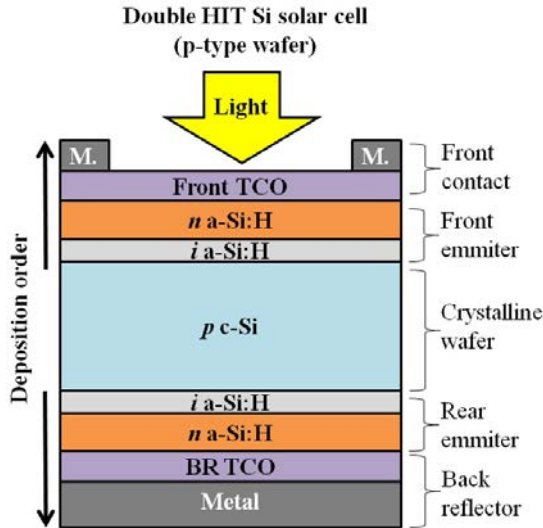


Figure 1.6: Schematic structure of a double junction HIT silicon solar cell. In this case, a p -wafer with n -emitters is shown. The layers are shown as flat to simplify, but they are normally textured.

heterojunction (SHJ) solar cells are obtained by depositing (by different techniques) thin layers of amorphous or microcrystalline silicon over crystalline silicon wafers to form the pn junction instead of diffusing the dopant on the wafer. So, the name 'heterojunction' makes reference to the fact that there are two different materials forming the pn junction. It was first reported by Fuhs in 1974 [33] and the first cell was deposited by Hamakawa *et al.* in 1983 [34] with efficiencies about 8%. Since then, the heterojunction had been widely studied as a consequence of the important advantage of being able to develop emitters at low temperature. They can be p a-Si:H over n -type c-Si wafers, or conversely, n a-Si:H over p c-Si wafers. Then, the TCOs are deposited and metallic contacts are developed. If this structure is implemented in both sides of the wafer, a double heterojunction solar cell is obtained.

One of the most important developments done in heterojunction technology was the introduction of a very thin intrinsic layer of a-Si:H

1 Introduction

between the doped a-Si:H and c-Si wafer. This intrinsic layer provides better surface passivation, which results in a lower saturation current and then in a higher V_{oc} than traditional technologies, and so the performance of the devices is increased. This conforms the so called Heterojunction with Intrinsic Thin layer (HIT) technology, first reported by Sanyo-Panasonic [35]. Nowadays, combining HIT technology (Sanyo-Panasonic) with interdigitated back-contact structure has made possible to reach an absolute efficiency record of 25.6% [9]. A scheme of a standard double HIT solar cell is shown in Fig. 1.6, and just like in the previous case, the layers are shown as flat while they are normally textured.

The technology involving heterojunction is currently highly investigated to improve the conversion efficiency. One of the most researched topics to obtain a better performance in this kind of devices is to enhance the passivation by using different configurations, techniques and materials. This is why the research on SHJ and HIT technology has been gaining relevance in the last years.

1.3 Hydrogenated amorphous silicon

The most studied material in this thesis is hydrogenated amorphous silicon, as it is used to develop thin film solar cells and to passivate crystalline wafers for c-Si based devices. Research on amorphous silicon has been developed for over fifty years. In 1965 Sterling and Swann first published the formation of silicon from silane through glow discharge [36], and ten years later, Spear and LeComber demonstrated that it was possible to dope the material both p - and n -type [37]. The first reported amorphous silicon solar cell was deposited by Carlson and Wronski in 1976 with an efficiency of 2.4% [19]. During the next years the investigation on a-Si:H solar cells experienced a great expansion and important improvements were achieved and traduced into a substantial growth in the conversion efficiency. However, since 1996 this growth slowed significantly for TF solar cells with a-Si:H as active layer (See Fig. 1.3). On the other hand, amorphous silicon has recently gained relevance to be used combined with other technologies, specially with crystalline silicon as passivating layer.

1.3.1 Advantages and drawbacks of a-Si:H

A full detailed description of the structure and the properties of amorphous silicon is out of the objective of this thesis. The interested reader can consult the book of R.A. Street for a complete study of a-Si:H [38]. However, to understand the work involved in this thesis it is necessary to point some of the main advantages and drawbacks of this material involving its use in solar cells. First, the main advantages for a-Si:H are summarized:

- Silicon based technology: It is evident that, being a technology based completely in silicon, it benefits of all the advantages associated to the use of this material. These are high availability traduced in lower cost, and non-toxic nor environmental harmful processes and waste products.
- Reduction of the material quantity: Amorphous silicon presents a higher band gap than crystalline silicon (1.7 vs. 1.1 eV approximately). This is initially a drawback because less photons are already theoretically bound not to be absorbed. However, c-Si is an indirect band gap semiconductor, which means that the minimum of the conduction band is not at the same crystal-momentum as the maximum of the valence band. This implies that a phonon is required to produce the band transition, lowering the absorption probability. In contrast, amorphous silicon presents less defined bands and the minimum of the conduction band and the maximum of valence band are closer, which leads to a much higher absorption rate [39]. In the end, this causes that the thickness of a-Si:H necessary to absorb the most of the photons over its band gap is around 1000 times less than the one needed for c-Si. This is why a-Si:H is an excellent candidate for thin film silicon solar cells, providing an important saving of precursor material [40].
- Low temperature production processes: While some steps in other technologies, like c-Si, require high temperature processes, the whole fabrication of thin film a-Si:H solar cells can be performed at temperatures below 300°C. This not only causes a reduction of the energy

1 Introduction

budget involved in the fabrication, but also permits the deposition of the cells over several substrates that can not be heated over a limiting temperature for different reasons. Certain glasses or plastic flexible foils are examples of these substrates.

- Scalable to large areas: The deposition techniques commonly used for a-Si:H solar cells in the laboratory are much easier to upscale to large areas than those for other technologies. This has an important industrial interest as it is possible to deposit very large substrates (sometimes over 5 m²) and then scribe the contacts by laser means, producing a cost reduction versus the individual soldering used for c-Si wafer cells.
- High energy yield and low payback time: It has been studied in power plants that a-Si:H modules present a higher energy yield than c-Si, due to their lower temperature coefficients [41]. Besides, less time is required to recover the employed energy in comparison with other technologies [42].

On the other hand, amorphous silicon presents some inconvenient features when it comes to be used as active material for solar cells. The main drawbacks are summarized next:

- Low conversion efficiencies: The higher band gap of a-Si:H causes that photons between 1.1 and 1.7 eV that would be absorbed by c-Si are, in this case, lost. This results in a theoretical reduction of the maximum efficiency that could be achieved. Furthermore, the amorphous nature of the material causes that the quality is intrinsically lower [43]. The coordination index of a-S:H is less than 4, which means that some silicon atoms are not linked to other four silicon atoms. The remaining links are normally filled with hydrogen atoms, but sometimes they are left vacant. This hydrogen absences are defects that act as recombination centers which provoke that carrier mobilities and lifetimes are much lower in a-Si:H than those found in crystalline material.
- Need of encapsulation: Some layers used in thin film silicon solar cells (specially those including microcrystalline layers or Aluminum Doped Zinc Oxide (ZnO:Al) as TCO) are affected by environmental

1.4 Fundamentals on Plasma Enhanced Chemical Vapor Deposition (PECVD)

issues, mainly humidity and dust. Then, encapsulation is needed to maintain the performance of the devices, causing an increase in the weight of the modules and the production cost.

- Light induced degradation: Maybe the most important drawback of amorphous silicon is that it experiences an important degradation of its properties during the first 1000 hours of illumination approximately. This causes a decrease in the cell parameters that leads to a significant loss in the conversion efficiency. Light induced degradation was first reported by Staebler and Wronski [44], so it is commonly called Staebler-Wronski effect (SWE). Several models have been developed to explain this phenomena, but it consists essentially in the creation of defects caused by light. SWE and its consequences are described and studied in detail in Chapter 4.

The drop in production prices of c-Si modules and the fact that the efficiency of amorphous silicon thin film solar cells has barely increased through the last 20 years has caused that a-Si:H has lost importance in PV market. However, the efficiency records in single a-Si:H cell and tandem structure with a-Si:H as top cell have been recently beaten in 2013, reaching 10.2% and 12.7% respectively [14][16], which proves that this technology still offers opportunities to research. Plus, amorphous silicon has been gaining relevance in the last few years as complement for other technologies, specially in heterojunction technology. The role of a-Si:H in c-Si based technologies is studied with more detail in Chapter 5.

1.4 Fundamentals on Plasma Enhanced Chemical Vapor Deposition (PECVD)

PECVD is the most extended technique to deposit hydrogenated amorphous and microcrystalline silicon. To obtain a-Si:H through classical Chemical Vapor Deposition (CVD), silane can be thermally decomposed between 450°C and 550°C. However, at this temperature hydrogen is not retained, so the films are very defective. On the contrary, in PECVD, the energy to dissociate the molecules is not provided thermally but by the plasma discharge instead. This makes possible to deposit the material

1 Introduction

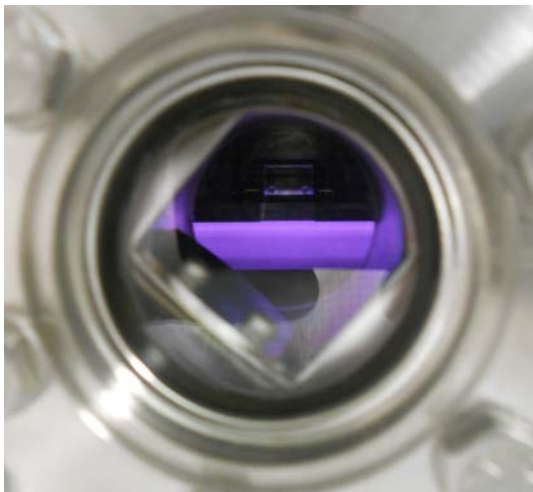


Figure 1.7: Photography of a plasma glow discharge in the PECVD reactor at the UB.

at lower temperatures in which hydrogen is retained [38], and then it is possible to obtain thin films of a-Si:H and $\mu\text{c-Si:H}$ of higher quality.

So, essentially PECVD consists in a glow discharge technique in which precursor gases (which in the case of a-Si:H are usually silane plus different doping or alloying gases) flow into a vacuum chamber, in which a plasma is initiated and maintained between two parallel plates which provide an electric field. This electric field can be either direct current (DC) or radio frequency (RF) (13.56 - 200 MHz), being this last the most common, as it allows the deposition over non conductive substrates. Pressure is typically maintained between 10 and 500 Pa approximately, depending on which type of material is being deposited. The geometry of the chamber is also important, and this is why the conditions that may work for one reactor are not optimal in a different one. A photograph of a plasma glow discharge in the UB reactor is shown in Fig. 1.7.

The deposition process is described in detail in Schropp *et al.* [23]. It can be summarized in four steps listed next:

1.5 Objectives and outlook of this thesis

1. Primary reactions in gas phase triggered by electron impact, causing excitation, dissociation and ionization of the precursor gases.
2. Secondary reactions where reactive species diffuse towards the substrate, positive ions bombard the growing film and negative ions are trapped and eventually pumped out or form dust. This is the phase which mostly controls the properties of the film.
3. Surface reactions, like hydrogen abstraction, radical diffusion and chemical bonding.
4. Surface release of hydrogen and silicon matrix relaxation.

All these processes are directly affected by a great number of parameters, which makes them difficult to control. Some of the properties that condition the plasma, and so the deposited films, are the power (P) and frequency (f) of the electric field, the geometry of the chamber (especially the distance between electrodes d_e), the process pressure (p), the composition, magnitude and pattern of precursor gases' flows (Φ), the substrate temperature (T_s), etc. Fundamental studies on plasma physics and its influence on the films have already been developed by several authors and are beyond the aim of this thesis; more useful information on this subject can be found in the bibliography [45][46][47].

The reactor at the UB used for this work is a multichamber reactor in cluster configuration. The electric field used for the plasma is a radio frequency (RF) field of 13.56 MHz. As this is the first thesis work developed with this equipment, it is described in full detail at Chapter 2, Sec. 2.1.1.

1.5 Objectives and outlook of this thesis

The recent acquisition of a multichamber PECVD reactor has conditioned most of the work in this thesis. Every equipment is different and the conditions that work for one might be completely unsuitable to another. This is why one of the main objectives of this thesis is obtaining and optimizing materials and devices deposited in this reactor, trying to

1 Introduction

reach the state of the art in photovoltaics. The aim is to obtain layers of device-quality material, both intrinsic and doped, and then complete solar cells whose performance are as close as possible to the state of the art. The most employed material is hydrogenated amorphous silicon, but also p -doped microcrystalline material is optimized. There are two main reasons to this choice: the first is that a-Si:H is probably the easiest material to develop in a new equipment, and the second and most important is that the group has previous important experience in working with this material [25][48][49][50][51][52][53][54][55][56][57].

In the context of improving a-Si:H solar cells, a stage of four months was done in the Laboratoire de Physique des Interfaces et des Couches Minces (LPICM) at L'École Polytechnique in Palaiseau. This group has broad experience working with amorphous silicon, having developed a special material called polymorphous silicon (pm-Si:H), which is deposited in the edge between amorphous and microcrystalline material. The work developed there aimed to increase the efficiency of single junction pm-Si:H cells over 10% stabilized [58][59] in both PIN and NIP configurations. Plus, the knowledge acquired there was then profited to improve the cells deposited at the UB.

Chapter 3 presents the experiments about development and optimization of solar cells in the new reactor. Numerous series varying several deposition conditions and techniques were developed for different materials. First, the optimization of materials in single layer is shown, including intrinsic and p -doped a-Si:H and p -doped μc -Si:H. Then, some experiments aiming to improve the complete device were developed. Finally, Sec. 3.6 refers itself to the work developed during the stage at the LPICM, involving open circuit voltage optimization in pm-Si:H solar cells.

Chapter 4 is dedicated to the experiments involving light induced degradation and seasonal effect, continuing previous group work [60] and as part of the optimization of the UB solar cells. First, an optimization of the i -layer thickness of the UB cell is developed. After, the results on the different degradation experiments concerning the seasonal effect and the real role of the temperature in LID are presented. They were done

1.5 Objectives and outlook of this thesis

over both commercial a-Si:H solar cells extracted from modules of the enterprise *T-Solar* and laboratory a-Si:H solar cells deposited at the UB. This allows to compare the behavior of a commercial tested cell and the device deposited in the laboratory.

Lastly, Chapter 5 treats the role of amorphous silicon in c-Si technology. The work in this chapter is developed in collaboration with the Universitat Politècnica de Catalunya (UPC), which has larger previous experience working on c-Si technology [61][62][63]. There are two main blocks in this chapter: the first studies passivation with alumina deposited by sputtering, and how a very thin layer of a-Si:H deposited by PECVD can improve the results by providing physical protection and serving as hydrogen source. The second is dedicated to the implementation of a *p*-type emitter to be deposited over a *n*-type wafer at the UB. The objective was to deposit the whole front part of the device at the UB. To achieve this goal, different materials are optimized to be used as part of the emitter and front TCO: Indium Tin Oxide (ITO), *p*-doped microcrystalline and amorphous silicon, and intrinsic a-Si:H. The first trials of complete devices with *p*-emitter are also shown and analyzed.

2 Experimental details

In this chapter, the equipments and techniques for deposition and characterization employed along this thesis work are described. The chapter is divided in three sections: Sec. 2.1 refers itself to the deposition equipments, especially focused on the PECVD reactor, as it is a recently acquired equipment that is first used for this thesis. One of the main objectives was to develop and optimize the deposition procedure and conditions specifically for this reactor. The equipment used to deposit transparent conductive oxides and metals, such as sputtering and thermal evaporator, is also described. In Sec. 2.2, some of the processes done on the samples before and after the deposition are explained, including the special case of light induced degradation. Sec. 2.3 gives an overview on the characterization techniques employed and the equipments used to measure the samples' properties, either single layers or cells.

2.1 Deposition methods

This section focuses specially on the PECVD reactor, including a detailed description and several schemes. The development of a working device with a minimum of quality whose silicon films were deposited with this reactor was one of the goals of this thesis. The sputtering and the thermal evaporator used for the front and back contacts of the cells are also described in this section. With these three equipments, whole working quality solar cells can be deposited completely at the UB.

During the stage at L'École Polytechnique, a different PECVD reactor (and also the rest of the equipment) was used. This equipment will be briefly described in the section corresponding to the work developed there (Chapter 3, Sec. 3.6).

2 Experimental details



Figure 2.1: Photography of the PECVD reactor in the cleanroom of the Universitat de Barcelona (before the HWCVD chamber installation.)

2.1.1 Plasma enhanced chemical vapor deposition

The equipment is shown in Fig. 2.1. It is a multichamber reactor in cluster configuration composed by a central distribution chamber that is used also as LoadLock (LL), with eight possible positions for different elements. At the moment, five positions are in use: two of them are for PECVD deposition chambers (DPC1 and DPC2), one is for the turbomolecular pump for the LoadLock and another one for the door to introduce the samples. The fifth used position corresponds to a HWCVD chamber which has been recently incorporated, but as it is not used in this thesis work, it will not be represented in the schematic views nor explained in detail. All the equipment is ultra high vacuum sealed.

The system is placed in a cleanroom ISO 7 (10000 class) in order to avoid contamination, as the particles over the substrate can lead to pinholes. A schematic view of the picture is shown in Fig. 2.2. As it has

been said, the HWCVD chamber, that would be placed in the position just behind the door, is not represented.

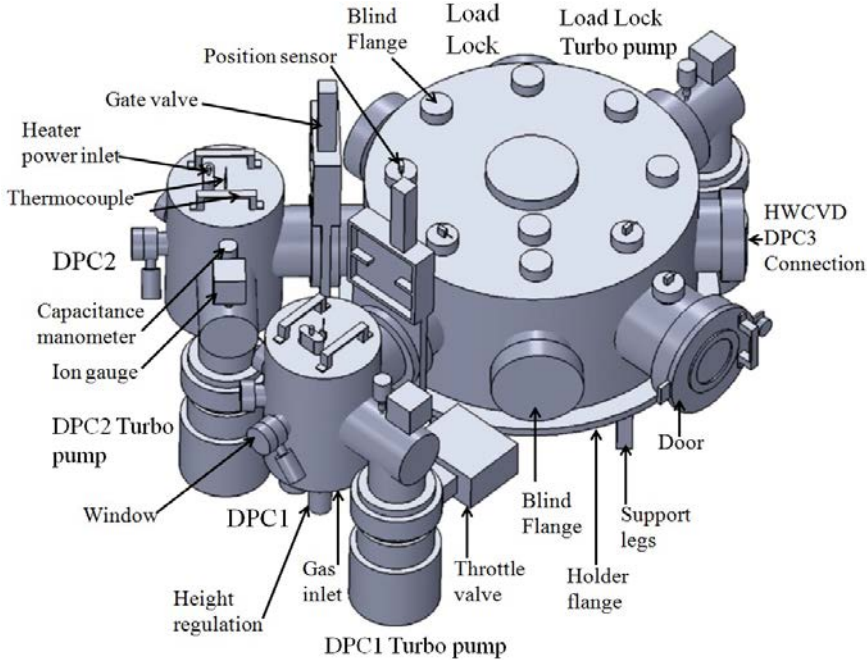


Figure 2.2: Schematic view of the equipment, with the conforming elements labeled.

The two plasma chambers with their corresponding pumps are identical. Since the beginning, DPC1 was assigned to deposit doped layers, while DPC2 was assigned to deposit intrinsic material only, in order to avoid any possible cross contamination [64][65] in the intrinsic material. However, this presents the problem that both *p*- and *n*-doped layers are deposited in the same chamber, and it could be possible that some cross contamination would appear due to the material deposited over the walls and electrode in previous depositions (history of the chamber). To avoid this, techniques as chamber evacuation [64] or starting the deposition with a different material [65] are used. In this work, to be sure that any possible cross contamination is avoided, an intrinsic a-Si:H layer of about

2 Experimental details

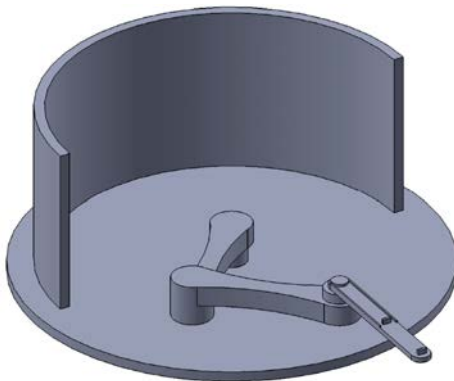


Figure 2.3: Schematic view of the inside of the LoadLock chamber, showing the robot used to move the samples.

200 nm is always deposited between depositions of different dopant gas, in order to cover any residual boron or phosphorus present in the chamber. This is called a 'burying layer'. The reproducibility of the doped layers using this technique has been successfully tested in the equipment by depositing alternatively p and n doped layers and comparing their properties.

The vacuum in the chambers is made through two different vacuum circuits, one for the LoadLock and one for the deposition chambers. In both cases, primary vacuum is made and then a turbomolecular pump starts functioning in each chamber to make high vacuum. For the LL circuit an *Adixen Pascal 2033 SD* rotary vane pump is used for primary vacuum and an *Elettrovava ETP450G* turbomolecular pump makes secondary vacuum, reaching values of 10^{-4} Pa. For all the deposition chambers, an *Adixen ACP120* roots primary dry pump is shared, and then, each chamber has an *Elettrovava ETP300G* turbomolecular pump. The vacuum in the DPC1 and DPC2 can reach values between 10^{-4} and 10^{-5} Pa, depending on the temperature and other conditions of the chamber. These values are measured with *IMG4000* ionization vacuum gauges placed in each chamber.

In order to move the substrates and the samples among the different

chambers of the reactor, a robot consisting in an articulated arm is used. A schematic view of the robot inside the LoadLock chamber can be seen in Fig. 2.3. It consists in a three-part arm with a central rotating point and two articulations in the arm. The whole system can go up and down in order to pick and place samples. In this scheme, the deposition chambers are not shown. These chambers are separated from the LL with *VAT10.8 DN150* ultrahigh vacuum gate valves, that only open and close when samples are moved, so the precursor gases never come out the deposition chambers. The position of the substrates and samples is followed by a series of *CX-44 SunX* photoelectric sensors, which control if there are any samples inside or in front of the chambers. This prevents any possible collision between the samples.

The interior of a plasma chamber can be seen in the left part of Fig. 2.4. The temperature of the substrate is controlled through an *Watlow EZ-Zone* autotune temperature controller that measures the temperature of the chamber with a thermocouple connected to the central lower part of the heater and then, if needed, provides power to the upper heater until the fixed temperature is reached. The substrate holder, placed downwards below the heater, functions as upper electrode, while the gas shower acts as lower electrode. Here, it is important to say that due to the fact that the heater is not in direct contact with the substrate holder and the thermocouple is actually measuring its temperature and not the samples' one, there is a shift between the temperature set and the real temperature of the substrate. The manufacturer provided a calibration which says that the substrate temperature is $2/3$ the set temperature, and some experiments developed with thermal indicator adhesive paper corroborated this factor. From now on, when a deposition temperature is given, it will be the real temperature of the substrate, and not the one set for the heater.

The separation between the electrodes can be varied by moving up and down the lower electrode. The precursor gases for the deposition come into the chamber through a pipe and then are distributed among the plasma area by the shower. The precursor gases are silane (SiH_4), methane (CH_4), hydrogen (H_2), H_2 -diluted phosphine (PH_3) and H_2 -diluted trimethylborane, commonly TMB ($\text{B}(\text{CH}_3)_3$). The flow of each precursor gas is controlled externally by a *MKS Mass Flo* flow controller.

2 Experimental details

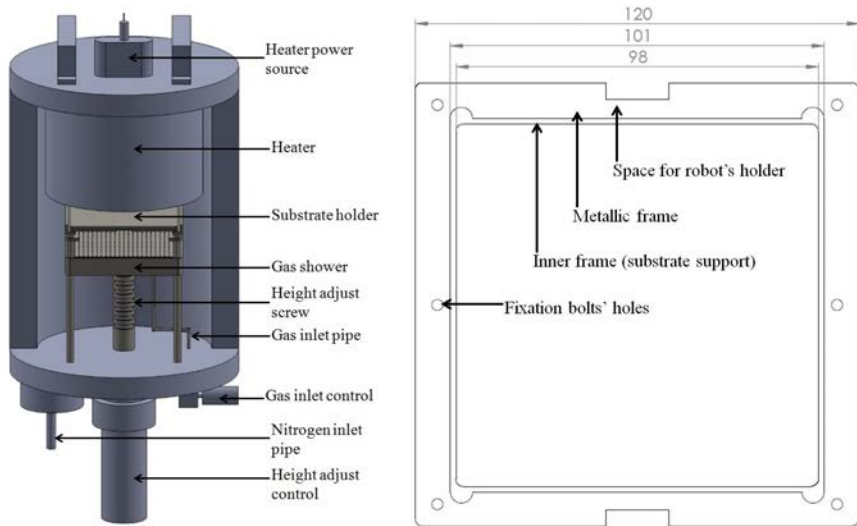


Figure 2.4: Left: Schematic view of the inside of the plasma deposition chambers. The outer elements have been removed for clarity. Right: Schematic view of the frontal piece of the substrate holder. The back piece is a whole piece, not a frame, but it has identical external shape.

Below in the chamber, there is also a nitrogen (N_2) inlet which is used to fill the chamber if needed. N_2 is also used to be injected in the lower part of the turbomolecular pumps to be used as pump purge gas, which means that during and after the depositions, N_2 is pumped in to dilute the active species in the vacuum system. This residual mixture of gases goes then through an *Edwards M150* gas reactor column. Also Argon (Ar) can be introduced in the chamber as manifold purge gas, and also to offer the possibility of making an Ar plasma in order to clean the substrate. Table 2.1 shows the characteristics of the gases used, all of them provided by *Praxair*. To control the pressure of the depositions, a control system similar to the temperature one is used. A *MKS Baratron 622B* measures the pressure and, if needed, a *VAT615* butterfly valve control opens or closes the way to the turbomolecular pump. This way, the pressure inside the chamber is controlled and kept constant (See Fig. 2.2). The whole system is operated through a Programmable Logic Controller (PLC) that

2.1 Deposition methods

controls all the mentioned equipments. The PLC control is done with a Profibus configurator program, and the interface is programmed in *Labview*.

Table 2.1: Precursor gases for the PECVD used in the reactor. Purity is written here as quality code, where the number before the dot represents the number of nines and the last number indicates the last decimal, *i.e.* 4.5 would mean a purity of 99.995 %.

| Gas | Massflow range(sccm) | Use | Dilution(% vol.) | Purity* |
|------------------|----------------------|--------------------------------|---------------------------|---------|
| Ar | None | Manifold purge/Cleaning plasma | None | 5.0 |
| N ₂ | None | Pump purge/Chamber refill | None | 5.0 |
| SiH ₄ | 0-100 and 0-10 | Precursor | None | 4.7 |
| CH ₄ | 0-100 | Precursor | None | 5.5 |
| H ₂ | 0-100 | Precursor | None | 5.0 |
| PH ₃ | 0-100 | Precursor (<i>n</i>) | 0.15 (in H ₂) | 5.5 |
| TMB | 0-100 | Precursor (<i>p</i>) | 0.2 (in H ₂) | 5.5 |

As it has been said, the upper electrode in the deposition chamber is the substrate holder itself, placed downwards. The substrate holder is composed of two pieces of stainless steel. The first piece can be seen on the right part of Fig. 2.4. It is designed to hold substrates of 10×10 cm², but substrates of other sizes can also be placed by adding additional central bars. There are holders of three different frame depths (1, 2 and 3 mm) to make it possible to deposit over substrates of different thicknesses. The second piece is a whole flat piece with the same shape of the frame. When the substrate is placed in the frame, the two pieces are fixed together using small bolts, keeping the substrate down faced between them. When the holder is all together inside the reactor, the robot can move it by fitting two small outgoing pieces into the spaces in the frame.

2.1.2 Magnetron sputtering

Sputtering is a physical vapor deposition (PVD) technique in which the surface of a bulk of source material, called target, is eroded by high energy ion bombardment, ejecting neutral particles of the material that are then deposited over the substrate. The bombarding ions are generated by a glow discharge in a noble gas atmosphere (normally Argon) produced by an electric field (either DC or RF) between a cathode (the target) and an anode (substrate and chamber walls). Cations within the glow discharge are accelerated towards the cathode, hitting the target, and if their energy is higher than the target's surface binding energy, target's atoms are ejected and can be deposited on the substrate, forming the film.

Magnetron sputtering is one of the ways to develop this deposition technique, and it is the one used in the sputtering equipment employed in this thesis. In magnetron sputtering, magnets are placed behind the cathode to make the traveling electrons to move in spirals along the magnetic field lines, aiming to cause a higher number of collisions so the ionization process is enhanced. This leads to a higher deposition rate of the films [66].

The equipment used at UB is a commercially available *ATC-ORION 8 HV* confocal magnetron sputtering from *AJA International, Inc.* It is placed in the same clean room as the PECVD reactor. The system has three magnetron guns tilted 3° off normal directed to an upper substrate holder, all placed in a single chamber of 34.7 cm of diameter and 39.8 cm of height. The distance between the holder and the target can be adjusted between 11.7 and 18 cm. The substrate holder can rotate up to 20 rpm (which provides homogeneity over a 10×10 cm² area) and can be heated up to 850°C using three halogen lamps placed behind it. The vacuum system consists of a turbo molecular pump (500 l s^{-1}) backed by a dry primary pump and can reach background pressures in the chamber of about 1×10^{-4} Pa.

During the process, argon and sometimes oxygen are introduced in the chamber by two different mass flow controllers. Pressure is adjusted by a three position gate valve, and measured with a capacitance manometer. Concerning the plasma, both DC and RF (13.56 MHz) electric fields can

2.1 Deposition methods

Table 2.2: Targets used for depositing TCOs and metals used in the front and back contacts of the cells.

| Material | Target | Purity | Size (diam.×Th.) | Supplier |
|--|--|---------|------------------|----------|
| ZnO:Al (AZO) | ZnO:Al ₂ O ₃ (98:2 wt.) | 99.99% | 3"×0.25" | Neyco |
| In ₂ O ₃ -SnO ₂ (ITO) | In ₂ O ₃ /SnO ₂ (90:10 wt.) | 99.99% | 3"×0.25" | Neyco |
| Al ₂ O ₃ (Alumina) | Al ₂ O ₃ | 99.99% | 3"×0.25" | Neyco |
| Aluminum | Al | 99.999% | 3"×0.25" | AJA |
| Silver | Ag | 99.999% | 3"×0.25" | AJA |

be used. Power can be adjusted up to 750 W for DC and 600 W for RF. An *MC2* automatic impedance matching network from *Seren* is used in conjunction with the RF power supply in order to maintain a constant plasma.

As far as the targets to deposit the materials are concerned, they have a diameter of 7.62 cm (3 inch) and are mounted in the guns placed on a copper support over the magnets. This system is cooled with a water circuit inside it. The guns are protected by metallic chimneys and flip-top shutters used to control the beginning and the end of the deposition process. Depending on the desired deposited material, different targets are used. Table 2.2 summarizes the targets used for each material deposited by sputtering.

The properties of the deposited films depend on several different parameters, like total pressure, oxygen partial pressure, substrate temperature, type and power of the electric field, substrate-electrode distance, etc. For a more detailed description of the sputtering process, equipment and experiments developed with it, previous group works can be checked [26] [27].

2.1.3 Resistive thermal evaporation

Resistive thermal evaporation is a simple process in which, inside a vacuum chamber, the source material is placed over a highly resistive part of an electric circuit (normally a filament or a boat-shaped piece). Then, a high electric current is made to pass through the circuit, so the

2 Experimental details

filament or boat gets its temperature raised by Joule effect, and the source material starts to melt and evaporate. The material atoms in gas phase move through the vacuum chamber until they reach the substrate and get deposited over it.

The thermal evaporation equipment used in this work (*Veeco VE-400*) has a vacuum bell jar with a volume of about 140 l. Inside, there are two electrodes where the resistive element is connected, and a support structure to hold the samples downwards. The distance between the source material and the substrate is 15.5 cm, which leads to a homogeneity area of about 15×15 cm². A quartz crystal thickness monitor is placed next to the substrate in order to control the deposition rate and the final thickness. Before the deposition, the chamber is put under vacuum below 5×10^{-3} Pa by pumping through a diffusion vacuum pump supported with a primary mechanical pump.

The source materials used in this thesis are aluminum and silver (both with a purity of 99.99%) with melting points of 660°C and 961°C respectively. Both materials come in rods, but Al rods are placed into a tungsten helical filament while Ag are placed over a boat-shaped piece of tungsten. This difference is because Ag needs higher temperatures that can not be reached with the filaments. To avoid cross contamination, the chamber is covered on the inside with vacuum aluminum foil which it is changed when the deposition is switched from one metal to another.

To control the deposition rate, a variable autotransformer is connected to the circuit, so the current can be modified, leading to an indirect temperature control. A shutter is also placed between the source material and the substrate, in order to control the beginning and the end of the deposition. Also, this is a way to evaporate eventual impurities of the metals before start depositing over the substrate.

One of the functions of metal evaporation is the deposition of the metallic contacts in both layers and solar cells. In the case of the layers, the contacts are used to perform measurements of coplanar conductivities, while in the case of the cells, they define the cell area and act both as back contact and reflector. The mask used for the layer contacts

2.2 Pre- and post- deposition treatments

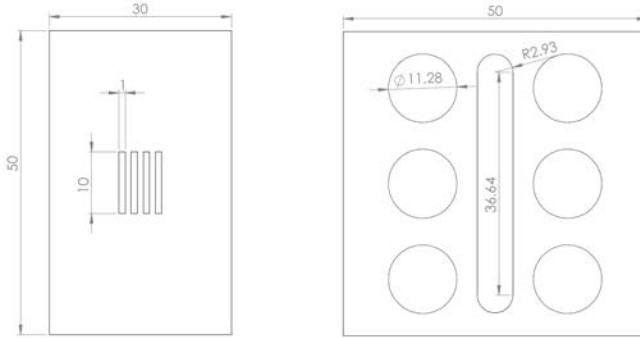


Figure 2.5: Schematic top view of the masks used for metal deposition in layers (left) and cells (right). The units of the dimension lines are mm.

is about 0.2 mm thick and is made of flexible metal; the open space is four 'lines' of $1 \text{ mm} \times 1 \text{ cm}$ that will be used to perform electrical measurements as it will be described in Sec. 2.3.3.1. For cells, the mask has a thickness of 0.5 mm and is made of stainless steel; the open space consists of two rows of three 1 cm^2 circles for solar cells with a central long area which will be used to make the front contact as described in Sec. 2.2.2. A schematic view of the masks is shown in Fig. 2.5.

2.2 Pre- and post- deposition treatments

In this section the processes developed before and after the depositions of layers and cells are explained. They are wafer cleaning, chemical etching, thermal annealing and light induced degradation. Wafer cleaning is a predeposition treatment done in c-Si wafers, while chemical etching is a postdeposition treatment done in thin film solar cells. As far as thermal annealing is concerned, both thin film and c-Si experiments commonly include this process at some point, as it has several effects on the devices. Light induced degradation process (and the equipment involved) is a special case, as a system to develop LID had to be designed and constructed. It will be analyzed with much more detail in Sec. 2.2.4.

2.2.1 **Wafer cleaning and preparation**

In Chapter 5 experiments involving c-Si wafers are developed, and it has been proved that a careful cleaning process of the wafer surface before the deposition is critical to obtain good passivation values. The importance of this cleaning process lays on that any possible impurities remaining in the wafer surface would act as recombination centers, which lead to a reduction of the carrier lifetime.

For this work, the samples were cleaned at the UPC using a standard wafer cleaning process called RCA sequence [67]. The process consists in two steps: the first one removes the organic surface contamination. This is achieved by a basic etching process (RCA1) with $\text{H}_2\text{O}:\text{H}_2\text{O}_2:\text{NH}_3$ (6:1:1) for 20 minutes at 70°C [68]. The second step removes the possible metal contamination of the surface by an acid etching (RCA2) with $\text{H}_2\text{O}:\text{H}_2\text{O}_2:\text{HCl}$ (6:1:1) for 10 minutes also at 70°C [69]. Between these two processes, a 60 seconds etching in 1% diluted hydrofluoric acid (HF) is required, in order to remove any possible SiO_2 grown on the surface during RCA1. This etching is also necessary after RCA2, just before the deposition of any passivation layer. After this second immersion in 1% HF, all possible silicon oxide (SiO_2) that had appeared after RCA2 is removed, and the wafer is ready for deposition. In order to prevent SiO_2 to form itself again over the surface of the wafer, it should be placed under vacuum and passivated with the corresponding layer as soon as possible. This process is done over the wafers in all the experiments just before any layer is deposited.

2.2.2 **Chemical etching**

Chemical etching has several uses involved in light management in thin film silicon solar cells [70] but in this work it is used essentially to remove the extra TCO (in this case, AZO) deposited on the back reflector of the solar cells. The idea is that in PIN cells, AZO is deposited over all the substrate area and then the area of the cells is delimited with the solar

cell mask described in Fig. 2.5. The mask is placed over the substrate and a scratching is made in the central area in order to reach the front TCO, aiming to establish electric contact with the metal deposited afterwards. After the metal deposition, samples are dipped in a HCl of 0.5 wt.% solution at room temperature during about 5 s and quickly rinsed with deionized water and isopropanol, and dried with nitrogen. This process removes the AZO that is not 'protected' by the metal, thus isolating the back reflector from the front contact. The steps of this process are schematically summarized in Fig. 2.6.

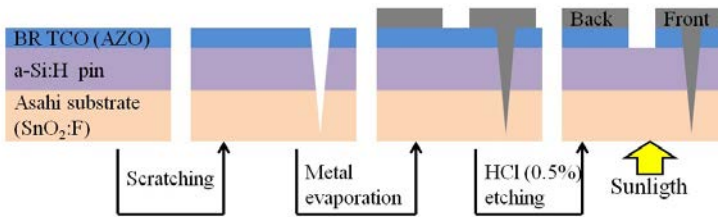


Figure 2.6: Process to finish a solar cell. From left to right: 1. Sample with AZO deposited over the whole area. 2. Sample scratched to let the metal reach the front TCO. 3. Sample with metal deposited with the mask. Front and back contacts are still connected. 4. Sample etched, extra AZO is removed. Front and back contacts are now isolated.

2.2.3 Thermal annealing

It is usual that thin film silicon layers and cells are submitted to thermal annealing processes, as they have multiple effects on them. When the annealing is made just after the cell is deposited (this is, after the chemical etching) it serves to remove any rests of water or isopropanol that the nitrogen would have failed to dry. Also, it is used to accomplish the dopant atoms activation, which leads to an improvement of the open circuit voltage.

The annealing has another important use, which is to revert the light induced degradation in amorphous silicon solar cells, leaving the cell in an annealed state that can be considered just like the initial state for

2 Experimental details

some practical purposes [39]. The thermal recovery process is explained by the annihilation of photogenerated defects by overcoming its various activation energies [71]. The standard annealing process consists in keeping the samples 1 hour at 160°C and, if nothing else is specified, this is the process that this work will refer to. However sometimes the temperature can be a little higher, up to 200°C, or maybe the time is modified. If this is the case, it will be specified in each situation. When it was not necessary that the samples were annealed under vacuum, a *Thermo Scientific M110* muffle furnace with a chamber of 9 l and capable to reach 1100°C was used. When vacuum was needed to avoid oxidation (for example in microcrystalline layers), the treatments were performed in the PECVD reactor described in Sec. 2.1.1, whose temperature can go up to 600°C (400°C of substrate temperature).

As far as c-Si wafers, the thermal annealing is used to activate the fixed charge of the front TCO, the emitters or the passivating layers. As it will be shown in Chapter 5, the annealing process is critical to obtain good values of the effective carrier lifetime ($\mu\tau_{eff}$) and Implied open circuit Voltage ($ImpV_{oc}$). The annealing process in wafer based experiments was developed at the UPC in a home-made oven in *forming gas* (95% N₂ + 5% H₂) atmosphere. The temperature and the annealing time are varied depending on the experiment, and will be detailed in each case.

2.2.4 Light induced degradation

To fully characterize amorphous silicon layers and devices it is necessary to perform light induced degradation (LID) on them, as their properties are widely affected by it. The group has previous experience studying LID and the associated seasonal effect in modules [60], but at the moment of the development of this work, it lacked a light induced degradation system that could be used to study LID in cells. So, it was necessary to design and construct a light soaking system that could be used to perform LID and study the seasonal effect in solar cells. The requirements of the equipment, its design and construction process and the calibrations performed on it are detailed next.

2.2.4.1 Requirements and construction of the system

In the process of designing the system, one of the most important points was that it had to be suitable for seasonal effect experiments. So, it was necessary to design and construct a system in which different samples' temperatures could be controlled and maintained independently during the process. The system had to provide stable, constant illumination that resembled to sun's as much as possible. It is usual for LID experiments to be developed with high intensity light for shorter periods, but in this case, the times had to be longer in order to well appreciate the evolution and the seasonal effect. So the light had to stay constant for long periods of time. And, in order to establish comparisons, it was necessary to have the possibility of multiple independent conditions for the degradation. With these conditions in mind, the requirements of the illuminator could be summarized as:

- It has to provide an illumination intensity of at least 1 sun (100 mW cm^{-2}).
- The spectrum of the used light has to resemble the solar spectrum as much as possible.
- The illumination has to be constant and stable during long periods of time (over 1000 h).
- The area of illumination has to be large enough to degrade several samples at time.
- The temperature of the samples needs to be controlled and stabilized at least between 30°C and 80°C .
- It has to be possible to develop multiple independent degradations at different temperatures simultaneously.
- Need to be low-cost.

The best alternative considering these requirements is a Light Emitting Diode (LED) based solar illuminator with independent temperature control. LED simulators have proved to be a suitable alternative for solar simulators [72]. The main advantage of the LED is that it almost does not

2 Experimental details

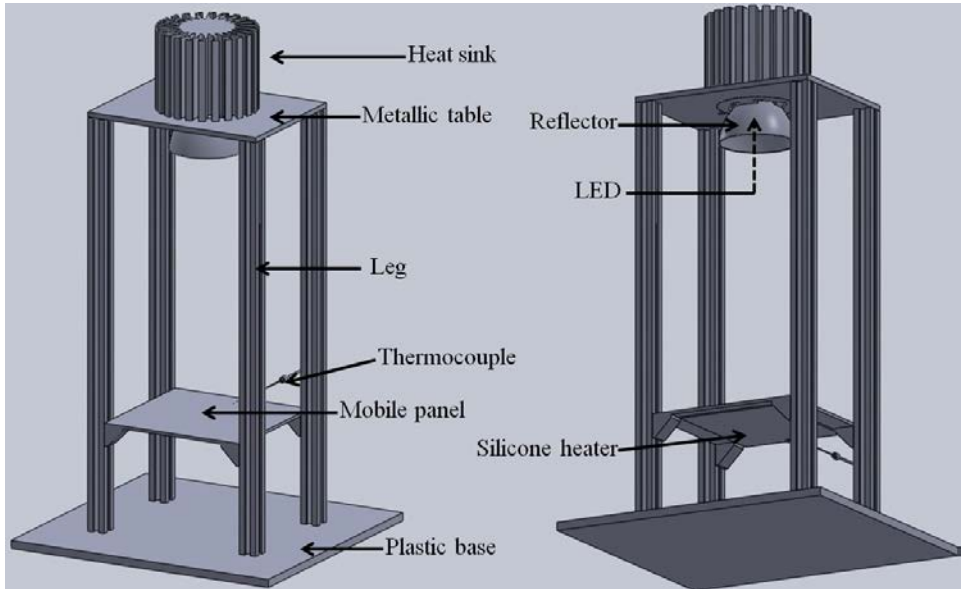


Figure 2.7: Scheme of one of the towers of the LED solar illuminator.

emit infrared light. This reduces the non intentional heating and allows to keep the solar cells at temperatures of about 30°C without a refrigeration system, which would make the construction more difficult and expensive [73]. Also, the LEDs are less sensitive than other technologies to environmental conditions, like external temperatures, and provide constant and stable light. Their durability is also higher. The used LEDs are from the *Bridgelux RS Array Series (BXRA-40E7500-J-03)* [74], which have a spectrum named 'warm white', that approximately fits with the solar spectrum, although it is not exactly the same.

The illuminator will be composed of four independent identical towers to allow the performance of several LID experiments at different temperatures simultaneously. A scheme of one of the towers can be seen in Fig. 2.7. The LED is attached to a heat sink to keep its operation temperature at the right point (about 80°C), and a reflector is added to concentrate the light, and all this system is fixed to an metallic



Figure 2.8: Photography of the operating solar cell illuminator.

table-like structure over a PVC base. Another metallic panel of about 12×12 cm² is placed between the base and the LED and fixed with mobile screws to the legs. This mobile panel enables to adjust the distance between the LED and the samples to make possible to adjust the illumination intensity if desired. Two *TTi QL355TP* power supplies with two outputs in each are used to provide current to the LEDs. In order to control the temperature of the samples, a *Watlow* flat silicone heater is fixed to the downside of the mobile panel of each tower, and a thermocouple is placed inside through a hole in a way such as the end of the thermocouple probe is placed in the center of the square platforms. The thermocouple and the silicone heater of each tower is connected to an independent *Watlow Ez-Zone* temperature controller. The desired temperature is set in the controller, which provides power to the silicon heater until the platform reaches that temperature, and then keeps it stabilized. A photography of the finished equipment is shown in Fig. 2.8.

2.2.4.2 Illumination intensity and temperature calibrations

With the structure ready, a calibration of the light was necessary. It was done by adjusting the distance between the LED and the mobile panel to get 1 sun illumination over the center of the panel. The current of a standard *T-Solar* a-Si:H solar cell was measured at different heights until the short circuit current corresponded to 1 sun illumination, obtained

2 Experimental details

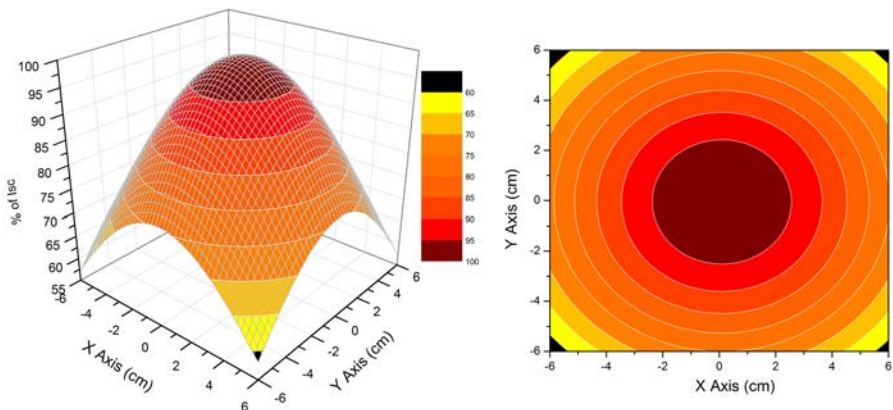


Figure 2.9: Map of the homogeneity of the J_{sc} over the sample panel. The center of the graphs corresponds to 100% of the J_{sc} under 1 sun in the T -Solar reference cell.

from the J - V measurement system that will be described in Sec. 2.3.5.1. Then, to study the homogeneity of the light over the sample panel, the position of the cell was varied and the current measured in several points, and then a Gaussian fit was made to obtain the whole homogeneity map. Fig. 2.9 shows the homogeneity map obtained from this measurements. In a $10 \times 10 \text{ cm}^2$ area, the current remains over 80% of the central value, and nearly 90% in $5 \times 5 \text{ cm}^2$. As the samples have normally $5 \times 5 \text{ cm}^2$, it is possible to degrade 4 samples with a homogeneity over 80%. As the degradation times are long, this difference is not very important. However, in order to avoid any possible difference, the orientation of the samples in the panel is changed regularly.

To calibrate the temperature, a second thermocouple was fixed to the surface of the solar cell, and several temperatures were set on the heating system. All the measurements were done with the LEDs on, so the heating effect of the light was taken into account. It is considered that the room temperature is going to remain constant ($\approx 22^\circ\text{C}$), so it is also taken in account in the calibration. Both temperatures, the set one (T_{set}) and the measured one (T_{cell}), were used to develop the calibration, and the result is shown in Fig. 2.10. Therefore, the correlation between the set and the

2.2 Pre- and post- deposition treatments

cell temperature is established by:

$$T_{cell} = 0.826T_{set} + 7.606 \leftrightarrow T_{set} = 1.221T_{cell} - 9.208 \quad (2.1)$$

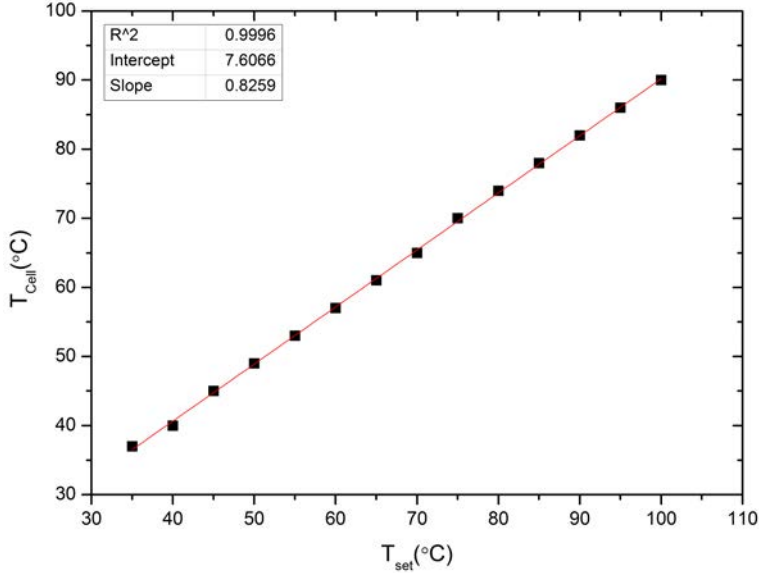


Figure 2.10: Straight line of calibration of the temperatures in the light soaking system.

With the light and the temperature calibrated, the equipment is ready to perform long term degradation experiments. From now on, when the temperature of an experiment is specified, it will be referring to the real temperature of the cell (T_{cell}), and the used light is kept constant at 1 sun power (the height is not changed). The degradation experiments are very time-consuming processes, as amorphous solar cells need about 1000 h of direct illumination to consider them degraded (stabilized) [75]. To reduce the number of days of the experiment, the illumination was kept always on, with no interruptions at night. These lack of dark cycles introduces another difference with on field conditions, but it was necessary to avoid the excessive prolongation of the degradation experiments.

2.3 Characterization techniques

2.3.1 Thickness measurements

To measure the thickness of the layers, three different techniques are used in this work. The first two are confocal microscopy and profilometry, and they are the ones that are mostly used, as they are available at the UB. The third technique is ellipsometry, which was used in the LPICM for some of the samples in Chapter 3, Sec. 3.3.3 and also at the UPC for some of the samples in Chapter 5.

2.3.1.1 Confocal microscopy

Confocal microscopy benefits from non-paraxial optics to obtain focus only over a single plane. Point illumination is sent through a pinhole aperture which eliminates out-of-focus light, that is, light from the planes above and below the focus plane. The measurement is taken and then the microscope changes the focus plane to a different height and measures again in the same way. By repeating this process, a scan of a series of different levels is obtained, and with these data it is possible to make a reconstruction and obtain a 3D image of the sample's surface. Considering this, getting the thickness of the layers with this technique requires that the sample has a step between two zones (with and without layer), so the microscope can measure the difference of height.

To create this step in the layers deposited in the PECVD reactor and the sputtering, a lift-off technique is used. A line is drawn with ink marker over the substrate before the deposition and then, after the deposition, it is removed using isopropanol. This way the sample deposited over the line is also removed and the step is created. For the layers deposited in the thermal evaporator, this technique can not be used, because the adhesion of the metal to the substrate is lower, and the whole sample would be removed when the isopropanol is used. Instead, a stripe of *Kapton*® tape is placed on the substrate before the deposit and removed afterwards, creating the step.

2.3 Characterization techniques

The confocal microscope used for this work is a *Sensofar Plμ 2300* confocal microscope with two *EPI* objectives: a 20× and a 150× with optical resolutions of 0.35 μm and 0.14 μm, respectively. The height step between the focus planes is 1 μm for the 20× and 0.10 μm for the 150×. Normally, the 20× objective is used to find the step and the 150× to obtain the final measurement.

2.3.1.2 Stylus profilometry

The stylus profilometry measures the morphology of the sample surface by contacting with a diamond tip and moving over it. While the scan is being done, a position transducer converts the movements of the tip into height values, obtaining a surface profile. So, to measure the thickness of the layers, a step is also needed just like in the case of the confocal microscope (and is obtained likewise).

The equipment used for profilometry is a surface profiler *Dektak 3030*, *Veeco* with a 25 μm diameter stylus. It has a vertical resolution of 1 nm and an associated error of ± 10 nm. This error is calculated as the standard deviation of a set of measures taken over a reference sample. Normally, the thickness of the samples is first measured with the confocal microscope and the profilometer is used to verify the results.

2.3.1.3 Ellipsometry

Ellipsometry measurements are used to obtain optical properties (like the refraction index n) and thicknesses of materials in thin films. Polarized light is sent to the sample, and part is transmitted and part reflected. Changes on the polarization of reflected light are measured (amplitude and phase). The results are compared to a model (normally Tauc-Lorenz model) so the thickness and the desired optical properties are obtained. At the LPICM, spectroscopic ellipsometry is developed with a *Horiba Uvisel* spectroscopic ellipsometer. At the UPC, the used equipment is a *Plasmos SD 2100* ellipsometer.

2.3.2 Optical and structural characterization

2.3.2.1 UV-VIS-NIR spectroscopy

UV-VIS-NIR Spectroscopy was the main technique used for optical characterization. It was essentially used to measure total transmittance (T) and total reflectance (R), which are used to obtain other important parameters such as absorptance (A), absorption coefficient (α) and Tauc optical bandgap (E_g). The means to obtain these parameters will be explained later on in Chapter 3, Sec. 3.3.2.2.

The used spectrophotometer at UB is a commercially available *Perkin Elmer Lambda 950* with a 150 mm integrating sphere. The range in which measurements can be performed is from 200 to 2500 nm of wavelength (λ). The illumination is provided by two different lamps depending on the wavelength: a deuterium lamp is used for the ultraviolet (UV) region while a halogen lamp is used for the visible (VIS) and infrared (IR) regions. For the measurement of the light, there are two detectors which change at 856 nm. For wavelengths above this value a photomultiplier detector (PMT) is used, while a Peltier-controlled PbS detector is used for lower wavelengths.

To perform T measurements the sample is placed in the path of the light beam before the integrating sphere, and a *Spectralon*® white diffuse reflectance standard (>99 %) reflector is placed on the opposite side of the sphere, so the transmitted beam is reflected back into the sphere and counted by the detector. For the R measurements, the reflector is removed from the rear side of the sphere, and the sample is put in its place with a black absorber behind it, in order to absorb the transmitted light. This way, only the light reflected by the sample is taken into account. To characterize the layers, the orientation in the spectrophotometer is such as the sample layer is first hit by the light beam. When a whole cell is measured, the light comes as it would on field performance, this is, first through the p layer.

2.3.2.2 Raman spectroscopy

Raman spectroscopy is a molecular spectroscopy based on observing inelastically scattered light which allows to identify vibrational states of molecules. This way, it is possible to obtain information about molecular bond structure of the materials. In this thesis work, Raman measurements are used to obtain the Raman crystalline fraction (χ_c) of microcrystalline silicon layers [76] [77] [78] [79]. χ_c is defined by the peak intensity relation for three values of the wavenumber (Raman Shift): 480, 500 and 520 cm^{-1} . The first is related with the amorphous phase, while the other two are assigned to the crystalline phase. So, it is possible to obtain χ_c through the relation:

$$\chi_c = \frac{I_{500} + I_{520}}{I_{480} + I_{500} + I_{520}} \quad (2.2)$$

where I_n is the intensity of each corresponding peak. χ_c gives a semi-quantitative measure of the crystalline volume fraction associated with the material structure, varying from 0 (completely amorphous) to 1 (fully crystalline).

The Raman measurements are developed in a *MicroRaman T64000 Jobin Yvon* with a laser of $\lambda=532$ nm and $P=4.3$ mW. Then, the Raman shift spectrum is deconvoluted by means of a home-made *Matlab* software into the three Gaussian peaks corresponding to the mentioned values and χ_c is obtained.

2.3.3 Electrical characterization

2.3.3.1 High impedance measurements

Thin film silicon layers, specially the amorphous ones, have very low conductivities, which means high impedance, so it is necessary to deposit metallic contacts over them before coplanar measurements can be developed. The mask used to deposit these contacts is shown on the left part of Fig. 2.5 in Sec. 2.1.3. This mask provides an space between stripes of 1 mm \times 1 cm. Here, the equipment will be described, but the conditions for the measurement of the layers and subsequent calculi will be described

2 Experimental details

later on in Chapter 3, Sec. 3.3.2.3.

The experimental equipment is a home-made two point probe setup that consists essentially in a small vacuum chamber with a heat plate where the sample rests and is contacted from the top by two tips. The schematic view of the vacuum chamber is shown in Fig. 2.11.

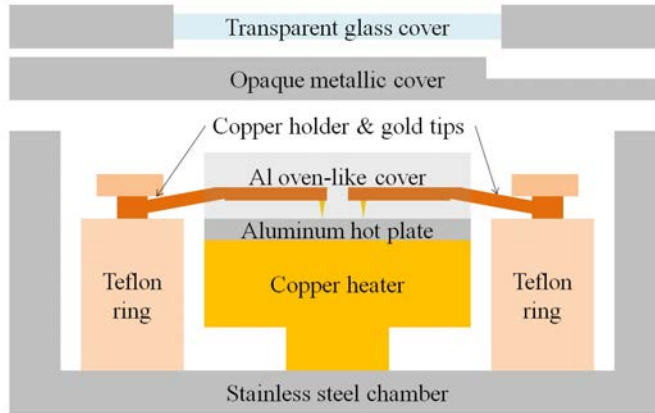


Figure 2.11: Scheme of the inside of the vacuum chamber of the two point probe device.

The two tips are connected to a programmable electrometer *Keithley 617* which serves both to provide voltage (-102 to 102 V) to the sample and measure the current. The range on current is very wide, going from 2×10^{-2} to 2×10^{-12} A, though towards the lower limit, the accuracy is quite worse. To control and stabilize the temperature of the sample, an *Eurotherm 2216e* temperature control system is used: the thermocouple (whose end is in the center inside the aluminum hot plate) measures the temperature and, if needed, power is provided through the heater to raise the temperature to the setpoint. No cooling system is installed. A small diaphragm pump is used to make vacuum in the chamber. This is necessary to avoid the effect of the humidity on the measurements, because any condensation on the surface of the layers leads to a relevant increment of the conductivity. This can result in a quite significant error,

specially in the samples with very low conductivities. The chamber can be closed either with an opaque metallic cover or a transparent glass cover, depending if the measurements are made in dark or under illumination.

This equipment is used to measure the dark conductivity (σ_{dark}), its activation energy (E_A) and the photoconductivity (σ_{ph}) under 1 sun illumination. These measurements are controlled by a home-made software written in *Phyton*. For the dark and photoconductivities, the software stabilizes the temperature and varies the voltages (V), measuring the current I in each one to obtain a linear fit of I vs. V in order to get the conductance G as:

$$G = \frac{1}{R} = \frac{I}{V} \quad (2.3)$$

where R is the resistance. Then, taking in account the size of the measured area (with a path length l and a path width w) and the thickness of the layer d , the conductivity (either σ_{dark} or σ_{ph}) can be obtained as:

$$\sigma = \frac{G l}{d w} \rightarrow \sigma[S/cm] = \frac{G[S]}{d[cm]} \times 0.1 \quad (2.4)$$

The right part of the previous equation is already cleared for the specific contacts used in this measurements (see Fig. 2.5) as the values of l and w are 0.1 and 1 cm respectively. Giving σ in S/cm allows to compare with the quality criteria given by the bibliography.

For the activation energy, the software stabilizes the voltage and keeps it constant, while the temperature is raised up to 200°C. Then, the heater is switched off and the temperature is let to drop while measurements of the current are taken each 0.5 to 1°C approximately. As the voltage is fixed, the values of G and so the ones of σ for each temperature can be obtained. The results are presented on an Arrhenius plot ($\log(\sigma)$ vs. $1000/T(K)$) obtaining a linear dependence. Being b the value of the obtained regression, E_a can be cleared as:

$$\sigma = \sigma_0 e^{-\frac{E_a}{kT}} \rightarrow E_a = b \times k \times 1000 \quad (2.5)$$

where k is Boltzmann constant, and the result is multiplied by 1000 as it came from an Arrhenius plot. Using the fit it is also possible to

2 Experimental details

extrapolate the value of σ at any temperature, by taking the obtained linear coefficient as σ_0 . This is used sometimes to compare the results obtained from conductivities by measurements with the extrapolated ones in order to verify the results.

2.3.3.2 Four point probe

For layers with higher conductivities like TCOs, it is not necessary to deposit metallic contacts and measure with the two point probe, as they can be measured directly using a four point probe system. These measurements are performed with a *JANDEL RM3* four point probe system. The procedure is to contact the layer with four lined and equally spaced tungsten carbide tips; then a current (I) is passed through the two outer probes and the voltage (V) is measured in the two inner. From these values, the sheet resistance can be calculated as [80]:

$$R_{sh} = \frac{V}{I} \frac{\pi}{\ln 2} \quad (2.6)$$

and by multiplying for the layer thickness d , the resistivity is obtained:

$$\rho = R_{sh} \times d \quad (2.7)$$

2.3.4 Effective carrier lifetime and implicit V_{oc} measurements

The effective carrier lifetime (τ_{eff}) is used as a parameter to evaluate the recombination and then the quality of the devices with c-Si. To obtain τ_{eff} , the used technique is the transient photoconductance measurements, first developed by Sinton and Cuevas [81]. The principle is based in detecting the increment of the conductance due to the excess of photogenerated carriers in a contactless sample. The system employed is a commercial *Sinton Instruments WCT-120* offline wafer lifetime measurement system [82]. It measures the transient photoconductance as the illumination level from a flash lamp varies. Normally, the situation used for the measurements is the Quasi-Steady PhotoConductance (QSPC), corresponding to

an illumination decay slow enough to reach an equilibrium between the photogeneration and the recombination. The obtained variation of the photoconductance ($\Delta\sigma$) is related to the average of photogenerated carrier excess over the wafer thickness (Δn_{av}) by:

$$\Delta\sigma = qW(\mu_n + \mu_p)\Delta n_{av} \quad (2.8)$$

where q is the elemental charge, W is the wafer thickness, and μ_n and μ_p are the electron and hole mobilities respectively. Then, $\Delta\sigma$ is used to obtain τ_{eff} :

$$\tau_{eff} = \frac{\Delta\sigma}{J_{ph}(\mu_n + \mu_p)} \quad (2.9)$$

where J_{ph} is the total photogenerated current, obtained also by the equipment by measuring a calibrated solar cell as reference.

It is also possible to obtain information about the open circuit voltage from the carriers excess. For example, for a p -type wafer with a doping density N_a , the implicit V_{oc} ($ImpV_{oc}$) can be obtained as

$$ImpV_{oc} = \frac{kT}{q} \ln \left(\frac{\Delta n(N_a + \Delta p)}{(n_i)^2} + 1 \right) \quad (2.10)$$

where $\Delta n \equiv \Delta p$ can be approximated by the average Δn_{av} . A more detailed explanation on the measurement process can be found in the bibliography [81].

2.3.5 Device characterization equipment

The device characterization equipment is a home-made set-up used to measure several properties of finished solar cells. The equipment is designed to develop different measurements over complete solar cells without making important changes on it. The most important measurements developed are the current-voltage characteristics (J - V curves) and the external quantum efficiency (EQE).

2.3.5.1 Current density-voltage characteristics

J - V curves are the main characteristic of solar cells. They are measurements of the current density of the cell as a function of the applied tension. They are used to extract several important parameters of the cell which determine its quality. These measurements can be performed under different illuminations and also in dark, but the most common situation is to develop them under a standard Air Mass 1.5 solar spectral irradiance reference, known as AM1.5 Illumination or AM1.5 Spectrum. Normally the given parameters of a solar cell are the ones obtained under these illumination, so from now on when no specification appears next to J - V curves or any parameters, it will be referring to this situation.

To perform the J - V curve measurements, the experimental setup is a solar simulator composed by a *Newport 67005* housing with a xenon lamp of 150 W with an AM1.5 filter. The light beam goes through a set of neutral filters that can be used to control the illumination intensity (for AM1.5 none is used). Then, the light is collected by an optical fiber and directed to a lenses focus system that allows to illuminate homogeneously a circular area of 1 cm of diameter from underneath. The sample is placed down-faced on a platform with a hole in it to let the light pass. The cell is placed at the center of this hole, aiming for maximum homogeneity in the light. The platform is refrigerated in order to maintain the cell temperature constant at 25°C. Concerning the electrical part, the four-point method is used, using four *SUSS Microtec PH100* probeheads. Two of these probes are used to polarize the cell and to measure the current with a *Keithley 2400 Source Measure Unit* (SMU) that acts both as voltage source and ammeter. The other two verify the real tension, so the resistance of the wires in the circuit is suppressed as series resistance in the sample. A schematic view of this configuration is shown in Fig. 2.12. All the system is controlled by home-made software written in *Python*.

The parameters extracted from the J - V curve are commonly called the characteristic parameters. The short circuit current density (J_{sc}) is the current density across the device when the voltage is zero. The open circuit voltage (V_{oc}) is the potential difference when no current is passing

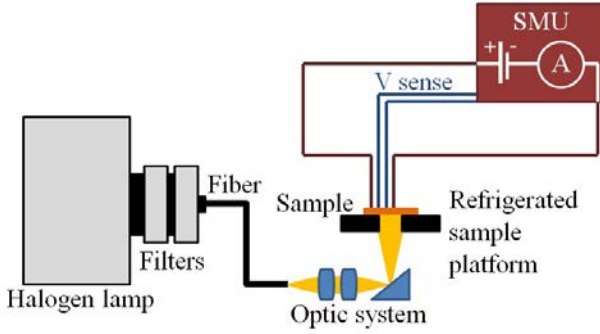


Figure 2.12: Scheme of the device characterization system configuration to perform J - V curve measurements.

through the device. The maximum power voltage and current density (V_m and J_m) are the values of V and J where the cell generates its maximum power. These values determine the fill factor (FF), which is the ratio between this maximum output power (density) of the cell to the product of the short circuit current density times the open circuit voltage. The fill factor is a very sensitive indicator of the cell quality [39][5][83].

$$FF = \frac{V_m \times J_m}{V_{oc} \times J_{sc}} \quad (2.11)$$

With these parameters, the energy conversion efficiency (η), understood as the ratio between the maximum converted power density ($V_m \times J_m$) to the power density of the incident light (P_0), can be calculated.

$$\eta = \frac{V_m \times J_m}{P_0} = \frac{FF \times V_{oc} \times J_{sc}}{P_0} \quad (2.12)$$

Two other parameters can be extracted from the J - V curve: open circuit and short circuit resistances (R_{oc} and R_{sc}). These are the resistances in the corresponding situations, and they are related with the performance of the cell. It is important to notice that in order to make the reading easier, they will be called 'resistances', but as the parameter that is commonly

2 Experimental details

used to obtain them is current density (J), the obtained resistances are actually area normalized resistances, whose units are normally $\Omega \text{ cm}^2$.

To understand the relevance of R_{oc} and R_{sc} , it has to be taken into account that thin films solar cells can be described using an equivalent circuit, field in which our group has developed an important work aiming to obtain the most possible accurate model [49][60][84][85]. Detailed information can be obtained in these references, but for the aim of this explanation, is enough to say that the equivalent circuit is a parallel circuit composed by the following elements (Fig. 2.13):

- A diode, which represents an ideal solar cell in dark.
- A voltage dependent current generator J_{ph} , which represents the photogenerated current when the cell is under illumination.
- A series resistance R_s , which represent parasitic effects related to the electric contacts and interfacial issues. For this resistance, a low value is desired, as it would mean good electric and interfacial contacts.
- A parallel resistance R_p (often called *shunt*). R_p represents an alternative route for current circulation, which mainly symbolize recombination losses and current leaks [60][75]. A small loss of current through these leaks is desirable, then higher values of R_p result in a more performing solar cell.

The key point is that R_s and R_p are directly related with R_{oc} and R_{sc} , which can be obtained from the J - V curve. The detailed relation is developed in Merten *et al.* [84], but for this section's purposes it is enough to say the high illumination limit for R_{oc} is R_s and the one for R_{sc} is R_p . Although 1 sun is not this level yet, it is still true that an increment of R_{oc} leads to an increment of R_p and, in the same way, and increment of R_{sc} means and increment of R_p .

In order to better understand the graphical meaning of these parameters, a standard J - V curve with all the parameters is shown in Fig. 2.14. As it can be seen, V_{oc} is the value where the curve cuts the x axis (voltage axis), while J_{sc} is the value where the curve cuts the y axes (current

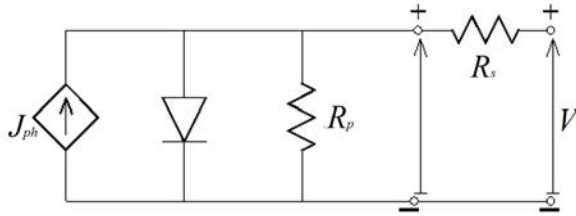


Figure 2.13: Equivalent circuit of a thin film silicon solar cell (Courtesy of R.Roldan [60]).

density axes). These two values conform the dark gray square. The power density curve (P - V curve) is included to make it easier to check where the maximum power of the cell is achieved. This point corresponds to V_m and J_m , values that conform a second square in the plot area (light gray). This light gray area divided by the dark gray area gives the FF . The higher the FF is, the more curved the J - V characteristic is, approaching to the behavior of an ideal diode [5][83]. Anyway it is clear that an increment in any of these parameters is traduced in an increment of the conversion efficiency.

As far as R_{sc} is concerned, it can be understood as the reverse of the slope of the straight line tangent to the J - V curve at the short circuit point. As it can be seen in Fig. 2.14, the lower this slope is, which means the higher R_{sc} (and subsequently R_p) is, the closer the cell is to the ideal diode. Conversely, R_{oc} corresponds to the reverse of the slope in the open circuit point and, unlike before, the higher the slope is; that is, the lower R_{oc} (and subsequently R_s) is, the closer to ideality the cell is. So, it is desirable to have high R_{sc} and low R_{oc} , which means having the most possible square-like J - V curve. With all these considerations, it is easy to obtain a good idea of the quality of the cell only by looking the J - V curve, making it not only an essential measure to obtain the characteristic parameters, but also a good way to obtain a quick evaluation about the quality of the solar cell.

2 Experimental details

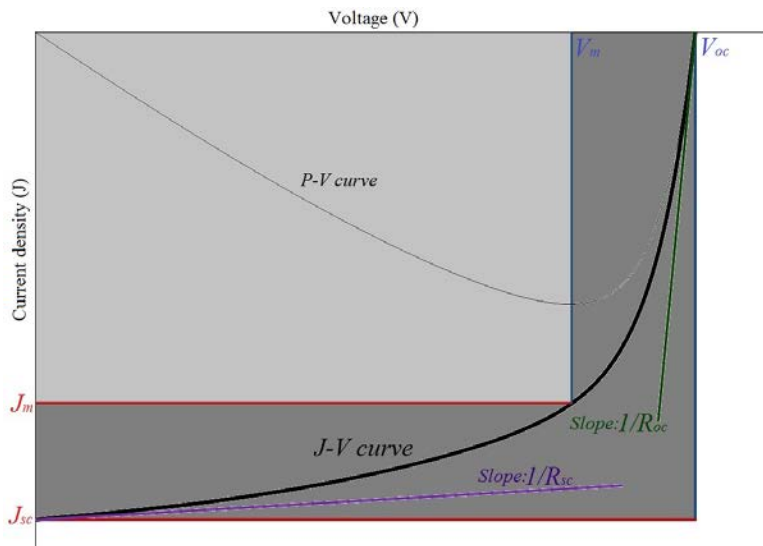


Figure 2.14: Standard J - V curve with all the parameters represented. The P - V curve is shown to guide the eye to V_m and J_m .

2.3.5.2 Spectral response (SR), external quantum efficiency (EQE) and internal quantum efficiency (IQE).

The spectral response, and consequently the external and internal quantum efficiencies, are a way to observe in which areas of the solar spectrum does the solar cell work better. SR is a function of the wavelength defined as the ratio between the photocurrent generated by the cell and the power incident on the solar cell.

$$SR(\lambda) = \frac{I_{ph}}{P_0} \quad (2.13)$$

By measuring the SR , the external quantum efficiency can be calculated. EQE is also a function of λ defined as ratio between the number of electron-hole pairs collected at the contacts of the device and the number of incident photons at that wavelength.

$$EQE(\lambda) = \frac{n_{collected\ carriers}(\lambda)}{n_{incident\ photons}(\lambda)} \quad (2.14)$$

2.3 Characterization techniques

The internal quantum efficiency (*IQE*) is defined (also for each λ) as the number of electron-hole pairs collected at the contacts of the device and the number of absorbed photons at that wavelength.

$$IQE(\lambda) = \frac{n_{\text{collected carriers}}(\lambda)}{n_{\text{absorbed photons}}(\lambda)} \quad (2.15)$$

The difference between *IQE* and *EQE* can then be understood as incident photons that are not absorbed, this is, as optical losses (i.e. reflexion or transmission). These magnitudes are related to each other by the following equations:

$$SR(\lambda) = EQE(\lambda) \frac{\lambda q_e}{hc} \quad (2.16)$$

$$IQE(\lambda) = \frac{EQE(\lambda)}{A(\lambda)} \quad (2.17)$$

where q_e is the electron charge, λ the incident light wavelength, h Planck's constant, c the speed of light in vacuum and $A(\lambda)$ is the absorptance for each wavelength.

To measure the *EQE* (as the system makes the calculus directly from *SR*), the same equipment used for *J-V* curves is employed, but some modifications are included. The light from the lamp now goes through a *PTI OC-4000* chopper that modulates it, and then a *Spex1680* monochromator is used to filter the light of each wavelength. It has a spectral range from 185 to 900 nm and an accuracy of 0.4 nm. The monochromatic light goes then into a beamsplitter that divides the light. At this point, a measure of the light intensity is taken by a *PerkinElmer 7265DSP* lock-in amplifier, it will serve as reference to obtain the number of photons and calculate the *EQE* after. The rest of the light reaches the cell through the same optical way as before. Concerning the electrical part, most of it is conserved, but now the signal of the SMU goes through a current amplifier acting as a current-voltage converter, and then reaches the lock-in, which compares the two signals and takes the final measurement. The modified equipment is shown in Fig. 2.15.

EQE and *IQE* measurements allow us to evaluate the behavior of the device in each wavelength range and extract conclusions. For example, a

2 Experimental details

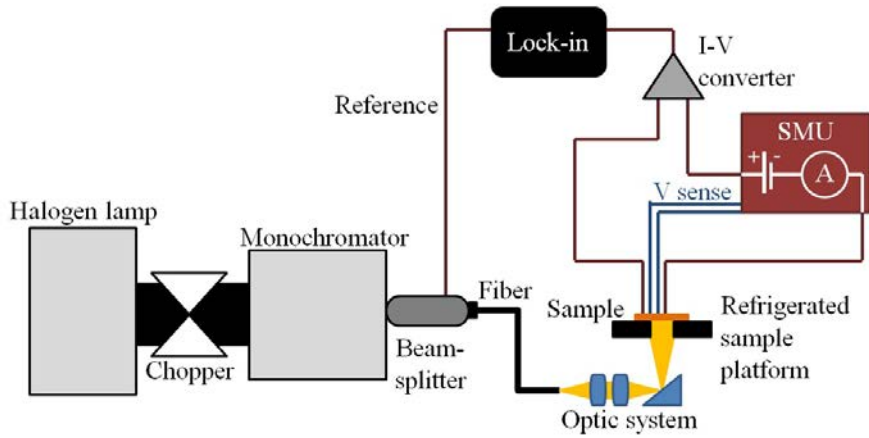


Figure 2.15: Scheme of the device characterization system configuration to perform EQE measurements.

low EQE in the blue wavelengths could imply an excessive thickness of the p layer that leads to too much light absorption in this part. On the other hand, a low EQE in the red and NIR wavelengths suggests a bad performance of the back reflector leading to non-absorbed light, which causes losses in this part of the spectrum. The conclusions extracted will be explained in detail for each experiment.

3 Optimization and improvements in thin film a-Si:H solar cells

3.1 Introduction

The optimization of thin film silicon layers and solar cells has been widely studied in the last few decades, and the Solar Energy Group at the University of Barcelona is not an exception. However, as the used reactor is a recently acquired equipment, it was necessary to adapt the deposition conditions to obtain good quality solar cells. The manufacturer provided standard recipes for the deposition of the layers of amorphous silicon solar cells, but they needed to be tested and improved.

In this chapter, the test and optimization trials that have been developed on the layers and the solar cells are shown. The aim was to obtain a working device, trying to reach the state of the art on solar technology or, not being this possible, at least a device good enough to perform experiments with it. The optimization started with the provided amorphous silicon layers conditions mentioned before trying to obtain an amorphous silicon solar cell. The availability of starting deposition conditions, the fact that this device is probably the less difficult to implement, and also the wide know-how of the group about this kind of cells, led to choose the amorphous silicon solar cell as the device that would be first optimized.

There are some considerations concerning some of the deposition situations that have to be taken into account from now on in this chapter. These are explained next and should be considered as the standard situation unless something else is pointed differently in a specific result.

- The silicon layers were deposited at the multichamber reactor at the UB (Chapter 2, Sec. 2.1.1). As it is a two chamber reactor, it was

3 Optimization and improvements in thin film a-Si:H solar cells

established that the doped layers were deposited always at deposition chamber 1, while intrinsic layers were deposited in chamber 2. This aims to suppress the boron and phosphorus contamination [86], so it was not necessary to make intermediate steps in the device fabrication to eliminate its effects [87][88].

- Since p and n layers were deposited in the same chamber, a burying layer consisting in about 200 nm of intrinsic silicon was always deposited between two depositions with different dopant gas. This way, the previous doped layer on the walls and electrode was covered with intrinsic material, avoiding cross contamination.
- The transparent conductive oxides (TCOs) were deposited at the sputtering also at the UB (Chapter 2, Sec. 2.1.2) and the metallic contacts were deposited at the thermal evaporator (Chapter 2, Sec. 2.1.3). Some of the metallic contacts were deposited at the sputtering, but this was not the usual.
- The single layer trials were deposited over commercial glass *Corning 1737*, while the solar cells were deposited over commercial *Asahi U* and *Asahi VU* glasses. The change in the cells substrate is due to the fact that *Asahi U* glass is no longer fabricated. A comparison between both glasses was done through a test amorphous solar cell, and no substantial difference was found.
- All the solar cells were deposited in superstrate configuration. This means that the *Asahi* substrate served as window and front contact and the deposition order of the layer is $p/i/n/BR(\text{TCO}+\text{metal})$.
- The finished solar cell area was defined with the metallic back contact and it is 1 cm^2 (Fig. 2.5).

3.2 Homogeneity and area definition

The first test developed was a homogeneity measurement of the layers. The reactor is prepared to deposit over substrates of $10 \times 10 \text{ cm}^2$, but as the substrate holder frame is metallic, the plasma on the sides is

3.2 Homogeneity and area definition

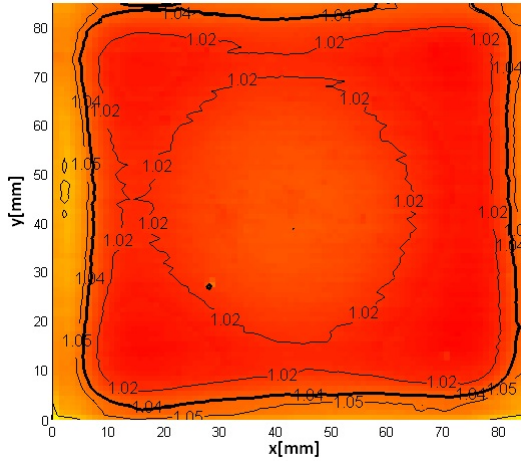


Figure 3.1: Homogeneity map over a $9 \times 9 \text{ cm}^2$ intrinsic silicon layer.

affected. The homogeneity measurements were done through an optical transmission measurements mapping. A scan of the samples was done with an *Ocean Optics USB2000* spectrophotometer and an optical fiber light source moving on an x - y table. The light source covered a wavelength range from 400 to 1000 nm. An area of $9 \times 9 \text{ cm}^2$ was scanned with a step of 1 mm in both x and y axes. After, the measurements were used to determine the thickness profile by the Swanepoel envelope method [89]. The software for both controlling the measurement taking process and obtaining the thickness profile from the measurements is home-made and was already used in previous group work [57].

The measurements were developed over an about $1 \mu\text{m}$ thick intrinsic layer, in order to obtain enough interference fringes. The results are shown in Fig. 3.1. As it can be seen, a difference of less than 5% is found in a $9 \times 9 \text{ cm}^2$ area. This seems small enough to consider the cells homogeneous in this area.

The final check of the homogeneity was developed when it was possible to deposit the first solar cells. It is important to notice that, at that moment, the cells were not optimized yet, and this is why the parameters

3 Optimization and improvements in thin film *a*-Si:H solar cells

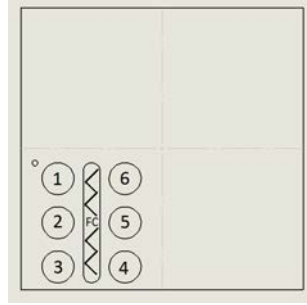


Figure 3.2: Position of 1 cm² solar cells and central front contact over them 10x10 cm² pin sample.

do not show good values. However, this was not critical yet as the aim of this experiment was to compare the cells between them. A 10×10 cm² *Ashai U+pin* sample was divided in four 5×5 cm² pieces, and in each one six 1 cm² solar cells were completed by delimiting the area with the back reflector mask and the scratching and etching procedure explained in Chapter 2, Sec. 2.2.2. The position of the mask over the sample and the cell numeration is shown in Fig. 3.2.

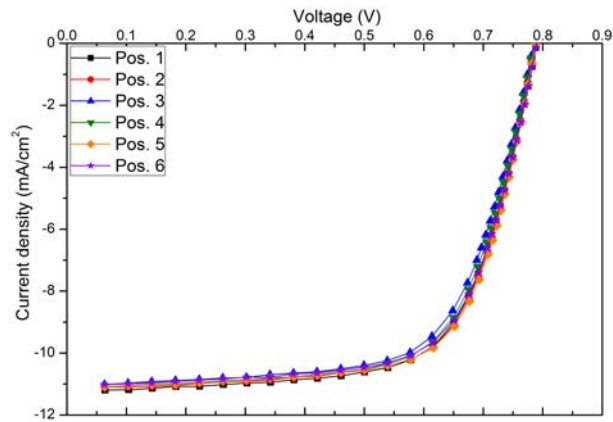


Figure 3.3: *J-V* curves of the six positions on the sample shown on Fig. 3.2.

3.3 Intrinsic amorphous silicon layer optimization

The current-voltage curves were measured and compared in order to check the difference between them. The J - V curves are shown on Fig. 3.3. As it can be seen, the six curves are almost coincident, with a very slight difference in the cell in position 3, which is the one closest to the corner. Although this difference is not very high, it was considered that unless four $5 \times 5 \text{ cm}^2$ pieces were needed, the central zone would be used to obtain the cells. Normally, two sets of six cells are deposited in the central zone of $10 \times 5 \text{ cm}^2$.

3.3 Intrinsic amorphous silicon layer optimization

3.3.1 Properties optimization

The intrinsic silicon layer is used as absorber layer (active layer) in amorphous silicon solar cells, which means that it has to fulfill a series of conditions in its properties in order to be suitable for this function. According to Ruud Schropp and Miro Zeman [23], the conditions for quality intrinsic amorphous silicon for absorber layers are those shown in Table 3.1.

Table 3.1: Criteria for 'device quality' amorphous silicon films [23].

| Property | Requirement |
|--|---|
| Dark conductivity | $< 10^{-10} \Omega^{-1} \text{cm}^{-1}$ |
| AM1.5(100 mW/cm ²) Photoconductivity | $> 10^{-5} \Omega^{-1} \text{cm}^{-1}$ |
| Band gap, Tauc | $< 1.8 \text{ eV}$ |
| Band gap, cubic | $< 1.6 \text{ eV}$ |
| Absorption coefficient at 600 nm | $\geq 3.5 \cdot 10^4 \text{ cm}^{-1}$ |
| Absorption coefficient at 400 nm | $\geq 5 \cdot 10^5 \text{ cm}^{-1}$ |
| Activation energy | $\approx 0.8 \text{ eV}$ |

In order to find the most suitable material for amorphous silicon solar cells, three optimization series of intrinsic a-Si:H layers were developed. The series were made varying one parameter in each case. These parameters are silane flow (so a series on depletion is obtained), hydrogen flow (so

3 Optimization and improvements in thin film a-Si:H solar cells

Table 3.2: Deposition parameters for intrinsic silicon layers. The bold quantity in varying parameters is the one kept constant in the rest of the series.

| Fixed parameters | |
|-----------------------|---|
| Pressure | 80 Pa |
| Power | 4 W (≈ 33 mW/cm ²) |
| Electrode distance | 15 mm |
| Time | 30 min |
| Background pressure | $< 2 \cdot 10^{-5}$ Pa |
| Varying parameters | |
| Silane flow | 2.5, 3.75, 5, 10, 20, 40 sccm |
| Hydrogen flow | 0 , 40, 80, 120, 160, 200 sccm |
| Substrate temperature | 150, 175, 200 , 225, 250, 300 °C |

a series on hydrogen dilution is obtained) and substrate temperature (this is, the real temperature according to the 2/3 relation found in Chapter 2, Sec. 2.1.1). The standard deposition conditions for the *i* a-Si:H layers are shown in Table 3.2, including the variations in the mentioned parameters. Over these layers, measurements of the upper mentioned properties were developed to find dependencies and try to obtain optimum values.

3.3.2 Developed measurements

3.3.2.1 Thickness and deposition rate

In order to measure thickness, two different techniques were used, in order to be sure of the obtained values. These techniques are confocal microscopy and profilometry, and the used equipments are described at Chapter 2, Sec. 2.3.1. Normally the two sets of measurements show almost the same values within a margin of error. In any case, the confocal measurement value is the one that is picked while the profilometer measurements are only developed to verify the confocal ones (except some exceptional cases).

3.3 Intrinsic amorphous silicon layer optimization

3.3.2.2 Optical measurements

The optical measurements, which are transmittance (T) and reflectance (R) were developed in the UV-VIS-NIR Spectrophotometer (Chapter 2, Sec. 2.3.2.1). The objective of these measurements was to obtain the Tauc optical bandgap (E_g) from them [39]. The procedure is explained in detail in Cristobal Voz's thesis [53]. The absorption coefficient (α) can be obtained from the equation

$$e^{\alpha} = \frac{4ns(1 + \frac{A}{T}) + \sqrt{[4ns(1 + \frac{A}{T})^2 + 4(n^2 - s^2)^2]}}{2(n + s)^2} \quad (3.1)$$

where n is the refractive index of the material (intrinsic amorphous silicon) which is obtained from Optical program measurements, s is the refractive index of the substrate (*Corning 1737* glass) provided by the manufacturer; and A is the absorbance of the material which is calculated as

$$A(\lambda) = 1 - T(\lambda) - R(\lambda) \quad (3.2)$$

With the obtained absorption coefficient, $\sqrt{\alpha(E)E}$ versus the energy (E) can be plotted, and a linear regression is made in the slope zone in order to obtain the cut point with energy axes, which is the optical Tauc bandgap E_g [39].

To try to minimize the error, a home-made Matlab program has been developed and optimized to make this fitting. The linear regression was normally made in the zone between 1.9 and 2.6 eV, except for those cases where that interval was clearly affected by interferences.

3.3.2.3 Electric measurements

To perform the electrical measurements of the layers, the equipment described in Chapter 2, Sec. 2.3.3.1 was used. Four silver contacts of $1\text{mm} \times 1\text{cm}$ separated this same area (Fig. 2.5) were deposited over the samples to make the two point conductivity measurements. The samples were put under vacuum and the heater was used to control the temperature.

3 Optimization and improvements in thin film a-Si:H solar cells

For the dark conductivity, the vacuum chamber was closed with a metallic opaque cover. The fact that the measurements were performed over very resistive samples led to very small currents, close to the electrometer lower limit, which could result in erratic measurements. To minimize the errors, the value of the conductivity was not obtained from a single point but from a linear regression of intensity versus voltage. Voltage was varied from -100 to 100 V with a step of 10 V. At each point, 5 measurements were taken with 10 seconds between them to check the error: if the standard deviation was too high, the point was not taken into account for the regression.

To measure the photoconductivity, a LED (described in Chapter 4, Sec. 2.2.4) was placed over the vacuum box at a height such as the sample was irradiated with an AM1.5 like illumination (1000 W/m^2). This height was obtained from a calibration with a standard *T-Solar* cell. Then, the vacuum box was closed with a transparent glass cover. In this case the measurements had to be done as fast as possible to avoid light induced degradation. Besides, since the currents are about 5 orders of magnitude higher, they are now far from the electrometer limit, which means that the values were much more accurate and much less time was needed to obtain reliable data.

A measurement of the evolution of the conductivities with the under illumination time was performed on an intrinsic amorphous silicon layer deposited in similar conditions to those used for the optimization series. In Fig. 3.4 the evolution in the first 10 hours is shown. It can be seen that the photoconductivity is reduced by a factor of almost 2 in about 15 minutes under illumination, so it was necessary to measure very quick to obtain reliable values for the initial state. In this situation, the measurement procedure was modified to be quicker, varying voltage from -70 to 70 V with a step of 20 V, measuring 5 times at each point with 2 s between them. This leads to a very quick measurement that avoids LID effect but keeping the standard deviation small enough.

To obtain the activation energy (E_a), measurements of the dark conductivity were taken at different temperatures. To measure the activation energy accurately, the temperature values must be reliable, so

3.3 Intrinsic amorphous silicon layer optimization

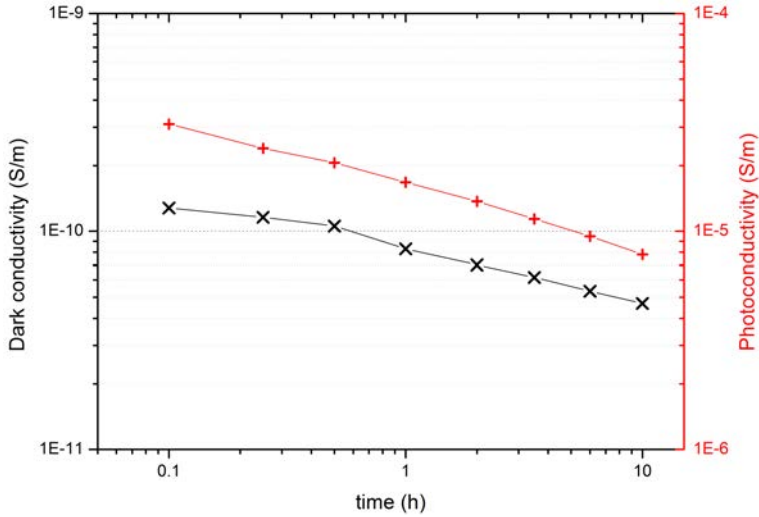


Figure 3.4: Evolution of the dark conductivity and photoconductivity of an a-Si:H layer with the under illumination time in the first 10 hours.

the configuration of dark conductivity is used but a metallic piece is added to cover the sample, which is also in contact with the heater. This way it conforms an oven-like space that makes the temperature of the sample more stable and reliable. With this configuration, the temperature was raised to 200°C and then stabilized, then the heater was switched off and values of conductivity were taken when there was a difference of at least 0.5°C with the previous value of the temperature. With these values, the activation energy was obtained as described in Chapter 2, Sec. 2.3.3.1.

3.3.3 Depletion series

3.3.3.1 Experimental

The depletion (D) is a parameter that somehow evaluates the deposition efficiency, this being understood as how many of the silicon atoms introduced in silane form are eventually deposited as part of the films. As D is habitually an intermediate parameter to evaluate other properties of

3 Optimization and improvements in thin film a-Si:H solar cells

the plasma, such as silane concentration or partial pressure, its definition can be given differently depending of how it has been obtained from indirect measurements.

According to Strahm *et al.* [90] depletion as parameter is a measure of the reduction of the silane partial pressure due to dissociation by the plasma, and is normally used to evaluate the difference in the silane concentration in a silane-hydrogen mixture between plasma on and plasma off situations. The depletion would be then defined as:

$$D = 1 - \frac{p(SiH_4)_{on}}{p(SiH_4)_{off}} \quad (3.3)$$

where $p(SiH_4)_{off}$ is silane partial pressure when the plasma is off, and $p(SiH_4)_{on}$ when it is on. These parameters can be either directly measured [91] or obtained from indirect measurements like Fourier Transform Infrared (FTIR) spectroscopy [90].

Another way to obtain D is evaluating the silane densities in the reactor at constant pressure before and during the plasma steady state [92]. Considering this, the depletion fraction would be defined as:

$$D = 1 - \frac{n(SiH_4)_{on}}{n(SiH_4)_{off}} \quad (3.4)$$

The silane density is deduced from a light absorption spectroscopic measurement, which is proportional to the density of absorbing molecules.

Another way to obtain the depletion is considering the ratio of the deposition rate R_d to the maximum deposition rate R_{dmax} , which would be reached if all silicon atoms contained in the input gas flow were deposited uniformly on the reactor walls, electrodes and substrate [93].

$$\frac{R_d}{R_{dmax}} = \frac{D}{1 + c(1 - D)} \quad (3.5)$$

where c is defined in terms of the input flow rates of the precursor gases as [94]

$$c = \frac{\Phi_{SiH_4}}{\Phi_{SiH_4} + \Phi_{H_2}} \quad (3.6)$$

3.3 Intrinsic amorphous silicon layer optimization

This is how D has been calculated in this series. Since the deposition time was fixed, R_d/R_{dmax} is equivalent to the fraction between thicknesses d/d_{max} ; and also as the area was equal (substrate, electrode and walls), this is equivalent to the fraction between number of atoms N_{Adep}/N_{Amax} . The thickness of the layers was measured, and with the areas of the sample, the lower electrode and the surrounding walls, the quantity of deposited atoms was calculated, based on the atomic density of amorphous silicon [95]. The same assumptions made by Feltrin *et al.*[93] and Bugnon *et al.*[94] were made: uniform deposition over walls and substrate and no loss of silicon atoms through polysilane or powder formation. As far as powder is concerned, the previous trials made in the deposition chamber with the initial a-Si:H recipe have shown that there is no powder formation in this regime, so this assumption can be made, at least at first.

To obtain N_{Amax} the quantity of silane in the chamber during the process was obtained from the flow and the total deposition time. Being the flows different, the quantity of total silane present during the process is also different, so as the residence time in the chamber. Considering this, D is obtained for the different flows using the cleared D definition (as in this case only silane is pumped in, c is equal to 1):

$$D = \frac{2F}{(1 - F)} \quad (3.7)$$

where F is the fraction N_{Adep}/N_{Amax} . A plot of D versus SiH_4 flow can be seen in Fig. 3.5. As it is shown, a wide range is covered in depletion. The values are different than others found on the bibliography due to the fact that in this series no additional hydrogen has been introduced.

3.3.3.2 Results and discussion

The first parameter measured was the thickness of the layers, as it had to be used to obtain the depletion values. In this case three different methods were used to measure the thickness: the regular confocal microscopy and profilometer measurements and also ellipsometry measurements (done in the LPICM in Palaiseau, Sec. 3.6). After the three measurements, the values obtained by ellipsometry were used, as the error in these was lower.

3 Optimization and improvements in thin film a-Si:H solar cells

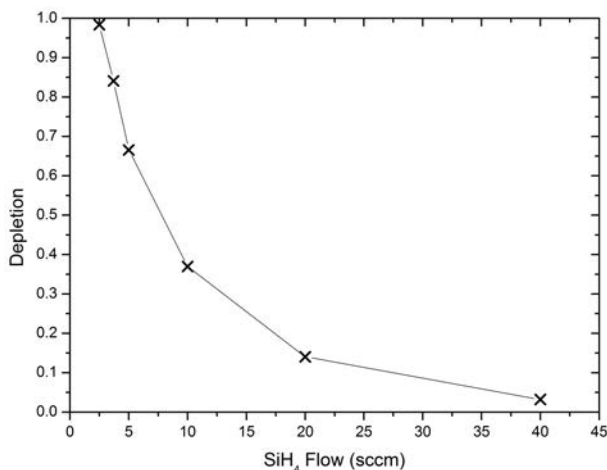


Figure 3.5: Calculated depletion versus silane flow. The points are the values used for the samples.

Results are shown in Fig. 3.6.

As it can be observed, there is an important dependence of the thickness and the deposition rate with the depletion, as R_d varies in a factor over 2 between the lowest and the highest value. R_d starts at its minimum at lower D values, reaches a maximum at about 0.37 and then goes down again. Different behaviors on R_d have been found at the literature, but in series with different parameters and usually in very high frequency (VHF) plasma [91][92][94][96].

If the reactions in amorphous silicon formation described by Schropp and Zeman [23] are considered, and knowing that pressure is kept stable during the process, this behavior suggests the contribution of two mechanisms: at low depletion values, that is high input silane flow, the residence time of the gas is short, so some of the active species are pumped out before the chemisorption takes place. On the other hand, at high depletion (lower flow) the residence time is higher, and the probability of polysilane species with two, three or even four atoms of silicon increases,

3.3 Intrinsic amorphous silicon layer optimization

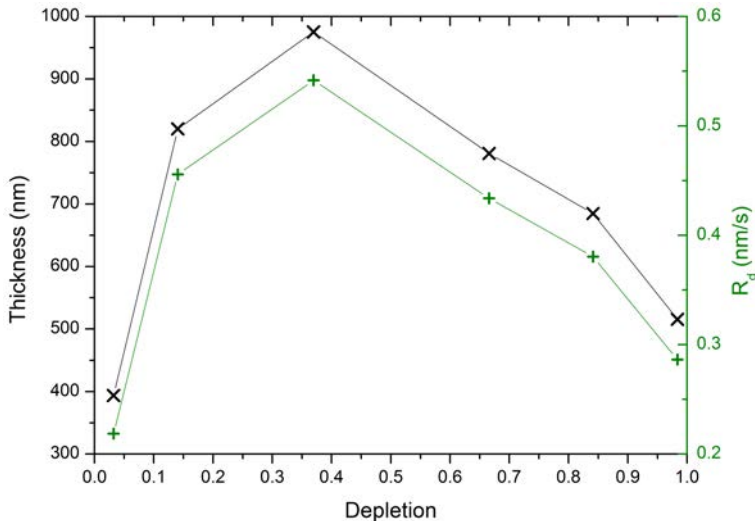


Figure 3.6: Thickness and deposition rate of depletion series samples.

reducing the deposition rate and affecting the plasma [97]. The maximum point in R_d is reached when these two mechanisms reach an equilibrium.

This behavior of central points being a relative maximum or minimum is reproduced in other parameters. If the results in the conductivities in the as deposited/annealed state are observed (Fig. 3.7), a minimum in both dark and photoconductivity is found in the 0.37 depletion sample, which is the same that presented the maximum in thickness and deposition rate. The difference between the two parameters is about 4 orders of magnitude, which is less than the quality condition exposed in Table 3.1.

If a relative comparison is made, the low depletion sample is the one that shows higher difference between dark and photoconductivity, and this difference becomes lower as the depletion grows, suggesting that low depletion material would be more performing on a device. This kind of dependence of conductivity with deposition rate has already been reported [98].

3 Optimization and improvements in thin film a-Si:H solar cells

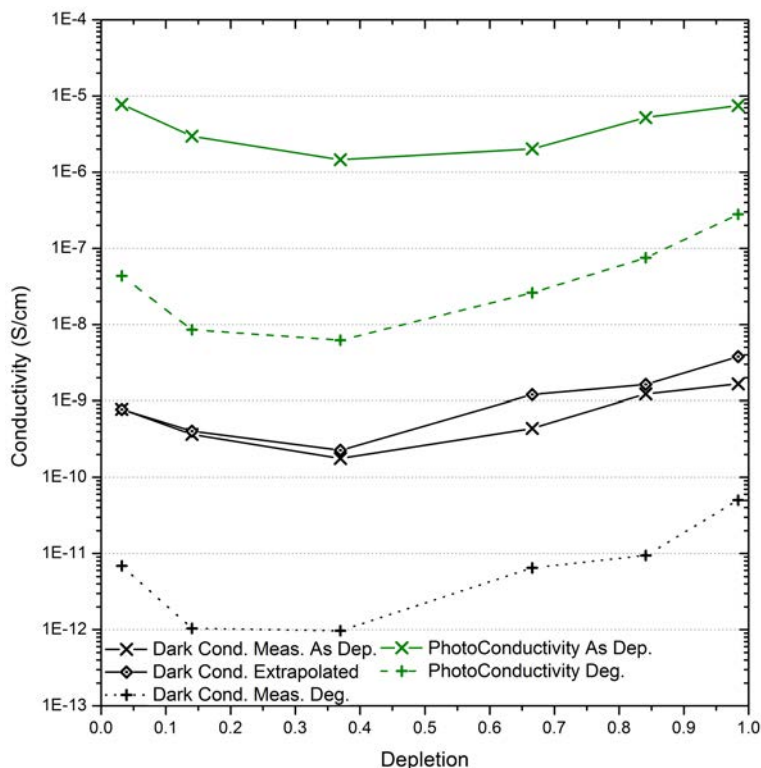


Figure 3.7: Dark and photoconductivity in the initial (continuous line) and degraded (dots line) states of depletion series samples.

To completely be sure of this difference, light induced degradation at 30°C has been performed over the samples over 1000 hours to get the stabilized state of the material. The results are also presented in Fig. 3.7 in dotted lines. The degradation is about two orders of magnitude in both conductivities, but it can be noticed that the samples with higher depletion values are a little less degraded by light, reaching a difference of about 1.5 orders of magnitude. This indicates that, although before LID the samples of low and high depletion showed similar values on the conductivities, after LID less defects are generated on the high depletion samples.

3.3 Intrinsic amorphous silicon layer optimization

The activation energy and the gap results are shown in Fig. 3.8. Similar behavior as before is found, this time with the 0.37 sample showing a maximum in the gap and a minimum in the activation energy. According to Table 3.1 several samples fulfill the requirement of having a gap lower than 1.8 eV, being the ones of higher deposition rate those that do not. If activation energy is evaluated, the sample with lowest depletion is the one that fit best with the ≈ 0.8 eV condition.

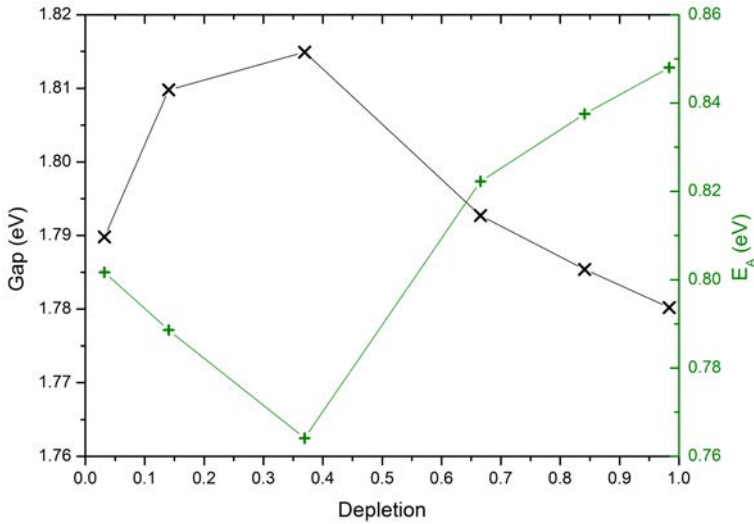


Figure 3.8: Gap and activation energy in depletion series samples.

The absorption coefficient was also obtained from the optical measurements. It was used to calculate the values of the gap showed before, but it is also one of the parameters used to determine the quality of the device. Fig. 3.9 shows the absorption coefficient as a function of the energy for all the samples. The requirements for device quality in Table 3.1 establish a minimum of $3.5 \times 10^4 \text{ cm}^{-1}$ at 600 nm and $5 \times 10^5 \text{ cm}^{-1}$ at 400 nm, which approximately correspond to energies of 2.07 eV and 3.10 eV respectively (obtained through the formula $E=hc/\lambda$). These two values are marked in the plot to guide the eye. The results show that all the samples are below

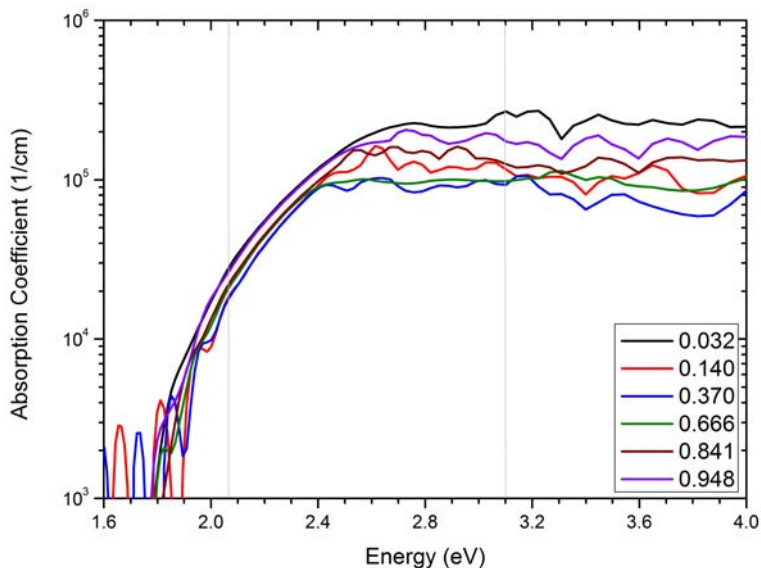


Figure 3.9: Absorption coefficient in depletion series samples. The gray lines correspond to 600 nm (≈ 2.07 eV) and 400 nm (≈ 3.10 eV) and are drawn to guide the eye.

this values in both cases, so probably further optimization is needed in this layer.

Focusing on direct comparison, a strong dependence is found in the absorption coefficient with depletion, specially from about 2.4 eV (516 nm). More accurately, the dependence is with the deposition rate, as the higher it is, the lower the absorption coefficient becomes in the mentioned wavelengths. This is consistent with the results obtained before, pointing the samples of higher R_d as less quality material samples.

3.3.3.3 Conclusions and future work

A series in depletion has been studied and from the results several conclusions can be extracted:

3.3 Intrinsic amorphous silicon layer optimization

- None of the samples fulfill all of the considered criteria for device use, specially in photoconductivity and absorption coefficient, where the values should be higher. Nevertheless, the values are good enough to obtain a working device.
- The deposition rate is highly influenced by depletion, finding a maximum at about 0.37, where the reaction equilibrium leads to a maximum in the speed.
- However, though this could be desirable, high deposition rate samples have shown worse performance, as higher speed leads to higher defect concentration.
- The sample with the lowest depletion, which corresponds with the lowest deposition rate, shows the best qualities to be used in solar cells as deposited, but after LID, the ones with higher depletion values showed better behavior against SWE.
- Solar cells with different silane flows should be deposited to check these results in devices. Even variable concentration could be tried, as it has been reported that this could offer good results [99].

3.3.4 Hydrogen series

3.3.4.1 Experimental

Hydrogen dilution, defined here as Φ_{SiH_4}/Φ_{H_2} , is a parameter that has been widely studied trying to find the amorphous to microcrystalline transition, aiming to obtain a material more resistant to light soaking [100]. However, this material is developed in much higher dilutions than those used in this work. Here, the objective is to study if adding hydrogen to the plasma leads to to obtain better performance of the material, but keeping it amorphous, as it has higher deposition rate [97]. So, hydrogen flow is varied then between 0 and 200 sccm, while silane flow is kept constant at 40 sccm, obtaining dilutions between 0 and 5. Although hydrogen is incorporated, these dilutions still keep the silane concentration in levels corresponding to amorphous material [96]. The protocrystalline (also called polymorphous) and microcrystalline layers

3 Optimization and improvements in thin film a-Si:H solar cells

require much higher hydrogen dilution [101].

3.3.4.2 Results and discussion

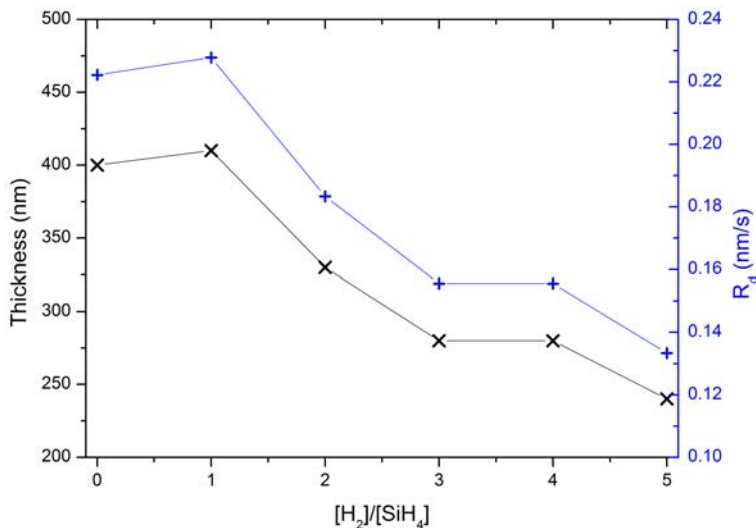


Figure 3.10: Thickness and deposition rate of hydrogen dilution series samples.

The results of the measurements of the thickness of the samples are shown in Fig. 3.10. As expected, the deposition rate decreases with the increment of hydrogen flow, due to a higher etching by atomic hydrogen [102]. The dependence is not as strong as in depletion series. What it is interesting is that the samples on higher dilution showed bad adhesion to the substrate. These hydrogen dilutions at the used pressure and temperature lead to unstable amorphous layers which detach themselves [101][103]. The 200 sccm (5:1) sample was even not taken into account for some further results as it was very difficult to perform reliable measurements on it due to the irregular detached surface.

The results in conductivities are shown Fig. 3.11. As it can be seen, the dark conductivity slightly decreases with dilution, while the photocon-

3.3 Intrinsic amorphous silicon layer optimization

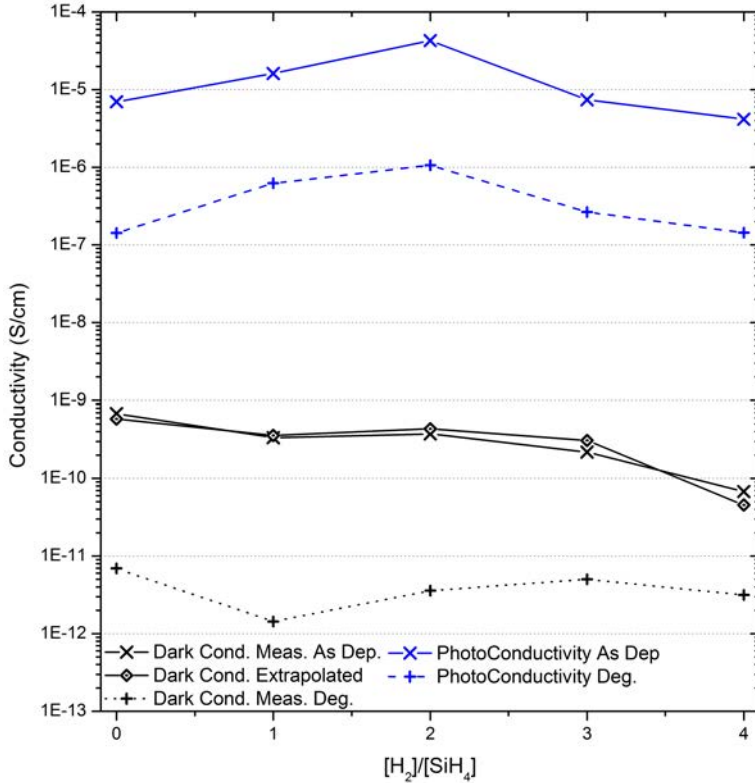


Figure 3.11: Dark and photoconductivity in the initial (continuous line) and degraded (dots line) states of hydrogen series samples.

ductivity shows a maximum at 2:1 sample. The difference between them at this point is about five orders of magnitude, which would fulfill the condition for device quality. Takai *et al.* [97] have already reported an optimum H₂ dilution ratio to obtain higher values of the fill factor after light soaking in a Schottky diode. Nishimoto *et al.* [104] obtained a maximum of stability (and then performance) in the minimum of electron temperature and trisilane fraction; according to them, this point appears at a hydrogen dilution of about 3, while in this case it is found a little earlier, at 2.

To check if this behavior is maintained in the degraded states, light

3 Optimization and improvements in thin film a-Si:H solar cells

induced degradation over the samples was developed just like in the depletion series. Results are also shown in Fig. 3.11. The shape of the curves is maintained, just like in depletion series. Here, the hydrogen content tends to reduce the LID, as it was expected. However, in this case, the sample 2:1 is still showing the best properties, specially the photoconductivity, which reaches a value a little over 10^{-6} S/cm.

As far as the activation energy and the gap are concerned, it can be observed in Fig. 3.12 that 2:1 sample shows a minimum in activation energy with a value of about 0.7 eV, which is probably a bit low, as a value of ≈ 0.8 eV is desired. On the other hand, the gap increases with hydrogen flow, so the 0 sample is the one that better fulfills the condition of having a gap under 1.8 eV.

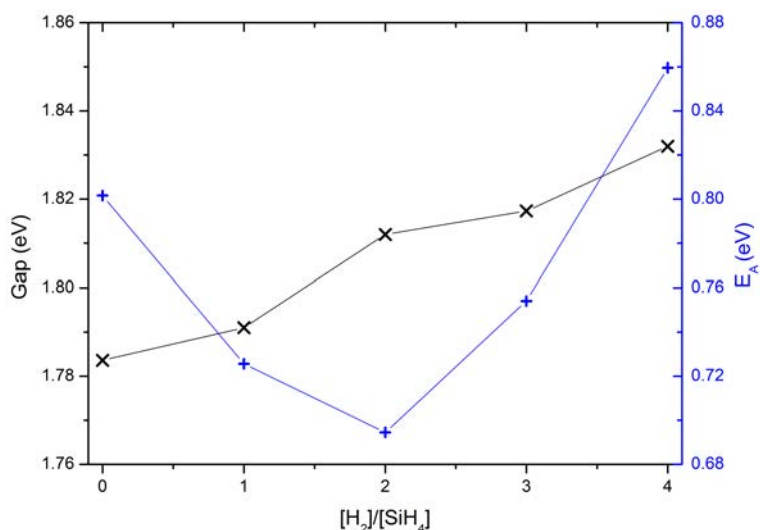


Figure 3.12: Gap and activation energy in hydrogen series samples.

The absorption coefficient in this case (Fig. 3.13) shows much less variation between the samples. The sample that shows higher absorption coefficients at 600 nm and 400 nm is the 3:1 sample, which is not the same optimum point as the one found for other parameters, but is coincident

3.3 Intrinsic amorphous silicon layer optimization

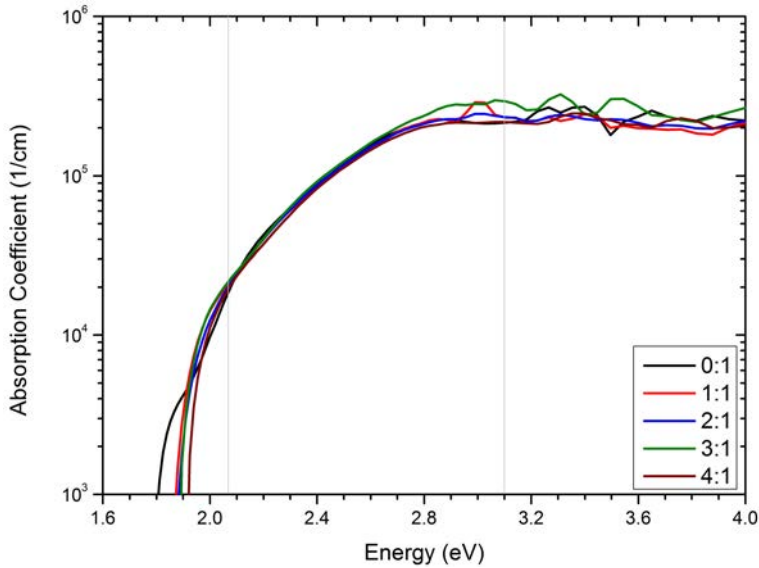


Figure 3.13: Absorption coefficient in hydrogen series samples. The gray lines correspond to 600 nm (≈ 2.07 eV) and 400 nm (≈ 3.10 eV) and are drawn to guide the eye.

with the one found by Nishimoto *et al.*[104]. However, the differences in the plot are not very big.

3.3.4.3 Conclusions and future work

According to the results in the hydrogen dilution series for amorphous silicon, some conclusions can be extracted and it is possible to set the bases to some future work that could lead to more performing layers.

- The 2:1 sample shows the difference of 5 orders of magnitude in the conductivities. However, this sample shows also a little low activation energy and absorption coefficient.
- A moderate inclusion of hydrogen reduces light induced degradation, as the drop in the conductivities is smaller for higher hydrogen dilutions.

3 Optimization and improvements in thin film a-Si:H solar cells

- One way to get further optimization is to combine both depletion and hydrogen dilution results, as normally depletion is used as a parameter in hydrogen presence.
- Increasing hydrogen dilution to get the protocrystalline situation has proven to be a way to get quality material, more resistant to LID [105][106]. Still, to get this kind of material much higher dilutions are required.
- In this case, the fact that the samples with higher hydrogen dilutions detached from the substrate suggests that they are being deposited in an incorrect plasma regime. Pressure or power should have to be modified to get suitable deposition conditions [91][94].

3.3.5 Temperature series

3.3.5.1 Experimental

The temperature series has been developed using samples with a $\Phi_{SiH_4} = 40$ sccm and a $\Phi_{H_2} = 0$ sccm. The temperatures of the substrates was 150, 175, 200, 250 and 300°C, which means that the chamber was set to 225, 262, 300, 375 and 450°C respectively, according to the 2/3 correlation exposed in Chapter 2, Sec. 2.1.1.

Series on temperature have already been made in this group [49][56] with different techniques and reactors, and the key point was to adapt the know-how to the new equipment. Lower temperatures have been tested for amorphous silicon [107], aiming to use it over plastic substrates. As it has been reported by Roca i Cabarrocas [108], the defect density is much higher in samples deposited at lower temperatures.

3.3.5.2 Results and discussion

As far as the thickness and the deposition rate are concerned (Fig. 3.14), the temperature is the parameter that presents the smaller variation. However, a slight tendency to grow with increasing temperature is found. This behavior has been already reported and is related to particle and

3.3 Intrinsic amorphous silicon layer optimization

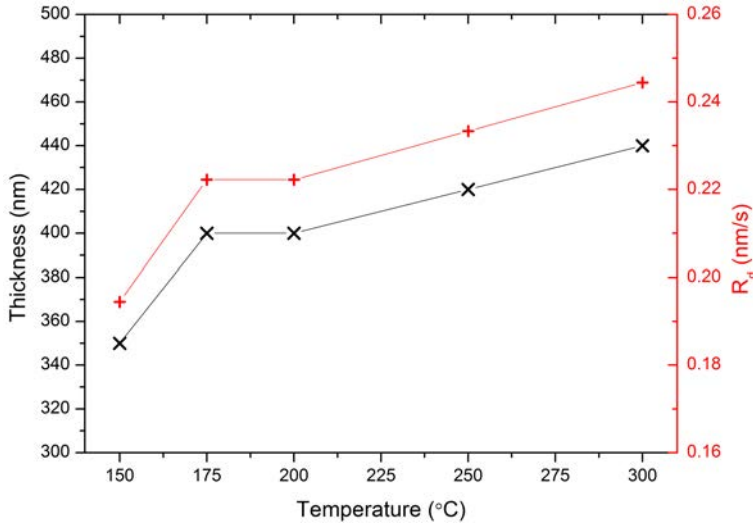


Figure 3.14: Thickness and deposition rate of temperature series samples.

powder formation [108][109] which affects the layer growing. However, this results do not match with Koch *et al.* [107] tendency of R_d decrease with increasing temperature, although this is a different temperature range.

The results in the conductivities are shown in Fig. 3.15. Both dark and photoconductivity have a tendency to grow with the deposition temperature, which matches with Maemura *et al.* results [109]. Still the difference of about four orders of magnitude remains constant.

After the light soaking, the conductivities show the same tendency but about two orders of magnitude below, being the 300°C sample the one that experiences higher degradation in the photoconductivity. However, it still presents the highest value. So the quality of the film seems to improve with the temperature, probably because low substrate temperature deposition at high deposition rate is quite often accompanied by powder formation and poor film stability [104].

3 Optimization and improvements in thin film a-Si:H solar cells

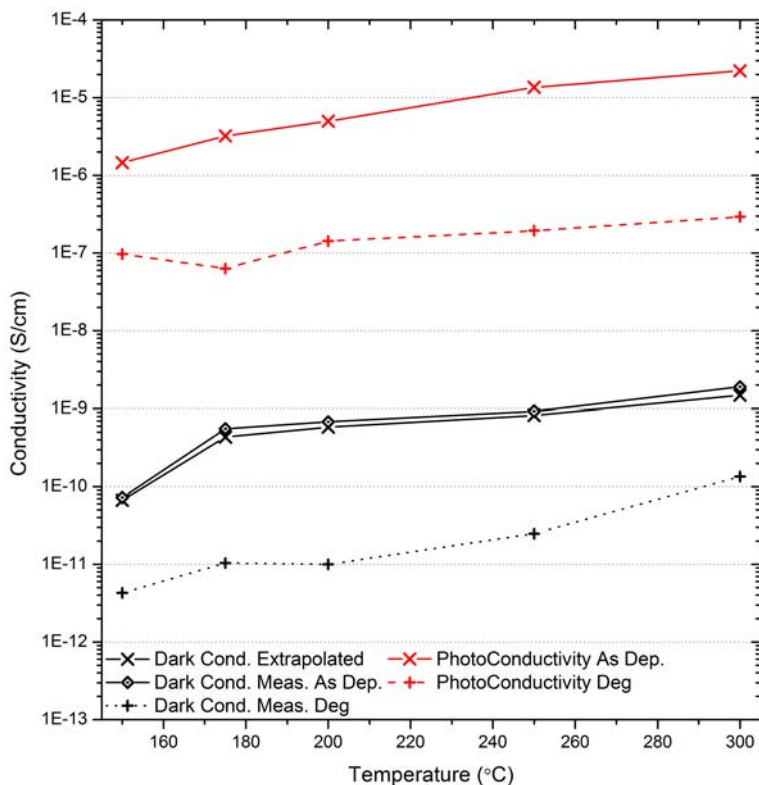


Figure 3.15: Dark and photoconductivity in the initial (continuous line) and degraded (dots line) states of temperature series samples.

Fig. 3.16 shows the results in activation energy and bandgap. The activation energy shows a maximum at 250°C and then decrease again. This behavior could be explained with the different dominant processes below and over this temperature [103]. As far as the band gap is concerned, a decrease with increasing temperature is observed as in Maemura *et al.* results [109].

3.3 Intrinsic amorphous silicon layer optimization

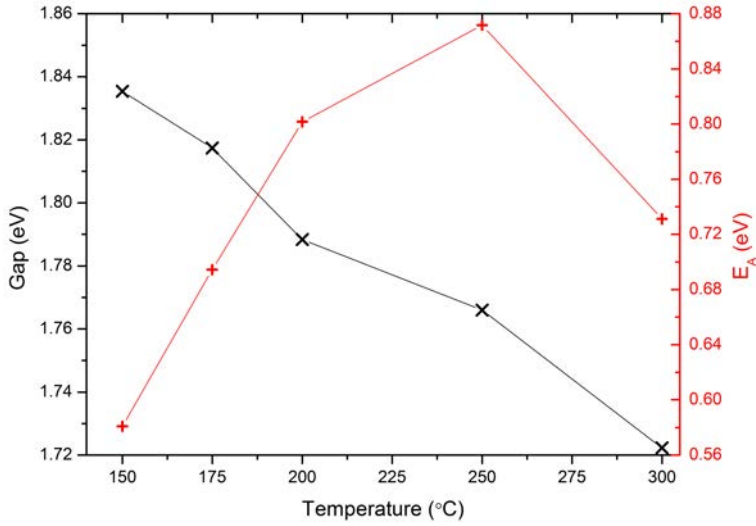


Figure 3.16: Gap and activation energy of temperature series samples.

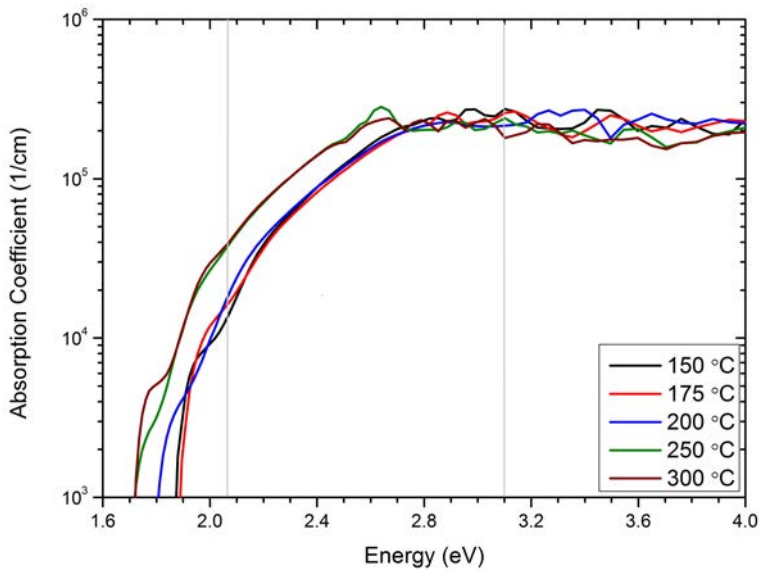


Figure 3.17: Absorption coefficient in temperature series samples. The gray lines correspond to 600 nm (≈ 2.07 eV) and 400 nm (≈ 3.10 eV) and are drawn to guide the eye.

3 Optimization and improvements in thin film *a*-Si:H solar cells

The absorption coefficient of the samples in the temperature series is shown in Fig. 3.17. An interesting effect is observed in the samples deposited at 250°C and 300°C: these samples show an important increase in the absorption coefficient at 600 nm (almost reaching the device quality level), but on the other hand, they show the lowest values at 400 nm, though the difference is not that big.

3.3.5.3 Conclusions and future work

A series in temperature has been studied and from the results several conclusions can be extracted:

- The deposition rate is almost constant but slightly increasing over 200°C.
- The activation energy shows a maximum at 250°C, and good values of E_a can be found both below and over this maximum.
- Increasing the temperature could lead to an improved layer, as the gap is lower and the photoconductivity is higher, while activation energy shows adequate values.
- Higher temperature samples show also better values of the absorption coefficient in the blue zone of the spectrum.
- With this in mind, raising the temperature could be a good option to improve the devices. However, this could lead to an reduced V_{oc} in the solar cells [110].

3.4 Boron doped silicon layer optimization

Before the deposition of the solar cells could be done, a working optimized boron doped (*p*) layer was necessary. Boron doped layer is bound to be the window layer, that means that light enters the solar cell through it before reaching the active layer. As doped layers are highly defective, the carriers generated here are not collected; so the *p* window layer should absorb the less possible quantity of light [39]. To achieve this objective the material has to have the higher possible gap; and the layer in the cell

3.4 Boron doped silicon layer optimization

has to be as thin as possible to reduce the absorption the minimum while the electric field is maintained in all the active layer.

Just as in the case of intrinsic layers, Schropp and Zeman [23] provide a set of considered minimum conditions for quality boron doped material, either amorphous or microcrystalline. These requirements are shown in tables 3.3 and 3.4, respectively.

Table 3.3: Criteria for boron doped amorphous silicon films for its application in solar cells [23].

| Property | Requirement |
|------------------------------------|--|
| Conductivity | $>10^{-5} \Omega^{-1} \text{ cm}^{-1}$ |
| Conductivity for a 20nm thick film | $>10^{-7} \Omega^{-1} \text{ cm}^{-1}$ |
| Band gap, T_{auc} | $>2.0 \text{ eV}$ |
| Activation energy | $<0.5 \text{ eV}$ |
| Absorption coefficient at 600 nm | $\geq 1 \times 10^4 \text{ cm}^{-1}$ |
| Absorption coefficient at 400 nm | $\geq 3 \times 10^5 \text{ cm}^{-1}$ |

Table 3.4: Criteria for boron doped microcrystalline silicon films for its application in solar cells [23].

| Property | Requirement 300nm | Requirement 20nm |
|----------------------------|-----------------------------------|--|
| Conductivity | $1.5 \Omega^{-1} \text{ cm}^{-1}$ | $2.6 \times 10^{-2} \Omega^{-1} \text{ cm}^{-1}$ |
| Band gap, T_{auc} | 1.4 eV | - |
| Activation energy | $<0.025 \text{ eV}$ | 0.059 eV |
| Crystalline volume faction | 67 % | 17 % |

3.4.1 Boron doped amorphous silicon

With these requirements in mind, the optimization of the layers started using as first reference the conditions developed by Bengali *et al.* [111], although these conditions are implemented for a different frequency.

3 Optimization and improvements in thin film a-Si:H solar cells

Several series on different parameters were performed in order to obtain the most suitable material. In this case, these were made consecutively, taking the best sample's recipe of the previous series as starting point for the subsequent one. The first series developed was in TMB partial flow ($\Phi_{TMB}/(\Phi_{TMB} + \Phi_{SiH_4})$), then temperature, then pressure and finally CH₄ partial flow ($\Phi_{CH_4}/(\Phi_{CH_4} + \Phi_{SiH_4})$). The values of the parameters are shown in Table 3.5

Table 3.5: Deposition parameters for boron doped amorphous silicon layers.

| | |
|------------------------------------|---|
| Fixed parameters | |
| Silane flow | 2.6 sccm |
| Power | 4 W (≈ 33 mW/cm ²) |
| Electrode distance | 15 mm |
| Time | 60 min |
| Background pressure | $< 5 \cdot 10^{-6}$ Pa |
| Varying parameters | |
| TMB (0.2% in H ₂) flow | 20, 40, 50 sccm |
| TMB partial flow | 0.13, 0.24, 0.29 |
| Substrate temperature | 150, 175, 200 °C |
| Pressure | 53, 80, 107, 133, 160, 187 Pa |
| CH ₄ flow | 2.1, 3.2, 5.2 sccm |
| CH ₄ partial flow | 0.44, 0.55, 0.67 |

The first parameter that was used as a discriminant to optimize the layer was σ_{dark} , as it was the easiest and quickest to be measured. The results are shown in Fig. 3.18. All the series are plotted in the same graph so the optimization is well seen. The series are chronologically tagged, this is, the numbers next to the series' name indicate the order of the series.

As it can be seen, the conductivity in the first series (TMB) increased with more dopant concentration, but in the limit of the equipment it slowed the growth ratio, and since being on the edge of the maximum flow rate was an issue to calibration, the central sample of 40 sccm of TMB

3.4 Boron doped silicon layer optimization

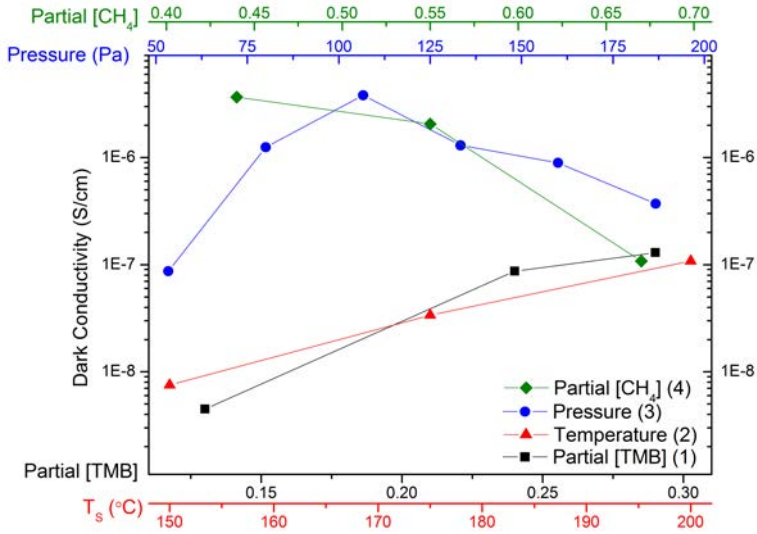


Figure 3.18: Results of dark conductivity optimization of boron doped amorphous layer series. The numbers next to the name of the series indicate the order.

(0.24 of partial flow) was selected as best concentration. Concerning the temperature, going down from 200°C to lower temperatures of deposition decreased the conductivity of the layers. Increasing the temperature could have been an option, but when the gap of the samples were checked, a tendency to decrease with increasing deposition temperature, showing the 150, 175 and 200°C gaps of 2.13, 2.10 and 2.08 eV respectively. As the gap has to be kept over 2 eV, the 200°C was for the moment kept as optimum.

The pressure series is the longest one, since two sets were made, making it a six samples series. This was made because at first, starting in 53 Pa and raising it until 107 Pa produced an increment in the conductivity but a maximum was not reached, so three more pressures were tried. When the results of this additional samples were added to the series, the maximum was now found at 107 Pa. Then, the flow of CH₄ was reduced conforming the last series. The reduction of CH₄ flow showed a maximum of the conductivity at 2.1 sccm (0.44 of partial flow). Besides, when the

3 Optimization and improvements in thin film a-Si:H solar cells

Table 3.6: Deposition parameters for the optimized boron doped amorphous silicon layers.

| Final values of modified parameters | |
|-------------------------------------|---|
| TMB partial flow | 0.24 |
| Substrate temperature | 200 °C |
| Pressure | 107 Pa |
| CH ₄ partial flow | 0.44 |
| Characteristic parameters (160 nm) | |
| Conductivity | $1.1 \times 10^5 \Omega^{-1} \text{ cm}^{-1}$ |
| Band gap, Tauc | 2.02 eV |
| Activation energy | 0.43 eV |

activation energy was measured, it showed a much stronger dependence: the 0.67, 0.55 and 0.44 of CH₄ partial flow showed an activation energy of 0.57, 0.51 and 0.43 eV respectively. With this considerations, the optimized amorphous *p* layer deposition conditions and characteristic parameters are listed in Table 3.6. These values fulfill the conditions for a device suitable amorphous *p* doped layer.

3.4.2 Boron doped microcrystalline silicon

Although *p* aSi:H was optimized to device quality level, it was considered that an optimization of boron doped microcrystalline silicon (*p* μ cSi:H) was also important for several reasons: First, the inclusion of a double *p* layer with both materials may lead to an important increase in V_{oc} ; then, as the HWCVD chamber has as objective the deposition of *i* μ cSi:H continuing the group work [57], to develop a cell, thus *p* μ cSi:H would be needed; finally, this material is also necessary to develop the emitters used in Chapter 5, Sec. 5.4.2.1.

The followed steps are almost the same as those used for *p* a-Si:H: from a starting recipe, some parameters are studied aiming to be optimized according to the requirements showed on Table 3.4.

3.4 Boron doped silicon layer optimization

The first series developed was in temperature, then TMB partial flow ($\Phi_{TMB}/(\Phi_{TMB} + \Phi_{SiH_4})$), then power and finally SiH_4 partial flow ($\Phi_{SiH_4}/(\Phi_{TMB} + \Phi_{SiH_4})$). The values of the used parameters are shown in Table 3.7. As μc -Si:H is more difficult to optimize, the series here are longer, of at least 4 samples.

Table 3.7: Deposition parameters for boron doped microcrystalline silicon layers. The numbers next to the name of the series indicate the order.

| | |
|--|--|
| Fixed parameters | |
| Pressure | 400 Pa |
| Hydrogen flow | 198 sccm |
| Electrode distance | 15 mm |
| Time | 20 min |
| Background pressure | $< 5 \cdot 10^{-6}$ Pa |
| Varying parameters | |
| Substrate temperature | 160, 170, 180, 190, 200 °C |
| TMB (0.2% in H_2) flow | 2, 2.5, 3, 3.5, 4 sccm |
| TMB partial flow | 0.0099, 0.0124, 0.0149, 0.0173, 0.0197 |
| Power | 20, 25, 30, 35 W |
| Silane flow | 0.35, 0.4, 0.45, 0.5, 0.6, 0.75 sccm |
| Silane partial flow ($\times 10^{-3}$) | 1.74, 1.99, 2.23, 2.48, 2.98, 3.72 |

Like before, σ_{dark} is the first parameter used to optimize the layer. Fig. 3.19 shows the results, chronologically tagged as before. The conductivity increases with the temperature, but since a-Si:H is being used in solar cells, it was not raised more than 200°C. In chapter 5, Sec. 5.4.2.1 the temperature is raised further, but the results will be showed there. After, the dopant concentration (TMB) is varied, obtaining a maximum in the concentration corresponding to a flow of 3 sccm (0.0149 of partial flow). Further increment or decrement of the flow results in lower σ_{dark} .

3 Optimization and improvements in thin film a-Si:H solar cells

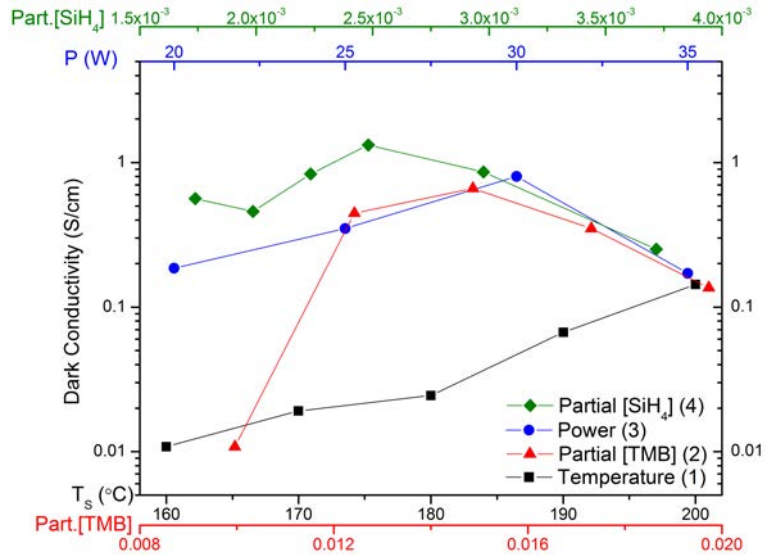


Figure 3.19: Results of dark conductivity optimization of boron doped microcrystalline layer series. The numbers next to the name of the series correspond to the order.

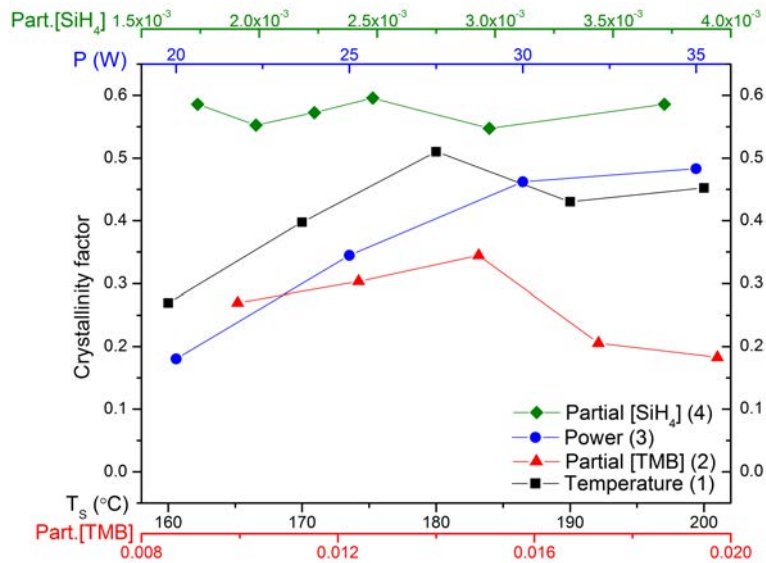


Figure 3.20: Results of crystalline fraction of boron doped microcrystalline layer series. The numbers next to the name of the series correspond to the order.

3.4 Boron doped silicon layer optimization

In the power series, a maximum is also found for 30 W, which would correspond to a power density of 0.25 W/cm^2 . Lastly, the longest series, concerning silane flow, shows also an optimum value with a flow of 0.5 sccm of silane (2.48×10^{-3}). At this point, the reached value is 1.32 S/cm , which is a little lower than the device quality criteria for 200 nm, but it has to be taken into account that the layer is thinner (120 nm). So, it can be considered that σ_{dark} fulfills the requirement.

Although dark conductivity already presented good enough values, other parameter was checked in order to verify that the maximum positions were really optimal. This parameter is the crystalline fraction χ_c , which was obtained through Raman spectroscopy measurements (Chapter 2, Sec. 2.3.2.2).

Fig. 3.20 shows the the results in crystalline fraction. The first thing that can be noticed is that the temperature series shows higher values than some other subsequent series, despite the fact that the conductivities were lower. This is because the boron concentration was not optimized at that point, and the effect of amorphization by boron content was lower.

After that, the results are mostly consistent with those on σ_{dark} , as the conductivity is linked with the cristallinity. The values for the crystalline fraction are still a little below the 0.67 mentioned in 3.4, but just like before, the films are thinner than 200 nm and the values of χ_c would increase in thicker layers.

With these considerations, the optimum parameters and some characteristic parameters of the optimized p doped microcrystalline layer are summarized in 3.8. This would be the $p \mu\text{cSi:H}$ layer which is employed when mentioned, unless something else is specified.

3 Optimization and improvements in thin film a-Si:H solar cells

Table 3.8: Deposition parameters for the optimized boron doped microcrystalline silicon layers.

| Final values of modified parameters | |
|-------------------------------------|---------------------------------------|
| Substrate temperature | 200 °C |
| TMB flow | 3 sccm |
| Power | 30 W (0.25 mW/cm ²) |
| SiH ₄ flow | 0.5 sccm |
| Characteristic parameters | |
| Conductivity | 1.32 Ω ⁻¹ cm ⁻¹ |
| Band gap, Tauc | 2.07 eV |
| Crystallinity factor | 0.596 eV |

3.5 Complete device optimization

3.5.1 Back reflector optimization

The rear part of the solar cells, normally called back reflector (BR), has a double role on the device: to act as an electrode that collects the photo-generated current; and to reflect the non-absorbed light back into the cell to provide a second chance for it to be absorbed. The BR can simply be a metallic layer, but normally a TCO is placed between the layer and the metal to provide a diffusion barrier for the metallic atoms into the cell, and to enhance the reflectance by adding an intermediate refractive index [112].

The BR optimization in the solar cells was one of the firsts optimizations developed, and an important part of the optimization process concerning the TCO was already presented in Paz Carreras' thesis [26]. In chapter 7, section 3 of this document, the trials over the first UB cells (this is, a not optimized device) are presented. In Fig. 3.21, the J - V curves of a subsequent trial are shown. It can be seen that two sets of ZnO:Al and ZnO:Ga with different conditions were tried over the same cell configuration. The conditions are shown Table 3.9. The difference between them is small, being the ZnO:Al(2) the best, providing an increase in the current of about 12% over the TCO-less sample.

3.5 Complete device optimization

Table 3.9: Deposition conditions for the TCO trials. All the samples were deposited at room temperature and with a power of 120 W.

| Sample | TCO doping | Pressure | Ar flow | O ₂ flow | T-S d | Thickness |
|-----------|------------|----------|---------|---------------------|-------|-----------|
| ZnO:Ga(1) | 2% | 0.13 Pa | 8 sccm | 0 sccm | 11 cm | 75 nm |
| ZnO:Ga(2) | 4% | 0.13 Pa | 8 sccm | 0 sccm | 11 cm | 80 nm |
| ZnO:Al(1) | 2% | 0.53 Pa | 12 sccm | 0.35 sccm | 15 cm | 85 nm |
| ZnO:Al(2) | 2% | 0.53 Pa | 12 sccm | 0 sccm | 15 cm | 75 nm |

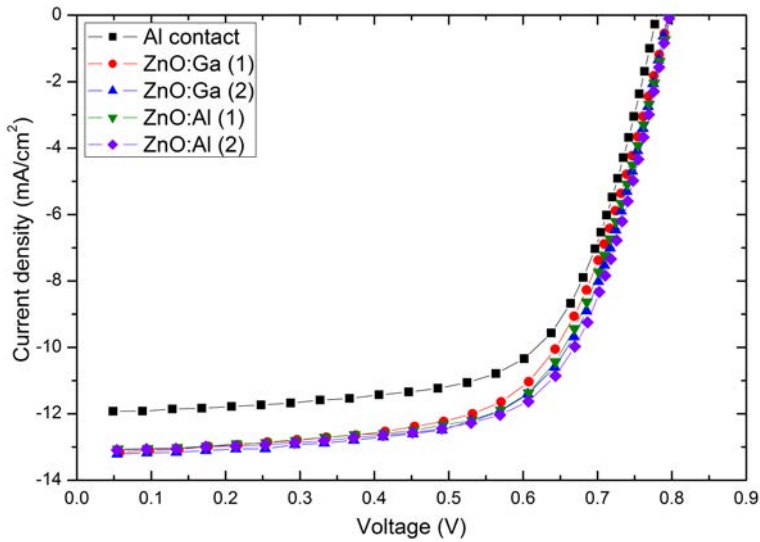


Figure 3.21: J - V curves of the best cell of each TCO deposition.

To check if the current is in fact a consequence of the TCO incorporation, an EQE measurement was developed, comparing the cell with only aluminum in the back reflector with the one with ZnO:Al(2wt.%). The curves in Fig. 3.22 show that the blue part of both cells is almost equal, but from 550 nm on, the sample with TCO shows much higher values of the EQE . This increase in the red part of the spectrum reveals that the

3 Optimization and improvements in thin film *a*-Si:H solar cells

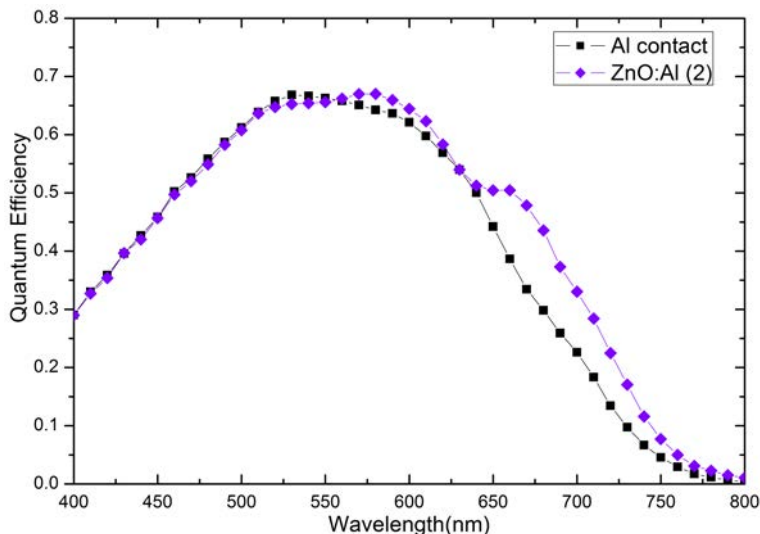


Figure 3.22: *EQE* curves of the best cells with and without TCO.

presence of the TCO increases the absorption of lower energy light, which means that this light that is lost in the TCO-less sample, now is absorbed due to an enhancement of the light path (more absorption chance).

Another trial that was developed is a comparison of the performance of different metals deposited by different means. That would be aluminum and silver both deposited by thermal evaporation and sputtering. A standard solar cell with TCO (ZnO:Al 2wt%) was split in four parts and over each part a different metalization was performed. Then, the spare TCO was removed by HCl(5%) dipping as usually. The *J-V* curves of the best cell of each set are shown in Fig. 3.23. While the V_{oc} is almost the same in all samples, there is a difference in the current between Al and Ag samples, showing this last ones a higher J_{sc} . This is due to the higher reflectivity of Ag. However, the Ag sample deposited by sputtering shows lower fill factor. This can be due to the superficial damage caused by high energy bombardment, as the arrival energy of atoms in thermal evaporation is about 0.2 eV while in sputtering is between 2 and 30 eV [27].

3.5 Complete device optimization

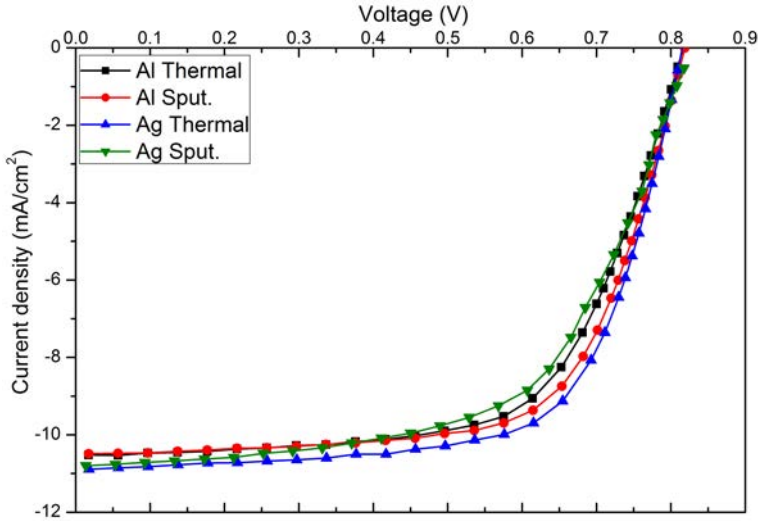


Figure 3.23: J - V curves of the best cell of each metal deposition.

3.5.2 p layer thickness optimization

After a device quality p doped layer had been developed, it was necessary to optimize its performance on solar cells. The critical parameter here is the thickness, as the layer has to be thick enough to maintain the electric field all over the layer, in order to prevent a vacuum zone, but also it has to be as thin as possible, as it will reduce the absorption on the p layer (were carriers are not collected), and so the optical losses, to the minimum.

Standard a-Si:H solar cells were deposited over *Asahi VU* glass in the UB. The only difference between the cells was the deposition time of the p layer, so the thickness was varied. After, the same back reflector was deposited over the cells. The real thickness of the layer can not be measured by the available techniques, so it was necessary to deduce the thickness from the deposition rate obtained in thicker layers, which was ≈ 7 nm/min. The deposited p layers for the cell had different deposition times, being this 3, 2 and 1 minutes, which would be a theoretical 21, 14 and 7 nm thicknesses. When a further reduction of the deposition time

3 Optimization and improvements in thin film a-Si:H solar cells

of the p layer was tried, aiming for a thickness of about 4 nm (30 s), the solar cells did not work and behaved as resistances, being the J - V curve a straight line.

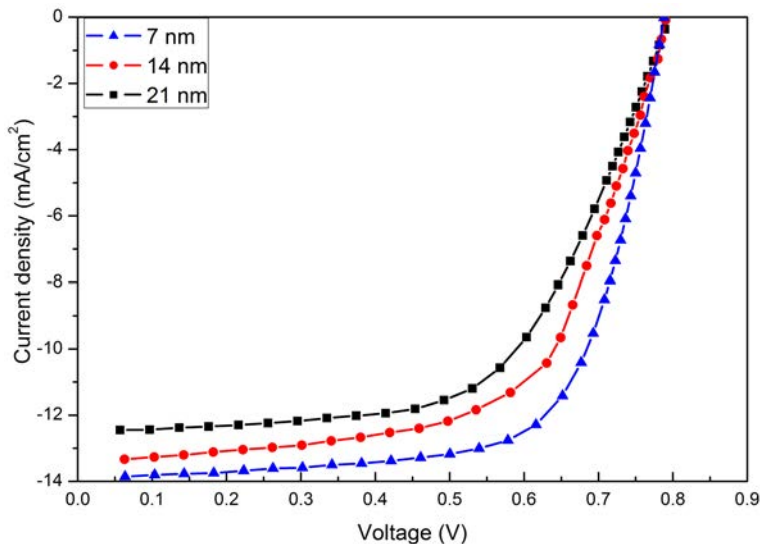


Figure 3.24: J - V curves of the best a-Si:H solar cells varying p layer thickness.

The results of the current-voltage curves of the best cell in each set are shown in Fig. 3.24. It is clearly observed that the best cell is the one with the thinner layer, not only because it shows the higher current (almost 1.4 mA/cm^2 over the cell with the thicker layer), but also because the series resistance of the cell is reduced, which results in an enhanced fill factor. Besides, it manages to keep the open circuit voltage at the same level as the rest of the cells, which means that 7 nm is enough to maintain the electric field in all the intrinsic layer (which is about 240 nm thick).

To check if this current effect was in fact due to the thickness of the p layer, EQE measurements were taken. The results (shown in Fig. 3.25) reveal that the thinner the p layer, the higher the response of the cell in the blue part of the spectrum. As light of shorter wavelengths is absorbed

3.5 Complete device optimization

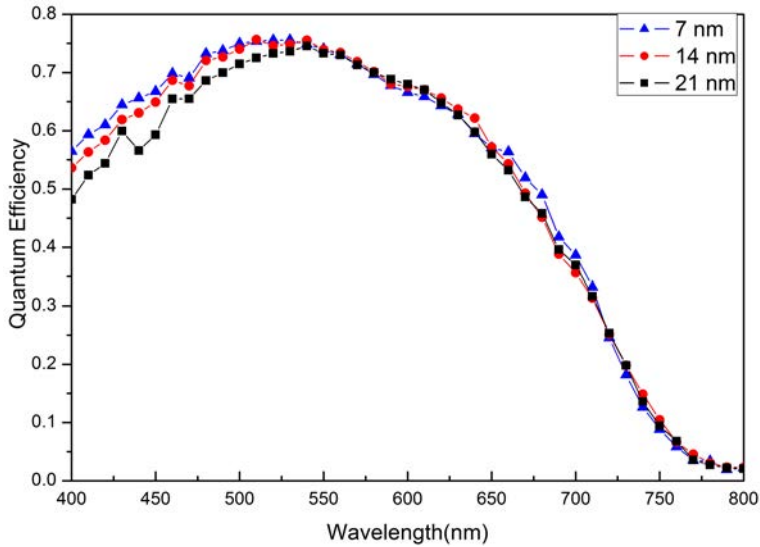


Figure 3.25: *EQE* curves of the best a-Si:H solar cells varying *p* layer thickness.

first and the carriers generated in the *p* layer are not collected, the fact that the EQE is higher in the blue area indicates that more light in these wavelengths is being absorbed in the intrinsic layer, and not in the doped one. This leads to higher current in the cell, which is consistent with the results observed in the *J-V* curves.

As it is shown, the optimum layer is the thinner one, of about 7 nm, is the most suitable for solar cells. This is the smallest thickness that managed to keep a solar cell behavior minimizing the absorption. It is important to notice that this value is linked to the roughness of the surface of the used substrate. If a different roughness was used, this value probably would be different. Anyway, as this is the substrate that is normally used for UB cells, this *p* doped amorphous layer thickness is the one used in standard amorphous silicon solar cells currently deposited in the UB.

3.6 Improvement of V_{oc} in polymorphous silicon solar cells

3.6.1 Introduction

As it has been explained, the main drawback of amorphous silicon solar cells is the light induced degradation (LID), first reported by Staebler and Wronski [44]. LID consists in the generation of different kind of defects by the light, including dangling bonds [38], but not being these the only ones [113][114]. This effect, which will be explained in more detail in Chapter 4, leads to an important decrease of the performance due to a reduction of the characteristic parameters of the solar cell, especially the fill factor.

The Laboratoire de Physique des Interfaces et des Couches Minces (LPICM) at L'École Polytechnique (Palaiseau), has developed and optimized an improved material deposited just before the edge of microcrystallinity, which is called polymorphous silicon (pm-Si:H). It consists in small silicon crystals embedded in an amorphous matrix [105][106]. This material has been widely studied in previous work related to the group [110] and maybe the most important feature is that it has shown an improved behavior against LID [106][100]. However, the efficiencies reached are still low to compete with c-Si technology.

One of the crucial parameters that determines the performance of a cell is the open circuit voltage (V_{oc}). The influence of the cell layers on this parameter has been studied in the LPICM [115] and recently it has been predicted that 12% of stabilized efficiency could be reached in pm-Si:H solar cells, through the increase of V_{oc} values [58][59]. The work developed in this section is based on previous attempts to enhance V_{oc} [116]. First of all, an analysis of these previous results was carried out and the different possible ways to increase V_{oc} were studied. Two of these ways are lowering the deposition temperature [117] and including intermediate buffer layers [118][119][120].

3.6.2 Experimental

Although the highest expectation in enhanced V_{oc} is in NIP configuration [121], PIN trials have also been developed. The idea is to check which mechanisms of V_{oc} enhancement are valid in both configurations or only in one of them.

The cells have been deposited in the ARCAM reactor at the LPICM [122]. The particularity of the ARCAM reactor is that although it is a monochamber PECVD reactor, it confines the plasma in different so-called 'plasma boxes'. During the cell fabrication, the substrate rotates from one box to another, and so crossed contamination is avoided. According to previous results, the most convenient doped layers (both n and p) are microcrystalline silicon oxide layers (μcSiO_x) which has proven itself a good material for doped window layers [123][124][125][126][127][128][129]. The active layer is made of the already mentioned polymorphous silicon. The used substrates were textured aluminum doped zinc oxide (ZnO:Al) from the IMT in Neuchâtel. For the PIN configuration, two back contacts have been used: evaporated silver and ZnO:Al+sputtered Ag. The second option showed the best results, so they are the ones that will be shown from now on. For the NIP configuration, the front contact is made of indium tin oxide (ITO). The different sets of deposited cells are shown next.

PIN solar cells:

- PINref: This cell was a test cell to verify reference values. It had the same configuration and parameters of the best PIN cell of the previous results [116]. It provides a good reference for comparison.
- PIN150: This whole cell was deposited at 150°C instead of 175°C. This lower temperature is supposed to enhance the V_{oc} . The pressure was adjusted in order to not produce powder. The rest of the layers remained equal to those in PINref, no additional buffer layers were used.
- PINpbuffer: This cell was also deposited at 150°C, and also added an intermediate layer of p doped amorphous silicon oxide ($pa\text{SiO}_x$). This buffer layer was deposited between the regular $p\mu\text{cSiO}_x$ and the

3 Optimization and improvements in thin film a-Si:H solar cells

intrinsic layer as barrier. The idea was to get a graded dopant and a sort of passivating layer over the intrinsic layer.

- PINnbuffer: This is a similar case to PINpbuffer: a n doped amorphous silicon oxide ($naSiO_x$) was deposited over the i pm-Si:H layer. This aimed to get the same effect as the p layer of the previous cell. Also, the fact that the aSiO_x layer requires much less deposition power than the $\mu cSiO_x$, implies that the i layer gets 'bombarded' with much less energy. That could lead to a reduction of the quantity of defects in the interface.
- PINrough This cell is the same as PINnbuffer but it was deposited over a different substrate, as the IMT provided two different texturizations. Both are made of ZnO:Al, but this one is rougher than the one used before.

NIP solar cells:

- NIPref: This cell was also a test cell. It had the same configuration and parameters of the best NIP cell of the previous results [116]. It provides the equivalent reference for comparison as PINref. In fact, the layers are the same but deposited in reverse order.
- NIPibuffer: This cell was also deposited at 175°C but added an intermediate layer of intrinsic amorphous silicon oxide ($iaSiO_x$). This buffer layer was deposited over the active layer, with the aim of obtaining better passivation and protecting the pm-Si:H from the high deposition power p layer.
- NIP150: This cell was identical to NIPref but deposited at 150°C instead of 175°C. This is an analogous case to PINref and PIN150 in PIN configuration.
- NIPpbuffer: This cell was deposited at 150°C and added an intermediate layer of $paSiO_x$ after the intrinsic layer. The function is equivalent to the $iaSiO_x$ in NIPibuffer, and also to the one of the $naSiO_x$ in PINnbuffer on PIN configuration.

3.6 Improvement of V_{oc} in polymorphous silicon solar cells

- NIPnbuffer: This cell presents two changes: the first one is the change of substrate from the smooth one to the rough one (like PINrough). And also, a $naSiO_x$ buffer layer was deposited between the $n\mu cSiO_x$ layer and the active layer. It aimed to a similar function of the $paSiO_x$ layer in cell PINpbuffer of the PIN series.

The measured cells had an area of 0.0314cm^2 (round cells of 2 mm of diameter). 15 samples of each trial were made, but not all of them worked. Over these cells, the current-voltage curve under 1 sun illumination measurements were performed in order to obtain the characteristic cell parameters. During the measurements, a big scatter in J_{sc} was found among the samples. This could be because any shadowing effect produced by the probes has a large impact in the result, as the area of the cell is quite small. The external quantum efficiency (EQE) was also measured to check in which wavelength zone the cells offer a better response and to verify the current values.

3.6.3 Results and discussion

3.6.3.1 J - V curves in PIN samples

Two different back reflectors (BR) were tried over PIN solar cells: first, a BR of evaporated Ag was tried, due to the unavailability of the sputtering. When the sputtering was operative, a standard back reflector made of ZnO:Al + sputtered Ag was deposited. Also, measurements were taken before and after annealing in some cases. It was found, as it was already predicted based on previous experience, that the standard BR and the after annealing measurements offered the best results. In order to make the reading more clear, only the tables of these results will be shown.

Fig. 3.26 and Table 3.10 show the curves and the parameters of the best cells, and Table 3.11 shows the average of the parameters of the working cells, which number is different in each sample. As it can be observed, the decrease in the temperature led to a growth in the V_{oc} of a little less than 0.01 V. This was expected but maybe the impact should have been higher [117]. The previous experiments done in reverse way (raising the temperature) [116] showed larger drops in V_{oc} than the gain experienced

3 Optimization and improvements in thin film a-Si:H solar cells

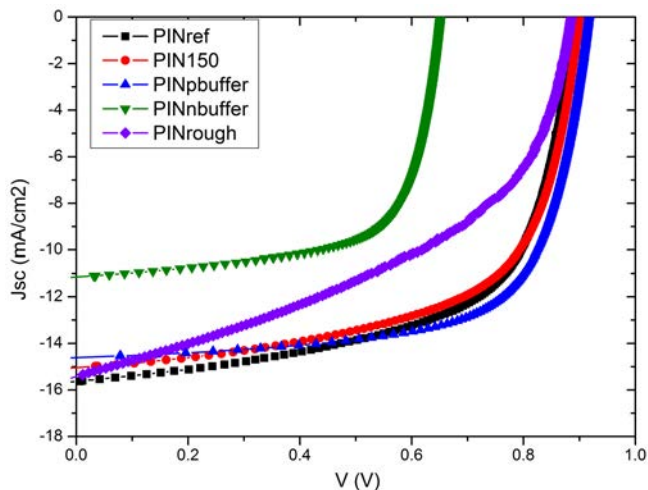


Figure 3.26: J - V curves of the best cells in PIN configuration trials.

Table 3.10: Characteristic parameters of the best PIN solar cells.

| Sample | V_{oc} (V) | J_{sc} (mA/cm ²) | FF(%) | η (%) |
|------------|--------------|--------------------------------|-------|------------|
| PINref | 0.892 | 15.82 | 61.28 | 8.64 |
| PIN150 | 0.900 | 15.05 | 61.96 | 8.39 |
| PINpbuffer | 0.917 | 14.60 | 68.55 | 9.18 |
| PINnbuffer | 0.652 | 11.15 | 67.33 | 4.89 |
| PINrough | 0.886 | 15.40 | 45.60 | 6.22 |

Table 3.11: Average of the characteristic parameters of the working PIN solar cells.

| Sample | V_{oc} (V) | J_{sc} (mA/cm ²) | FF(%) | η (%) |
|------------|--------------|--------------------------------|-------|------------|
| PINref | 0.891 | 15.71 | 61.36 | 8.59 |
| PIN150 | 0.899 | 15.05 | 61.73 | 8.35 |
| PINpbuffer | 0.917 | 13.47 | 67.76 | 8.38 |
| PINnbuffer | 0.646 | 11.21 | 66.71 | 4.83 |
| PINrough | 0.886 | 15.40 | 45.60 | 6.22 |

3.6 Improvement of V_{oc} in polymorphous silicon solar cells

with this reduction. The inclusion of $paSiO_x$ layer deposited before the intrinsic layer produced an improvement in V_{oc} of almost 0.02 V. However, in the next two sets, the inclusion of the $naSiO_x$ layer deposited over the intrinsic layer led to a great drop in the performance of the cell. In one of the cases, the voltage and the current dropped significantly, and in the other, the fill factor showed an important decrease. In any case, the cells did not work properly with this kind of buffer layer.

3.6.3.2 J - V curves in NIP samples

For the NIP configuration, a front contact of ITO was deposited over the cells. This contact also limited the area of the cells. Three sets of ITO were deposited. Two of them were identical and are the ones that are taken into account for the results. The third ITO was deposited at lower temperature, and had as objective to verify that the cells were not affected by the higher ITO deposition temperature. The results with this low temperature ITO were worse, so they are not shown here. Fig. 3.27 and Table 3.12 show the J - V curves and the parameters of the best cells, and Table 3.13 shows the average of the parameters of the working cells.

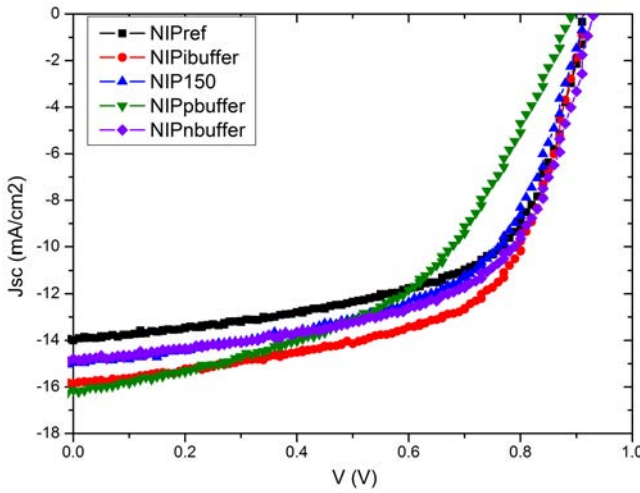


Figure 3.27: J - V curves of the best cells in NIP configuration trials.

3 Optimization and improvements in thin film *a*-Si:H solar cells

Table 3.12: Characteristic parameters of the best NIP solar cells.

| Sample | V_{oc} (V) | J_{sc} (mA/cm ²) | FF (%) | η (%) |
|------------|--------------|--------------------------------|----------|------------|
| NIPref | 0.922 | 13.95 | 60.73 | 7.81 |
| NIPibuffer | 0.914 | 15.85 | 61.28 | 8.88 |
| NIP150 | 0.914 | 14.93 | 57.99 | 7.92 |
| NIPpbuffer | 0.891 | 16.14 | 49.78 | 7.16 |
| NIPnbuffer | 0.930 | 14.74 | 59.87 | 8.21 |

Table 3.13: Average of the characteristic parameters of the working NIP solar cells.

| Sample | V_{oc} (V) | J_{sc} (mA/cm ²) | FF (%) | η (%) |
|------------|--------------|--------------------------------|----------|------------|
| NIPref | 0.912 | 13.90 | 58.34 | 7.40 |
| NIPibuffer | 0.909 | 14.56 | 60.52 | 8.01 |
| NIP150 | 0.910 | 13.80 | 57.23 | 7.19 |
| NIPpbuffer | 0.896 | 14.24 | 49.19 | 6.28 |
| NIPnbuffer | 0.928 | 13.47 | 59.80 | 7.47 |

As expected, the V_{oc} in the NIP set is initially higher. However, the modifications introduced did not lead to an improvement in the V_{oc} as big as in PIN set. Focusing on V_{oc} , the inclusion of the *pa*SiO_{*x*} over the intrinsic layer has a similar effect as the one found in PIN when a *na*SiO_{*x*} is deposited over the *i* layer. The cell is somehow damaged and the parameter values considerably drop. On the other hand, in NIPnbuffer sample, the inclusion of the *na*SiO_{*x*} before the intrinsic layer results in an increase of the V_{oc} ; getting an increment of 0.016 V over the test cell and 0.018 V over the original cell at the same temperature.

3.6.3.3 External quantum efficiency measurements

To complement the results, external quantum efficiency measurements of the best cells of each sample were performed. They were really hard to make because the smallest light spot that could be used for the calibration was almost as big as the cell area. So, it was difficult to place all the light

3.6 Improvement of V_{oc} in polymorphous silicon solar cells

exactly over the cell area. Any displacement led to an underestimation of the EQE . The measurements shown in Fig. 3.28 correspond to the best cells in PIN configuration, and Fig. 3.29, the ones in NIP configuration.

The response in the blue zone is similar in both configurations. Then, while NIP solar cells show a higher absorption in the central zone of the visible spectrum, PIN cells show a better performance in the long wavelength zone. This is probably due to the fact that the NIP solar cells do not have a reflector in the back, and part of light is lost. The integration of the area under the curve, weighted with the solar spectrum, has been made in order to obtain the integrated current and recalculate the efficiency.

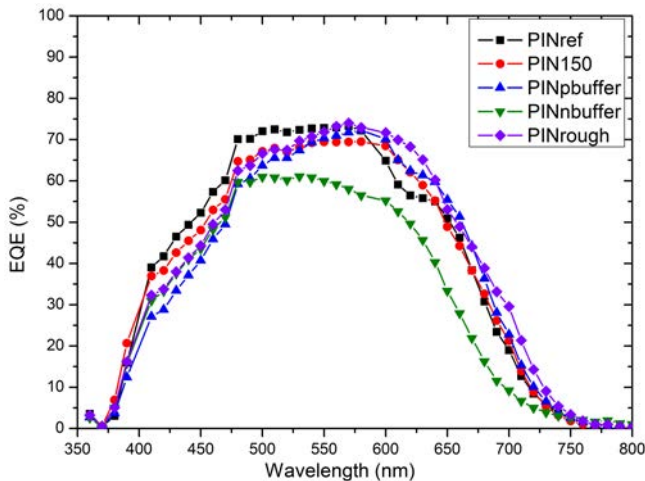


Figure 3.28: EQE curves of the best cells in PIN configuration trials.

The values are shown in Tables 3.14 and 3.15. The obtained integrated current is, in almost all cases, notably lower than the obtained current in the $J-V$ measurement. The reason for this is probably that as cells are very small, the measured current in the $J-V$ curves is overestimated, as some photons from the border of the cell are contributing, something that does not happen in the EQE measurement. In this case, the

3 Optimization and improvements in thin film a-Si:H solar cells

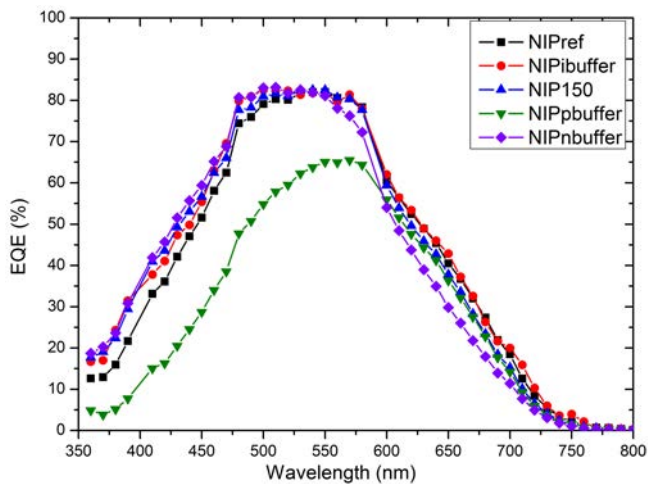


Figure 3.29: *EQE* curves of the best cells in NIP configuration trials.

Table 3.14: Characteristic parameters of the best PIN solar cells with integrated current.

| Sample | V_{oc} (V) | J_{sc} (mA/cm ²) | FF (%) | η (%) |
|------------|--------------|--------------------------------|----------|------------|
| PINref | 0.892 | 12.26 | 61.28 | 6.70 |
| PIN150 | 0.900 | 12.05 | 61.96 | 6.69 |
| PINpbuffer | 0.917 | 11.97 | 68.55 | 7.53 |
| PINnbuffer | 0.652 | 10.04 | 67.33 | 4.41 |
| PINrough | 0.886 | 12.65 | 45.60 | 5.11 |

Table 3.15: Characteristic parameters of the best NIP solar cells with integrated current.

| Sample | V_{oc} (V) | J_{sc} (mA/cm ²) | FF (%) | η (%) |
|------------|--------------|--------------------------------|----------|------------|
| NIPref | 0.922 | 12.49 | 60.73 | 6.99 |
| NIPibuffer | 0.914 | 13.96 | 61.28 | 7.82 |
| NIP150 | 0.914 | 12.63 | 57.99 | 6.69 |
| NIPpbuffer | 0.891 | 9.39 | 49.78 | 4.16 |
| NIPnbuffer | 0.930 | 12.11 | 59.87 | 6.74 |

3.6 Improvement of V_{oc} in polymorphous silicon solar cells

currents extracted from the EQE would be more reliable. However, maybe these currents are underestimated as some light is lost during the measurement, as it was explained before. Besides, it could be expected that if these values of currents are true, though J_{sc} will decrease, fill factor could increase a bit, and the efficiency loss is not as big as calculated.

Some other conclusions can be obtained from the EQE results: It can be noticed that the integrated current is quite similar in almost all the cases. This could be positive in the cases when V_{oc} increases, because this increase would lead to a direct increment of the efficiency, as no other parameter is affected. It is also possible to observe that the samples with the rough substrate show better response in the blue, but worse in the red. This happens also with the temperature: lower the temperature tends to increase the absorption in the blue and central zone, but there is a tendency to lose absorption in the red part. In any case, the small size of the measured cells makes the results in the current not very reliable.

3.6.4 Conclusions and future work

The temperature reduction, has proven itself a good way to increase V_{oc} in PIN solar cells, but it has not provided any enhancement in NIP. The reason of this different behavior is not clear. Further information would be needed to answer this question. About the inclusion of buffer layers, a similar behavior has been found in both configurations: when $paSiO_x$ is deposited over $p\mu cSiO_x$ in PIN configuration, an increase of V_{oc} is obtained. The same thing happens when $naSiO_x$ is deposited over $n\mu cSiO_x$ in NIP configuration. This means that when an $aSiO_x$ layer is deposited as a buffer layer before the intrinsic layer, an improvement in the open circuit voltage is obtained. However, in the opposite case, when the $aSiO_x$ (respectively doped) is deposited over the intrinsic layer, the cell does not work properly, and sees its characteristic parameters considerably reduced.

These results suggest that polymorphous silicon forms a better interface when it grows over amorphous material than the one that it forms over microcrystalline material. It is possible that this amorphous buffer layer provides better passivation and acts a barrier for diffusion. Or maybe it

3 Optimization and improvements in thin film a-Si:H solar cells

prepares a more similar material layer that favors the pm-Si:H growth.

On the other hand, the reason of the failure of the cell when depositing amorphous material over the intrinsic layer could be just the opposite as before: The amorphous material is not suitable to grow microcrystalline material over it, and perhaps an amorphization of the layer deposited after is caused, lowering its capacity to produce an enhancement of the V_{oc} . Also, it is possible that the deposition of the intrinsic layer at lower temperature for a long time produce an increase of powder formation. This powder could fall over the intrinsic layer, and then, the interface formed over it is defective.

More experiments would have been necessary to verify the results. Some of them could be:

- To deposit a metallic back reflector in the NIP cells to check the increase in the current.
- To make a 200°C annealing in the cells deposited at 150°C, which would activate the boron atoms on the p doped layer and increase the V_{oc} . As the annealing temperature is higher than the deposition one, the cell could be affected, and it could be whether positive or negative.
- To expose the samples to LID to check if the increase of the values of the parameters is constant or is only present in the initial state or it persists after the degradation.
- To repeat the experiments in larger cells to get more accurate results in the current and fill factor.

3.7 Conclusions and perspectives

The main objective of the work in this chapter was to obtain an amorphous silicon solar cell whose parameters were at the state of the art of a-Si:H technology. Also, another goal was to obtain optimized independent layers that could serve to other purposes. The intrinsic silicon layer has been

3.7 Conclusions and perspectives

optimized in three different parameters (depletion, hydrogen content and temperature), checking also the behavior against LID. Both amorphous and microcrystalline p doped layers were also optimized. These layers are already fulfilling the requirements for device quality material given by Schropp and Zeman [23]. A little more optimization might be possible in some other parameters, and also some experiments involving the n -doped layer. Some of the developed optimizations have already been used over complete devices, but some others have not yet. Anyway, at the moment, a working a-Si:H solar cell with 200 nm thickness whose parameters present good enough values has been implemented. The parameters values of the average of the best set of cells obtained for the moment are listed in 3.16.

Table 3.16: Characteristic parameters of a standard solar cell (1 cm^2) currently implemented at UB (1 sun illumination).

| Parameter | Value |
|-----------|---|
| V_{oc} | 0.838 V |
| J_{sc} | 12.51 mA/cm ² |
| R_{oc} | $1.11 \times 10^3 \text{ } \Omega\text{cm}^2$ |
| R_{sc} | 6.52 Ωcm^2 |
| FF | 0.714 |
| η | 7.485% |

Despite the efficiency is still a bit low if it is compared with the state of the art due to smaller V_{oc} and J_{sc} , the device shows a really good value of the fill factor. However, these values correspond to the 'as deposited state'. So the first thing that had to be studied was how is the cell affected by light induced degradation. The results found in this study are exposed in Chapter 4. Also, all the optimizations should be finally tried together in a cell to verify if they are still working when they are implemented together.

In this chapter, the work developed at the Laboratoire de Physique des Interfaces et des Couches Minces at L'École Polytechnique is also presented. This work has shown possible ways to increase some of the

3 Optimization and improvements in thin film a-Si:H solar cells

parameters of the solar cells, specially V_{oc} . This parameter has been absolutely increased in about 3% in both PIN and NIP configurations through different techniques. Some experiments could still be developed to increase V_{oc} , like different metalizations or annealing processes, but most of all, combining all the working solutions in one single device. The implementation of larger cells would be also necessary in order to verify the results.

The experience acquired at the LPCIM in PIN configuration (the one deposited at UB) has provided some ideas to obtain better results in the developed devices. This experience strongly suggest that UB cells should include buffer layers to increase the open circuit voltage; fact that was already found in several references. Some experiments involving buffer layers should then be tried. This will be confirmed also by the results in LID found in the next chapter.

4 Light induced degradation

4.1 Introduction

As it has been explained, the main drawback of amorphous silicon, apart from its low conversion efficiency, is its lack of stability and the reduction of a-Si:H cells performance due to light induced degradation (LID). Staebler and Wronski [44] first reported LID in 1977, so LID is also called Staebler-Wronski effect (SWE). SWE causes a significant drop of the efficiency of the cell that comes as a result of an important reduction of the fill factor, a moderate loss of the short circuit current and a minor decrement of the open circuit voltage [75].

Since it was reported, SWE has been widely studied in cells, modules and power plants, developing several models aiming to completely explain this phenomenon. First, it was assumed that the main cause of LID is the creation of dangling bonds (DBs) and the consequent increment of the defect density [130][131] about 1 or 2 orders of magnitude [75]. These dangling bonds have several negative effects on the performance of the cell, as they act as recombination centers, and also they can capture free electrons or holes and become ionized defects. This leads to a deformation and a reduction of the internal electric field. These two effects cause a diminution of the drift length [75] and so of the photoconductivity.

This increase in dangling bond density can be reverted by thermal annealing, which causes hydrogen migration that results in saturation of the DBs. So, the role of hydrogen is crucial for LID and DBs [106]. However, when more accurate studies on SWE were developed, it was clear that the creation of DBs is not the only effect caused by LID, being a main indicator the fact that the thermal annealing does not reach to fully recover the cell [132][133][134].

4 *Light induced degradation*

The existence of different contributions to LID makes it difficult to find a simple model that explains the whole phenomenon. Some examples of models given to try to explain LID are weak bond breaking [135][136], weak bond bimolecular recombination [131], hydrogen collision model [137][138], floating bonds [139], hydrogen molecule complex [140] and network rebonding model [141], among others.

More recently, some more different descriptions appeared, involving other factors like the so called 'strained silicon bonds' [142]. And also the influence of other factors like microvoids has been studied for many years [143][144]. On the other hand, some attempts to explain the phenomenon using the variation and nature of defect density of states as main reason have been reported [145][146]. Despite of the mentioned theoretical difficulties, the experimental facts of LID are very clear, and have been broadly measured by different means and extensively reported.

Apart from the mentioned diminution on the quality, one important effect related to LID detected in a-Si:H is the seasonal effect, which is the difference in the performance of the a-Si:H cells and modules between summer and winter. The seasonal effect has been reported by several groups by different indoor experiments and outdoor measurements under different climate conditions, and it has been observed in cells [147][148], modules [149][150][151][152][153] and power plants [154][155].

This chapter explains the experiments and the results involving SWE and seasonal effect in this thesis. First, an optimization of the thickness of the UB cell was developed, and the results are explained. With the optimized thickness, LID at controlled temperatures was performed over both commercial and UB cells in order to fully characterize the effect of SWE on them and compare its behavior. These experiments involving temperature changes had as main objective to obtain a better understanding on seasonal effect, continuing previous group work on this field [60][84][151][156].

4.2 Motivation: Seasonal effect found in power plants

Studying and understanding the seasonal effect in modules of a-Si:H has been a very important topic in some recent group work [60]. One of the main conclusions obtained was that the variation of the efficiency due to the seasonal effect could be divided in two contributions: spectral and metastable. While the seasonal variation caused by spectral effects was estimated about 15%, the metastable contribution was only about 2%. It has been reported that spectral variations produce important changes in a-Si:H performance [157][158][159] but also there are several works reporting a significant relevance of the temperature of operation and the thermal recovery [160][161][162].

One of the reasons to continue the group work studying LID and seasonal effect was to try to correlate the experiments over solar cells with the analysis of the seasonal effect and the permanent degradation of photovoltaic modules in a power plant. Not all the degradation of the performance of a-Si:H modules comes from SWE, since there are other factors that affect the long term performance of solar modules in a permanent way. Ageing and climate conditions (specially humidity) are harmful for a-Si:H modules and several other photovoltaic technologies.

To evaluate the long term degradation of the technology, a PV power station with a nominal power of 10 MW AC made of frameless *T-Solar* a-Si:H modules of $1.1 \times 1.3 \text{ m}^2$ was selected. The studied amorphous silicon modules in the plant were manufactured by *T-Solar* [163] over glass substrates and the encapsulation was provided by lamination of the front glass, and a rear glass with a polymer polyvinyl butyral (PVB) foil between them. These modules were formed of standard amorphous silicon *T-Solar* cells [156]. The encapsulation has demonstrated a good protection of the devices with no visual damage on the modules. In addition the PVB was only at the rear of the cell, so it was out of the path of the light that entered the cell. The plant is located in Saelices (100 km south of Madrid, Spain) and has been operated and monitored since May 2010 with a detailed data acquisition of every inverter. The

4 Light induced degradation

total nominal power of DC fields is 11.4 MW.

The full study can be consulted elsewhere [154], but key point of this study for seasonal effect is that an approach to evaluate the interannual degradation is to consider the evolution of the performance ratio (PR) of the plant. The performance ratio of a module is defined by:

$$PR_m = Y_m/Y_r \quad (4.1)$$

where the module yield Y_m is defined as the ratio of the electric energy produced by the set of module in a particular time-frame (E , in Wh) to the nominal power of the modules (P_n , in W) by:

$$Y_m = E/P_n \quad (4.2)$$

The radiation yield Y_r is defined as the ratio of the global irradiation in the array plane (H , in Wh m⁻²) in the time-frame to the reference irradiance ($G_0=1000$ W m⁻²) by:

$$Y_r = H/G_0 \quad (4.3)$$

The performance ratio provides an indication of the mean efficiency of the modules in the considered time-frame compared with the nominal efficiency. The plot of the monthly values of the performance ratio in the Saelices plant is presented in Fig. 4.1. The availability of the plant and the energy yield are also shown, so they can be also taken into account when the results are analyzed.

If a linear adjustment of the mean annual performance ratio shown in Fig. 4.1 is made, the result corresponds to an inter-annual decrease of the performance ratio of $-0.69\%/year$. This would be the inter-annual degradation of the modules. However, the important part as far as the motivation of this work is concerned, is that with this methodology, the seasonal variation of the module performance can be easily appreciated in Fig. 4.1. The results show that there is a variation of the PR between a maximum monthly mean value of 75.2% in winter and of 83.5% in summer. As it will be demonstrated in Sec. 4.4, if only thermal effects (using

4.3 Thickness optimization against LID

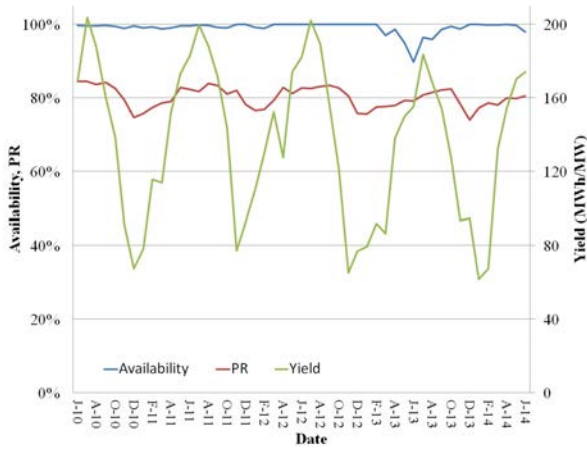


Figure 4.1: Evolution of the monthly plant availability, energy yield and performance ratio of the Saelices PV power station.

the joint temperature coefficient) are taken into account, the efficiency in summer would be only 1% higher than the efficiency in winter; but the difference in the PR between seasons is much higher. This seasonal variation is then explained as a consequence of the spectral variation due to higher short wavelength light in summer than in winter, which is more adapted to the a-Si:H spectral response [149][150][151]. This behavior in modules and power plants has motivated the next experiments over single cells in the laboratory. These experiments tried to verify if this difference of more than 8% is only because of the light influence or there are more effects involved, like slow thermal annealing [160][164].

4.3 Thickness optimization against LID

Before the experiments about seasonal effect could be developed, it was necessary to be sure that the cells deposited at the UB had an adequate thickness to make them comparable to the commercial *T-Solar* cells. So, an optimization of the thickness of the intrinsic layer in a-Si:H solar cells

4 Light induced degradation

deposited at the UB was developed. As this is also an optimization of the cell, it could be included at Chapter 3. However, as the need to optimize the thickness is deeply related with LID, it has finally been included in the present chapter. It is known that the thicker the cell is, the more quantity of light is absorbed and so the higher the current is. However, the thicker the cell, the higher the experienced LID. The most affected parameter is the fill factor, but also the short circuit current is degraded [23]. On the other hand, open circuit voltage is theoretically not degraded in thin quality cells but, if the cell is too thick, the internal electric field can be affected and V_{oc} is reduced. An optimum thickness between 200 and 250 nm has already been reported by Shah [39]. As far as continuous studies are concerned, Klaver *et. al* [146] observe the degradation of the cell parameters in the first 100 min for different thicknesses, but in a larger range of thicknesses (300 to 900 nm with a step of 150 nm). Here, the thickness range is much smaller (160 to 280 nm with a step of 40 nm), as the experiment is not aiming for a model but for an optimization.

4.3.1 Experimental

For the thickness optimization, it is assumed that the cell is currently in a proper range of thickness [39], so very big modifications did not make sense. As a consequence, the variation in the thickness was small but enough to detect variations on the parameters. The used cells were deposited with the conditions shown in Table 4.1 but varying the deposition time of the intrinsic layer, in order to obtain different thicknesses. These thicknesses were 160, 200, 240 and 280 nm. The deposition time for this layer was adjusted according to the deposition rate obtained in Chapter 3, Sec. 3.3 for the corresponding layer. The back reflector it is the exactly same for all four samples, as TCO and metallic contacts were deposited in the same run for all the samples. This makes the cells essentially identical except the mentioned thickness variation.

There are two considerations that have to be taken into account before the results are analyzed. First, the fact that the cells have different thickness made it impossible to deposit them in the same run. This means that although the recipe for the a-Si:H layers was the same, they were deposited separately and some differences could exist. And second,

4.3 Thickness optimization against LID

Table 4.1: Deposition parameters for the UB cells used in the thickness optimization experiment. The thickness of the i -layer is varied, having the four used samples 160, 200, 240 and 280 nm.

| Param./Layer | p -layer | i -layer | n -layer |
|--|-------------|--------------------|--------------|
| Pressure (Pa) | 107 | 80 | 73 |
| Power (W) | 4 | 4 | 4 |
| Electrode distance (mm) | 15 | 15 | 21 |
| Time (mm:ss) | 1:20 | Varying | 3:20 |
| Thickness (nm) | ≈ 8 | Varying | ≈ 30 |
| Substrate temperature ($^{\circ}\text{C}$) | 200 | 200 | 200 |
| Background pressure (Pa) | $<10^{-5}$ | $<2 \cdot 10^{-5}$ | $<10^{-5}$ |
| Silane flow (sccm) | 2.6 | 40 | 40 |
| Methane flow (sccm) | 2.1 | 0 | 0 |
| TMB flow (sccm) | 40 | 0 | 0 |
| Phosphine flow (sccm) | 0 | 0 | 22 |

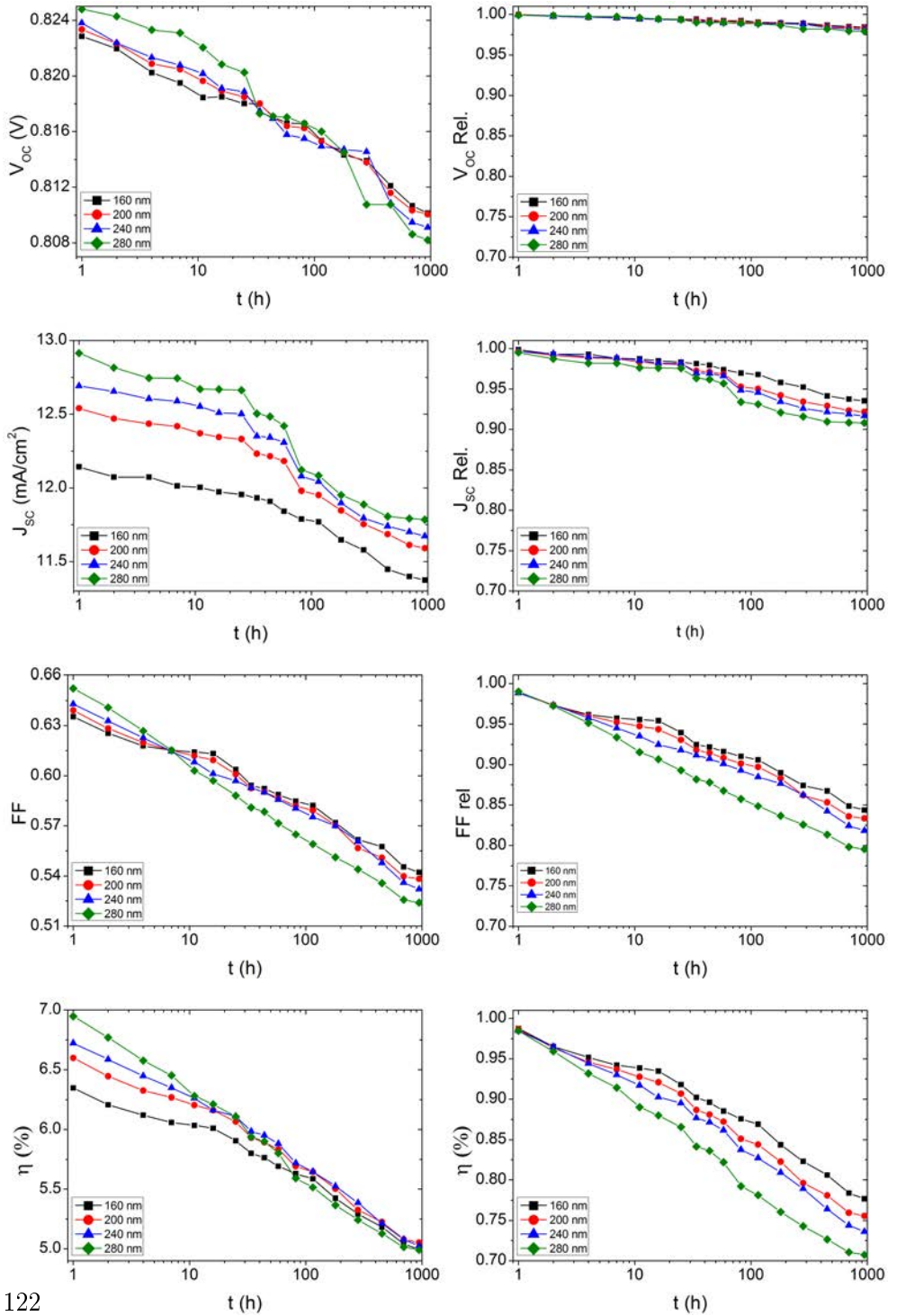
the intrinsic layer used for these samples contains no additional hydrogen to mitigate LID (see Chapter 3, Secs. 3.3.4 and 3.6). Although the performance is lower this way, it was intentionally done as it was easier to observe the difference if the degradation is higher.

In this experiment, the cells underwent a light induced degradation process at 50°C for about 1000 h. J - V curves were measured during the process, first every few hours and then more separately, in order to obtain the parameters of the cell providing several points per decade. This aimed to study not only the difference in the final state but also how the samples evolved as function of the thickness.

4.3.2 Results analysis

In Fig. 4.2, the evolution of the parameters with the exposure time to LID can be observed. In this figure, V_{oc} , J_{sc} , FF and η (left) and their corresponding relative values (right) are shown from top down. The

4 Light induced degradation



122

Figure 4.2: Evolution of V_{oc} , J_{sc} , FF and η (from top down) during the LID of the UB samples of different thickness. The left column shows the actual values and the right column shows the relative values.

4.3 Thickness optimization against LID

relative values are calculated, as usually, as the fraction between the actual value and the initial value (as deposited). While the graphs of actual values are presented with the most convenient scale in the y axis, the relative values graph present the same scale in the y axis for all the parameters. This is done to make it easier to get a quick idea of the relative influence of LID among the parameters.

The first result that can be observed is that all the parameters are affected by LID, even V_{oc} . However, in the relative graphs it can be quickly appreciated that the level of degradation is very different among the parameters. V_{oc} is degraded very slightly, staying over 97.5% of the initial value. J_{sc} experiences a moderate degradation with final values between 90 and 95% of the initial one, while FF suffers the highest degradation, reaching relative values between 79 and 85% of the initial FF . The degradation in the efficiency is a result of all these effects combined, which lead to final relative values of η between 70 and 78%.

In order to better evaluate these final losses, Table 4.2 shows the initial and final values and the percentage of loss. At this point, another important appreciation in the graphs must be pointed: although some of the parameters start to stabilize at the final measurements, maybe higher degradation time would be needed to get higher stabilization. However, longer degradation times that allow to obtain values in the next decade would be extremely time consuming.

When the results are compared, it is found that the thicker the sample, the higher the loss, and this happens for all the parameters in different degrees. J_{sc} is, as it has been said, the parameter that is more influenced by the thickness. After the LID, J_{sc} final loss is between 5 and 10%. The thicker cells still exhibit higher values than the thinner ones, despite they experience higher relative degradation. The difference between the thinner and the thicker cell was initially of 0.820 mA/cm², but in the end, it is reduced to half that value (0.411 mA/cm²).

If V_{oc} is observed, although the thicker samples started with slightly higher V_{oc} , after about 100 h this tendency was reversed and maintained; and in the end, the thinner cells show higher values of the V_{oc} , unlike the

4 Light induced degradation

Table 4.2: Initial and final values and relative losses of the parameters of UB cells of different thicknesses.

| V_{oc} (V) | | | |
|----------------|---------|-------|----------|
| Thickness (nm) | Initial | Final | Loss (%) |
| 160 | 0.823 | 0.810 | 1.56 |
| 200 | 0.824 | 0.810 | 1.65 |
| 240 | 0.824 | 0.809 | 1.84 |
| 280 | 0.825 | 0.808 | 2.09 |

| J_{sc} (mA/cm ²) | | | |
|--------------------------------|---------|--------|----------|
| Thickness (nm) | Initial | Final | Loss (%) |
| 160 | 12.158 | 11.374 | 6.45 |
| 200 | 12.577 | 11.591 | 7.84 |
| 240 | 12.736 | 11.673 | 8.35 |
| 280 | 12.978 | 11.785 | 9.20 |

| FF | | | |
|----------------|---------|-------|----------|
| Thickness (nm) | Initial | Final | Loss (%) |
| 160 | 0.643 | 0.542 | 15.64 |
| 200 | 0.646 | 0.538 | 16.65 |
| 240 | 0.650 | 0.532 | 18.17 |
| 280 | 0.659 | 0.524 | 20.45 |

| η (%) | | | |
|----------------|---------|-------|----------|
| Thickness (nm) | Initial | Final | Loss (%) |
| 160 | 6.430 | 4.995 | 22.31 |
| 200 | 6.689 | 5.054 | 24.45 |
| 240 | 6.826 | 5.025 | 26.38 |
| 280 | 7.057 | 4.991 | 29.27 |

case of J_{sc} . As the relative losses in V_{oc} are so small, these results are not very relevant in efficiency issues, but still, the fact that some slight degradation exists indicates that the doped material can be improved.

A similar tendency is found in FF , with the important difference that this is the most influenced parameter by LID. Although the initial value

4.3 Thickness optimization against LID

was higher for thicker cells, this tendency was reversed in less than 10 h of LID, and continued to increase during all the degradation process. In the final point, the thinner cell's FF is 0.18 over the thicker one despite it started 0.16 below.

The effect on the efficiency comes as a consequence of the effects on the other parameters. So, as the relative losses of all the parameters are higher in the thicker cells, the relative loss in η is accentuated, varying from 22.21% for the thinner cell to 29.27% for the thicker one. The interesting result for the optimization is that although the initial maximum efficiency difference was 0.627%, in the final state this maximum difference between samples is reduced to only 0.063%, this is 10 times smaller. This means that the difference in the efficiency provided by the difference in the current is canceled in about 1000 h due to a more severe degradation in the thicker cells. In the final point, the cell with 200 nm shows a slightly higher efficiency, so it can be considered as the optimized thickness for UB cells. However, if longer degradation times were tested, maybe the thinner cell (160 nm) could also outreach the final efficiency of this cell too. Anyway, the efficiency values at this point are very similar and several other factors could mask these small differences (like errors in the measurements). Which is clear is that higher thicknesses would provide better performance initially, but in the stabilized state this difference would be canceled, and even poorer performances would be obtained.

4.3.3 Discussion: the role of the $\mu\tau$ product

There are two results that have to be discussed in detail: the first is the fact that the thicker cells present better initial performance. It is expected that the thicker the cell is, the higher the current is, but this is not expected for other parameters. The second effect is the higher degradation of the thicker cells.

A possible explanation arises from the analysis of the mobility-lifetime product ($\mu\tau$) found in Asensi *et al.*[165]. In this work, the existence of different zones in the intrinsic layer are proposed: a 'bulk' zone, which corresponds to the central main part of the layer (i -region) and two zones

4 Light induced degradation

in both sides, affected by the doped layers and interfacial defects (*pi* and *in* regions).

So, the defect density (Ndb) in the whole intrinsic region (whose thickness is L) is the result of the contribution of the defect densities in two regions, bulk (Ndb_{bulk}) and surface-affected (Ndb_{sur}), whose thicknesses are L_{bulk} and L_{sur}), respectively:

$$Ndb = \frac{Ndb_{bulk}L_{bulk} + Ndb_{sur}L_{sur}}{L} \quad (4.4)$$

When the solar cell is under constant illumination, it is possible to assume that $L_{bulk} \gg L_{sur}$ (and $L \approx L_{bulk}$) [165], and the equation can be expressed as follows:

$$Ndb = Ndb_{bulk} + Ndb_{sur} \frac{L_{sur}}{L} \quad (4.5)$$

On the other hand, it is known that $\mu\tau$ is inversely proportional to Nd [166]. Considering a highly simplified situation in which the capture cross section values are equal for both carriers in all kinds of dangling bonds (positive, negative or neutral), the expression for τ would be:

$$\tau = \frac{1}{\nu_{th}\sigma Ndb} \quad (4.6)$$

where ν_{th} is the thermal velocity and σ is the capture cross section of the free carriers by the dangling bonds. In the simple situation proposed, these values and the can be considered constants and equal in both bulk and surface-affected regions. Relating Eqs.4.5 and 4.6, the next expression is found:

$$\frac{1}{\mu\tau} = C \left(\frac{1}{\mu\tau_{bulk}} + \frac{1}{\mu\tau_{sur}} \frac{L_{sur}}{L} \right) \quad (4.7)$$

So, it is clear that a way to evaluate the defect influence in the cells is studying the value of $\mu\tau$. A expression to obtain $\mu\tau$ from the J - V measurements is found in Merten *et al.* [85]. As the samples were deposited

4.3 Thickness optimization against LID

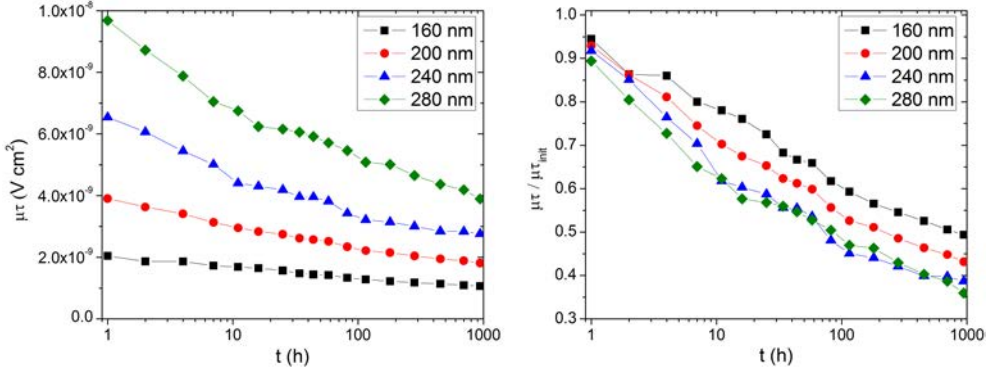


Figure 4.3: Evolution of $\mu\tau$ with the LID time for the UB cells of different thicknesses. The relative value is obtained as the ratio of the actual value to the initial one for each sample.

in the same conditions, it will be assumed that V_{bi} is equal to 1V in all the cases. In this situation, $\mu\tau$ is obtained as:

$$\mu\tau = I_{sc}R_{sc}L^2 \quad (4.8)$$

where L is the thickness of the i -layer, which is known; and I_{sc} and R_{sc} are the short circuit current and resistance respectively, parameters that are obtained from the measurements. The obtained absolute and relative values of $\mu\tau$ for the UB cells are shown in Fig. 4.3.

The first thing that is noticed is that the absolute values of $\mu\tau$ in the thicker samples are initially much higher than those for the thin ones. The reason for this is found in Eq. 4.5. Ndb_{bulk} and Ndb_{sur} are considered equal for all the samples, as they are characteristics of the material. If L_{sur} is considered also a parameter only related with the formed interface between the layers, as they are equal in all the samples, it would be equal for all of them too. That makes L the only varying parameter, and it can be observed that the higher is L , the lower is the contribution of Ndb_{sur} and so, the lower the value of Ndb .

This can be understood as an evaluation of the role of the surface defects in the total surface density. It is known that the surface re-

4 Light induced degradation

gions are much more defective than the bulk region, specially if the interface is not very good [39]. As the thinner cells have less 'bulk region', the relative weight of the surface-affected regions is higher, so the total density of defects is also higher. This would explain why the thicker cells present better performance in the initial stages of degradation.

However, as it has been observed, the final performance of the thicker cells is lower. One of the parameters that has an important role explaining this behavior is $\mu\tau$. As it can be observed in the relative graph in Fig. 4.3, the degradation of $\mu\tau$ is higher in the thicker samples, which means that the increment of Ndb is higher in the thicker cells.

The intuitive explanation would be found again in Eq. 4.5. Ndb increases with time, as more defects are generated, but there are two possible reasons (or actually three) for this to happen: Ndb_{bulk} is increasing, Ndb_{sur} is increasing, or both of them are increasing in a different level. This last situation is the most likely to be happening, but is also the most difficult to evaluate through a simple model. To try to evaluate it at least qualitatively, the work of Beck *et al.*[167] is used. In this work it is found that for intrinsic layers, the evolution of $\mu\tau$ for neutral defects is related to the defect density variation:

$$\frac{(\mu\tau_0)_{Init}}{(\mu\tau_0)_{Deg}} \approx \frac{Ndb_{Deg}}{Ndb_{Init}} \quad (4.9)$$

In order to clearly observe the evolution of the defect density, the results for these fractions for UB cells are shown in Fig. 4.4.

As it can be observed, the ratio of degraded to initial defect densities is higher in the thicker cells, as the final ratio is 2.78 in the thicker sample (280 nm) while it is 2.02 for the thinner sample (160 nm). An interesting conclusion can be extracted from the right part of the figure: it can be observed that the thinner the cell, the smaller the difference between the initial and final densities of states.

This tendency suggests that in the thickness limit ($L \rightarrow 0$), Ndb will experience no degradation, which would mean that the degradation effect is

4.3 Thickness optimization against LID

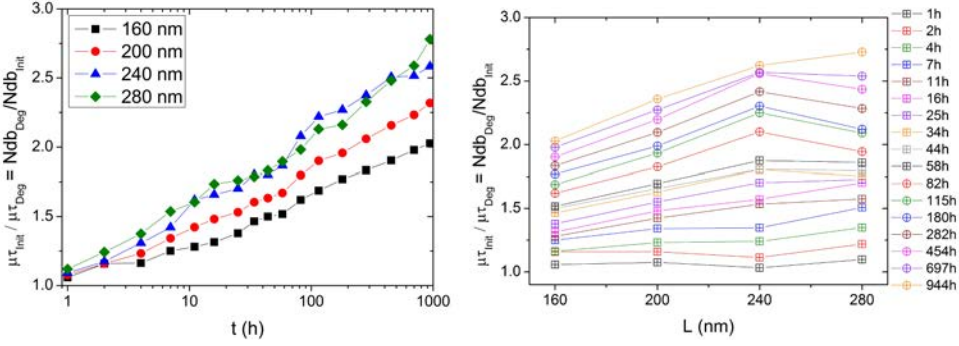


Figure 4.4: $\mu\tau_{Init}/\mu\tau_{Deg} \approx Ndb_{Deg}/Ndb_{Init}$ evolution. The left graph shows the evolution with time for different thicknesses. Conversely, the right graph shows the dependence with thickness for different degradation times.

a bulk effect. Linear regressions have been developed for all the lines in the right part of Fig. 4.4, aiming to obtain this kind of correlation:

$$\frac{Ndb_{Deg}}{Ndb_{Init}} = A + B(t)L \quad (4.10)$$

In this situation, A is the intercept and B is the value of the slope. If the degradation is a bulk phenomenon, as A is the value when $L=0$ (hypothetical), it has to be independent of the time and equal to 1 (the density of defects does not change). On the other hand, the value of B should increase with the degradation time. The values of A and B for each time with the corresponding error are shown in Fig. 4.5.

As it can be observed, the errors (specially in A) are quite large, as it has been obtained only with four points, so the results are not very reliable. However, the values for the intercept are scattered around 1, and it is clear that the slope (value which multiplies L in Eq. 4.10) increases with time. These results point to the fact that the defect generation is mainly produced in the bulk region, and so, the samples with larger bulk zone will be more degraded with time under LID.

Of course this model is very simple, and it should be corroborated with

4 Light induced degradation

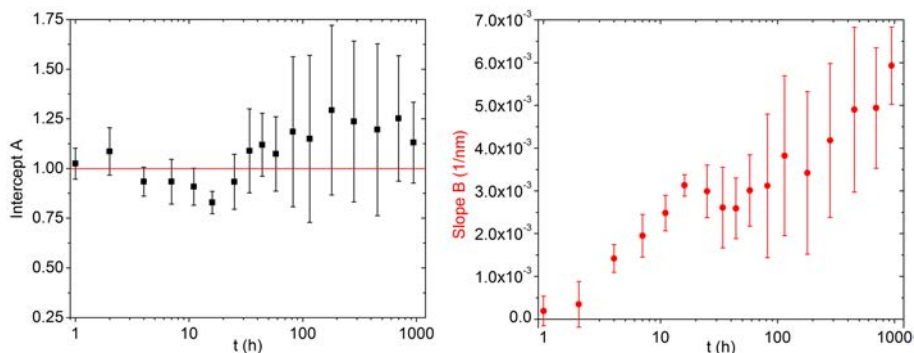


Figure 4.5: Intercept value (left) and slope (right) for each time, obtained through linear regressions from the right graph in Fig. 4.4, corresponding to Eq. 4.10.

more samples of different thicknesses in a wider range. Anyway, it suffices to explain why the thicker cells present a higher initial performance and why this tendency is reversed after some hours of degradation. It has to be taken in account that to evaluate the final performance of the cell, $\mu\tau$ is not the only parameter to be considered. Some other properties of the cell, like the series resistance or the open circuit voltage, are also affected by LID and condition the degraded state of the cell.

4.3.4 Conclusions and future work

In this section, a study of the evolution of the parameters during light soaking has been developed, and the optimum thickness for UB cells at this point has been found at 200 nm. Thicker cells are not advisable as their performance would be initially higher, but this would be reverted in a few hours of LID, resulting in a lower performance at the stabilized state. Slightly thinner cells might work as well as the 200 nm cell at longer degradation times, but the difference at this point would be very small and some other effects could be more crucial.

Future experiments should aim to combine the optimization of the material and thickness. If more performing doped layers and less defective

intrinsic layers (with higher hydrogen concentration) are used in the cell, and buffer layers are included to make the interface less defective, probably lower LID would occur, and maybe the thinner cells would achieve higher performance and the thickness can even be slightly reduced without stabilized efficiency loss, as in commercial *T-Solar* cells.

4.4 Temperature influence on seasonal effect

To study the behavior of a-Si:H solar cells with seasonal effect and compare it with the one found for modules, a temperature varying degradation experiment was designed. The objective was to somehow recreate the situation of different on field conditions for modules, but excluding the spectral effect, and study the evolution of the performance of the solar cells. The objective is to further understand SWE by performing LID on the cells and then, develop a thermal annealing to try to recover them, and observe the parameters.

The procedure of the experiment was to pick identical sets of a-Si:H solar cells as deposited and characterize them; then the sets were degraded at different temperatures for times of about 1000 h to obtain the stabilized state and then the parameters were measured again. The next step was to change the degradation temperature of each set of samples, and perform LID again for over 1000 h, obtaining a new stabilized state. This new state was characterized again and compared with the previous one. As the only parameter that has changed is the temperature of degradation (not the spectrum of the light), if there any difference is found, it is due to the effect of the temperature. In the end, the samples underwent an annealing process (Chapter 2, Sec. 2.2.3) to get recovered. After, they were characterized once again and the results were compared with the initial and degraded states in order to check the thermal recovery effect. This experiment has been developed over commercial cells from *T-Solar* (which are the ones used in the previously studied modules) and over cells deposited at the UB. Both experiments were quite similar but some differences existed, which will be detailed in each case.

4 Light induced degradation

4.4.1 *T-Solar* samples

For the experiment with *T-Solar* samples, two sets of solar cells deposited at the same run (almost identical) were used. These sets were deposited at *T-Solar* factory in the same conditions used for module manufacturing. The small solar cells of 1 cm^2 were cut from a very large $2.2\times 2.6\text{ m}^2$ substrate.

Initially, both cells were characterized at their annealed state, performing standard and dark $J-V$ measurements. Then, the first degradation was performed: Sample A was degraded at 60°C and sample B was degraded at 30°C . During the degradation, the same characterization measurements were taken regularly to control the evolution of the sample. When the samples had been over 1000 h of degradation, they were characterized again. After, the degradation temperature was switched, so Sample A was degraded at 30°C and sample B at 60°C . During this second degradation, characterizations were regularly developed. Due to technological issues, it was not possible to perform the degradation for such long term as the previous one; however, it lasted over 100 h and it was enough to observe the tendency of all the parameters.

4.4.1.1 Results and discussion

The results show that the degradation temperature of the samples clearly influences the dynamics of the process. Fig. 4.6 shows the evolution of the parameters. For all of them, the first degradation performed at 60°C shows less decrement in all the parameters than the one at 30°C , as it was expected. The only possible exception is the current. However, the current is not a reliable parameter as there is a large scatter and an important shift in the last part of the first degradation, due to calibration issues caused by an illumination failure in the equipment. This is also traduced in the efficiency. As far as the V_{oc} and the FF are concerned, the difference in the degradation is more clear, specially in the fill factor.

An important result that can be appreciated in the plots is that when the degradation temperature was switched, sample A (going from 60°C to

4.4 Temperature influence on seasonal effect

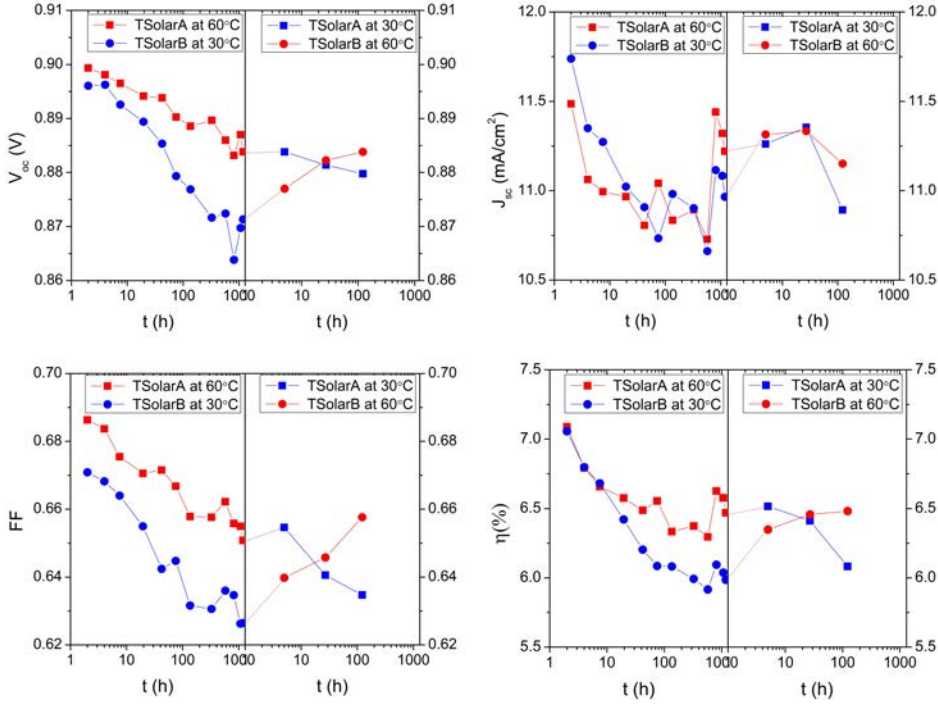


Figure 4.6: Evolution of V_{oc} , J_{sc} , FF and η during the degradation of samples T -Solar A (squares) and T -Solar B (circles). When degradation is performed at 60°C the plot is shown in red, and when it is at 30°C , in blue. The central vertical line indicates the temperature switch.

30°C) experienced a quick drop in its parameters, while sample B (going from 30°C to 60°C) experienced a recovery. As the spectrum used to degrade the samples was the same, this effect is only caused by the role of the temperature in thermal recovery. Due to the lack of data over 150 h in the second degradation, it is not possible to fully verify it, but the tendency of the plots seems to be to reach the same stabilized state as the other sample after its first degradation: This is, sample A's parameters after its second degradation at 30°C would reach the same values as sample B's after its first degradation (also at 30°C); and conversely, sample B's parameters degraded at 60°C after being degraded at 30°C

4 Light induced degradation

Table 4.3: Evolution of J - V curve parameters in T -Solar samples.

| Sample | V_{oc} (V) | J_{sc} (mA/cm ²) | FF | η (%) |
|-----------------------|--------------|--------------------------------|-------|------------|
| A Initial state | 0.906 | 11.61 | 0.714 | 7.51 |
| B Initial state | 0.905 | 11.53 | 0.714 | 7.45 |
| A (deg.@60°C) | 0.884 | 11.22 | 0.651 | 6.57 |
| B (deg.@30°C) | 0.873 | 10.96 | 0.629 | 5.99 |
| A (deg.@60°C to 30°C) | 0.880 | 10.89 | 0.635 | 6.08 |
| B (deg.@30°C to 60°C) | 0.884 | 11.35 | 0.657 | 6.48 |

would reach the values of sample A's after its first degradation at 60°C.

The conclusion would be that the stabilized parameters of the solar cell are independent of the previous degradation or annealing history; they only depend on the degradation temperature (assuming identical light spectrum). The values of J - V curve parameters before and after every degradation process are presented in Table 4.3. Even though the second degradation was only for 122 h, it is already possible to see that the tendency of the parameters is to stabilize according to the temperature and not to the history of the sample. This is completely proved in the next section with UB samples, where the technological issues and the calibration problems were solved and the degradation processes were finished.

4.4.1.2 Evaluation of the temperature coefficients

All the J - V curves in Table 4.3 were measured under standard test conditions (25°C). From the previous results, assuming a linear dependence of the parameters with the annealing temperature, the temperature coefficients for the light induced performance stabilization can be determined. The values of these coefficients are presented in Table 4.4.

In order to relate these values with the real operation situation is important to take in account an additional effect of temperature on the field performance, which is the temperature dependence of module efficiency

4.4 Temperature influence on seasonal effect

Table 4.4: Temperature coefficients for *T-Solar* samples ($^{\circ}\text{C}^{-1}$).

| $\alpha_{V_{oc}}^{SW}$ | $\alpha_{J_{sc}}^{SW}$ | α_{FF}^{SW} | α_{η}^{SW} |
|------------------------|------------------------|--------------------|----------------------|
| 0.03% | 0.07% | 0.10% | 0.19% |

for fast temperature changes, which is present in all photovoltaic technologies. This effect can be evaluated with the difference between mean temperature and 25°C (the temperature at STC) using the temperature coefficient for module efficiency (α_{η}), which is provided by the manufacturer in the specifications sheet. For *T-Solar* cells and modules, this coefficient is $-0.21\%/^{\circ}\text{C}$. To be used with mean temperatures, a joint temperature coefficient (α_{η}^{joint}) for the two temperature effects can be defined as:

$$\alpha_{\eta}^{joint} = \alpha_{\eta} + \alpha_{\eta}^{SW} \quad (4.11)$$

So, its value in *T-Solar* samples is only $-0.02\%/^{\circ}\text{C}$. This coefficient can be used to account for the efficiency difference as a function of mean module temperature. The very low value of this coefficient means that the field efficiency change for a-Si:H modules is almost independent of temperature, as it is compensated with the fast temperature change coefficient. As conventional technologies do not experience the thermal annealing recovery effect, the joint temperature coefficient for amorphous silicon should be compared to the standard temperature coefficient of conventional c-Si technology (α_{η}), which is close to $-0.45\%/^{\circ}\text{C}$.

4.4.2 UB samples

In order to verify some of the results obtained with *T-Solar* samples, another degradation experiment was performed over solar cells deposited in the UB. A standard solar cell was deposited over a $10 \times 10 \text{ cm}^2$ Asahi VU glass, and then, after the TCO of the back reflector was deposited, it was divided in four $5 \times 5 \text{ cm}^2$ pieces, numbered 1 to 4. The deposition conditions are shown in Table 4.1, taking into account that for this

4 Light induced degradation

experiment the thickness of the intrinsic layer was 200 nm.

Over each of these pieces, a set of six 1 cm^2 cells was deposited as it is explained in Chapter 2, Sec. 2.2.2. The metalization was also done in the same deposition, which means that all the cells were identical. J - V measurements were taken just after the deposition, and then each sample underwent two subsequent degradations of over 1000 h at different temperatures, and finally, an annealing process. The aim was to study the dependence of the parameters with the degradation temperature only (no spectral effect), to confirm the fact that the stabilized values of the parameters do not depend on the sample history, and to extract additional conclusions concerning light induced degradation and seasonal effect. The degradation process for each sample is shown next:

- Sample 1: $40^\circ\text{C} \rightarrow 60^\circ\text{C}$
- Sample 2: $50^\circ\text{C} \rightarrow 40^\circ\text{C}$
- Sample 3: $50^\circ\text{C} \rightarrow 60^\circ\text{C}$
- Sample 4: $60^\circ\text{C} \rightarrow 40^\circ\text{C}$

These temperature cycles allow the verification of several conclusions that had not been entirely confirmed with *T-Solar* samples. The difference in the degradation temperature allows the study of the influence of the temperature already observed in the bibliography and in previous section. Also, as samples 1 and 3 go from 40°C and 50°C to 60°C , and conversely, samples 2 and 4 go from 50° and 60°C to 40°C ; looking at the values of the final parameters it is possible to verify that the history of the sample does not influence the final stabilized state, which depends only on the degradation temperature (if the spectrum of the degrading light is the same).

4.4.2.1 J - V curves: Results and discussion

For this experiment, the evolution was not studied again, this is, the characterizations were only developed at the stabilized states (initial, after both degradation cycles, and after the annealing). Fig. 4.7 shows

4.4 Temperature influence on seasonal effect

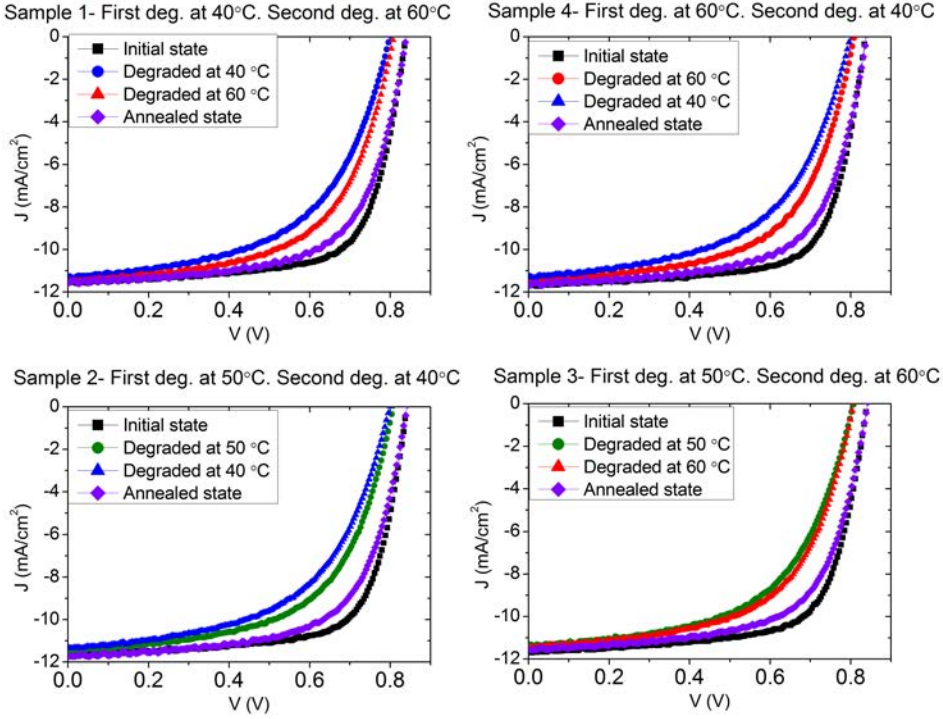


Figure 4.7: J - V curves of the samples 1, 4 (upper) and 2, 3 (lower) in the different stages of degradation. The colors indicate the temperature of degradation and the symbols, the order of the degradation processes.

the J - V curves of each sample at the four different stages of degradation. In order to make the plots as clear as possible, two codes are used: The different symbols refer to the different stages of degradation, being initial state squares, first degradation circles, second degradation triangles and annealed state diamonds. On the other hand, the color of the plot references the temperature of degradation, being black the initial state, blue 40°C, green 50°C, red 60°C and violet the annealed state.

The order of the graphs has been altered, being the two upper samples 1 (40°C to 60°C) and 4 (60°C to 40°C), and the two lower samples 2 (50°C to 40°C) and 3 (50°C to 60°C). This is done to make it easier

4 Light induced degradation

Table 4.5: Evolution of J - V curve parameters in UB samples.

| Sample | Status | V_{oc} (V) | J_{sc} (mA/cm ²) | FF | η (%) |
|--------|-----------|--------------|--------------------------------|-------|------------|
| 1 | Initial | 0.836 | 11.583 | 0.700 | 6.781 |
| 1 | Deg.@40°C | 0.795 | 11.351 | 0.552 | 4.985 |
| 1 | Deg.@60°C | 0.804 | 11.536 | 0.592 | 5.489 |
| 1 | Annealed | 0.836 | 11.570 | 0.649 | 6.284 |
| 2 | Initial | 0.838 | 11.655 | 0.711 | 6.946 |
| 2 | Deg.@50°C | 0.805 | 11.477 | 0.587 | 5.425 |
| 2 | Deg.@40°C | 0.795 | 11.398 | 0.558 | 5.052 |
| 2 | Annealed | 0.838 | 11.615 | 0.654 | 6.372 |
| 3 | Initial | 0.835 | 11.632 | 0.696 | 6.753 |
| 3 | Deg.@50°C | 0.803 | 11.406 | 0.572 | 5.238 |
| 3 | Deg.@60°C | 0.804 | 11.587 | 0.593 | 5.525 |
| 3 | Annealed | 0.837 | 11.625 | 0.646 | 6.287 |
| 4 | Initial | 0.836 | 11.699 | 0.710 | 6.925 |
| 4 | Deg.@60°C | 0.804 | 11.579 | 0.606 | 5.641 |
| 4 | Deg.@40°C | 0.795 | 11.398 | 0.554 | 5.015 |
| 4 | Annealed | 0.836 | 11.659 | 0.656 | 6.392 |

for the observer to establish comparisons between the graphs. The first thing that is noticed is that the difference between the samples is not at all negligible, being clear that it is over the 2% established for modules [60].

Looking at the two upper graphs, it can be seen that they are almost identical, as both show a degradation at 40°C and one at 60°C, being the only difference the order of the degradation. Concerning the lower graphs, both show an almost equal J - V curve corresponding to the first degradation at 50°C. Then, the subsequent degradations at 40°C and 60°C are also almost equal to those on the upper graphs at the same temperature. All these facts confirm the idea that the temperature has a role in degradation apart from the variation of the spectrum, and so it could have an important influence on the seasonal effect. Also, the comparisons exposed finally prove that the final J - V curve does not

4.4 Temperature influence on seasonal effect

depend on the previous annealing nor temperature history, but only on the temperature of the last degradation.

The values of the parameters for each sample in chronological order stage are shown in Table 4.5 and confirm the conclusions that were visually extracted of the J - V curves in Fig. 4.7. If the parameters are analyzed, it can be observed that the values obtained at the same temperature are very similar, no matter the sample nor the previous temperature. In order to make it easier to see this fact, Table 4.6 shows the relative values of the parameters arranged by temperature of degradation. These relative values are obtained as the ratio of the degraded/annealed value to the initial value.

Table 4.6: Values of relative parameters in UB samples arranged by degradation temperature.

| Temperature | Sample | Deg. point | V_{oc} | J_{sc} | FF | η |
|-------------|--------|------------|----------|----------|-------|--------|
| 40°C | 1 | First | 0.951 | 0.980 | 0.789 | 0.735 |
| 40°C | 2 | Second | 0.948 | 0.978 | 0.785 | 0.727 |
| 40°C | 4 | Second | 0.954 | 0.974 | 0.780 | 0.724 |
| 50°C | 2 | First | 0.960 | 0.985 | 0.826 | 0.781 |
| 50°C | 3 | First | 0.963 | 0.981 | 0.822 | 0.776 |
| 60°C | 1 | First | 0.962 | 0.996 | 0.845 | 0.809 |
| 60°C | 3 | Second | 0.963 | 0.996 | 0.853 | 0.818 |
| 60°C | 4 | Second | 0.965 | 0.990 | 0.852 | 0.815 |
| Annealed | 1 | Final | 1.000 | 0.999 | 0.927 | 0.927 |
| Annealed | 2 | Final | 1.000 | 0.997 | 0.921 | 0.917 |
| Annealed | 3 | Final | 1.003 | 0.999 | 0.929 | 0.931 |
| Annealed | 4 | Final | 1.003 | 0.997 | 0.924 | 0.923 |

It can be observed that the losses in each parameter are related with the temperature, being higher when the temperature is lower, and conversely. As far as V_{oc} is concerned, the degradation is a bit higher than the one in T - $Solar$ samples, probably due to a slightly higher thickness [146]. This might also contribute to the fact that the FF experiences higher

4 Light induced degradation

degradation in these cells that in *T-Solar* cells, in which the maximum relative degradation of the FF was 0.881 at 30°C, while these samples show lower values of FF_{rel} even at 60°C. However, the higher thickness would not explain such a big difference, so it has to be also due to less quality of the material. Finally, if the values of J_{sc} are observed, here it is possible to find a slight tendency with the temperature that was not so clear in *T-Solar* samples due to calibration issues. The current behavior with the degradation temperature is checked with EQE measurements that will be shown afterwards.

4.4.2.2 Role of short and open circuit resistances

Another significant result found in UB samples is that the thermal annealing provides full recovery in V_{oc} and J_{sc} , but does not provide a full recovery in the fill factor, that only reaches about 92.5% of the initial value after the annealing process.

To try to explain this, the values of R_{sc} and R_{oc} obtained from the initial and annealed state J - V curves were studied. The absolute and relative (degraded R /annealed R) values of R_{sc} and R_{oc} are shown in Table 4.7. As it can be seen, R_{sc} values in the annealed state are about 85% of the initial ones, while R_{oc} values are about 120%.

As it is explained in Chapter 2, Sec. 2.3.5.1, R_{sc} is related with R_p , which is expected to have high values in order to achieve higher FF . So, the decrement of R_{sc} in the cells can lead to a decrement of R_p and then, lower FF . Conversely, R_{oc} is related with R_s , in which low values are desirable to reach higher FF . So, in this case, the increment of R_{oc} in the cells can cause an increment of R_s which results again in lower values of the FF . These two effects combined result in the difference between the initial and the annealed values of the FF detected in the cells.

The difficulty here lies in determining what is the reason of these variations of the resistances. Although some irreversible degradation is found in cells [132] due to the creation of stable defects with infinite E_a [168], the difference found for these samples is too large. It is possible

4.4 Temperature influence on seasonal effect

Table 4.7: Values and relative values of the short circuit (up) and open circuit (down) resistances in UB samples in the initial and annealed states.

| Sample | R_{sc} initial ($\text{k}\Omega \text{ cm}^2$) | R_{sc} annealed ($\text{k}\Omega \text{ cm}^2$) | R_{sc} relative |
|--------|--|---|-------------------|
| 1 | 0.962 | 0.842 | 0.875 |
| 2 | 0.948 | 0.837 | 0.883 |
| 3 | 0.912 | 0.793 | 0.869 |
| 4 | 1.028 | 0.850 | 0.826 |

| Sample | R_{oc} initial ($\text{k}\Omega \text{ cm}^2$) | R_{oc} annealed ($\text{k}\Omega \text{ cm}^2$) | R_{oc} relative |
|--------|--|---|-------------------|
| 1 | $6.982 \cdot 10^{-3}$ | $8.243 \cdot 10^{-3}$ | 1.181 |
| 2 | $6.460 \cdot 10^{-3}$ | $8.101 \cdot 10^{-3}$ | 1.254 |
| 3 | $7.220 \cdot 10^{-3}$ | $8.641 \cdot 10^{-3}$ | 1.197 |
| 4 | $6.582 \cdot 10^{-3}$ | $8.118 \cdot 10^{-3}$ | 1.233 |

that during the light soaking or the annealing, some pinholes or leaks have been created in the sample, that the exposure to environment has an negative influence or that the contact with the probes during the measurements has scratched the sample causing damage.

Another possible explanation is found in the work of Kail *et al.*[169], which presents that hydrogen can effuse from silicon thin films during light soaking, causing hydrogen loss. As the samples were deposited without any additional hydrogen, the hydrogen loss could be critical when the annealing is performed. If a relevant quantity of hydrogen has effused, it would be possible that there is not enough hydrogen left in the cell to saturate the created dangling bonds. So, the annealed state would present more defects than the initial state, and the cell would be less performing, just like in the presented situation.

4.4.2.3 EQE and absorptance: Results and discussion

To complement the J - V curves, EQE and absorptance measurements were made in the degraded and annealed states to obtain additional information. In this case, it was assumed that the transmittance is equal

4 Light induced degradation

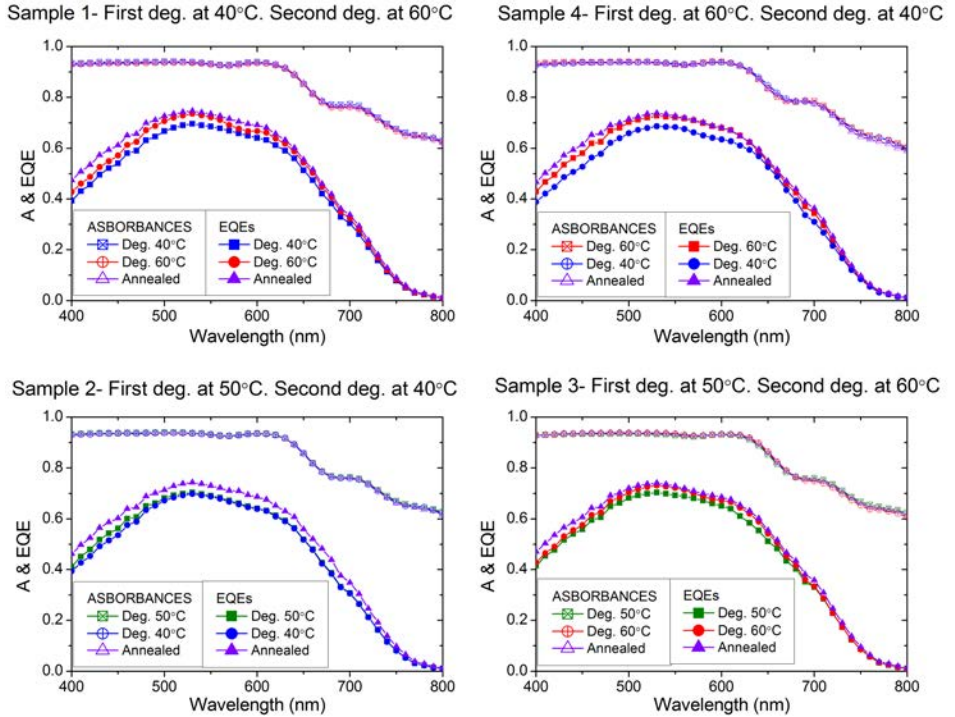


Figure 4.8: A and EQE curves of the samples 1, 4 (upper) and 2, 3 (lower) in the different stages of degradation. The colors indicate the temperature of degradation and the symbols, the order of the degradation processes.

to 0 and all the optical losses were due to the reflected light; so the absorbance was obtained from the measured reflectance, as $A=1-R$. The objective was to verify the current degradation and to observe the causes. These measurements serve also to observe in which wavelengths the cell experienced higher EQE degradation.

The results for A and EQE for each sample at both degraded and annealed states are shown in Fig. 4.8. The first thing that can be noticed is that the absorbance of the cell does not change with the degradation status, while the EQE shows certain dependence. This means that the cell absorbs the same quantity of photons in all the states, but not the

4.4 Temperature influence on seasonal effect

same quantity of electron-hole pairs are collected, this is, the losses are not caused by optical reasons but for electrical issues, such as an increase of the recombination. As the absorptance is constant, IQE is not shown in the graphs, because the difference between the IQE of the different degradation states would not provide any new information from the difference between the EQE .

As far as the difference between the $EQEs$ is concerned, it can be observed that just like in the $J-V$ curves, the EQE curves corresponding to LID at higher temperatures show higher values, which in this case means higher J_{sc} . The graphs in Fig. 4.8 are placed in the same order as in Fig. 4.7. This is again to make it easier to compare the graphs and observe that, just like in $J-V$ measurements, the curves only depend on the final temperature and not on the history of the sample. The existence of differences on the $EQEs$ verifies that J_{sc} experiences a degradation, so the difference between values observed in the $J-V$ curves was not caused by calibration issues.

To verify this degradation and its relation with the temperature, a weighted integration with the solar spectrum has been done in order to obtain the current corresponding to the area under the curve. In this case, the relative values are obtained as the fraction between the degraded and the annealed state. The values arranged by temperature are shown in Table 4.8. The values obtained with this integration are quite higher than the ones measured with the $J-V$ curves. This could be due to an overestimation of the EQE current, or to an illumination lower than 1 sun when the $J-V$ measurements were done due to the same calibration issues explained before. In any case, this causes that the difference found in the relative values is higher; but despite this difference, the fact that the higher the temperature, the lower provoked LID remains clear, just like the rest of the parameters.

4 Light induced degradation

Table 4.8: Short circuit current values obtained from EQE curves integrations for UB cells.

| Deg. status | Sample | J_{sc} (mA/cm ²) | Relative J_{sc} |
|-------------|--------|--------------------------------|-------------------|
| Annealed | 1 | 12.833 | - |
| Annealed | 2 | 12.853 | - |
| Annealed | 3 | 12.862 | - |
| Annealed | 4 | 12.841 | - |
| Deg.@40°C | 1 | 11.741 | 0.915 |
| Deg.@40°C | 2 | 11.768 | 0.916 |
| Deg.@40°C | 4 | 11.723 | 0.913 |
| Deg.@50°C | 2 | 11.923 | 0.928 |
| Deg.@50°C | 3 | 12.027 | 0.935 |
| Deg.@60°C | 1 | 12.370 | 0.964 |
| Deg.@60°C | 3 | 12.452 | 0.968 |
| Deg.@60°C | 4 | 12.533 | 0.976 |

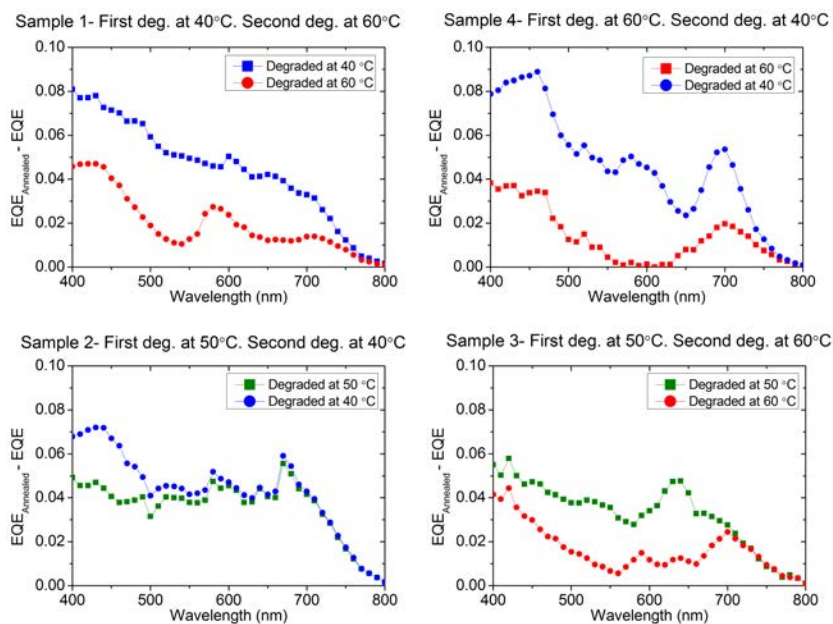


Figure 4.9: Difference between the EQE of the annealed and the degraded states of the samples 1, 4 (upper) and 2, 3 (lower) in the different stages of degradation. The colors indicate the temperature of degradation and the symbols, the order of the degradation processes.

4.4 Temperature influence on seasonal effect

Graphs of the difference between the EQE of the annealed and the degraded state for each sample are shown in Fig. 4.9, in order to observe more clearly which wavelengths zones are more affected by the degradation. It can be observed that although it can generally be considered a global effect, as almost all the wavelengths are affected (specially at lower temperatures), the shorter wavelengths are more affected while the central ones (about from 500 to 650 nm) are less affected, specially at 60°C, where curves show very low values, which means that the values are almost equal to those of the annealed state. It is important to notice that due to the lower values of the EQE in the long wavelength zone (over 650 nm), the difference is also very small in graph.

This behavior can be understood by taking in account that the interfacial zone between the p doped layer and intrinsic layer is more defective [146] and so the recombination there is enhanced. So, the light absorbed here do not contribute to the photogenerated current [39]. LID can produce a diffusion of the dopant species, specially boron, due to temperature and time issues [170][171], which causes a formation of a non intentionally doped area [39] in which absorbed carriers do not contribute as in the intentionally doped area. As a result, an enhanced recombination in the zones close to the doped layer is found. To be sure it would be necessary to perform measurements of the defect concentration in the cell profile. This would be also useful to verify the model proposed in Sec. 4.3.3.

4.4.2.4 Evaluation of the temperature coefficients

If the temperature coefficients associated to SWE are calculated just like with T -Solar samples, the obtained values are shown on Table 4.9. These values are just slightly higher than T -Solar cells for V_{oc} and J_{sc} , but on the other hand, the values obtained for FF , and subsequently for η , are much higher. The main reason seems to be that the i -aSi:H used in this cell has less quality against SWE, as it is not the optimized material with additional hydrogen to reduce LID.

As during the LID, the illumination was constant (never turned off), the rapid temperature change has not been measured yet for these cells.

4 Light induced degradation

Table 4.9: Temperature coefficients for UB samples ($^{\circ}\text{C}^{-1}$).

| $\alpha_{V_{oc}}^{SW}$ | $\alpha_{J_{sc}}^{SW}$ | α_{FF}^{SW} | α_{η}^{SW} |
|------------------------|------------------------|--------------------|----------------------|
| 0.05% | 0.08% | 0.30% | 0.39% |

So, the joint coefficient that was obtained for *T-Solar* cell can not be obtained for UB cells, so the comparison is not completely finished. A way to try to deduce this coefficient would be to perform the LID with cycles of light and dark and also variations of the temperature per hours trying to recreate the on field conditions.

4.4.3 Conclusions and further work

Combining the three experiments, several conclusions can be extracted at this point. Looking at the results corresponding to the power plant, it can be observed that the seasonal effect is clearly appreciated in the performance ratio of the power plant, being a 8.3% higher in summer than in winter. When solar cells from *T-Solar*, identical to the module ones, were used in a LID experiment at different degradation temperatures with constant spectrum, a significant difference in the parameters was found. The results show evidence of the role of the temperature difference in internal thermal annealing, as the temperature shift produces either recovery or further degradation, depending on if it was going up or down. However, when α_{η} is calculated, it is found that the thermal annealing term related to SWE almost cancels the temperature dependence of efficiency due to fast temperature changes. This means that on field operation, there is almost no dependence on thermal annealing, and then the higher efficiency and *PR* of the a-Si:H power plants in summer is almost exclusively due to spectral effects [154].

In order to better understand the role of temperature, a similar experiment was developed with solar cells deposited at the UB. It can be seen that if the spectral effect and the fast temperature changes are not taken into account (as the illumination and the temperature were constant

during LID), the final state of the cell depends only in the last degradation temperature, and not on the history of the sample. Also, if the light spectrum is not changed, it is clear that the higher the temperature, the lower the LID, due to the thermal annealing. To actually evaluate the role of the temperature in this cells on field conditions, the fast temperature changes coefficient should be calculated from different measurements.

The behavior of the different parameters under LID at different temperatures allows to extract some conclusions about the UB cell. The higher degradation of V_{oc} and J_{sc} than in *T-Solar* cells shows that probably the cells deposited at the UB are thicker, which provokes higher LID in these parameters [146]. It also suggests that the quality of the doped layers and interfaces requires further optimization by means of buffer layers inclusion or the use different p and n doped materials, like μc -Si:H or μc -SiO_x. The higher degradation of the FF indicates that the intrinsic material has also to be further optimized, including a certain amount of hydrogen in the plasma deposition to reduce LID. It is important to notice that the used cell still has not the optimized material extracted from Chapter 3.

4.5 Conclusions and perspectives

In this chapter, the role of light induced degradation in a-Si:H is studied in the cells deposited at UB. Also some of the work of the group concerning seasonal effect present in LID has been continued. The first important conclusion arises from the development and construction of a low cost LED-based light soaking system described at Chapter 2, Sec. 2.2.4. The comparison with several degradation experiments in the bibliography shows that the behavior of the cells degraded in system is very similar to the behavior of cells degraded in several different illumination systems (both commercial and home-made). So, the constructed LID system has proved itself to be reliable and functional to conduct degradation in cells for experimental purposes. Furthermore, the fact that several temperatures of degradation can be controlled precise and independently provides the opportunity to develop interesting LID experiments involving temperature.

4 Light induced degradation

As far as the i -layer thickness optimization for UB cells is concerned, the maximum in the final efficiency has been found at 200 nm. A very simple model to justify the results has been explained. Further experiments could be developed in order to refine the result, aiming to obtain as less degradation as possible. Modifications of the doped layers, addition of buffer layers to reduce interfacial effects, use of the optimized intrinsic material with additional hydrogen or longer LID processes are some examples.

Then, the degradation experiments involving T have proved its influence in solar cells. Higher degradation is found when the temperature is lower, and if the degradation temperature is raised, the cell experiences some thermal recovery. Conversely, reducing the degradation temperature provokes a sudden decrement of the parameters. This leads to an important conclusion: The stabilized state of the cells does not depend on the degradation temperature history but only on the final temperature. This suggest that thermal annealing is the responsible of this behavior, proving its role in LID.

When the temperature dependence coefficients associated to SWE are obtained for solar cells, it is found that their values almost compensate the effect of rapid temperature change on the efficiency of the modules, leaving the spectral variations as the most dominant effect in seasonal effect, just as previous group work pointed [60]. In contrast, UB cells show much higher values for FF and η SWE temperature coefficients. To fully evaluate the influence of the temperature and compare it to commercial cells, the fast temperature changes coefficient for UB cells must be obtained by introducing illumination cycles.

5 Thin film passivation for advanced solar cell structures

5.1 Introduction

Through the years, technologies involving crystalline silicon (c-Si) have managed to keep themselves at the top of solar energy technologies, due to their higher efficiency conversion [8]. As this thesis is mostly based on amorphous silicon, this chapter is focused in the role of this material combined with these technologies. Here, a-Si:H is not the active part of the solar cell, as this role corresponds to c-Si, but it acts as a complementary material for passivation. All this work has been developed in collaboration with the Universitat Politècnica de Catalunya (UPC), which has larger previous experience working on c-Si PV technology [50][61][62][63].

5.1.1 Fundamentals

In c-Si technology, like in any other PV technologies, there are two steps in the process of obtaining energy: absorbing the light to generate the carriers and collect those carriers in the electrodes to get electric current. So, there are two possible ways to increase the conversion efficiency: Enhancing the absorption of photons to generate more carriers and making the carrier collection more efficient. In the first case, several strategies and techniques are used to maximize the absorbed light as much as possible. In the second, the increase of the collection is mostly linked to the reduction of the recombination; this is, avoiding that the electrons and the holes cancel each other before reaching the electrodes.

5.1.1.1 Efficient light absorption

In order to obtain an efficient light absorption, two different strategies are followed: the first is to maximize the light that comes into the cell and the second is to avoid that light escaping the cell without being absorbed. Some of the employed techniques are listed next:

- **Reduction of shadowing:** A metallic front contact is needed in solar cells to collect the carriers, so the incident light in this contact's area is reflected and does not come into the cell. This means that the front contact provokes a shadowing in the device, reducing the amount of incoming light. As a consequence, it is necessary to reduce this shadowing effect as much as possible. The use of metallic grids reduces the shadowing effect, and some technologies like IBC (Chapter 1, Sec. 1.2.3.2) place both contacts in the rear part to eliminate the shadowing.
- **Anti-reflection coatings (ARC):** ARCs are used to avoid the reflection of the light in the front surface of the cell. They operate under the principle of negative interference: the silicon wafer surface reflects a certain amount of light, so the idea is to deposit a thin layer of a dielectric material such as the reflected wave in its top surface is out of phase with the wave reflected on the c-Si top surface. If this is accomplished, both waves are canceled and there is no reflected energy. To achieve this situation, the thickness of the dielectric layer has to be chosen to fulfill the anti-reflection condition:

$$d = \frac{\lambda}{4n} \quad (5.1)$$

where λ is the wavelength in which the reflection needs to be minimized and n is the refractive index of the layer. If this is the implemented thickness, the light travels a quarter of its wavelength in the ARC, then it is reflected by the silicon surface, travels another quarter of its wavelength and finally it gets out of the ARC. This means that it has traveled half the wavelength of the light that was first reflected by the ARC, so both are canceled. It is usual that the front TCO is used also as ARC, but there are different techniques to reduce the reflection with ARCs.

- **Back reflectors:** The use of back reflectors, explained in Chapter 1, Sec. 1.2.3.1 for thin film solar cells, is also valid for c-Si technologies: the inclusion of a metallic layer in the rear side of the cell that acts as a mirror provides a second chance for the light to be absorbed when it comes out. Sometimes, additional layers with different refraction indexes and textures are included between the wafer and the rear metal in order to increase the light path and so the chance of absorption.
- **Textured surfaces:** Texturing both front and rear surfaces is an extended technique, very commonly employed, as it provides several advantages: Textured front surfaces reduce the reflection and make the light to disperse, increasing the mean path through the cell, and so enhancing the absorption probability. The same happens at the rear surfaces, where the non-absorbed light is reflected in different angles, and so the light-trapping is highly increased; however, textured rear surface is relevant for thin film solar cells but is less important for thick wafer based cells. There are several techniques to texture the surfaces, resulting in both ordered or random textures. For c-Si, for example, it is common the random pyramid texturing by etching [172].
- **Thickness optimization:** It is complicated to obtain the optimum thickness for c-Si, as the the thicker the wafer, more light is absorbed as the light path is longer, but on the other hand, the bulk recombination also increases, the emitter has to improve its quality and also, the cost of the device increases. So, the optimum thickness on the wafer depends on several factors, like the quality of the wafer and the enhancement of the light path provided by texturing and BR. Anyway, this optimization is important for thin cells (a few μm) but much less relevant in wafer based cells, where the thickness of the wafer is normally limited by technological reaches. In fact, the optimal thickness cannot be manufactured.

5.1.1.2 Reduction of the recombination

The second strategy to improve the conversion efficiency of c-Si solar cells is the reduction of the recombination. The performance of c-Si solar cells is highly related to the quantity of carriers that can be collected on the electrodes, which means that recombination must be reduced as much as possible in order to increase the conversion efficiency. The recombination can be evaluated through a parameter called recombination velocity (U), defined as:

$$U = \frac{\Delta n}{\tau} \quad (5.2)$$

where Δn is the minority carrier excess [6] and τ is the effective carrier lifetime. There are two main mechanisms that contribute to the recombination: bulk recombination and surface recombination. As far as bulk recombination is concerned, three different processes limit the lifetime of the carriers: radiative, Auger and Shockley-Read-Hall recombinations:

- In radiative recombination, an electron from the conduction band and a hole from the valence band disappear; and the energy of the e-h pair is emitted as a photon with an energy approximately equal to the value of the gap of the material.
- Auger recombination is also a band-to-band recombination, like radiative recombination, but in this case the excess of energy is not emitted but transferred to a third carrier, either an electron or a hole.
- Shockley-Read-Hall (SRH) recombination was first reported by these three authors in 1952 [173][174]. It is related to the crystallographic defects, impurities and imperfections present in the bulk of the wafer. These defects act as recombination centers, as they are states in the middle of the bandgap. Four types of process can occur: electron capture, electron emission, hole capture and hole emission.

The fourth recombination process, surface recombination, is caused by the abrupt end of the crystalline net, and the consequent free bonds on the surface. Some impurity defects can also appear on the surface as a result of subsequent depositions. So, the effective carrier lifetime (τ_{eff}) would be result of the inverse addition of the lifetime associated to each

mechanism as:

$$\frac{1}{\tau_{eff}} = \left(\frac{1}{\tau_{rad}} + \frac{1}{\tau_{Auger}} + \frac{1}{\tau_{SRH}} \right) + 2 \frac{S_{eff}}{W} \quad (5.3)$$

where the last term corresponds to surface recombination: S_{eff} is the effective surface recombination velocity, W is the wafer thickness, and the 2 refers to both sides of the sample, assuming symmetry of wafer surfaces.

Crystalline silicon is an indirect gap semiconductor, which makes the probability of band-to-band recombination processes low compared to those of other processes. On the other hand, if the quality of the wafer is high enough, the SRH recombination probability is also low compared to the surface recombination probability. This means that, in high quality crystalline silicon wafers, the bulk recombination is negligible against the surface recombination, specially when wafers become thinner (less bulk material). So, assuming that the wafer is symmetrical and that surface processes dominate the recombination, the effective surface recombination velocity (S_{eff}) can be obtained from τ_{eff} as:

$$S_{eff} \cong \frac{W}{2\tau_{eff}} \rightarrow \tau_{eff} \cong \frac{W}{2S_{eff}} \quad (5.4)$$

So, a crucial step in crystalline silicon solar cell technology in order to achieve high efficiency is the reduction of surface recombination, which is called surface passivation. There are two mechanisms to achieve good surface passivation: The first one is chemical passivation, which consists in reducing the quantity of free bonds on the surface by saturation of the interface defects. And the second is field effect passivation, which consists in inducing band bending in order to reduce the concentration of one of the carriers on the surface, and so decreasing the recombination rate [175].

The traditional passivation technique for c-Si surfaces is to provoke thermal oxidation to grow a native silicon oxide (SiO_2) layer on the surface to obtain passivation. However, this technique requires high temperatures which affect negatively to the bulk carrier lifetime and implies

an important thermal budget in the fabrication process [176][177][178][179].

Nowadays, different techniques are being developed and used in passivation, involving the deposition of layers of different materials over the wafer to substitute the native SiO_2 . Some of these materials are hydrogenated amorphous silicon nitride ($\text{a-SiN}_x\text{:H}$) [180][181], hydrogenated amorphous silicon carbide ($\text{a-SiC}_x\text{:H}$) [179], hydrogenated amorphous silicon (a-Si:H) [182][183][184] and alumina (Al_2O_3) [185][186].

5.2 Motivation of the work

The work developed in this chapter has two main blocks. The first is intended to achieve good surface passivation with sputtering deposited alumina layers. Alumina has been gaining relevance in passivation in the last few years as a promising alternative to more traditional technologies and materials. Currently, it is commonly used in HIT structures based on n -type wafers. On the other hand, the use of sputtering to deposit Al_2O_3 would provide some other additional advantages.

The second refers to the development of a p -type emitter, aiming to its use over n -type c -Si wafers. Wafer based solar cells on n -type silicon have recently attracted attention, mainly due to lower recombination related to oxygen contamination. As an example, commercial HIT solar cells (from *Sanyo-Panasonic*) use n -type wafers. However, to develop these structures, the deposition of a p -type emitter is required. Obtaining a quality p -type emitter is challenging, due to the poor doping efficiency of p -doped a-Si:H layers. So, the deposition of p -emitters is an important and complicated step in which the acquired experience in p -type a-Si:H and μc - Si:H optimization can be useful. With these considerations, the motivation for this work is detailed next.

5.2.1 Passivation with alumina deposited by sputtering

5.2.1.1 Al₂O₃ advantages over SiN_x

As it has been explained, one of the ways to reduce surface recombination is the so-called field-effect passivation. It is based on the fact that surface recombination processes involve both electrons and holes. By the application of an internal electric field below the c-Si surface, either the electron or hole concentration can dramatically be reduced at the position of the c-Si surface. The absence of one of the carriers results in a reduction of the recombination.

Alumina has recently been gaining relevance as a novel solution for this type of passivation, as an alternative to other materials like SiN_x. SiN_x has traditionally been used to passivate *n*-emitters diffused in *p*-wafers [180][181][187], as it traps positive charge, which provokes a major concentration of electrons over holes. More recently, SiN_x has also been used to passivate *p*-type emitters in *n*-wafers [178], but the results are not as good as in *n*-emitters, because to achieve passivation in this situation, it is required that the charge in SiN_x is notably higher than the one on the *p*-emitter to create an inversion layer. Still, values of the implied V_{oc} of over 700 mV were obtained.

The use of alumina in passivation has been increasing in the last years because there are two advantages of alumina over SiN_x: The first is that Al₂O₃ layers trap negative charge, thus producing a hole accumulation on the silicon surface [185], which is the opposite situation of SiN_x. This makes Al₂O₃ a more suitable material for the passivation of *n*-type silicon surfaces. The second is that alumina is capable of trap more charge than SiN_x, which makes it easier to create the inversion layer and passivate effectively *p*-type silicon surfaces. These advantages places alumina as a suitable material to achieve good passivation in both *n*- and *p*-type silicon wafer surfaces.

5.2.1.2 Advantages of sputtering over ALD, and the need of an a-Si:H layer

Normally Al_2O_3 layers for passivation are deposited by atomic layer deposition (ALD) [188][189][190], as they have shown the best passivation results (reviewed by Dingermans *et al.*[185]). However, some other techniques have been employed to deposit Al_2O_3 aiming for passivation uses, like pulsed laser deposition (PLD) [191][192], PECVD [186] or catalytic vapor deposition [193]. The UPC has already obtained improved results in rear surface passivation using stacks of layers including alumina deposited by ALD [194].

Sputtered Al_2O_3 has already proved itself as an alternative for wafer passivation [177][195][196][197][198]. The main interest of using Al_2O_3 deposited by sputtering for passivation is that this technique presents some advantages over ALD:

- Sputtering is industrially scalable, so it is already used for large area depositions.
- The deposition rate is higher, which means less time to obtain the required thicknesses. This has special importance in industry.
- The facilities needed for ALD are more expensive than the sputtering ones, specially in large-scale production.

These advantages places sputtered Al_2O_3 as a promising alternative to atomic layer deposited Al_2O_3 . However, deposition by sputtering produces a bombardment with high-energy ions [199] which has been associated with a silicon surface damage. This damage is traduced in the creation of surface defects, which leads to poor passivation results [198].

Assuming this effect, the idea behind this work is to substitute the native SiO_x proposed as physical protection [198] by an intermediate layer of a-Si:H deposited by PECVD that could provide physical protection to the surface from the ion bombardment of the sputtering. Additionally, it could serve as a source of hydrogen atoms that will improve the passivation results, adding a chemical component to the passivation which

5.3 Results in Al₂O₃ passivation: role of an a-Si:H interlayer

is present in ALD.

5.2.2 Development of *p*-type emitters for *n*-type wafers

It has been reported that *n*-type c-Si wafers present several benefits over *p*-type wafers. *n*-wafers are electrically superior, less affected by oxidation [200] and also present less recombination caused by metallic impurities on the surface [201][202][203]. However, despite this advantages, the challenge for the use of *n*-type c-Si wafers in heterojunction technology is the deposition of quality *p*-type emitter, which are technologically more difficult to develop, as it is harder to dope a-Si:H *p*-layers than *n*-layers [38]. Besides, the passivation of *p*-type emitters is also more complicated, although several alternatives are being researched, like the mentioned a-SiC_x:H and Al₂O₃.

The results obtained in *p*-layer optimization (Chapter 3, Sec. 3.4.1) and the previous group experience working with ITO [26] provide a good starting point to develop the whole front side of an *n*-wafer based c-Si device, including the *p*-emitter. The final idea would be to combine the developed *p*-emitter and the passivation with Al₂O₃ to obtain a quality c-Si device based in an *n*-type wafer.

5.3 Results in Al₂O₃ passivation: role of an a-Si:H interlayer

5.3.1 Layer deposition and measurements

The objective of this block of experiments was to study the role of a-Si:H in passivation with sputtered alumina. The procedure to do so was to compare the passivation achieved with sputtered alumina with the one achieved with the use of a stack *ia*-Si:H/Al₂O₃. The wafers used for this experiment were single-side polished *n*-type (1.5 Ω⁻¹cm⁻¹) and *p*-type (2.6 Ω⁻¹cm⁻¹) float zone silicon wafers.

5 Thin film passivation for advanced solar cell structures

First of all, the cleaning process mentioned in Chapter 2, Sec. 2.2.1 is performed over the wafers. Then, they were divided in quarters. Over a quarter of each type of wafer, alumina is directly deposited on both sides. These samples will be known from now on as $n\text{-Si}/\text{Al}_2\text{O}_3$ and $p\text{-Si}/\text{Al}_2\text{O}_3$. Over another quarter of wafer of each type, a very thin (≈ 6 nm) layer of a-Si:H is deposited before the alumina, both materials also on both sides. These samples will be referred to as $n\text{-Si}/\text{a-Si:H}/\text{Al}_2\text{O}_3$ and $p\text{-Si}/\text{a-Si:H}/\text{Al}_2\text{O}_3$. The configuration of the samples are shown in Fig. 5.1.

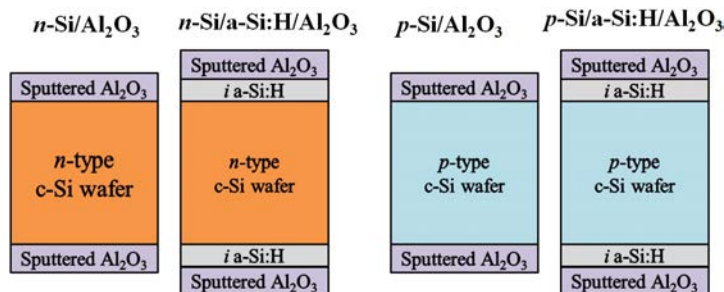


Figure 5.1: Configuration of the samples used for the experiments in passivation with alumina deposited with sputtering. The depositions are symmetrical, so the layers in both sides are almost identical.

The deposition conditions for the thin intrinsic a-Si:H layers used in $n\text{-Si}/\text{a-Si:H}/\text{Al}_2\text{O}_3$ and $p\text{-Si}/\text{a-Si:H}/\text{Al}_2\text{O}_3$ were, in this case, the same used when a-Si:H is used as absorber layer (Chapter 3, Sec. 3.3.1). These layers were deposited in the UB PECVD reactor described in Chapter 2, Sec. 2.1.1. The deposition time was calculated so the layers had a thickness of about 6 nm. As far as the alumina is concerned, it was deposited in the UB magnetron sputtering described in Chapter 2, Sec. 2.1.2, and the estimated thickness was approximately 50 nm. The chemical and structural characteristics of the used alumina were obtained by different measurements, but they are out of the aim of this section, and can be consulted elsewhere [204]. A summary of the deposition conditions for both materials is shown in Table 5.1.

5.3 Results in Al_2O_3 passivation: role of an a-Si:H interlayer

Table 5.1: Deposition parameters for intrinsic silicon layers and alumina layers used in passivation results. a-Si:H is deposited by PECVD and Al_2O_3 by sputtering.

| Intrinsic a-Si:H | |
|---------------------------|--|
| Pressure | 80 Pa |
| Substrate temperature | 200 °C |
| Power | 4 W (≈ 33 mW/cm ²) |
| Silane flow | 40 sccm |
| Electrode distance | 15 mm |
| Time | 30 s (estimated thickness ≈ 6 nm) |
| Background pressure | $< 2 \cdot 10^{-5}$ Pa |
| Alumina | |
| Pressure | 0.667 Pa |
| Substrate temperature | Room temperature |
| Power | 300 W |
| Argon flow | 12 sccm |
| Target-substrate distance | 12 cm |
| Time | 38 min (estimated thickness ≈ 50 nm) |
| Background pressure | $\approx 3.3 \cdot 10^{-4}$ Pa |

The passivation was evaluated by effective carrier lifetime measurements, which were performed at the UPC with the *Sinton WCT-120*. Both the equipment and the procedure to obtain the parameters are described at Chapter 2, Sec. 2.3.4. As first, the four silicon quarters of wafer samples, with the passivation layers in 'as deposited state', presented a very short τ_{eff} of the minority carriers. However, previous experiments [63] showed that an important increment of τ_{eff} is achieved in the samples after an annealing process. The conditions of the annealing process were previously optimized [63], obtaining the best results with a temperature of 350°C during 20 to 25 minutes in forming gas.

So, this annealing process was performed and τ_{eff} measured again in the 'annealed state'. Fig. 5.2 shows the τ_{eff} of the samples as a function of the excess carrier density (Δn). It can be observed that the samples which the a-Si:H layer deposited before the alumina show quite higher

carrier lifetime than the ones without it in all the range of carrier injection analyzed.

Assuming that τ_{eff} is mainly limited by surface recombination as it has been explained, knowing the wafer thickness and assuming that similar passivation occurs on both sides, it is possible to estimate the effective surface recombination velocity for all the illumination levels according to Eq. 5.4. The graphs of S_{eff} versus Δn are also presented in Fig. 5.2.

The implied open circuit voltage has also been obtained from the measurements in the annealed samples, and its values are also evaluated. Table 5.2 summarizes the values of these parameters under one sun illumination, obtained from the figure.

Table 5.2: Effective lifetime, implicit open circuit voltage and effective surface recombination velocity of the minority carriers for the annealed samples under one sun illumination.

| Sample | τ_{eff} (ms) | $ImpV_{oc}$ (mV) | S_{eff} (cm/s) |
|--|-------------------|------------------|------------------|
| <i>n</i> -Si/Al ₂ O ₃ | 0.082 | 613 | 172 |
| <i>n</i> -Si/a-Si:H/Al ₂ O ₃ | 1.415 | 740 | 9.9 |
| <i>p</i> -Si/Al ₂ O ₃ | 0.043 | 618 | 329 |
| <i>p</i> -Si/a-Si:H/Al ₂ O ₃ | 1.252 | 741 | 5.5 |

5.3.2 Discussion, conclusions and perspectives

To summarize, it has been exposed that direct Al₂O₃ passivation of silicon surfaces has proved itself capable of very high lifetimes; being the most successful deposition technique ALD, which reached lifetimes higher than 1 ms in high quality wafers with doping levels in the order of 1 Ω cm [177]. Although the results for sputtering-deposited Al₂O₃ [176] show good passivation, they are generally worse than those reported for ALD-deposited Al₂O₃ [177]. Two possible differences between the ALD and sputtering techniques can be relevant to the superior surface

5.3 Results in Al_2O_3 passivation: role of an *a*-Si:H interlayer

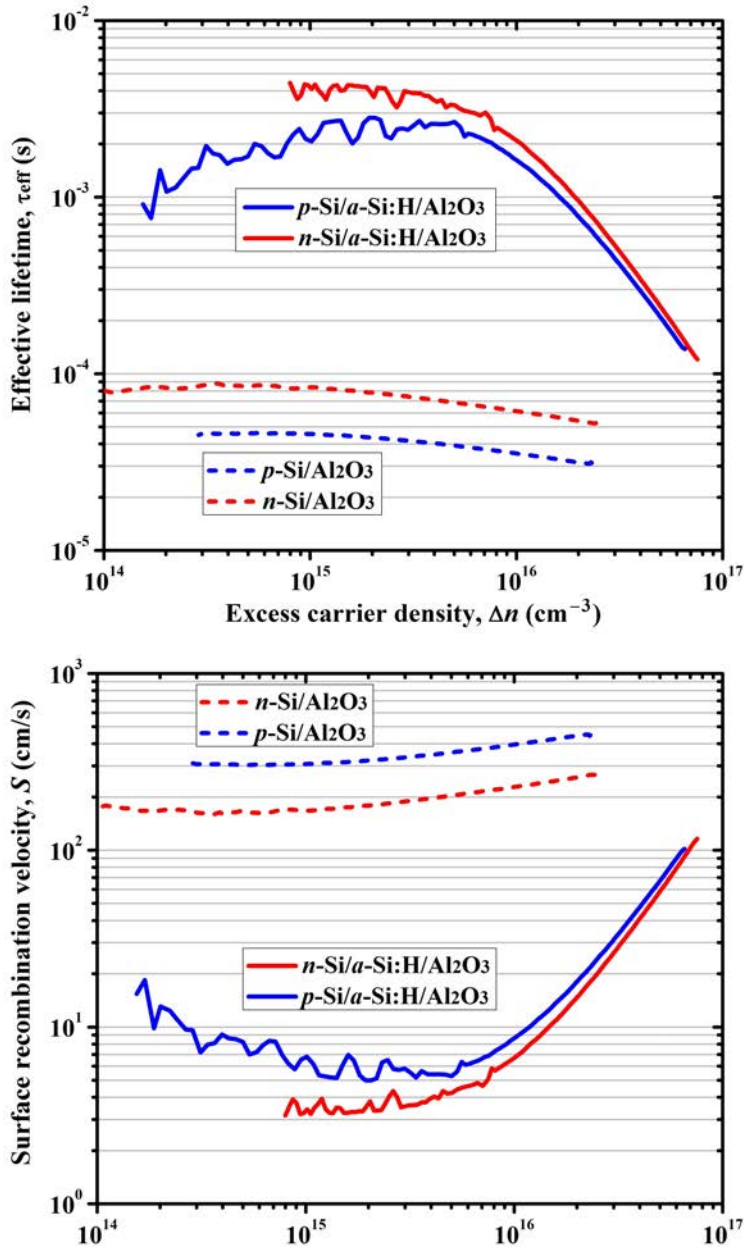


Figure 5.2: Effective lifetime (top) and effective surface recombination velocity (bottom) of *p*-Si and *n*-Si samples passivated with Al_2O_3 and *a*-Si:H/ Al_2O_3 layers after the annealing at 350°C .

passivation of ALD. The first one is the high energy bombardment of the silicon wafer surface by argon ions during the sputtering process, not present in ALD deposition. The second one is the presence of hydrogen in the precursor gases used for ALD, which can lead to chemical passivation of the silicon wafer surfaces. The objective in the presented experiments was to test if introducing a very thin a-Si:H could overcome this problems.

It can be observed that the wafers protected with an a-Si:H layer before the Al_2O_3 deposition present significantly higher carrier lifetimes than the samples without such silicon layer. The use of an intrinsic a-Si:H intermediate layer avoids the damage on the wafer surface due to direct argon ion bombardment. Also, it could be acting as a source of hydrogen for the chemical passivation of the silicon surface, overcoming the absence of hydrogen in sputtering compared to ALD. This means that the deposition of the a-Si:H thin layer immediately after cleaning the silicon wafers covers two deficiencies of the Al_2O_3 layer deposited by sputtering: surface protection, that makes less critical the damage of the ion bombardment, and chemical passivation with hydrogen, which is absent in the sputtering process.

It is also interesting to deal on the relevance of the thermal treatment to reach good passivation. This requirement is common for passivation with Al_2O_3 and it is independent of the deposition technique. It has as function to charge the defects of the Al_2O_3 layer, increasing the passivation caused by charge accumulation. On the other hand, it is well known that temperatures around 300 to 350°C for 20 minutes periods allow an efficient diffusion of hydrogen without resulting in a significant hydrogen effusion from the surface that would take place at higher temperatures. As a consequence, a possible explanation of the increase of the lifetime after the thermal annealing (in addition to the Al_2O_3 defects charge) is the hydrogen passivation of defects in the silicon surface by its diffusion movement and bonding to the surface defects.

The main conclusion that can be extracted is that the inclusion of a very thin layer of a-Si:H before the deposition of the alumina by sputtering allows to obtain values of the effective lifetime of more than 1 ms, although these values are still a little lower than the ones obtained

5.4 Results in *p*-type hetero-emitter development

with alumina deposited by ALD. This role of a-Si:H as protective layer is very promising, not only combined with Al₂O₃ passivation, but also in contacting with doped layers. New manufacturing approaches for heterojunctions solar cells then appear by using very thin a-Si:H interlayers. The developed techniques only make use of low-temperature (<400°C) processes and provide flexibility to select the ratios between the surfaces used for contacting or for passivation, thus reducing the requirements of the deposition and patterning process thanks to the protection of the full surface of the silicon wafer with the a-Si:H layer.

Additional experiments are required to evaluate the contribution of each passivation mechanism: chemical and field effect passivation. New experiments to study the dependence of passivation on a-Si:H interlayer thickness are planned and will be the object of future research.

5.4 Results in *p*-type hetero-emitter development

The objective of this section was to develop the whole front part of an *n*-type c-Si wafer solar cell based on the group experience with the involved layers: ITO was studied in previous group work [26] and the silicon layers were optimized for thin film a-Si:H solar cells in Chapter 3. With these results as starting point, several experiments with the layers (both individually and combined) were developed aiming to adapt and optimize their characteristics to c-Si technologies, and form a quality *p*-type emitter.

5.4.1 Indium tin oxide optimization

Indium tin oxide (ITO) is a transparent conductive oxide (TCO) composed of In₂O₃ doped with SnO₂, which is commonly used in thin film silicon solar cells as front electrode. ITO presents both high conductivity and transparency. In fact, its properties initially place it as a better material than ZnO for this role, but ITO has one important drawback which is the expensiveness of indium [205]. However, ITO is still the best option in many situations because it can be deposited at room temperature without a significant loss in its properties. For example, the front contact

of ZnO:Al deposited at the University of Barcelona is optimized at 300°C [26] which makes it not suitable for its use in substrate configuration in thin film solar cells.

In this case, the experiments aimed to obtain quality ITO to be used as front electrode in c-Si wafer based devices. Previous experiments at the UPC revealed that the effective carrier lifetime and the implicit V_{oc} of the devices tend to decrease when the ITO is deposited over them [63]. The objective was to reduce this loss by depositing ITO at different conditions, trying to obtain the most suitable material. The ITO has to serve also as anti-reflective coating, in order to minimize the reflection, according to Eq. 5.1. If $n = 1.87$ is assumed for ITO [206] and a wavelength of 600 nm is selected, the desired thickness is about 80 nm. Also, the possibility of developing the whole front side of the cell (emitter+ITO) at the same cleanroom is very attractive in order to avoid any accidental contamination.

5.4.1.1 Optimization over glass

Before the trials over wafer were developed, two series of ITO films were deposited on Corning 1737 glass and analyzed, aiming to optimize the transparency and de conductivity of the material. The first series was in oxygen partial pressure, which is calculated as:

$$p_{O_2} = p \frac{\Phi_{O_2}}{\Phi_{Ar} + \Phi_{O_2}} \quad (5.5)$$

where p is the total pressure and Φ_{Ar} and Φ_{O_2} are the argon and oxygen flow respectively. The total pressure and the argon flow were kept constant in all the samples, so the parameter that is used to vary the oxygen partial pressure is the oxygen flow. It is known that adding oxygen to the sputtering plasma leads to more transparent TCOs, but on the other hand, they are also less conductive, so it is necessary to find a compromise between these properties. This is why the partial pressure series was developed.

5.4 Results in *p*-type hetero-emitter development

Table 5.3: Deposition parameters for indium tin oxide layers. The bold quantity in varying parameters is the one kept constant in the other series.

| | |
|-----------------------------------|---|
| Fixed parameters | |
| Pressure p | 0.173 Pa |
| RF Power P | 100 W |
| Subs.-Electrode distance d_e | 15.5 cm |
| Background pressure Bp | $<5 \times 10^{-4}$ Pa |
| Varying parameters | |
| Oxygen partial pressure p_{O_2} | 0, 2.98, 4.91 , 6.93, 8.91 mPa |
| Temperature T | Room T (≈ 20), 100, 200 °C |

The second series was made varying the substrate temperature. The starting point was the conditions used in previous group work which are shown in Table 5.3. In this table, the values for the varying parameters are also shown, with p_{O_2} already calculated with the corresponding values of Φ_{O_2} . Radio frequency plasma (RF) was used and the composition of the target is shown in Table 2.2 (Chapter 2, Sec. 2.1.2). For the oxygen partial pressure series, the deposition time is fixed at 30 minutes while in the temperature series the time was reduced to 24 minutes. The ITO deposited in the UPC was used as comparative reference was deposited at room temperature, 50 W of power, 40 sccm of Ar flow and with no intentional additional oxygen. The sheet resistance is about 100 Ω_{sq} for 80 nm.

The first measured parameters were the thickness and the sheet resistance. The thickness was used to calculate the deposition rate, in order to make possible to calculate the time necessary to obtain an ARC in future depositions. The films deposited in these series resulted slightly thicker than the mentioned 80 nm. Then, as second parameter, the resistivity ρ was obtained through the measured sheet resistance R_{sh} through the equation 2.7 (Chapter 2, Sec. 2.3.3.2).

The last parameter used to test the quality of the ITO is the transmittance, which is evaluated by integrating the area under the curve in

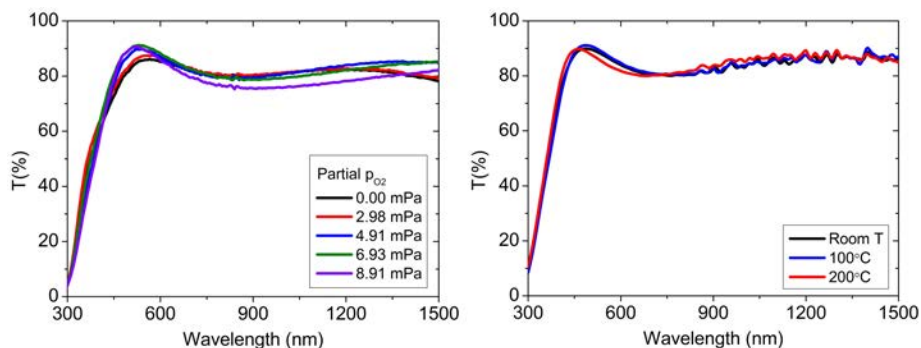


Figure 5.3: Transmittance of the ITO samples of the partial pressure series (left) and temperature series (right).

the wavelength regions relevant for solar cells. These are 400-800 nm, which corresponds to the absorption wavelengths for amorphous silicon; and 400-1100 nm, which corresponds to crystalline and microcrystalline silicon. Although both results are shown, in fact only the second one would be necessary, as the layer is bound to be deposited over a crystalline silicon device.

The measured transmittances for the oxygen partial pressure and temperature series are shown in Fig. 5.3. In the partial pressure series, it can be seen that the samples with low oxygen contents are less transparent than the ones with higher content, as it was expected, except the one with highest content which presents the worst behavior. In the temperature series, the difference between samples is quite smaller.

Table 5.4 summarizes both series results, and some of the parameters are plotted in Fig. 5.4 to make the comparison between the samples easier.

5.4 Results in *p*-type hetero-emitter development

Table 5.4: Summary of the results of the measured parameters in ITO series. The deposition times for p_{O_2} and temperature series are 30 min and 24 min respectively.

| p_{O_2} (mPa) | d (nm) | R_d ($\frac{nm}{min}$) | R_{sq} (Ω_{sq}) | ρ (Ω cm) | $\%T_a$ | $\%T_{\mu c}$ |
|-----------------|----------|----------------------------|----------------------------|-----------------------|---------|---------------|
| 0.00 | 130 | 4.33 | 34 | $4.42 \cdot 10^{-4}$ | 80.52 | 80.61 |
| 2.98 | 130 | 4.33 | 35 | $4.42 \cdot 10^{-4}$ | 81.84 | 81.46 |
| 4.91 | 135 | 4.50 | 35 | $4.73 \cdot 10^{-4}$ | 82.21 | 81.42 |
| 6.93 | 140 | 4.73 | 58 | $8.12 \cdot 10^{-4}$ | 83.77 | 81.87 |
| 8.91 | 150 | 5.00 | 220 | $3.34 \cdot 10^{-3}$ | 81.55 | 79.18 |

| T ($^{\circ}C$) | d (nm) | R_d ($\frac{nm}{min}$) | R_{sq} (Ω_{sq}) | ρ (Ω cm) | $\%T_a$ | $\%T_{\mu c}$ |
|---------------------|----------|----------------------------|----------------------------|-----------------------|---------|---------------|
| RT | 118 | 4.92 | 45 | $5.31 \cdot 10^{-4}$ | 83.63 | 83.35 |
| 100 | 114 | 4.75 | 39 | $4.45 \cdot 10^{-4}$ | 84.16 | 83.70 |
| 200 | 107 | 4.46 | 34 | $3.63 \cdot 10^{-4}$ | 83.21 | 83.87 |

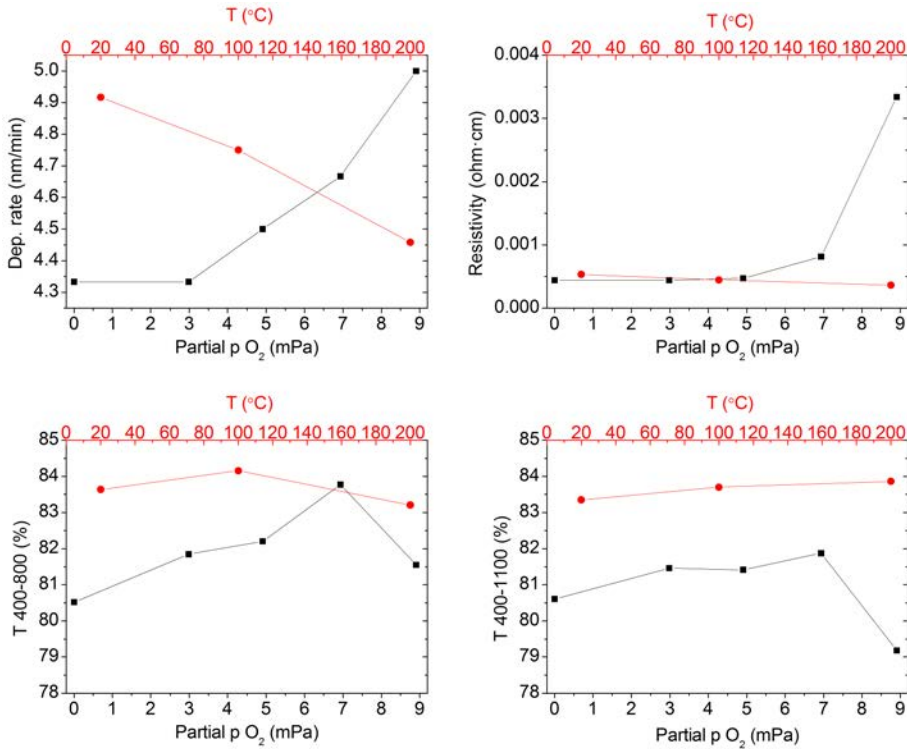


Figure 5.4: Parameter comparison for both oxygen partial pressure (black) and temperature (red) series. $\%T_a$ and $\%T_{\mu c}$ is the percentage of the area integrated under the curve of the *EQEs*.

As far as oxygen partial pressure is concerned, it is clear that there is a direct relation between $\sigma_{DC}\sigma_{OP}$ and resistivity and transmittance: increasing oxygen quantity leads to an increase of the transmittance, which is desirable, but also there is an increase of the resistivity, which is not. This behavior was expected as it has been previously reported both in ITO [207] and on other TCOs [208][209], including the research on ZnO developed in this group [26]. The last sample shows worse properties than all the others, which suggest that including oxygen further than certain point is detrimental for the layers. As the idea was to get the best layer, a balance between conductivity and transmittance had to be reached. In this work, the figure of merit 'electrical to optical conductivity'[210] is used as reference parameter. It is defined as:

$$\frac{\sigma_{DC}}{\sigma_{OP}} = \frac{118.5}{R_{sh}(T^{-1/2} - 1)} \quad (5.6)$$

In this case, the samples of the partial pressure series (0, 2.98, 4.91, 6.93, 8.91 mPa) show values of σ_{DC}/σ_{OP} of 48.7, 49.8, 50.1, 30.9 and 6.9 Ω^{-1} . This places the central sample (4.91 mPa of p_{O_2}) as the best option, although the difference with some of the other samples is not very big.

On the other hand, looking at the results of the temperature series, it can be observed that the dependence in this range of temperatures is very slight. It would be possible to obtain different results if the temperature was raised up to 300°C or more [211] but as the layers are going to be deposited over devices, it is not possible to further raise the temperature as it could affect the previously deposited materials. As a clear optimal temperature was not found in this kind of trial over glass, it was determined that all three temperatures would be tested over device to check which one offered better performance.

5.4.1.2 ITO deposited over devices

To check the behavior of the different ITOs in a c-Si device, a structure developed at the UPC was used but varying the ITO deposited in the front side of the cell. First, in the UPC, an *n*-type emitter was deposited in the front side of a *p*-type c-Si wafer; and a 30 nm thick intrinsic

5.4 Results in p -type hetero-emitter development

passivating layer and a 70 nm $a\text{-SiC}_x$ layer were deposited in the rear side. The wafer was divided in four quarters and, at this point, the first measurement of the carrier lifetime was done. After, different ITO layers (standard UPC's at RT and UB's at room temperature, 100°C and 200°C) were deposited over each quarter, and τ_{eff} was measured again. Then, all the samples underwent an annealing process at 160°C in air during 1 hour, and the last measurements of τ_{eff} were taken. Finally, the active area was delimited by lithography, the grid for the front contacts was made and an aluminum back reflector was deposited and the rear contacts were made by laser firing. The finished structures were characterized by measuring the J - V curve and the EQE of square 1×1 cm² cells. The process is shown in Fig. 5.5.

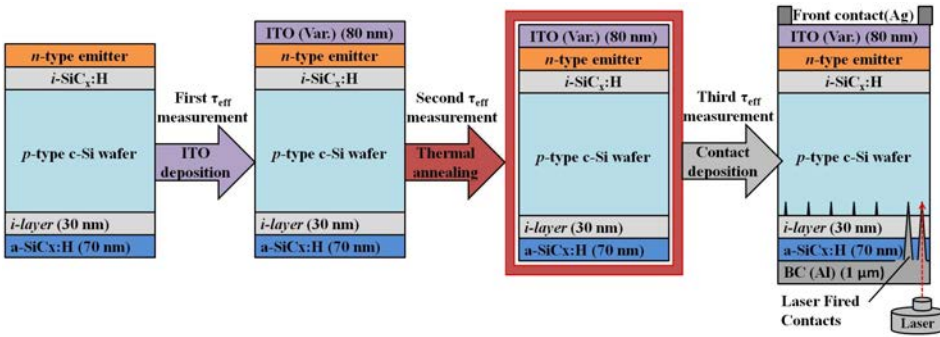


Figure 5.5: Evolution of the structure of the device used for ITO optimization in the different stages of measurement.

The results of the effective carrier lifetime measurements are shown in Table 5.5. The first thing that is noticed is that after the emitter is deposited a dispersion is found in the effective lifetimes measured in each quarter of the wafer. Although the emitter is the same, maybe there is some inhomogeneity in the deposition that provokes these differences. Anyway, they are not very big so a similar 'initial' state can be considered.

Then, it can be observed that there is an important drop of the properties just after the ITO is deposited, but when the samples are

5 Thin film passivation for advanced solar cell structures

Table 5.5: Summary of the results of the measured parameters in ITO over devices in the three stages of deposition (see Fig. 5.5). From top down: as the emitter is deposited, as the ITO is deposited over the emitter and after the thermal annealing (1 h at 160°C in air). The name of the sample refers itself to the quarter of the same wafer over which each ITO is deposited (the center and the temperature of deposition are detailed).

| Emitter as deposited | | | |
|----------------------|---------------------|-----------------|--------------|
| Sample | $\tau_{eff}(\mu s)$ | $S_{eff}(cm/s)$ | $V_{oc}(mV)$ |
| UPC@RT | 890 | 15.89 | 714.3 |
| UB@RT | 833 | 16.98 | 710.8 |
| UB@100°C | 828 | 17.08 | 712.0 |
| UB@200°C | 852 | 16.61 | 712.9 |

| After ITO deposition | | | |
|----------------------|---------------------|-----------------|--------------|
| Sample | $\tau_{eff}(\mu s)$ | $S_{eff}(cm/s)$ | $V_{oc}(mV)$ |
| UPC@RT | 34.9 | 405.44 | 610.0 |
| UB@RT | 391 | 36.18 | 686.5 |
| UB@100°C | 470 | 30.11 | 693.9 |
| UB@200°C | 672 | 21.05 | 707.4 |

| With ITO after annealing | | | |
|--------------------------|---------------------|-----------------|--------------|
| Sample | $\tau_{eff}(\mu s)$ | $S_{eff}(cm/s)$ | $V_{oc}(mV)$ |
| UPC@RT | 896 | 15.79 | 715.4 |
| UB@RT | 975 | 14.51 | 717.5 |
| UB@100°C | 718 | 19.70 | 718.8 |
| UB@200°C | 896 | 15.79 | 718.2 |

measured after the annealing, the properties recover in a different degree. This effect is less evident as the temperature of deposition grows, this is, the higher the deposition temperature of the ITO the lower the loss after deposition.

Although it has been reported that ITO suffers different changes on its properties after different annealing conditions [212][213], this happens at

5.4 Results in *p*-type hetero-emitter development

higher temperatures. This means that the annealing process affects the amorphous silicon *n* layer or the interface between them. The reason for this could be that the dopant atom activation of the emitter, normally achieved by annealing, is accomplished during the ITO deposition at higher temperatures. This suggests that depositing the ITO at higher temperatures could lead to the possibility of avoiding later annealing. However, going to higher temperatures could affect the existing layers, and also the loss on τ_{eff} should have to be overcome.

Analyzing the effect of the temperature of deposition of the ITO, it can be observed that although higher temperatures caused less reduction in τ_{eff} , after the annealing was done, the sample with the ITO deposited at room temperature shows the higher value of τ_{eff} (0.975 ms), with 0.1 ms over the next sample. So, as far as the temperature optimization is concerned, the best option is to deposit the ITO at room temperature and then perform a thermal annealing.

If the behavior of UPC's and UB's ITOs samples is compared, it can be noticed that although the quarter of wafer on which the UPC ITO was deposited had initially higher τ_{eff} , it experienced higher loss after the deposition of the ITO and, which is more important, the final value of τ_{eff} in the sample with this material is almost 0.1 ms lower than the one obtained with the best sample with UB's ITO. The final $ImpV_{oc}$ is almost equal in both samples. These results point to the ITO deposited in the UB as the most suitable material to be used in the front contact.

To verify this result, a final test was made finishing the devices, implementing the punctual back contacts by diffusing aluminum by laser firing (LFC) and measuring the parameters of the finished solar cell. The distance between contacts (also called fingers), normally called pitch, is varied, being used 800 and 600 μm in different areas of the quarter of the wafer. Then, *J-V* and *EQE* measurements were developed at the UPC for 1 cm^2 cells with different pitch distances. The values for the best cell with each pitch are shown in Table 5.6.

5 Thin film passivation for advanced solar cell structures

Table 5.6: Values of the parameters of the best solar cells (1 cm^2) with different ITOs for each finger pitch.

| Sample | UPC@RT | | UB@RT | | UB@100°C | | UB@200°C | |
|--------------------------------|--------|-------|-------|-------|----------|-------|----------|-------|
| | 800 | 600 | 800 | 600 | 800 | 600 | 800 | 600 |
| V_{oc} (V) | 0.635 | 0.625 | 0.635 | 0.626 | 0.630 | 0.623 | 0.632 | 0.624 |
| J_{sc} (mA/cm ²) | 31.11 | 31.13 | 33.61 | 33.27 | 31.87 | 31.97 | 32.48 | 32.01 |
| FF | 0.593 | 0.599 | 0.680 | 0.699 | 0.691 | 0.705 | 0.678 | 0.704 |
| η (%) | 11.72 | 11.65 | 14.51 | 14.53 | 13.86 | 14.01 | 13.91 | 14.01 |

First, a comparison between pitch lengths was established: J_{sc} behavior is variable but without big differences. As far as V_{oc} is concerned, the samples with 800 nm of pitch show higher values. However, the FF is always lower than the one found for 600 nm of pitch. So, the efficiencies are higher for the 600 nm samples (except for the UPC sample) but with differences under 0.16%.

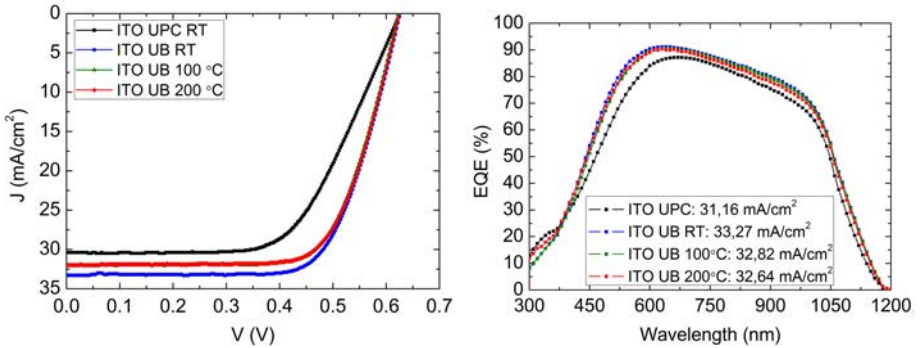


Figure 5.6: J - V and EQE curves for the 600 nm pitch samples with different ITOs. The values on the legend in the EQE s graph are the integrated J_{sc} for each sample.

In order to easily compare the performance of the different ITOs, Fig. 5.6 shows the J - V and EQE curves of the best sample of 600 nm of pitch (as this length has proved itself better). The integrated current values

5.4 Results in *p*-type hetero-emitter development

(weighed with the solar spectrum) are also shown in the legend of the *EQE* graph.

Looking both the graphs and the values of the parameters in Table 5.6 it is clear that all three samples with ITO deposited at UB are better for the performance of the cells, in spite of the previous measurements of τ_{eff} which were lower in the case of the samples deposited at 100 and 200°C. The main reason is that the cell with ITO deposited at the UPC presents much higher series resistance than the cells with ITO deposited at UB. The short circuit current is also lower. Among the devices deposited at the UB, the cell with ITO deposited at room temperature shows higher J_{sc} , which is consistent with the result obtained for the measured τ_{eff} . These improvements in R_s (which is traduced in a 0.1 absolute increase in *FF*) and J_{sc} results in an absolute efficiency increase of almost 3% in the cell with UB's ITO at RT (14.53%) over the one with ITO deposited at the UPC (11.65%).

However, even the cells with the ITO deposited in the UB present an high series resistance, probably due to a very high sheet resistance. A possible solution would be to further raise the deposition temperature. It is known that the conductivity of ITO is much improved when the deposition temperature is about 300°C, because the layer is microcrystalline instead of amorphous. Some commercial devices use TCOs deposited at these higher temperatures. So, probably higher deposition temperatures could reduce the sheet resistance to the range of 8 Ω , which the requirement for low series resistance.

5.4.1.3 Conclusions

The ITO deposited at the UB has proved itself a better material to finish the devices than the ITO deposited at the UPC, mainly due to its lower series resistance in the devices. The optimization of the material over glass showed that it had the potential to achieve this goal, and then, the trials over completed devices showed that a gain of almost 3% in absolute efficiency is obtained. As far as the temperature optimization is concerned, the ITO deposited at room temperature is finally the best

option, as it presents higher carrier lifetime after the annealing, which is traduced in higher short circuit current in the device. The fact that device quality ITO can be developed at UB offers the possibility of depositing the p -type emitter and the ITO in the same cleanroom, which is very useful to avoid contamination.

5.4.2 Silicon layers optimization

5.4.2.1 Deposition temperature of the p -doped layers

The p layer optimization developed in Chapter 3, Sec. 3.4 was developed aiming use the material for doped layers in a-Si:H solar cells, so the temperature was limited to 200°C. However, for emitter over c-Si wafers purposes, the temperature can be raised to try to obtain better values for some parameters. For this experiment, the tried temperatures were 200°C (reference), 250°C and 300°C for both types of p layer (amorphous and microcrystalline). The rest of the deposition conditions remained equal to those exposed in the mentioned sections, but the time is increased to 30 min. These conditions are summarized in Table 5.7. The layers were deposited over Corning 1737F glass.

Table 5.7: Deposition parameters for p -doped a-Si:H and μc -Si:H layers in the temperature optimization.

| Parameter | Amorphous | Microcrystalline |
|-----------------------------------|----------------------|----------------------|
| Substrate temperature (°C) | 200, 250, 300 | 200, 250, 300 |
| Pressure (Pa) | 80 | 400 |
| Power (W) | 4 | 30 |
| Electrode distance (mm) | 15 | 15 |
| Background pressure (Pa) | $<5 \cdot 10^{-4}$ | $<5 \cdot 10^{-4}$ |
| Silane flow (sccm) | 2.6 | 0.5 |
| C ₄ flow (sccm) | 2.1 | 0 |
| TMB flow (sccm) | 40 | 3 |
| H ₂ flow (sccm) | 0 | 198 |

5.4 Results in *p*-type hetero-emitter development

The developed characterization was the same made for the previous optimization, this is, measurements of the conductivity, which should be enhanced, and the activation energy and absorptance, which should be minimized. Fig. 5.7 shows the evolution of these parameters for both types of material.

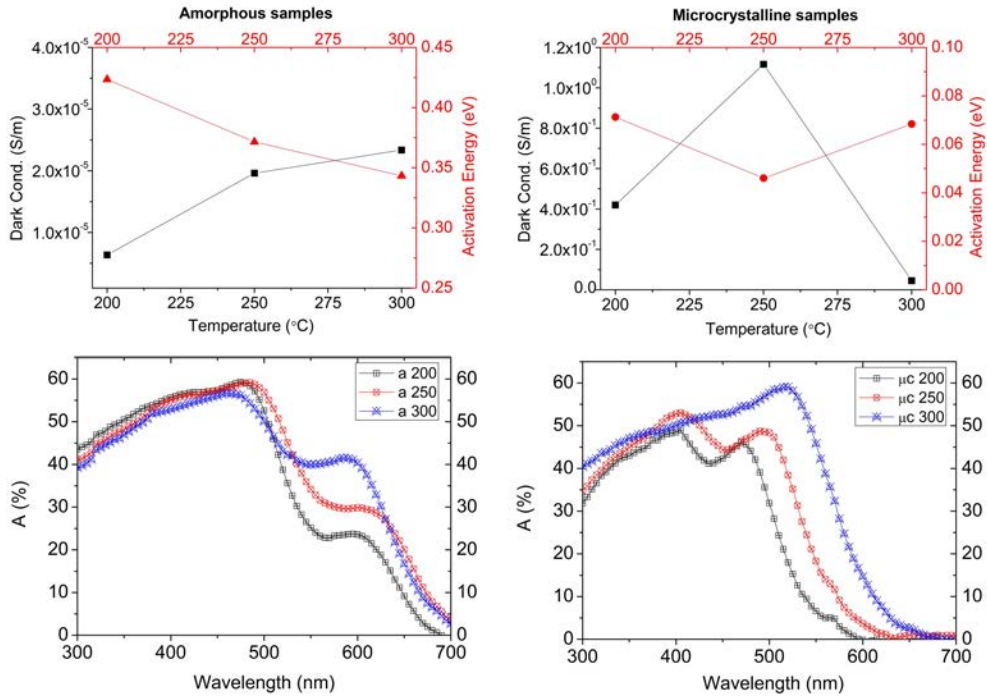


Figure 5.7: Values of the dark conductivity and activation energy with the temperature (top) and absorbances (bottom) of the amorphous (left) and microcrystalline (right) layers used in the temperature optimization for emitters.

The values of the measured parameters are summarized in Table 5.8. As far as the conductivity and activation energy are concerned, it can be observed that the microcrystalline sample has an optimal point at 250°C, in which σ shows a maximum and E_a a minimum. In the case of the amorphous sample, the best parameters are found at 300°C. However,

Table 5.8: Parameters obtained from the measurements of the p -doped layers over 1737 Corning glass.

| p -doped amorphous silicon | | | | |
|------------------------------|----------|----------------|-----------------------|------------|
| T ($^{\circ}\text{C}$) | d (nm) | R_d (nm/min) | σ_{dark} (S/m) | E_a (eV) |
| 200 | 180 | 6.00 | 6.38×10^{-6} | 0.423 |
| 250 | 190 | 6.33 | 1.96×10^{-5} | 0.371 |
| 300 | 230 | 7.67 | 2.34×10^{-5} | 0.343 |

| p -doped microcrystalline silicon | | | | |
|-------------------------------------|----------|----------------|-----------------------|------------|
| T ($^{\circ}\text{C}$) | d (nm) | R_d (nm/min) | σ_{dark} (S/m) | E_a (eV) |
| 200 | 125 | 4.17 | 0.420 | 0.071 |
| 250 | 145 | 4.83 | 1.117 | 0.046 |
| 300 | 175 | 5.83 | 0.045 | 0.068 |

the difference between the 250 $^{\circ}\text{C}$ and 300 $^{\circ}\text{C}$ amorphous samples is not very big. The fact that amorphous layer is less critical in the emitter and the important amount of time that is saved if both depositions are made at the same temperature point led to choose 250 $^{\circ}\text{C}$ as the optimal temperature to develop both depositions. If the absorptance is checked, some differences are appreciated between the layers, but they are not very large and are probably due to the thickness difference between layers. To check this, the thicknesses were measured and, as expected, the thicker samples showed the higher absorptance values. For future layers, the deposition rate has to be taken in account in order to obtain the desired thickness.

5.4.2.2 Silicon layers thickness optimization for the p -emitter

Just like when it is used as doped layer for a-Si:H solar cells, the thicknesses of the p -layers used for the emitters must be optimized by reducing the thickness as much as possible to avoid absorption while keeping the highest possible V_{oc} . In this case, as two layers are used, the thickness of both of them combined has to be optimized. To evaluate

5.4 Results in p -type hetero-emitter development

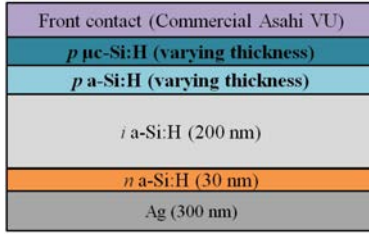


Figure 5.8: Structure of the a-Si:H solar cell used to optimize the thicknesses of the p -layers.

this, the procedure was to deposit a standard a-Si:H solar cells in which the p -doped layer was substituted by a stack formed by a $p \mu\text{c-Si:H}$ layer and a $p \text{a-Si:H}$ layer, whose thicknesses were varied. The rest of the layers were equal to those in the optimized cell in Chapter 3. As the experiment aims for direct comparison, no TCO is deposited in the back reflector of the cells in order to save time by avoiding some steps. The resulting cell structure is shown in Fig. 5.8. The deposition times for the layers and the estimated thicknesses are shown in Table 5.9.

Table 5.9: Deposition times for both amorphous and microcrystalline p -layers, and its corresponding estimated thicknesses. The name references the deposition times (min) of the layers.

| Sample | t for μc (min) | $\approx d$ for μc (nm) | t for a(min) | $\approx d$ for a(nm) |
|--------|-----------------------------|------------------------------------|----------------|-----------------------|
| 41 | 4 | 19.33 | 1 | 6.33 |
| 405 | 4 | 19.33 | 0.5 | 3.17 |
| 21 | 2 | 9.67 | 1 | 6.33 |
| 205 | 2 | 9.67 | 0.5 | 3.17 |

The parameters extracted from the J - V and EQE curves measured in these cells are presented in Table 5.10. As they have been developed without TCO in the back reflector, the cells are not very performing, as J_{sc} and FF values are very low. However, as the cells are being used to

5 Thin film passivation for advanced solar cell structures

Table 5.10: Characteristic parameters and integrated transmittance values of the a-Si:H solar cells with the varying thicknesses of the amorphous and microcrystalline p -layers in the stack. $\%EQE_{400-800}$ and $\%EQE_{400-550}$ correspond to the percentages of the areas integrated under the curves of the $EQEs$ in the specified range.

| Sample | V_{oc} (V) | J_{sc} (mA/cm ²) | $\%EQE_{400-800}$ | $\%EQE_{400-550}$ |
|--------|--------------|--------------------------------|-------------------|-------------------|
| 41 | 0.866 | 6.410 | 28.99 | 39.22 |
| 405 | 0.875 | 6.972 | 30.55 | 48.68 |
| 21 | 0.864 | 5.801 | 25.49 | 31.80 |
| 205 | 0.875 | 6.670 | 30.50 | 43.88 |

test the possible emitters, the crucial parameters to evaluate are the V_{oc} and the quantity of light absorbed by the p -layer.

As it can be observed, the V_{oc} is quite high in all the samples, even higher than the one found in the standard a-Si:H solar cell developed in Chapter 3. On the other hand, the current is much lower, and not only because the loss caused by the lack of TCO in the BR. There is also an important difference in the blue part of the spectrum, as the integration of the area in the 400-550 nm zone is normally about 65%, while here is about 50% in the best case.

As far as the amorphous layer is concerned, it can be observed that the cells with 0.5 min amorphous layers are better in all the parameters by an important difference. The reason for the absorption loss in the blue part is clear, as a thicker layer absorbs more photons. For the voltage loss, the reason might be a higher screening effect on the μc layer contribution to the V_{oc} .

So, focusing on the samples with thinner amorphous layers, the voltage is equal in both of them, which means that the thickness limit to maintain the V_{oc} is still not reached. However, unlike before, the cell with the thicker microcrystalline layer presents higher values of J_{sc} and integrated EQE in the blue part. This was not expected, as normally

higher absorption is produced in thicker layers. One possible reason for this behavior is that as microcrystalline silicon grows in conical shape [214][215][216], if the layer is not thick enough, the microcrystalline grains may not form a path and the properties of the layer are poorer, presenting a loss in the conductivity and so in the J_{sc} of the cell.

There are several conclusions to be extracted from this experiment: the first is that looking at the voltage values, all combinations are potentially usable as emitters, being the 405 sample (4 min of microcrystalline and 0.5 min of amorphous) the best among them. However, as the thickness limit for the V_{oc} is not reached and the absorption on the *p* layer is still high, it would probably be possible to further optimize the thicknesses of the stack. Anyway, to really evaluate the performance of the stack as emitter, it has to be tested and optimized over wafer devices.

5.4.2.3 First trials of complete *p*-type emitter

After previous experiments with ITO and *p* layers were developed and their quality was considered enough, the first trials of emitters completely deposited at the UB could be developed. The structures used for *p*-emitter trials are a combination of HIT (front part) and PERC (rear part) structures (Chapter 1, Sec. 1.2.3.2). They are shown in Fig. 5.9.

First, the rear passivating stack (which is different depending on the type of wafer) was deposited in the UPC over flat polished wafers of both *p* and *n* type. Then, the *p*-emitters with the optimized materials and thicknesses were deposited in the UB. The structure of the deposited emitter consisted in an intrinsic a-S:H layer of about 6 nm deposited at 200°C, a *p*-doped a-Si:H layer of about 3.2 nm deposited at 250°C and a *p*-doped μ c-Si:H layer of about 20 nm also deposited at 250°C. Then, 80 nm of the optimized ITO were deposited over it. Then, both structures underwent subsequent annealings, aiming to find the optimum temperature. Finally, for the *n*-wafer, the laser firing was developed.

To evaluate the potential quality of the resulting device, the effective carrier lifetime and implicit open circuit voltage were measured after the

5 Thin film passivation for advanced solar cell structures

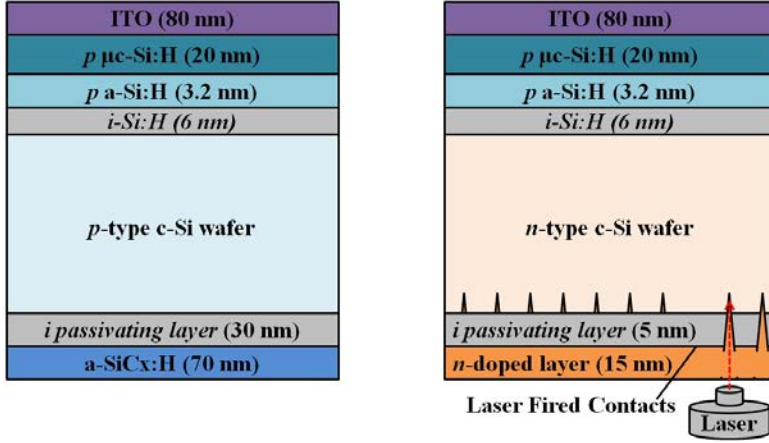


Figure 5.9: Structures used for p -type emitter trials over p - and n -type wafers. The front part (i -layer, p -emitter and ITO) was deposited in the UB. The rear passivating stacks were deposited in the UPC before the emitters. In the case of the n -wafer, the laser firing was performed after the last annealing process.

different annealing stages (as deposited, 200, 250 and 275°C) and, in the case of the n -wafer, after the laser firing is done. The idea was to obtain the optimum annealing temperature for this emitter over wafer and test the influence of the LFC process. The graphs corresponding to the lifetime versus the minor carrier concentration are shown in Fig. 5.10.

In the graphs, it can be observed that the measured lifetimes are strongly dependent on the annealing process, being the best results obtained after the annealing at 250°C, and raising the temperature further to 275°C provokes an decrement in τ_{eff} . It can also be observed that the values obtained for the n -wafer are higher than those obtained for p -wafer. For the n -wafer, when the laser firing was developed after the last annealing, a decrement on the parameters was found, but much smaller than expected. The absolute values are shown in Table 5.11.

Even at the best point of the n -wafer sample, the values (531 μ s, 682.9 mV) are still lower than those obtained at the UPC at this stage for n

5.4 Results in *p*-type hetero-emitter development

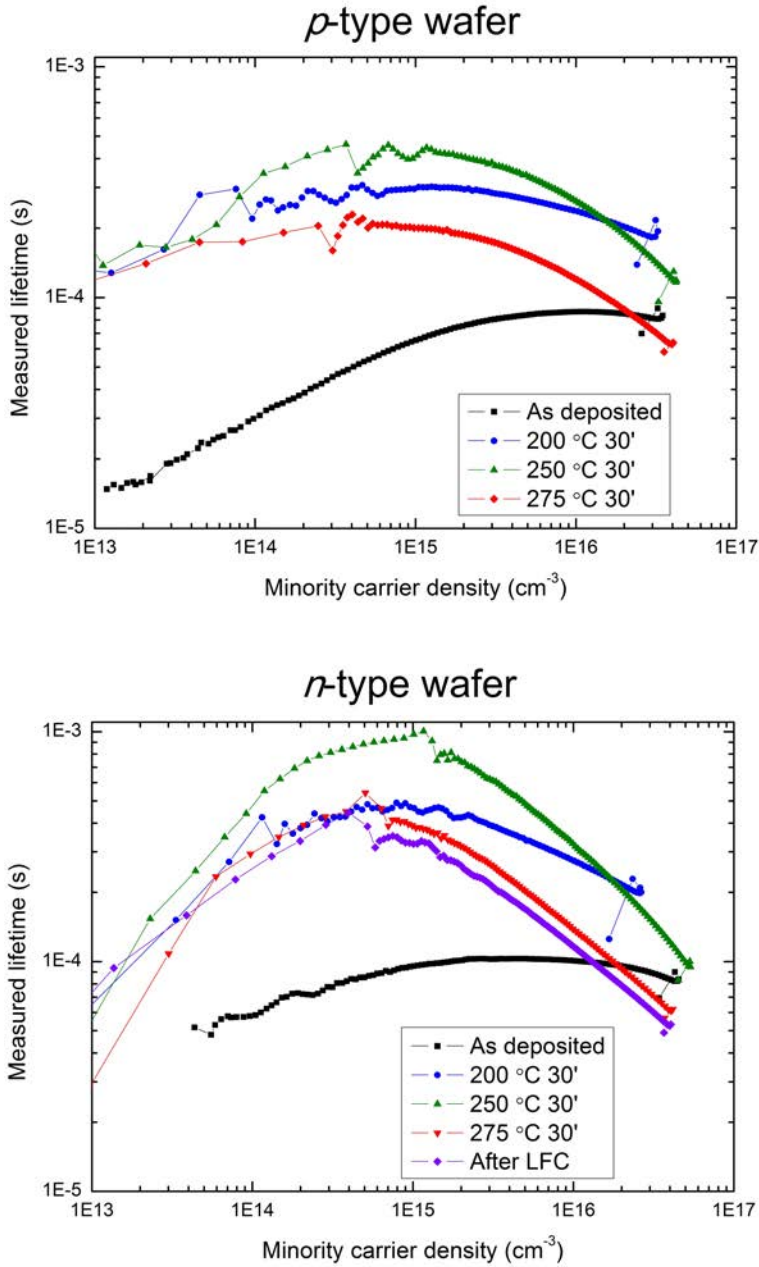


Figure 5.10: Measured carrier lifetimes for both *p* (top) and *n* (bottom) wafers with the *p*-type emitter and ITO deposited in the UB. Several curves at different stages after consecutive annealing or laser firing processes are shown.

Table 5.11: Effective lifetime and implicit open circuit voltage after the successive annealings or LFC processes for both p (left) and n (right) wafers with the p -type emitter and ITO deposited at the UB. The annealings were performed at the UPC in a forming gas atmosphere.

| Status | p -wafer | | n -wafer | |
|------------------|---------------------|-----------------|---------------------|-----------------|
| | $\tau_{eff}(\mu s)$ | $ImpV_{oc}(mV)$ | $\tau_{eff}(\mu s)$ | $ImpV_{oc}(mV)$ |
| As ITO deposited | 36.5 | 599.9 | 86.6 | 605.9 |
| Ann.200°C 30 min | 298 | 666.1 | 385 | 672.3 |
| Ann.250°C 30 min | 388 | 679.4 | 531 | 682.9 |
| Ann.275°C 30 min | 194 | 620.2 | 293 | 658.8 |
| Afrer LFC | - | - | 247 | 655 |

emitter, which are over 750 μs and 700 mV. An interesting result is that the degradation of the parameters caused by laser firing is quite smaller than expected. This suggests that the lifetime is already limited by the passivation of the front side of the wafer, this is, the passivation achieved by the deposited intrinsic a-Si:H of the emitter. After the laser firing, the cell was eventually not finished and measured because the values of the carrier lifetime were too low to obtain quality devices.

The conclusions extracted for this experiment are that it is possible to deposit functional p -type emitters at UB with the p -doped layers detailed at the previous section. On the other hand, the results suggest that further optimization of the intrinsic a-Si:H aiming for better passivation is needed, as it is currently limiting the values of the effective carrier lifetime.

5.4.3 Intrinsic a-Si:H passivating layer optimization

5.4.3.1 Carbon concentration and annealing temperature

As it was explained in previous sections, the surface defect saturation is critical to obtain good passivation results, and a-Si:H has proved itself a useful material in this field [182][183][184][217]. Several parameters have been optimized, like the thickness [218] or the carbon inclusion

5.4 Results in *p*-type hetero-emitter development

[179]; and also some treatments have been included in the fabrication process, like thermal annealing [219]. In the present case, the thickness of the intrinsic layer is only a few nm, so the heterojunction is essentially preserved [220]. The objective in this section was to overcome the problems associated to the a-Si:H passivation that resulted in the low lifetimes found in the *p*-type emitters of the previous section, aiming to obtain similar lifetimes to the ones obtained for *n*-emitter over *p*-wafer [63].

So, an experiment was developed to study the passivation that the a-Si:H of the UB could provide and the influence of the inclusion of some carbon in the layer. To do so, a deposition of intrinsic a-Si:H layers was made over both sides of *p*-type polished wafers. The first sample set kept the silane flow at 40 sccm and no flow of methane nor hydrogen (*i* a-Si:H). The second set added some CH₄ to include carbon in the layer, but keeping the total flow. This is, instead 40 sccm of SiH₄, the flows used were 30 sccm of SiH₄ and 10 sccm of CH₄ (*i* a-SiC_{*x*}:H).

The deposition time used was 3 min, which corresponds to a thickness of about 33 nm. This is thicker than the layer that would be used in the emitter, but it serves to check the passivation that both layers could provide, and compare them. The rest of the deposition conditions were the same as those used for standard *i* a-Si:H for thin film solar cells, shown in Table 3.2 (Chapter 3, Sec. 3.3).

To try to recreate the effect of the ITO deposition in the carrier lifetime observed in the devices, ITO at room temperature was deposited over the intrinsic layers. This is an unusual configuration, but it allowed that the reduction on lifetimes due to the ITO deposition was somehow taken into account. The configuration used for this experiment is shown in Fig. 5.11.

The evaluated parameters were again τ_{eff} and $ImpV_{oc}$, which were measured after the ITO was deposited and after each subsequent annealing process. The results are shown in Table 5.12.

5 Thin film passivation for advanced solar cell structures

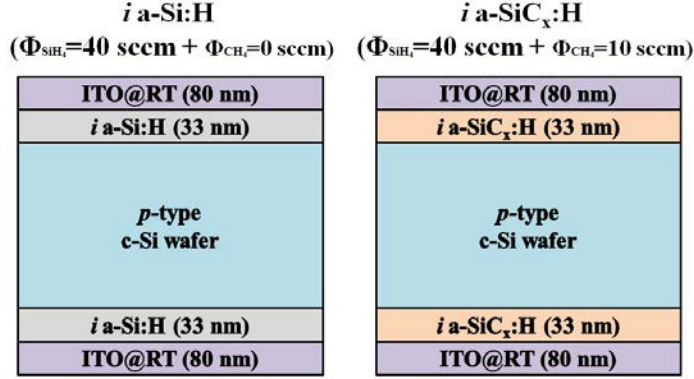


Figure 5.11: Structure used for *i*-layer passivation trials. The depositions are symmetrical, so the layers on both sides are identical. The ITO is deposited at room temperature with the same conditions as in Sec. 5.4.1.

Table 5.12: Effective lifetime and implicit open circuit voltage after the successive annealing processes for the *i* a-Si:H and *i* a-SiC_x:H deposited at the UB (at 200°C). The thickness of both intrinsic layers (a-SiH and a-SiC_x:H) are about 33 nm.

| Passivating layer | <i>i</i> a-Si:H | | <i>i</i> a-SiC _x :H | |
|-------------------|---------------------|-----------------|--------------------------------|-----------------|
| | $\tau_{eff}(\mu s)$ | $ImpV_{oc}(mV)$ | $\tau_{eff}(\mu s)$ | $ImpV_{oc}(mV)$ |
| As ITO deposited | 0.99 | 517 | 0.80 | 521 |
| Ann.160°C 30' | 149 | 651 | 133 | 649 |
| Ann.200°C 30' | 528 | 692.8 | 445 | 687.4 |
| Ann.250°C 30' | 1040 | 716.8 | 910 | 719.3 |
| Ann.300°C 30' | 1050 | 720.9 | 908 | 717.7 |

The successive thermal treatments managed to produce a significant increase in the parameters until the process at 250°C, and then they stabilize. This is consistent with the result found in for *p*-emitters in the previous section. However, the need of an annealing at this point could be a drawback, as it is a time and energy consuming process.

5.4.3.2 Deposition temperature increase to avoid thermal annealing

In this section, the objective was to improve the passivation and, if possible, achieving it without the need of an annealing. To do so, an experiment raising the deposition temperature of the intrinsic passivating was performed, aiming to somehow include the thermal effects in the process. A total of six samples were studied, divided in two sets, one of each kind of material, with the same structure shown in Fig. 5.11. The temperature of both sets was varied, being the substrate temperatures 200, 250 and 300°C. 300°C has been set as the maximum temperature, as higher values could be prejudicial for the existing material in the wafer, like the rear passivating stack. The results are shown in Table 5.13.

Table 5.13: Effective lifetime and implicit open circuit voltage in the *i* a-Si:H samples deposited at the UB at different temperatures (200, 250 and 300°C). The thickness of both intrinsic layers (a-SiH and a-SiC_x:H) are about 33 nm.

| Passivating layer | <i>i</i> a-Si:H | | <i>i</i> a-SiC _x :H | |
|-------------------|---------------------|-----------------|--------------------------------|-----------------|
| Dep. T | $\tau_{eff}(\mu s)$ | $ImpV_{oc}(mV)$ | $\tau_{eff}(\mu s)$ | $ImpV_{oc}(mV)$ |
| 200°C | 0.71 | 515.9 | 1.51 | 529.0 |
| 250°C | 10.4 | 577.2 | 29.5 | 605.2 |
| 300°C | 1280 | 730.8 | 1310 | 726.8 |

As it can be observed, when the deposition temperature is raised to 300°C the results without thermal treatment are much better, overcoming even the previous values for annealed samples. Furthermore, not only these values are the best by far, but also they are good absolute values, as an effective carrier lifetime of more than 1.3 ms corresponds to a good passivation.

There are two possible reasons that justify this result. The first is that the higher temperature of deposition could somehow substitute the effect of the annealing, and the surface defects are more effectively saturated. However, as the deposition time (3 minutes) is short compared to a standard annealing time, probably this is not the main reason. The

second and most likely reason to this large increment is related to the bulk defects on the a-Si:H. As the deposition rate is higher, the quantity of bulk defects is also a higher (Chapter 3, Sec. 3.3.5). So, higher deposition temperature leads to an increase in the defect density. On the other hand, the higher temperature helps to charge these defects, which results in more trapped charge that contribute to avoid recombination through the field-effect mechanism explained before.

The main conclusion is that among the tried temperatures for the deposition of the intrinsic layer before the emitter, the optimum one is 300°C, as it not only provides good passivation, but also manages to avoid the annealing at this point. However, as some of the subsequent layers equally require an annealing process (like ITO), it would eventually not be possible to avoid it in the whole device fabrication process. As far as the carbon content is concerned, the a-SiC_x layer presents slightly better passivation results than the a-Si:H layer.

5.5 Conclusions and future work

The work in this chapter presents amorphous silicon not as active layer but as support material to other technologies. Its main role now was to contribute to the passivation of c-Si wafers. The experiments presented were developed in cooperation with the UPC and had two main objectives: the use of sputtered alumina as rear side passivation material and the development of a *p*-type emitter in order to be used in *n*-wafers.

As far as the passivation with sputtered alumina is concerned, acceptable values of the effective lifetime and implicit open circuit voltage were found when depositing directly over the wafer and after a thermal annealing, but still low compared to the values achieved with alumina deposited by ALD. This was likely caused by the superficial damage induced by the high energy ion bombardment produced by the sputtering process. The inclusion of a very thin intermediate a-Si:H layer produced an important improvement in the passivation, as it fulfills a double function: it saturates the free surface bonds providing chemical passivation, and also protects

the crystalline surface from the ion bombardment. The values obtained are very promising but they still have to be improved by trying different thicknesses and stacks combining a-Si:H and Al₂O₃.

The second objective was to develop a *p*-type emitter in the UB, in order to use it for *n*-type wafer devices. The first step was the optimization of ITO layers in order to be used as front TCO in these emitters. The ITO deposited in the UB not only fulfilled this condition, but also improved the *p*-wafer device performance in about an absolute 3% when used over *n*-type emitters deposited in the UPC. However, the ITO has to be improved to reduce the series resistance of the cells. Raising the deposition temperature to about 300°C to try to obtain microcrystalline layers instead of amorphous would be an interesting future experiment.

After, the *p*-layers were adapted to be used as a stack bound to be employed as emitter. The values of the effective carrier lifetime obtained were good but still lower than those obtained with *n*-emitters over *p*-wafers. It was also found that the optimum annealing temperature is 250°C and the values after laser firing pointed to the need of an optimization of the a-Si:H layer for passivation processes. The subsequent optimization of the *i* a-Si:H layer revealed that adding methane to the plasma and increasing the deposition temperature until 300°C leads to higher values of the lifetime and the implicit V_{oc} . Also, when the passivation is performed with a-Si:H at 300°C, the annealing process was not necessary to achieve good values. An option to further improve passivation would be raising even more the deposition temperature, as the tendency shows that passivation increases with it.

Future experiments projected are trials with different thicknesses of the intrinsic layer in the a-Si:H/Al₂O₃ stack, in order to evaluate the real contribution of both materials and passivation mechanisms (chemical and field-effect). As far as the *p*-type emitters are concerned, the experiments are in their initial stage and there is still plenty of work to do. The first experiment that should be performed is the deposition of the emitter with the intrinsic a-Si:H deposited at 300°C and check if the passivation is increased, and continue from there aiming to a complete working device based on *n*-wafer with good quality.

6 Conclusions and perspectives

The development of this thesis has been marked by the need to start up a PECVD reactor of recent acquisition. This new reactor is bound to be an important equipment for further experiments in the group, and it was imperative to match the quality of the materials and the devices with the state of the art of photovoltaics. Amorphous silicon was selected as the most suitable material to perform the optimization of the reactor working recipes and techniques, as it is a material that has been long studied in PV technology. The group has historically very large experience involving deposition and characterization of this material, not only at laboratory device level, but also with modules and power plants on field operation; so continuing this work was also one of the objectives of this thesis.

The first important conclusion extracted is that the layers and cells deposited at the reactor present high homogeneity (over 95% in the central $9 \times 9 \text{ cm}^2$ area), which allows to have several identical cells for subsequent experiments. The reproducibility was also tested and verified through several comparisons between depositions with the same conditions. This is important because it allowed that the subsequent studies were reliable. The most relevant conclusions of these studies are shown next.

Chapter 3 was focused in the optimization of the materials involved in thin film silicon solar cells, specially amorphous silicon. Experiments in layers and complete devices were developed, aiming to obtain a complete working thin film a-Si:H solar cell with good performance. First, the conclusions in intrinsic a-Si:H are exposed:

- The depletion series in pure a-Si:H showed a behavior with a maximum in the deposition rate in the central values ($D = 0.37$) which comes as a result of an equilibrium between the chemisorption and the absence of polysilane species, reached at this maximum point. It

6 Conclusions and perspectives

is also found that the increase of the deposition rate leads to poorer properties of the thin films, probably due to a higher defect formation during the deposition. The best results are obtained for low depletion values.

- The inclusion of hydrogen reduces the deposition rate due to a higher atomic hydrogen etching. The layers deposited with higher hydrogen flows present attachment problems, which suggests that these layers were deposited in an inadequate plasma regime. The increase of hydrogen content reduces light induced degradation. The optimum ratio between hydrogen and silane flows that was found to be 2:1.
- The influence of the temperature in the deposition rate and the conductivities is small compared with those of other parameters. The activation energy and the gap revealed an optimum point at 250°C. However, the difference with the 200°C layer did not compensate the potential loss in the open circuit voltage in complete devices.
- The optimizations in all the layers should be tested together to check if the combined optimized parameters are still optimal when used together as absorber layer.

The *p*-doped layer optimization included the optimization of two different materials, amorphous and microcrystalline silicon. For both, several series varying different parameters were developed aiming to obtain quality material to be used as doped layer for a-Si:H solar cells.

- For *p*-doped amorphous silicon, four optimization series (TMB partial flow, temperature, pressure and methane partial flow) were developed, which led to an increase of the dark conductivity by more than three orders of magnitude. The obtained final values of the dark conductivity, activation energy and bandgap fulfill the requirements for device implementation (1.1×10^5 S/cm, 0.43 eV and 2.02 eV).
- *p*-doped microcrystalline silicon was also optimized by the same procedure of four subsequent series: temperature, TMB partial flow, power and SiH₄ partial flow. The dark conductivity was raised by more than 2 orders of magnitude (to 1.32 S/cm), the crystalline fraction from less than 0.2 to almost 0.6, and the bandgap

reached a value of 2.07 eV. These values are also suitable for device implementation.

With the layers optimized, complete a-Si:H solar cells were deposited using the optimized materials. Trials involving the back reflector and the p -layer thickness were developed, with the objective of increasing the cell efficiency trying to reach the state of the art or get as close as possible.

- The inclusion of a TCO in the back reflector provided an important increase in the short circuit current as a result of an enhanced absorption in the long wavelength part of the spectrum. Several options for the TCO deposited with different conditions optimized in previous group work were tested. Aluminum doped zinc oxide proved itself the best choice, providing a slight increase in the open circuit voltage and an important increment of 12% in the short circuit current, as a result of an enhanced absorption in the long wavelengths (>550 nm). Different metalizations have been also tested, being found that thermal evaporated silver is the most suitable option.
- Reducing the p -layer thickness also resulted in an increase of the short circuit current, as the absorption in this layer (which produces no current) is reduced, and so the light is absorbed in the intrinsic layer. This can be clearly observed in the short wavelength range of the EQE measurements. The optimal thickness found for the used substrate is 7 nm, and it is considered the lower limit. If the p -layer is reduced beyond this value, the resulting device is not a cell but a resistance, as the pin junction is not formed anymore.

After these experiments, working a-Si:H solar cells can be deposited at the UB, showing a 7.08% of conversion efficiency as deposited. The V_{oc} reaches 0.84 V, which is still lower than expected for a-Si:H solar cells (≈ 0.9 V). This suggests the need of further optimization of the doped layers. The J_{sc} has a value of 12.5 mA/cm² and the FF presents a value of 0.714. Although the devices show good enough performance to develop further experiments, these values, specially V_{oc} , are still a bit low. In order to improve the quality of the device, some work can still be developed:

- Combine the optimizations developed in the i layer over a device.

6 Conclusions and perspectives

- Use a bi-layer stack $\mu c/a$ as p doped layer aiming to enhance V_{oc} .
- Include a suitable buffer layer between the p and the i layers.
- Develop some optimizations in the n -doped material.

The work developed during the stage at the LPICM in Palaiseau was also aiming to increase the efficiency of solar cells through an increment of the open circuit voltage, in both PIN and NIP configurations. The active material in this case was polymorphous silicon, which means silicon deposited on the edge between amorphous and microcrystalline silicon. The two main trials developed were to reduce the temperature of deposition and to include an amorphous silicon oxide ($a\text{-SiO}_x$) buffer layer between the doped ($\mu c\text{-SiO}_x$) and intrinsic ($pm\text{-Si:H}$) layers. This buffer layer can be either intrinsic, p -doped or n -doped.

- Reducing the temperature works for PIN configuration, providing a slight increase in the V_{oc} , but it has no effect in the NIP configuration. The reasons for this behavior are not clear, further experiments would be needed.
- Depositing $a\text{-SiO}_x$ before the intrinsic layer ($pa\text{-SiO}_x$ over $p\mu c\text{-SiO}_x$ in PIN configuration; $na\text{-SiO}_x$ over $n\mu c\text{-SiO}_x$ in NIP configuration) results in an increase on the open circuit voltage. This suggests that growing $pm\text{-Si:H}$ over amorphous material produces a better interface than the one obtained when growing over microcrystalline material, either due to better passivation of the μc surface, the creation of a diffusion barrier or simply that the growth of $pm\text{-Si:H}$ is favored when it is over amorphous material.
- On the contrary, depositing $a\text{-SiO}_x$ with the corresponding dopant (p for NIP, n for PIN) over the intrinsic $pm\text{-Si:H}$ causes a dramatic drop of the cell properties. This points to the fact that the subsequent microcrystalline doped layers do not grow properly over the amorphous material of the buffer layers. Also, it is possible that some eventual powder formed during the intrinsic layer deposition affects the deposition of the buffer layers.

The second main block of results in this thesis, shown in Chapter 4, come from the study of light induced degradation and seasonal effect in a-Si:H, continuing previous work developed by the group over commercial modules and operating power plants. Also, the study of the SWE was necessary in order to evaluate the real performance of the materials and the devices developed in Chapter 3. This is why the first stage to obtain results from laboratory devices in this field was to design and construct a low cost light induced degradation system with the possibility of implementing and controlling different degradation temperatures. A LED based light soaking system with four identical 'towers' with independent temperature control was constructed, and it has proved itself a valid solution, as the results obtained from LID experiments developed with this equipment are consistent with experiments developed with solar simulators found in the bibliography.

An optimization of thickness of the intrinsic layer in UB solar cells was developed. To test it, four samples whose only difference was the *i*-layer thicknesses were degraded in the same exact conditions. The thicker cells present a higher initial performance, but this tendency is reversed after a few hours of degradation. A simple model based on the mobility-lifetime product has been used to explain this phenomena: Initially the interfacial defects have more weight in thinner cells making them have much smaller values of $\mu\tau$. However, as the degradation is mostly a bulk process, the defect generation is higher in the thicker cells, and in the end, their performance is more affected. The *i*-layer thickness that was considered optimal (as the cell presented the highest final efficiency) is 200 nm.

Focusing in the studies on seasonal effect, both commercial *T-Solar* and UB deposited cells were light soaked varying the degradation temperature, studying their parameters at different stages of degradation. The experiments aimed to isolate the effect of the temperature by removing the spectral effect (as the illumination was constant and identical for all samples). Several conclusions were extracted from the *J-V* and *EQE* measurements in both set of samples.

- The light induced degradation is higher when the temperature is lower, and this is appreciable since the first stages of the degradation

6 Conclusions and perspectives

(less than 10 hours of exposure). All the parameters are affected in different degree, being the V_{oc} the less affected, and the FF the most (J_{sc} shows an intermediate behavior between them).

- If the temperature of degradation is switched, the samples going from lower to higher temperatures experience a recovery in all the parameters. On the contrary, those going from higher to lower temperatures suffer from a sudden degradation. This is also appreciable after few hours after the switch.
- When LID was performed again for over 1000 h at the new temperature, the results proved that the values of the parameters do not depend on the previous history of the sample, but only on the final temperature of degradation.
- The temperature coefficient for the efficiency was calculated for *T-Solar* cells and it was found that, in modules, it is almost compensated by the fast temperature change coefficient, provided by the manufacturer. So, in field conditions, the temperature effect is very little compared with the spectral effect, as the results in previous work showed.
- The temperature coefficient for the fill factor in UB cells is almost three times the one found for *T-Solar* samples. This means that further optimization in the UB intrinsic material against LID is needed.
- Analyzing the current loss with the *EQE* measurements, it was found that the degradation is higher in the short and long wavelengths. This indicates that more degradation is produced in the material close to the interfaces (blue for *p-i* and red and NIR for *i-n*). The inclusion of buffer layers and the improvement of the doped layers could help to avoid this effect.

Several studies can be projected to further understand seasonal effect, like the inclusion of cyclical variations of the temperature and the illumination in order to better recreate the on-field conditions and obtain the adapted coefficient. Also, studies varying the material instead of the light would be interesting, specially the ones involving the inclusion of

hydrogen in the *i*-layer.

Finally, Chapter 5 treats the role of amorphous silicon in c-Si technology. The experiments were developed in collaboration with the UPC and are divided in two blocks. The first had as objective to develop alumina deposited by sputtering in order to be used in passivation, as an alternative to other materials or to alumina deposited by other techniques (specially ALD). The experiments included testing the influence of a very thin layer of a-Si:H deposited between the wafer and the sputtered Al₂O₃, aiming for physical protection for the wafer surface and some chemical passivation through hydrogen. The results of both unprotected and protected layers were compared between them and with the values obtained in other technologies.

- The unprotected samples showed values of the carrier lifetime below 0.1 ms, while the protected samples reached values over 1.2 ms for *p*-wafers and 1.4 ms for *n*-wafers, which are not very far from the values reached with alumina deposited by ALD. So, the role of the amorphous silicon is very important in passivation with alumina deposited by sputtering. The a-Si:H layer provides protection against the ion bombardment in the sputtering, and also could be providing a certain amount of hydrogen that results in chemical passivation.
- A thermal annealing is required in both unprotected and protected wafers in order to obtain acceptable values of the carrier lifetime. This comes as a result of the need of the annealing process to charge the defects in the alumina layer. Also, in the case of the protected samples it could be enhancing hydrogen movement, which helps the defect saturation.

Although these values of the passivation with alumina are still a little below those achieved with ALD, the combination of PECVD a-Si:H and sputtered Al₂O₃ seems very promising. The next step would be trials varying the thickness of the a-Si:H layer, aiming to evaluate the contribution of each passivation mechanism: chemical and field-effect; and maximize both to obtain better passivation.

6 Conclusions and perspectives

The second set of experiments in passivation aimed to develop a p -type hetero-emitter (containing amorphous and microcrystalline silicon) to be used in n -wafers. The objective was to develop the whole front part of the cell at the UB (emitter + front ITO). So, several optimization series were developed for both the ITO and the p -type layers.

- ITO was first optimized over glass. Two series were developed, oxygen partial pressure and temperature, and the optimum point was chosen by evaluating the sheet resistance and the transparency. While the oxygen partial pressure series presented an optimum point at 4.91 mPa (over a total pressure of 173 mPa), the temperature series did not revealed a clear optimum point.
- To try to obtain an optimal temperature, ITO was deposited over an n -type emitter deposited over a p -type c -Si wafer. Before the device is finished, the carrier lifetime was measured, obtaining that the highest value after annealing (0.975 ms) is obtained with the ITO deposited in the UB at room temperature. The finished device showed an absolute improvement in efficiency of 3% over the one with UPC's ITO, due to a lower R_s (which increases FF) and a higher J_{sc} .
- As the p -layers were going to be used as part of the emitter, it was possible to raise the deposition temperature of p -doped amorphous and microcrystalline silicon, aiming for better values of the parameters. It was found that the p μc -Si:H at 250°C shows a maximum in the dark conductivity and a minimum in the activation energy; and they increase also for p a -Si:H at this temperature. So, 250°C was selected as optimal temperature.
- The thickness for the p -type layers in the hetero-emitters was optimized based in the V_o and the absorption in the blue part of the spectrum in an a -Si:H solar cell. The cell with 20 nm of p μc -Si:H and 3.2 nm of p a -Si:H showed the lowest absorption in the blue part while maintaining the highest open circuit voltage.

The optimized emitter (both p -doped layers and ITO) was tested over p and n -wafers by evaluating the lifetime and $ImpV_{oc}$ in several stages: as

deposited, after subsequent annealings, and in the case of *n*-wafer, after laser firing.

- The optimum annealing temperature is 250°C. When the temperature is raised beyond this point, the effective carrier lifetime value decreases.
- τ_{eff} is higher in the *n*-wafer in all the annealing stages.
- Even the best values of τ_{eff} and $ImpV_{oc}$ (521 μs , 682.9 mV) are still lower than those obtained at the UPC at this stage for *n*-emitters over *p*-wafers.
- It was found that the degradation of the parameters caused by laser firing was much smaller than expected, which suggests that the values of the lifetime are already limited by the front side passivation provided by the *i*-layer of the emitter.
- An experiment over wafers has proved that increasing the temperature of the *i* a-Si:H to 300°C results in better passivation, due to hydrogen mobility and to the fact that a-Si:H deposited at 300°C has more defects that could get charged, which leads to trapped charge that contributes to field-effect passivation. Also, depositing the a-Si:H suppresses the need of thermal annealing at this point.

The emitter development is still a starting work. Further experiments can also be developed on the thicknesses of the *p*-layer. The next step would be trying the emitter with *i* a-Si:H at 300°C and make the annealing only at 250°C before finishing the device, and then study the complete parameters of the cell, and compare them with the results for *n*-emitters over *p*-wafers.

Bibliography

- [1] Enerdata, “Global Energy Statistical Yearbook 2015,” 2015.
- [2] T. Foley, K. Thornton, R. Hinrichs-Rahlwes, S. Sawyer, M. Sander, R. Taylor, S. Teske, H. Lehmann, M. Alers, and D. Hales, *Renewables 2015 Global Status Report*. 2015.
- [3] IEA Statistics, “Key Trends in CO2 Emissions,” 2015.
- [4] D. Feldman, G. L. Barbose, R. Margolis, T. James, S. Weaver, N. R. Darghouth, R. Fu, C. Davidson, S. Booth, and R. H. Wiser, “Photovoltaic System Pricing Trends: Historical, Recent, and Near-Term Projections - 2015 Edition,” 2015.
- [5] M. A. Green, *Solar cells: operating principles, technology, and system applications*. U.S.A.: Prentice-Hall, Englewood Cliffs, NJ, 1982.
- [6] P. Würfel, “Physics of Solar Cells : From Principles to New Concepts,” 2005.
- [7] A. Jäger-Waldau, *PV Status Report 2014*. 2014.
- [8] M. A. Green, K. Emery, Y. Hishikawa, W. Warta, and E. Dunlop, “Solar cell efficiency tables (version 47),” *Progress in Photovoltaics: Research and Applications*, vol. PP, 2015.
- [9] Panasonic Global, “Panasonic HIT(R) Solar Cell Achieves World Highest Energy Conversion Efficiency of 25.6% at Research Level,” 2014.
- [10] J. Zhao, A. Wang, F. Yun, G. Zhang, D. M. Roche, S. R. Wenham, and M. Green, “20 000 PERL Silicon Cells for the ‘ 1996 World Solar Challenge ’ Solar Car Race,” *Progress in Photovoltaics: Research and Applications*, vol. 5, pp. 269–276, 1997.
- [11] W. Deng, D. Chen, Z. Xiong, P. J. Verlinden, J. Dong, F. Ye, H. Li, H. Zhu, M. Zhong, Y. Yang, Y. Chen, Z. Feng, and P. Altermatt, “20.8% PERC Solar Cell on 156 mm x 156 mm P-Type Multicrystalline Silicon Substrate,” *IEEE Journal of Photovoltaics*, vol. PP, no. 99, pp. 1–7, 2015.
- [12] S. Zhang, X. Pan, H. Jiao, W. Deng, J. Xu, Y. Chen, P. Altermatt, Z. Feng, and P. Verlinden, “335-W World-Record p-Type Monocrystalline Module With 20.6% Efficient PERC Solar Cells,” *IEEE Journal of Photovoltaics*, vol. PP, no. 99, pp. 1–8, 2015.

Bibliography

- [13] FirstSolar, “First Solar achieves world record 18.6% thin film module conversion efficiency,” tech. rep., First Solar, New York, 2015.
- [14] T. Matsui, H. Sai, T. Suezaki, M. Matsumoto, K. Saito, I. Yoshida, and M. Kondo, “Development of highly stable and efficient amorphous silicon based solar cells,” *28th European Photovoltaic Solar Energy Conference and Exhibition*, pp. 2213 – 2217, 2013.
- [15] H. Sai, T. Matsui, K. Matsubara, M. Kondo, and I. Yoshida, “11.0%-Efficient Thin-Film Microcrystalline Silicon Solar Cells With Honeycomb Textured Substrates,” *IEEE Journal of Photovoltaics*, vol. 4, no. 6, pp. 1349–1353, 2014.
- [16] T. Matsui, H. Sai, K. Saito, and M. Kondo, “High efficiency thin film silicon solar cells with improved light-soaking stability,” *Progress in Photovoltaics: Research and Applications*, vol. 21, pp. 1363–1369, 2013.
- [17] TEL-Solar, “TEL solar press release July 9 2014,” tech. rep., Trubbach, 2014.
- [18] NREL, “Solar cell efficiency explanatory notes,” 2015.
- [19] D. E. Carlson and C. R. Wronski, “Amorphous silicon solar cell,” *Applied Physics Letters*, vol. 28, no. 11, p. 671, 1976.
- [20] M. Hack and M. Shur, “Physics of amorphous silicon alloy pin solar cells,” *Journal of Applied Physics*, vol. 8, no. 58, pp. 97–1020, 1985.
- [21] W. Shockley and W. Read, “Statistics of the Recombinations of Holes and Electrons,” *Physical Review*, vol. 87, pp. 835–842, sep 1952.
- [22] D. E. Carlson and B. F. Williams, “US Patent 4442310: Photodetector having enhanced back reflection,” 1984.
- [23] R. Schropp and M. Zeman, *Amorphous and Microcrystalline Silicon Solar Cells: Modeling, Materials and Device Technology*. USA: Kluwer Academic Publishers, 1998.
- [24] H. W. Deckman, “Optically enhanced amorphous silicon solar cells,” *Applied Physics Letters*, vol. 42, no. 11, p. 968, 1983.
- [25] J. Escarré, *Tècniques de confinament òptic en cel·lules solars sobre substrat plastic*. PhD thesis, Universitat de Barcelona, (<http://www.tdx.cat/handle/10803/1775>), 2008.
- [26] P. Carreras, *Transparent Conducting Oxides for silicon thin film solar cells: Doped and multi-compound ZnO-based transparent conducting oxides for silicon thin lm solar cells*. PhD thesis, Universitat de Barcelona, (<http://www.tdx.cat/handle/10803/109157>), 2012.

- [27] M. Llusà, *Novel light management techniques for thin lm solar cells: Nanotextured substrates and transparent conducting upconverters*. PhD thesis, Universitat de Barcelona, 2015.
- [28] J. Nijs, E. Demesmaeker, J. Szlufcik, J. Poortmans, L. Frisson, K. De Clercq, M. Ghannam, R. Mertens, and R. Van Overstraeten, "Latest Efficiency Results With the screenprinting technology and comparison with the buried contact structure," in *First WCPEC*, pp. 1242–1249, 1994.
- [29] M. A. Green, C. M. Chong, F. Zhang, A. Sproul, J. Zolper, and S. R. Wenham, "Efficient laser grooved buried contact silicon solar cells," in *Photovoltaic Specialists Conference*, pp. 411–414, 1988.
- [30] P. J. Verlinden, R. M. Swanson, and R. A. Crane, "7000 High Efficiency Cells for a Dream," *Progress in Photovoltaics: Research and Applications*, vol. 2, pp. 143–152, 1994.
- [31] A. Faes, M. Despeisse, J. Levrat, J. Champlaud, N. Badel, M. Kiaee, T. Söderström, Y. Yao, R. Grischke, M. Gragert, J. Ufheil, P. Papet, B. Strahm, B. Cattaneo, J. Cattin, Y. Baumgartner, A. Hessler-Wyser, and C. Ballif, "Smartwire solar cell interconnection technology," in *29th European Photovoltaic Solar Energy Conference*, (Amsterdam), pp. 2555–2561, 2014.
- [32] A. W. Blakers, A. Wang, A. M. Milne, J. Zhao, and M. A. Green, "22.8% efficient silicon solar cell," *Applied Physics Letters*, vol. 55, no. 13, p. 1363, 1989.
- [33] W. Fuhs, "Heterojunctions of amorphous silicon and silicon single crystals," *Bulletin of American Physical Society*, vol. 19, p. 393, 1974.
- [34] Y. Hamakawa, "New types of high efficiency solar cells based on a-Si," *Applied Physics Letters*, vol. 43, no. 7, p. 644, 1983.
- [35] H. Sakata, T. Nakai, T. Baba, M. Taguchi, S. Tsuge, K. Uchihashi, and S. Kiyama, "20.7% highest efficiency large area (100.5cm²) HIT cell," *Photovoltaic Specialists Conference, 2000. Conference Record of the Twenty-Eighth IEEE*, pp. 7–12, 2000.
- [36] H. Sterling and R. Swann, "Chemical vapour deposition promoted by r.f. discharge," *Solid-State Electronics*, vol. 8, no. 8, pp. 653–654, 1965.
- [37] W. Spear and P. Le Comber, "Substitutional doping of amorphous silicon," *Solid State Communications*, vol. 17, no. 9, pp. 1193–1196, 1975.
- [38] R. A. Street, *Hydrogenated amorphous silicon*. USA: Cambridge Solid State Science Series, 1991.
- [39] A. Shah, *Thin-Film Silicon Solar Cells*. Switzerland: EPFL Press, 2010.

Bibliography

- [40] M. E. Stuckelberger, *Amorphous silicon : Impact of process conditions on material properties and solar cell efficiency*. PhD thesis, EPFL, 2014.
- [41] S. Hegedus, "Review of photovoltaic module energy yield (kWh/kW): comparison of crystalline Si and thin film technologies," *Wiley Interdisciplinary Reviews: Energy and Environment*, vol. 2, no. 2, pp. 218–233, 2013.
- [42] E. A. Alsema and E. Nieuwlaar, "Energy viability of photovoltaic systems," *Energy Policy*, vol. 28, no. 14, pp. 999–1010, 2000.
- [43] A. Shah, H. Schade, M. Vanecek, J. Meier, E. Vallat-Sauvain, N. Wyrsch, U. Kroll, C. Droz, and J. Bailat, "Thin-film silicon solar cell technology," *Progress in Photovoltaics: Research and Applications*, vol. 12, no. 23, pp. 113–142, 2004.
- [44] D. Staebler and C. Wronski, "Reversible conductivity changes in discharge produced amorphous Si," *Applied Physics Letters*, vol. 31, p. 292, 1977.
- [45] Y. Werner Luft and S. Tsuo, *Hydrogenated amorphous silicon alloy deposition processes*. USA: Taylor&Francis, 1993.
- [46] J. Perrin, *Deposition of amorphous silicon*. France: Academic Press, 1993.
- [47] G. Bruno, P. Capezutto, and A. Madan, *Plasma deposition of amorphous silicon-based materials*, vol. 4. Italy: Academic Press, 1995.
- [48] J. Bertomeu, *Estructures multicapa basades en el silici amorf i el seus aliatges amb carboni*. PhD thesis, Universitat de Barcelona, (<http://www.tdx.cat/handle/10803/1778>), 1993.
- [49] J. M. Asensi, *Células solares de silicio amorfo: obtención, caracterización y modelización*. PhD thesis, Universitat de Barcelona, (<http://www.tdx.cat/handle/10803/1777>), 1994.
- [50] J. Puigdollers, *Obtenció de fotodiodes de silici amorf hidrogenat amb estructura P-I-N*. PhD thesis, Universitat de Barcelona, 1995.
- [51] J. Merten, *Photovoltaics with Amorphous Silicon: Aspects of Technology, Physics and Application*. PhD thesis, Universitat de Barcelona, 1996.
- [52] D. Peiró, *Microcrystalline silicon obtained by hot-wire chemical vapour deposition for photovoltaic applications*. PhD thesis, Universitat de Barcelona, 1999.
- [53] C. Voz, *Thin film nanocrystalline silicon solar cells obtained by Hot-Wire*. PhD thesis, Universitat de Barcelona, 2001.
- [54] D. Soler Vilamitjana, *Amorphous silicon solar cells obtained by Hot-Wire Chemical Vapour Deposition*. PhD thesis, Universitat de Barcelona, 2004.

- [55] M. Stella, *Study of Organic Semiconductors for Device Applications*. PhD thesis, Universitat de Barcelona, (<http://www.tdx.cat/handle/10803/21620>), 2009.
- [56] F. Villar, *Dispositivos Fotovoltaicos de Capa Delgada a Baja Temperatura*. PhD thesis, University of Barcelona, 2010.
- [57] O. Nos, *HWCVD technology development addressed to the high rate deposition of microcrystalline-Si:H*. PhD thesis, Universitat de Barcelona, (<http://www.tdx.cat/handle/10803/98346>), 2012.
- [58] S. Abolmasov, P. Chattrejee, and P. Roca i Cabarrocas, “LPICM Internal Report: Can we attain over 10% stabilized efficiency in single junction amorphous silicon solar cells?,” 2013.
- [59] S. Abolmasov, P. Chattrejee, and P. Roca i Cabarrocas, “LPICM Internal Report: Towards 12% stabilized efficiency in single junction amorphous silicon solar cells: experimental developments and model predictions,” 2013.
- [60] R. Roldán, *Módulos fotovoltaicos de silicio en capa delgada: Caracterización y modelización*. PhD thesis, Universitat de Barcelona, (<http://www.tdx.cat/handle/10803/144938>), 2013.
- [61] I. Martín, *Silicon surface passivation by Plasma Enhanced Chemical Vapor Deposited amorphous silicon carbide films*. PhD thesis, Universitat Politècnica de Catalunya, 2003.
- [62] D. Muñoz Cervantes, *Silicon heterojunction solar cells obtained by Hot-Wire CVD*. PhD thesis, Universitat Politècnica de Catalunya, 2008.
- [63] A. B. Morales, *Desarrollo de tecnologías de baja temperatura para la fabricación de células solares de heterounión de silicio*. PhD thesis, Universitat Politècnica de Catalunya, 2015.
- [64] T. Merdzhanova, J. Woerdenweber, T. Zimmermann, U. Zastrow, A. Flikweert, H. Stiebig, W. Beyer, and A. Gordijn, “Single-chamber processes for a-Si:H solar cell deposition,” *Solar Energy Materials and Solar Cells*, vol. 98, pp. 146–153, 2012.
- [65] J. Woerdenweber, T. Merdzhanova, T. Zimmermann, a.J. Flikweert, H. Stiebig, W. Beyer, and a. Gordijn, “Cross-contamination in single-chamber processes for thin-film silicon solar cells,” *Journal of Non-Crystalline Solids*, vol. 358, no. 17, pp. 2183–2186, 2012.
- [66] M. Ohring, *The materials science of thin films*. USA: Academic Press, 1992.
- [67] W. Kern and D. a. Puotinen, “Cleaning solutions based on hydrogen peroxide for use in silicon semiconductor technology,” *Rca Review*, vol. 31, no. 2, pp. 187–206, 1970.

Bibliography

- [68] K. Yamamoto, A. Nakamura, and U. Hase, "Control of cleaning performance of an ammonia and hydrogen peroxide mixture (APM) on the basis of a kinetic reaction model," *IEEE Transactions on Semiconductor Manufacturing*, vol. 12, no. 3, pp. 288–294, 1999.
- [69] A. G. Aberle, *Crystalline Silicon Solar Cells: Advanced Surface Passivation and Analysis*, vol. 1. Australia: Centre for Photovoltaic Engineering UNSW, 1998.
- [70] K. Ellmer, A. Klein, and B. Rech, *Transparent conductive zinc oxide. Basics and application in thin film solar cells*. Germany: Springer, 2008.
- [71] H. Yamagishi, K. Asoka, W. A. Nevin, M. Yamaguchi, and Y. Tawada, "Light induced changes of amorphous silicon solar cells by long term exposure," in *Photovoltaic Specialists Conference*, pp. 1342–1346, 1991.
- [72] M. Bliss, T. Betts, and R. Gottschalg, "An LED-based photovoltaic measurement system with variable spectrum and flash speed," *Solar Energy Materials and Solar Cells*, vol. 93, no. 6-7, pp. 825–830, 2009.
- [73] D. S. Codd, A. Carlson, J. Rees, and A. H. Slocum, "A low cost high flux solar simulator," *Solar Energy*, vol. 84, no. 12, pp. 2202–2212, 2010.
- [74] Bridgelux, "Bridgelux RS Array Series Data Sheet."
- [75] A. Shah, J. Krc, M. Despeisse, F. Meillaud, and C. Ballif, "Internal Electric Field and Fill Factor of Amorphous Silicon Solar Cells," no. 2, pp. 1569–1574, 2010.
- [76] E. Bustarret, M. Hachicha, and M. Brunel, "Experimental determination of the nanocrystalline volume fraction in silicon thin films from Raman spectroscopy," *Applied Physics Letters*, vol. 52, pp. 1675–1677, 1988.
- [77] L. Houben, M. Luysberg, P. Hapke, P. Carius, F. Finger, and H. Wagner, "Structural properties of microcrystalline silicon in the transition from highly crystalline to amorphous growth," *Philosophical Magazine A*, vol. 77, pp. 1447–1460, 1988.
- [78] C. Smit, R. van Swaaij, H. Donker, A. Petit, W. Kessels, and M. van de Sanden, "Determining the material structure of microcrystalline silicon from Raman spectra," *Journal of Applied Physics*, vol. 94, pp. 3582–3588, 2003.
- [79] E. Vallat-Sauvain, C. Droz, F. Meillaud, J. Bailat, a. Shah, and C. Ballif, "Determination of Raman emission cross-section ratio in hydrogenated microcrystalline silicon," *Journal of Non-Crystalline Solids*, vol. 352, no. 9-20, pp. 1200–1203, 2006.
- [80] B. Smits, "Measurement of Sheet Resistivities with the Four-Point Probe," *Bell System Technical Journal*, vol. 37, no. 3, p. 711, 1958.

- [81] R. A. Sinton and A. Cuevas, "Contactless determination of current voltage characteristics and minority carrier lifetimes in semiconductors from quasi steady state photoconductance data," *Applied Physics Letters*, vol. 69, no. 17, p. 2510, 1996.
- [82] "Sinton Instruments WCT-120 Manual."
- [83] M. A. Green, "Accuracy of analytical expressions for solar cell fill factors," *Solar Cells*, vol. 7, pp. 337–340, dec 1982.
- [84] J. Merten, J. M. Asensi, C. Voz, A. Shah, R. Platz, and J. Andreu, "Improved equivalent circuit and analytical model for amorphous silicon solar cells and modules," *Electron Devices, IEEE Transactions on*, vol. 45, no. 2, pp. 423–429, 1998.
- [85] J. Merten, C. Voz, A. Muñoz, J. M. Asensi, and J. Andreu, "The role of the buffer layer in the light of a new equivalent circuit for amorphous silicon solar cells," *Solar Energy Materials and Solar Cells*, vol. 57, no. 2, pp. 153–165, 1999.
- [86] B. Drévilion, S. Kumar, and P. Roca i Cabarrocas, "In situ study of the thermal decomposition of B₂H₆ by combining spectroscopic ellipsometry and Kelvin probe measurements," *Journal of Applied Physics*, vol. 66, no. 66, pp. 3286–3292, 2004.
- [87] J. Ballutaud, C. Bucher, C. Hollenstein, A. Howling, U. Kroll, S. Benagli, A. Shah, and A. Buechel, "Reduction of the boron cross-contamination for plasma deposition of p-i-n devices in a single-chamber large area radio-frequency reactor," *Thin Solid Films*, vol. 468, no. 1-2, pp. 222–225, 2004.
- [88] O. Cubero, F. J. Haug, Y. Ziegler, L. Sansonnens, P. Couty, D. Fischer, and C. Ballif, "Reduction of the phosphorous cross-contamination in nip solar cells prepared in a single-chamber PECVD reactor," *Solar Energy Materials and Solar Cells*, vol. 95, no. 2, pp. 606–610, 2011.
- [89] R. Swanepoel, "Determination of the thickness and optical constants of amorphous silicon," *Journal of Physics E: Scientific Instruments*, vol. 16, no. 12, pp. 1214–1222, 2000.
- [90] B. Strahm, A. Howling, L. Sansonnens, and C. Hollenstein, "Plasma silane concentration as a determining factor for the transition from amorphous to microcrystalline silicon in SiH₄/H₂ discharges," *Plasma Sources Science and Technology*, vol. 16, no. 1, pp. 80–89, 2006.
- [91] C. Shin, S. M. Iftiqar, J. Park, Y. Kim, S. Baek, J. Jang, M. Kim, J. Jung, Y. Lee, S. Kim, and J. Yi, "Optimization of intrinsic hydrogenated amorphous silicon deposited by very high-frequency plasma-enhanced chemical vapor deposition using the relationship between Urbach energy and silane depletion fraction for solar cell application," *Thin Solid Films*, vol. 547, pp. 256–262, 2013.

Bibliography

- [92] A. Descoedres, L. Barraud, R. Bartlome, G. Choong, S. De Wolf, F. Zicarelli, and C. Ballif, "The silane depletion fraction as an indicator for the amorphous/crystalline silicon interface passivation quality," *Applied Physics Letters*, vol. 97, no. 18, pp. 4–7, 2010.
- [93] A. Feltrin, B. Strahm, G. Bugnon, C. Ballif, and A. Howling, "Input silane concentration effect on the a-Si:H to mc-Si:H transition width," *Solar Energy Materials and Solar Cells*, vol. 94, no. 3, pp. 432–534, 2000.
- [94] G. Bugnon, A. Feltrin, F. Meillaud, J. Bailat, and C. Ballif, "Influence of pressure and silane depletion on microcrystalline silicon material quality and solar cell performance," *Journal of Applied Physics*, vol. 105, no. 6, 2009.
- [95] J. S. Custer, M. O. Thompson, D. C. Jacobson, J. M. Poate, S. Roorda, W. C. Sinke, and F. Spaepen, "Density of amorphous Si," *Applied Physics Letters*, vol. 64, no. 4, p. 437, 1994.
- [96] U. Kroll, J. Meier, P. Torres, J. Pohl, and A. Shah, "From amorphous to microcrystalline silicon films prepared by hydrogen dilution using the VHF (70 MHz) GD technique," *Journal of Non-Crystalline Solids*, vol. 227-230, pp. 68–72, 1998.
- [97] M. Takai, T. Nishimoto, T. Takagi, M. Kondo, and a. Matsuda, "Guiding principles for obtaining stabilized amorphous silicon at larger growth rates," *Journal of Non-Crystalline Solids*, vol. 266-269, pp. 90–94, 2000.
- [98] M. Isomura, M. Kondo, and A. Matsuda, "High-pressure plasma CVD for high-quality amorphous silicon," *Solar Energy Materials and Solar Cells*, vol. 66, no. 1-4, pp. 375–380, 2001.
- [99] S. Muthmann and A. Gordijn, "Amorphous silicon solar cells deposited with non-constant silane concentration," *Solar Energy Materials and Solar Cells*, vol. 95, no. 2, pp. 573–578, 2011.
- [100] K. H. Kim, E. V. Johnson, and P. Roca i Cabarrocas, "Irreversible light-induced degradation and stabilization of hydrogenated polymorphous silicon solar cells," *Solar Energy Materials and Solar Cells*, vol. 105, pp. 208–212, 2012.
- [101] C. R. Wronski and R. W. Collins, "Phase engineering of a-Si:H solar cells for optimized performance," *Solar Energy*, vol. 77, no. 6, pp. 877–885, 2004.
- [102] E. B. Hamers, A. Fontcuberta i Morral, C. Niikura, R. Brenot, and P. Roca i Cabarrocas, "Contribution of ions to the growth of amorphous, polymorphous, and microcrystalline silicon thin films," *J. Appl. Phys.*, vol. 88, no. 6, pp. 3674–3688, 2000.
- [103] R. W. Collins and A. S. Ferlauto, "Advances in plasma-enhanced chemical vapor deposition of silicon films at low temperatures," *Current Opinion in Solid State and Materials Science*, vol. 6, no. 5, pp. 425–437, 2002.

- [104] T. Nishimoto, M. Takai, H. Miyahara, M. Kondo, and A. Matsuda, "Amorphous silicon solar cells deposited at high growth rate," *Journal of Non-Crystalline Solids*, vol. 299-302, pp. 1116–1122, apr 2002.
- [105] C. Longeaud and P. Roca i Cabarrocas, "A new type of material for photovoltaic devices: hydrogenated polymorphous silicon," in *Proc. 2nd WPVSEC*, (Vienna), p. 10, 1998.
- [106] K. H. Kim, *Hydrogenated polymorphous silicon: establishing the link between hydrogen microstructure and irreversible solar cell kinetics during light soaking*. PhD thesis, Ecole Polytechnique, 2014.
- [107] C. Koch, M. Ito, and M. Schubert, "Low temperature deposition of amorphous silicon solar cells," *Solar Energy Materials and Solar Cells*, vol. 68, no. 2, pp. 227–236, 2001.
- [108] P. Roca i Cabarrocas, "Plasma enhanced chemical vapor deposition of amorphous, polymorphous and microcrystalline silicon films," *Journal of Non-Crystalline Solids*, vol. 266-269, pp. 31–37, 2000.
- [109] Y. Maemura, H. Fujiyama, T. Takagi, and R. Hayashi, "Particle formation and a-Si: H film deposition in narrow-gap RF plasma CVD," *Thin solid films*, vol. 345, pp. 80–84, 1999.
- [110] U. Dutta and P. Chatterjee, "The open circuit voltage in amorphous silicon p-i-n solar cells and its relationship to material, device and dark diode parameters," *Journal of Applied Physics*, vol. 96, no. 4, pp. 2261–2271, 2004.
- [111] S. Bengali, D. Borrello, E. Vallat-Sauvain, J. Meier, and U. Kroll, "US Patent: US2011/0186127A1: Method for depositing an amorphous silicon film for photovoltaic devices with reduced light induced degradation for improved stabilized performance," 2011.
- [112] H. S. Wal, "US Patent A7668849: Amorphous silicon/polycrystalline thin film solar cells," 1991.
- [113] J. Liang, E. a. Schiff, S. Guha, B. Yan, and J. Yang, "Hole-mobility limit of amorphous silicon solar cells," *Applied Physics Letters*, vol. 88, no. 6, pp. 98–101, 2006.
- [114] C. R. Wronski and X. Niu, "The limited relevance of SWE dangling bonds to degradation in high-quality a-Si:H solar cells," *IEEE Journal of Photovoltaics*, vol. 4, no. 3, pp. 778–784, 2014.
- [115] S. Abolmasov, H. Woo, R. Planques, J. Holovský, E. Johnson, A. Purkrt, and P. Roca i Cabarrocas, "Substrate and p-layer effects on polymorphous silicon solar cells," *EPJ Photovoltaics*, vol. 5, p. 55206, 2014.

Bibliography

- [116] M. Diouf and P. Roca i Cabarrocas, "LPICM Rapport de stage de reseche: Optimisation de cellules solaires a base de silicium polymorphe," 2014.
- [117] J. Ni, J. Zhang, Y. Cao, X. Wang, X. Chen, X. Geng, and Y. Zhao, "Low temperature deposition of high open circuit voltage ($>1.0V$) pin type amorphous silicon solar cells," *Solar Energy Materials and Solar Cells*, vol. 95, no. 7, pp. 1922–1926, 2011.
- [118] S. Kim, J. W. Chung, H. Lee, J. Park, Y. Heo, and H. M. Lee, "Remarkable progress in thin-film silicon solar cells using high-efficiency triple-junction technology," *Solar Energy Materials and Solar Cells*, vol. 119, pp. 26–35, 2013.
- [119] G. Yue, B. Yan, C. Teplin, J. Yang, and S. Guha, "Optimization and characterization of ip buffer layer in hydrogenated nanocrystalline silicon solar cells," *Journal of Non-Crystalline Solids*, vol. 354, no. 19-25, pp. 2440–2444, 2008.
- [120] B. Rech, C. Beneking, and H. Wagner, "Improvement in stabilized efficiency of a-Si:H solar cells through optimized p/i-interface layers," *Solar Energy Materials and Solar Cells*, vol. 41-42, pp. 475–483, jun 1996.
- [121] K. H. Kim, S. Kasout, E. V. Johnson, and P. Roca I Cabarrocas, "Substrate versus superstrate configuration for stable thin film silicon solar cells," *Solar Energy Materials and Solar Cells*, vol. 119, pp. 124–128, 2013.
- [122] P. Roca i Cabarrocas, "A fully automated hot-wall multiplasma-monochamber reactor for thin film deposition," *Journal of Vacuum Science & Technology A: Vacuum, Surfaces, and Films*, vol. 9, no. 4, p. 2331, 1991.
- [123] R. Biron, C. Pahud, F. J. Haug, J. Escarre, K. Soderstrom, and C. Ballif, "Window layer with p doped silicon oxide for high Voc thin-film silicon n-i-p solar cells," *Journal of Applied Physics*, vol. 110, no. 12, p. 124511, 2011.
- [124] V. Smirnov, A. Lambertz, B. Grootnoonk, R. Carius, and F. Finger, "Microcrystalline silicon oxide (mc-SiOxH) alloys A versatile material for application," *Journal of Non-Crystalline Solids*, vol. 358, no. 17, pp. 1954–1957, 2011.
- [125] A. Lambertz, F. Finger, B. Hollander, J. Rath, and R. Schropp, "Boron-doped hydrogenated microcrystalline silicon oxide (mc-SiOxH) for application in thin-film silicon solar cells," *Journal of Non-Crystalline Solids*, vol. 358, no. 17, pp. 1962–1965, 2011.
- [126] K. Yoon, Y. Kim, J. Park, C. H. Shin, S. Baek, J. Jang, S. Iftiqar, and J. Yi, "Preparation and characterization of p-type hydrogenated amorphous silicon oxide film and its application to solar cell," *Journal of Non-Crystalline Solids*, vol. 357, no. 15, pp. 2826–2832, 2011.

- [127] K. Sriprapha, N. Sitthiphol, P. Sangkhawong, V. Sangsuwan, A. Limmanee, and J. Sritharathikhun, "p-Type hydrogenated silicon oxide thin film deposited near amorphous to microcrystalline phase transition and its application to solar cells," *Current Applied Physics*, vol. 11, no. 1, pp. 47–49, 2011.
- [128] P. K. Chang, W. T. Hsu, P. T. Hsieh, C. H. Lu, C. H. Yeh, and M. P. Houn, "Improved stability of amorphous silicon solar cells with p-type nanocrystalline silicon carbide window layer," *Thin Solid Films*, vol. 520, no. 7, pp. 3096–3099, 2012.
- [129] T. Krajangsang, S. Kasashima, A. Hongsingthong, P. Sichanugrist, and M. Konagai, "Effect of p-mcSi1-xOx:H layer on performance of hetero-junction microcrystalline silicon solar cells under light concentration," *Current Applied Physics*, vol. 12, no. 2, pp. 515–520, 2012.
- [130] H. Dersch, J. Stuke, and J. Beichler, "Light-induced dangling bonds in hydrogenated amorphous silicon," *Applied Physics Letters*, vol. 38, pp. 456–458, 1981.
- [131] M. Stutzmann, W. B. Jackson, and C. C. Tsai, "Light-induced metastable defects in hydrogenated amorphous silicon: A systematic study," *Phys. Rev. B*, vol. 32, no. 1, pp. 23–47, 1985.
- [132] D. Carlson, K. Rajan, and D. Bradley, "Irreversible light-induced degradation in amorphous silicon solar cells," *Conference Record of the Twenty Sixth IEEE Photovoltaic Specialists Conference - 1997*, pp. 595–598, 1997.
- [133] H. Fritzsche, "Development in understanding and controlling the Staebler-Wronski Effect in a-Si : H," *Annual Reviewers of Material Research*, vol. 31, pp. 47–79, 2001.
- [134] S. Heck and H. M. Branz, "Fingerprints of two distinct defects causing light-induced photoconductivity degradation in hydrogenated amorphous silicon," *Applied Physics Letters*, vol. 79, no. 19, pp. 3080–3082, 2001.
- [135] I. Hirabayashi, K. Morigaki, and S. Nitta, "New Evidence for Defect Creation by High Optical Excitation in Glow Discharge Amorphous Silicon," *Japanese Journal of Applied Physics*, vol. 19, no. 7, p. 357, 1980.
- [136] J. Pankove and J. Berkeyheiser, "Light-induced radiative recombination centers in hydrogenated amorphous silicon," *Applied Physics Letters*, vol. 37, p. 705, 1980.
- [137] H. M. Branz, "Hydrogen Collision Model Of Light-Induced Metastability In Hydrogenated Amorphous Silicon," *Solid State Communications*, vol. 105, no. 6, pp. 387–391, 1998.
- [138] H. M. Branz, "The hydrogen collision model of metastability after 5 years: experimental tests and theoretical extensions," *Solar Energy Materials and Solar Cells*, vol. 78, no. 1-4, pp. 425–445, 2003.

Bibliography

- [139] T. Shimizu, "Staebler-Wronski Effect in Hydrogenated Amorphous Silicon and Related Alloy Films," *Japanese Journal of Applied Physics*, vol. 43, no. 6, pp. 3257–3268, 2004.
- [140] V. Nadazdy and M. Zeman, "Origin of charged gap states in a-Si:H and their evolution during light soaking," *Phys. Rev. B*, vol. 69, no. 16, p. 165213, 2004.
- [141] R. Biswas and B. C. Pan, "Mechanisms of metastability in hydrogenated amorphous silicon," *Solar Energy Materials and Solar Cells*, vol. 78, pp. 447–467, 2003.
- [142] L. K. Wagner and J. C. Grossman, "Microscopic Description of Light Induced Defects in Amorphous Silicon Solar Cells," *Physical Review Letters*, vol. 101, no. 26, p. 265501, 2008.
- [143] D. Carlson, "Hydrogenated microvoids and light-induced degradation of amorphous-silicon solar cells," *Applied Physics A*, vol. 41, no. 4, pp. 305–309, 1986.
- [144] M. Fehr, A. Schnegg, B. Rech, O. Astakhov, F. Finger, R. Bittl, C. Teutloff, and K. Lips, "Metastable Defect Formation at Microvoids Identified as a Source of Light-Induced Degradation in a-Si:H," *Physical Review Letters*, vol. 112, no. 6, p. 066403, 2014.
- [145] P. Kounavis, "Light-induced Changes in the Gap States Above Midgap of Hydrogenated Amorphous Silicon," *Journal of Applied Physics*, vol. 97, no. 2, pp. 23707–237079, 2004.
- [146] A. Klaver and R. van Swaaij, "Modeling of light-induced degradation of amorphous silicon solar cells," *Solar Energy Materials and Solar Cells*, vol. 92, pp. 50–60, 2008.
- [147] T. Yanagisawa, "Long-term Degradation Tests of Amorphous Silicon Solar Cells: Correlation between light- and current- induced Degradation Characteristics," *Microelectronics Reliability*, vol. 35, no. 2, pp. 183–187, 1995.
- [148] F. Meillaud, E. Vallat-Sauvain, X. Niquille, M. Dubey, J. Bailat, A. Shah, and C. Ballif, "Light-induced degradation of thin film amorphous and microcrystalline silicon solar cells," *Conference Record of the Thirty-First IEEE Photovoltaic Specialists Conference - 2005*, pp. 1412–1415, 2005.
- [149] R. R  ther and J. Livingstone, "Seasonal variations in amorphous silicon solar module outputs and thin film characteristics," *Solar Energy Materials and Solar Cells*, vol. 36, no. 1, pp. 29–43, 1995.
- [150] Y. Hirata and T. Tani, "Output variation of photovoltaic modules with environmental factors - I. The effect of spectral solar radiation on photovoltaic module output," *Solar Energy*, vol. 55, no. 6, pp. 463–468, 1995.

- [151] J. Merten and J. Andreu, "Clear separation of seasonal effects on the performance of amorphous silicon solar modules by outdoor I/V -measurements," *Solar Energy Materials and Solar Cells*, vol. 52, pp. 11–25, 1998.
- [152] L. Fanni, A. Virtuani, and D. Chianese, "Seasonal Power Fluctuations of Single Junction Amorphous Silicon Modules It Is Possible To Distinguish Between Spectral Variations and Staebler-Wronski," in *25th European Photovoltaic Solar Energy Conference*, no. September, pp. 4265–4268, 2010.
- [153] E. Sanchez, J. Izard, and M. Dominguez, "Experimental Study of Light Induced Degradation in a-Si:H Thin Film Modules under different climate conditions," in *27th European Photovoltaic Solar Energy Conference*, no. 5, pp. 651–653, 2014.
- [154] A. Caballero, L. Morrone, M. LLuscà, J. M. Asensi, J. Bertomeu, and J. Andreu, "Light induced degradation and long term stability of a-Si solar cells and modules," in *Proc. 29th W-PVSEC, Amsterdam*, 2014.
- [155] M. Hussin, S. Shaari, a.M. Omar, and Z. Zain, "Amorphous silicon thin-film: Behaviour of light-induced degradation," *Renewable and Sustainable Energy Reviews*, vol. 43, pp. 388–402, 2015.
- [156] R. Roldan, J. M. Asensi, J. Bertomeu, and J. Andreu, "Studies on stability of a-Si PV modules by field dark IV measurements," in *Proc. 29th W-PVSEC, Amsterdam*.
- [157] R. Rütther, G. Kleiss, and K. Reiche, "Spectral effects on amorphous silicon solar module fill factors," *Solar Energy Materials and Solar Cells*, vol. 71, no. 3, pp. 375–385, 2002.
- [158] R. Gottschalg, D. G. Infield, and M. J. Kearney, "Experimental study of variations of the solar spectrum of relevance to thin film solar cells," *Solar Energy Materials and Solar Cells*, vol. 79, no. 4, pp. 527–537, 2003.
- [159] R. Gottschalg, T. R. Betts, D. G. Infield, and M. J. Kearney, "The effect of spectral variations on the performance parameters of single and double junction amorphous silicon solar cells," *Solar Energy Materials and Solar Cells*, vol. 85, no. 3, pp. 415–428, 2005.
- [160] T. Yamawaki, S. Mizukami, A. Yamazaki, and H. Takahashi, "Thermal recovery effect on light-induced degradation of amorphous silicon solar module under the sunlight," *Solar Energy Materials and Solar Cells*, vol. 47, no. 1-4, pp. 125–134, 1997.
- [161] M. Kondo, H. Nishio, S. Kurata, K. Hayashi, A. Takenaka, A. Ishikawa, K. Nishimura, H. Yamagishi, and Y. Tawada, "Effective conversion efficiency enhancement of amorphous silicon modules by operation temperature elevation," *Solar Energy Materials and Solar Cells*, vol. 49, no. 1-4, pp. 1–6, 1997.

Bibliography

- [162] M. Shima, M. Isomura, K. I. Wakisaka, K. Murata, and M. Tanaka, "The influence of operation temperature on the output properties of amorphous silicon-related solar cells," *Solar Energy Materials and Solar Cells*, vol. 85, pp. 167–175, 2005.
- [163] P. Otero, I. Quelle, M. Fonrodona, S. Santos, J. Rodriguez, E. Grande, C. Mata, M. Vetter, and J. Andreu, "Improvement of very large area (5.7 m²) a-Si:H PV module manufacturing by PE-CVD process control," in *Proc. 27th W-PVSEC, Frankfurt*, 2012.
- [164] A. Louwen, W. van Sark, A. de Wall, A. Faaji, and R. Schropp, "Evaluation of the effect of outdoor solar spectrum variations on the performance of different PV technologies," in *Proc. 29th W-PVSEC, Amsterdam*.
- [165] J. M. Asensi, J. Merten, C. Voz, and J. Andreu, "Analysis of the role of mobility-lifetime products in the performance of amorphous silicon p-i-n solar cells," *J. Appl. Phys.*, vol. 85, no. 5, pp. 2939–2951, 1999.
- [166] J. Hubin and A. Shah, "Effect of the recombination function on the collection in a pin solar cell," *Phil*, vol. 72, pp. 589–599, 1995.
- [167] N. Beck, N. Wyrsh, C. Hof, and A. Shah, "Mobility lifetime product—A tool for correlating a-Si:H film properties and solar cell performances," *Journal of Applied Physics*, vol. 79, no. 12, p. 9361, 1996.
- [168] P. Stradins, "Light-induced degradation in a-Si:H and its relation to defect creation," *Solar Energy Materials and Solar Cells*, vol. 78, no. 1-4, pp. 349–367, 2003.
- [169] F. Kail, S. Fellah, A. Abramov, A. Hadjadj, and P. Roca i Cabarrocas, "Experimental evidence for extended hydrogen diffusion in silicon thin films during light-soaking," *Journal of Non-Crystalline Solids*, vol. 352, no. 9-20 SPEC. ISS., pp. 1083–1086, 2006.
- [170] V. Venezia, R. Duffy, L. Pelaz, M. Hopstaken, G. Maas, T. Dao, Y. Tamminga, and P. Graat, "Boron diffusion in amorphous silicon," *Materials Science and Engineering: B*, vol. 124-125, pp. 245–248, 2005.
- [171] D. De Salvador, E. Napolitani, S. Mirabella, E. Bruno, G. Impellizzeri, G. Bisognin, E. Pecora, F. Priolo, and a. Carnera, "Experimental investigations of boron diffusion mechanisms in crystalline and amorphous silicon," *Materials Science and Engineering: B*, vol. 154-155, pp. 240–246, 2008.
- [172] W. L. Bailey, M. G. Coleman, C. B. Harris, and I. A. Lesk, "US Patent: 4137123 - Texture etching of silicon: method," 1979.
- [173] W. Shockley and W. Read, "Statistics of the recombinations of holes and electrons," *Physical Review Letters*, vol. 87, pp. 835–842, 1952.

- [174] R. Hall, "Electron-Hole recombination in Germanium," *Physical Review Letters*, vol. 87, pp. 387–387, 1952.
- [175] A. G. Aberle, "Surface passivation of crystalline silicon solar cells: a review," *Progress in Photovoltaics: Research and Applications*, vol. 8, no. 5, pp. 473–487, 2000.
- [176] X. Zhang, A. Cuevas, and A. Thomson, "Process control of reactive sputter deposition of AlO_x and improved surface passivation of crystalline silicon," *IEEE Journal of Photovoltaics*, vol. 3, no. 1, pp. 183–188, 2013.
- [177] J. Schmidt, B. Veith, and R. Brendel, "Effective surface passivation of crystalline silicon using ultrathin Al₂O₃ films and Al₂O₃/SiN_x stacks," *Physica Status Solidi*, vol. 3, no. 9, pp. 287–289, 2009.
- [178] F. W. Chen, T. Li, and J. E. Cotter, "Passivation of boron emitters on n-type silicon by plasma-enhanced chemical vapor deposited silicon nitride," *Applied Physics Letters*, vol. 88, no. 26, p. 263514, 2006.
- [179] I. Martin, M. Vetter, A. Orpella, C. Voz, J. Puigdollers, and R. Alcubilla, "Surface passivation of n-type crystalline Si by plasma-enhanced-chemical-vapor-deposited amorphous SiC_xH and amorphous SiC_xN_y:H films," *Applied Physics Letters*, vol. 81, no. 23, pp. 4461–4463, 2002.
- [180] J. Schmidt and M. Kerr, "Highest-quality surface passivation of low-resistivity p-type silicon using stoichiometric PECVD silicon nitride," *Solar Energy Materials and Solar Cells*, vol. 65, no. 1, pp. 585–591, 2001.
- [181] M. J. Kerr, J. Schmidt, A. Cuevas, and J. H. Bultman, "Surface recombination velocity of phosphorus-diffused silicon solar cell emitters passivated with plasma enhanced chemical vapor deposited silicon nitride and thermal silicon oxide," *Journal of Applied Physics*, vol. 89, no. 7, pp. 3821–3826, 2001.
- [182] S. Dauwe, J. Schmidt, and R. Hezel, "Very low surface recombination velocities on p- and n-type silicon wafers passivated with hydrogenated amorphous silicon films," in *29th IEEE Photovoltaic Specialists Conference*, pp. 1246–1249, 2002.
- [183] M. Schaper, J. Schmidt, H. Plagwitz, and R. Brendel, "20.1%-Efficient Crystalline Silicon Solar Cell With Amorphous Silicon Rear-Surface Passivation," *Progress in Photovoltaics: Research and Applications*, vol. 13, no. 5, pp. 381–386, 2005.
- [184] S. De Wolf and G. Beaucarne, "Surface passivation properties of boron-doped plasma-enhanced chemical vapor deposited hydrogenated amorphous silicon films on p-type crystalline Si substrates," *Applied Physics Letters*, vol. 88, no. 2, pp. 1–3, 2006.

Bibliography

- [185] G. Dingemans and W. M. M. Kessels, "Status and prospects of Al₂O₃-based surface passivation schemes for silicon solar cells," *Journal of Vacuum Science & Technology A: Vacuum, Surfaces, and Films*, vol. 30, no. 4, p. 040802, 2012.
- [186] S. Zhao, Q. Qiao, S. Zhang, J. Ji, Z. Shi, and G. Li, "Rear passivation of commercial multi-crystalline PERC solar cell by PECVD Al₂O₃," *Applied Surface Science*, vol. 290, pp. 66–70, 2014.
- [187] J. Schmidt, T. Lauinger, A. G. Aberle, and R. Hezel, "Record low surface recombination velocities on low-resistivity silicon solar cell substrates," *IEEE Photovoltaic Specialists Conference*, pp. 413–416, 1996.
- [188] B. Hoex, J. Schmidt, R. Bock, P. P. Altermatt, M. C. M. van de Sanden, and W. M. M. Kessels, "Excellent passivation of highly doped p-type Si surfaces by the negative-charge-dielectric Al₂O₃," *Applied Physics Letters*, vol. 91, no. 11, p. 112107, 2007.
- [189] B. Hoex, J. Schmidt, P. Pohl, M. C. M. van de Sanden, and W. M. M. Kessels, "Silicon surface passivation by atomic layer deposited Al₂O₃," *Journal of Applied Physics*, vol. 104, no. 4, p. 044903, 2008.
- [190] J. Benick, B. Hoex, M. C. M. van de Sanden, W. M. M. Kessels, O. Schultz, and S. W. Glunz, "High efficiency n-type Si solar cells on Al₂O₃-passivated boron emitters," *Applied Physics Letters*, vol. 92, no. 25, p. 253504, 2008.
- [191] M. Ion, C. Berbecaru, S. Iftimie, M. Filipescu, M. Dinescu, and S. Anothe, "PLD deposited Al₂O₃ thin film for transparent electronics," *Digest Journal of Nanomaterials and Biostructures*, vol. 7, no. 4, pp. 1609–1614, 2012.
- [192] P. Nayar and A. Khanna, "Optical properties of alumina films grown by pulsed laser deposition," *European Physical Journal. Applied Physics*, vol. 64, no. 10301, pp. 1–8, 2013.
- [193] Y.-I. Ogita and M. Tachihara, "Reduction of surface recombination velocity by rapid thermal annealing of p-Si passivated by catalytic-chemical vapor deposited alumina films," *Thin Solid Films*, vol. 575, pp. 56–59, 2015.
- [194] G. López, P. R. Ortega, C. Voz, I. Martín, M. Colina, A. B. Morales, A. Orpella, and R. Alcubilla, "Surface passivation and optical characterization of Al₂O₃/a-SiC_x stacks on c-Si substrates," *Beilstein Journal of Nanotechnology*, vol. 4, no. 1, pp. 726–731, 2013.
- [195] J. Schmidt, B. Veith, and R. Brendel, "Effective surface passivation of crystalline silicon using ultrathin Al₂O₃ films and Al₂O₃/SiN_x stacks," *Physica Status Solidi*, vol. 3, pp. 287–289, 2009.
- [196] T. Li and A. Cuevas, "Effective surface passivation of crystalline silicon by rf sputtered aluminum oxide," *Physica Status Solidi*, vol. 5, pp. 160–162, 2009.

- [197] M. Bhaisare, A. Misra, A. Kottantharayil, and S. Member, “Aluminum Oxide Deposited by Pulsed-DC Reactive Sputtering for Crystalline Silicon Surface Passivation,” vol. 3, no. 3, pp. 930–935, 2013.
- [198] S. Chen, L. Tao, L. Zeng, and R. Hong, “RF magnetron sputtering aluminum oxide film for surface passivation on crystalline silicon wafers,” *International Journal of Photoenergy*, vol. 2013, 2013.
- [199] M. Ohring, “Discharges, Plasmas, and Ion-Surface Interactions,” in *Materials Science of Thin Films*, vol. 226, ch. 4, p. 794, Academic Press, 2001.
- [200] J. E. Cotter, J. H. Guo, P. J. Cousins, M. D. Abbott, F. W. Chen, and K. C. Fisher, “P-type versus n-type silicon wafers: Prospects for high-efficiency commercial silicon solar cells,” *IEEE Transactions on Electron Devices*, vol. 53, no. 8, pp. 1893–1901, 2006.
- [201] A. Cuevas, S. Riepe, M. J. Kerr, D. Macdonald, G. Coletti, and F. Ferrazza, “n-type multicrystalline silicon: a stable, high lifetime material,” in *3rd WCPVEC*, (Osaka), pp. 1312–1315, 2003.
- [202] D. Macdonald and L. J. Geerligs, “Recombination activity of interstitial iron and other transition metal point defects in p- and n-type crystalline silicon,” *Applied Physics Letters*, vol. 85, no. 18, pp. 4061–4063, 2004.
- [203] S. Martinuzzi, O. Palais, M. Pasquinelli, D. Barakel, and F. Ferrazza, “n-type multicrystalline silicon wafers for solar cells,” in *31st IEEE PSC*, (New York), pp. 919–922, 2005.
- [204] J. A. García-Valenzuela, Á. Caballero, J. M. Asensi, J. Bertomeu, J. Andreu, L. G. Gerling-Sarabia, A. B. Morales, P. Ortega, and C. Voz, “Intermediate amorphous silicon layer for crystalline silicon passivation with alumina,” in *30th European Photovoltaic Solar Energy Conference and Exhibition*, (Hambourgh), 2015.
- [205] T. Minami, “Transparent conducting oxide semiconductors for transparent electrodes,” *Semiconductor Science and Technology*, vol. 20, no. 4, pp. S35–S44, 2005.
- [206] B.-S. Chiou and J.-H. Tsai, “Antireflective coating for ITO films deposited on glass substrate,” *Journal of Materials Science: Materials in Electronics*, vol. 10, no. 7, pp. 491–495, 1999.
- [207] L.-j. Meng and M. dos Santos, “Study of the effect of the oxygen partial pressure on the properties of rf reactive magnetron sputtered tin-doped indium oxide films,” *Applied Surface Science*, vol. 120, no. 3-4, pp. 243–249, 1997.
- [208] H. Zhu, J. Hüpkes, E. Bunte, and S. M. Huang, “Oxygen influence on sputtered high rate ZnO:Al films from dual rotatable ceramic targets,” *Applied Surface Science*, vol. 256, no. 14, pp. 4601–4605, 2010.

Bibliography

- [209] S. Rahmane, M. Abdou, M. Salah, and N. Barreau, "Oxygen effect in radio frequency magnetron sputtered aluminium doped zinc oxide films," *Thin Solid Films*, vol. 562, pp. 70–74, 2014.
- [210] M. Dressel and G. Grüner, *Electrodynamics of Solids*. UK: Cambridge University Press, 2002.
- [211] L.-j. Meng and M. dos Santos, "Properties of indium tin oxide films prepared by rf reactive magnetron sputtering at different substrate temperature," *Thin Solid Films*, vol. 322, no. 1-2, pp. 56–62, 1998.
- [212] L. R. Cruz, C. Legnani, I. G. Matoso, C. L. Ferreira, and H. R. Moutinho, "Influence of pressure and annealing on the microstructural and electro-optical properties of RF magnetron sputtered ITO thin films," *Materials Research Bulletin*, vol. 39, no. 7-8, pp. 993–1003, 2004.
- [213] Y. Hu, X. Diao, C. Wang, W. Hao, and T. Wang, "Effects of heat treatment on properties of ITO films prepared by rf magnetron sputtering," *Vacuum*, vol. 75, no. 2, pp. 183–188, 2004.
- [214] E. Vallat-Sauvain, U. Kroll, J. Meier, N. Wyrsch, and a. Shah, "Microstructure and surface roughness of microcrystalline silicon prepared by very high frequency-glow discharge using hydrogen dilution," *Journal of Non-Crystalline Solids*, vol. 266-269, no. 2000, pp. 125–130, 2000.
- [215] R. W. Collins, A. S. Ferlauto, G. M. Ferreira, C. Chen, J. Koh, R. J. Koval, Y. Lee, J. M. Pearce, and C. R. Wronski, "Evolution of microstructure and phase in amorphous, protocrystalline, and microcrystalline silicon studied by real time spectroscopic ellipsometry," *Solar Energy Materials and Solar Cells*, vol. 78, no. 1-4, pp. 143–180, 2003.
- [216] R. E. I. Schropp, *Amorphous (Protocrystalline) and Microcrystalline Thin Film Silicon Solar Cells*. The Netherlands: Elsevier, 2006.
- [217] U. K. Das, M. Z. Burrows, M. Lu, S. Bowden, and R. W. Birkmire, "Surface passivation and heterojunction cells on Si (100) and (111) wafers using dc and rf plasma deposited Si:H thin films," *Applied Physics Letters*, vol. 92, no. 100, pp. 10–12, 2008.
- [218] H. Fujiwara and M. Kondo, "Effects of a-Si:H layer thicknesses on the performance of a-Si:H/c-Si heterojunction solar cells," *Journal of Applied Physics*, vol. 101, no. 5, pp. 1–9, 2007.
- [219] S. De Wolf and M. Kondo, "Abruptness of a-Si:H/c-Si interface revealed by carrier lifetime measurements," *Applied Physics Letters*, vol. 90, no. 4, p. 042111, 2007.

- [220] S. Olibet, E. Vallat-Sauvain, and C. Ballif, “Model for a-Si:H/c-Si interface recombination based on the amphoteric nature of silicon dangling bonds,” *Physical Review B - Condensed Matter and Materials Physics*, vol. 76, no. 3, pp. 1–14, 2007.

List of Figures

| | | |
|-----|--|----|
| 1.1 | Solar PV global capacity, 2004-2014. Courtesy of REN21, 2015, <i>Renewables 2015 Global Status Report</i> (ISBN 978-3-9815934-6-4) [2]. | 10 |
| 1.2 | Median reported installed prices of residential and non-residential PV systems over time in the United States. This plot is extracted from SunShot Photovoltaic System Pricing Trends 2015 edition, courtesy of the National Renewable Energy Laboratory (NREL), Golden, CO. [4]. . | 10 |
| 1.3 | Evolution of the conversion efficiency of photovoltaic technologies. This plot is courtesy of the National Renewable Energy Laboratory (NREL), Golden, CO. | 14 |
| 1.4 | Schematic structure of a single junction silicon thin film solar cell in superstrate (left) and substrate (right) configuration. The layers are shown as flat to simplify, but they are normally textured. | 16 |
| 1.5 | Schematic structure of a PERC silicon solar cell. In this case, a <i>p</i> -wafer with <i>n</i> -emitter is shown. The layers are shown as flat to simplify, but they are normally textured. | 18 |
| 1.6 | Schematic structure of a double junction HIT silicon solar cell. In this case, a <i>p</i> -wafer with <i>n</i> -emitters is shown. The layers are shown as flat to simplify, but they are normally textured. | 19 |
| 1.7 | Photography of a plasma glow discharge in the PECVD reactor at the UB. 24 | |
| 2.1 | Photography of the PECVD reactor in the cleanroom of the Universitat de Barcelona (before the HWCVD chamber installation.) | 30 |
| 2.2 | Schematic view of the equipment, with the conforming elements labeled. | 31 |
| 2.3 | Schematic view of the inside of the LoadLock chamber, showing the robot used to move the samples. | 32 |
| 2.4 | Left: Schematic view of the inside of the plasma deposition chambers. The outer elements have been removed for clarity. Right: Schematic view of the frontal piece of the substrate holder. The back piece is a whole piece, not a frame, but it has identical external shape. | 34 |
| 2.5 | Schematic top view of the masks used for metal deposition in layers (left) and cells (right). The units of the dimension lines are mm. | 39 |
| 2.6 | Process to finish a solar cell. From left to right: 1. Sample with AZO deposited over the whole area. 2. Sample scratched to let the metal reach the front TCO. 3. Sample with metal deposited with the mask. Front and back contacts are still connected. 4. Sample etched, extra AZO is removed. Front and back contacts are now isolated. | 41 |
| 2.7 | Scheme of one of the towers of the LED solar illuminator. | 44 |
| 2.8 | Photography of the operating solar cell illuminator. | 45 |

List of Figures

| | | |
|------|--|----|
| 2.9 | Map of the homogeneity of the J_{sc} over the sample panel. The center of the graphs corresponds to 100% of the J_{sc} under 1 sun in the <i>T-Solar</i> reference cell. | 46 |
| 2.10 | Straight line of calibration of the temperatures in the light soaking system. | 47 |
| 2.11 | Scheme of the inside of the vacuum chamber of the two point probe device. | 52 |
| 2.12 | Scheme of the device characterization system configuration to perform $J-V$ curve measurements. | 57 |
| 2.13 | Equivalent circuit of a thin film silicon solar cell (Courtesy of R.Roldan [60]). | 59 |
| 2.14 | Standard $J-V$ curve with all the parameters represented. The $P-V$ curve is shown to guide the eye to V_m and J_m | 60 |
| 2.15 | Scheme of the device characterization system configuration to perform EQE measurements. | 62 |
| 3.1 | Homogeneity map over a $9 \times 9 \text{ cm}^2$ intrinsic silicon layer. | 65 |
| 3.2 | Position of 1 cm^2 solar cells and central front contact over them $10 \times 10 \text{ cm}^2$ pin sample. | 66 |
| 3.3 | $J-V$ curves of the six positions on the sample shown on Fig. 3.2. | 66 |
| 3.4 | Evolution of the dark conductivity and photoconductivity of an a-Si:H layer with the under illumination time in the first 10 hours. | 71 |
| 3.5 | Calculated depletion versus silane flow. The points are the values used for the samples. | 74 |
| 3.6 | Thickness and deposition rate of depletion series samples. | 75 |
| 3.7 | Dark and photoconductivity in the initial (continuous line) and degraded (dots line) states of depletion series samples. | 76 |
| 3.8 | Gap and activation energy in depletion series samples. | 77 |
| 3.9 | Absorption coefficient in depletion series samples. The gray lines correspond to 600 nm ($\approx 2.07 \text{ eV}$) and 400 nm ($\approx 3.10 \text{ eV}$) and are drawn to guide the eye. | 78 |
| 3.10 | Thickness and deposition rate of hydrogen dilution series samples. | 80 |
| 3.11 | Dark and photoconductivity in the initial (continuous line) and degraded (dots line) states of hydrogen series samples. | 81 |
| 3.12 | Gap and activation energy in hydrogen series samples. | 82 |
| 3.13 | Absorption coefficient in hydrogen series samples. The gray lines correspond to 600 nm ($\approx 2.07 \text{ eV}$) and 400 nm ($\approx 3.10 \text{ eV}$) and are drawn to guide the eye. | 83 |
| 3.14 | Thickness and deposition rate of temperature series samples. | 85 |
| 3.15 | Dark and photoconductivity in the initial (continuous line) and degraded (dots line) states of temperature series samples. | 86 |
| 3.16 | Gap and activation energy of temperature series samples. | 87 |
| 3.17 | Absorption coefficient in temperature series samples. The gray lines correspond to 600 nm ($\approx 2.07 \text{ eV}$) and 400 nm ($\approx 3.10 \text{ eV}$) and are drawn to guide the eye. | 87 |
| 3.18 | Results of dark conductivity optimization of boron doped amorphous layer series. The numbers next to the name of the series indicate the order. | 91 |

| | | |
|------|---|-----|
| 3.19 | Results of dark conductivity optimization of boron doped microcrystalline layer series. The numbers next to the name of the series correspond to the order. | 94 |
| 3.20 | Results of crystalline fraction of boron doped microcrystalline layer series. The numbers next to the name of the series correspond to the order. . . | 94 |
| 3.21 | $J-V$ curves of the best cell of each TCO deposition. | 97 |
| 3.22 | EQE curves of the best cells with and without TCO. | 98 |
| 3.23 | $J-V$ curves of the best cell of each metal deposition. | 99 |
| 3.24 | $J-V$ curves of the best a-Si:H solar cells varying p layer thickness. . . . | 100 |
| 3.25 | EQE curves of the best a-Si:H solar cells varying p layer thickness. . . . | 101 |
| 3.26 | $J-V$ curves of the best cells in PIN configuration trials. | 106 |
| 3.27 | $J-V$ curves of the best cells in NIP configuration trials. | 107 |
| 3.28 | EQE curves of the best cells in PIN configuration trials. | 109 |
| 3.29 | EQE curves of the best cells in NIP configuration trials. | 110 |
| 4.1 | Evolution of the monthly plant availability, energy yield and performance ratio of the Saelices PV power station. | 119 |
| 4.2 | Evolution of V_{oc} , J_{sc} , FF and η (from top down) during the LID of the UB samples of different thickness. The left column shows the actual values and the right column shows the relative values. | 122 |
| 4.3 | Evolution of $\mu\tau$ with the LID time for the UB cells of different thicknesses. The relative value is obtained as the ratio of the actual value to the initial one for each sample. | 127 |
| 4.4 | $\mu\tau_{Init}/\mu\tau_{Deg} \approx Ndb_{Deg}/Ndb_{Init}$ evolution. The left graph shows the evolution with time for different thicknesses. Conversely, the right graph shows the dependence with thickness for different degradation times. . . | 129 |
| 4.5 | Intercept value (left) and slope (right) for each time, obtained through linear regressions from the right graph in Fig. 4.4, corresponding to Eq. 4.10. | 130 |
| 4.6 | Evolution of V_{oc} , J_{sc} , FF and η during the degradation of samples $T-Solar$ A (squares) and $T-Solar$ B (circles). When degradation is performed at 60°C the plot is shown in red, and when it is at 30°C , in blue. The central vertical line indicates the temperature switch. | 133 |
| 4.7 | $J-V$ curves of the samples 1, 4 (upper) and 2, 3 (lower) in the different stages of degradation. The colors indicate the temperature of degradation and the symbols, the order of the degradation processes. | 137 |
| 4.8 | A and EQE curves of the samples 1, 4 (upper) and 2, 3 (lower) in the different stages of degradation. The colors indicate the temperature of degradation and the symbols, the order of the degradation processes. . . | 142 |
| 4.9 | Difference between the EQE of the annealed and the degraded states of the samples 1, 4 (upper) and 2, 3 (lower) in the different stages of degradation. The colors indicate the temperature of degradation and the symbols, the order of the degradation processes. | 144 |

List of Figures

| | | |
|------|--|-----|
| 5.1 | Configuration of the samples used for the experiments in passivation with alumina deposited with sputtering. The depositions are symmetrical, so the layers in both sides are almost identical. | 158 |
| 5.2 | Effective lifetime (top) and effective surface recombination velocity (bottom) of p -Si and n -Si samples passivated with Al_2O_3 and a-Si:H/ Al_2O_3 layers after the annealing at 350°C | 161 |
| 5.3 | Transmittance of the ITO samples of the partial pressure series (left) and temperature series (right). | 166 |
| 5.4 | Parameter comparison for both oxygen partial pressure (black) and temperature (red) series. $\%T_a$ and $\%T_{\mu c}$ is the percentage of the area integrated under the curve of the $EQEs$ | 167 |
| 5.5 | Evolution of the structure of the device used for ITO optimization in the different stages of measurement. | 169 |
| 5.6 | J - V and EQE curves for the 600 nm pitch samples with different ITOs. The values on the legend in the $EQEs$ graph are the integrated J_{sc} for each sample. | 172 |
| 5.7 | Values of the dark conductivity and activation energy with the temperature (top) and absorbances (bottom) of the amorphous (left) and microcrystalline (right) layers used in the temperature optimization for emitters. | 175 |
| 5.8 | Structure of the a-Si:H solar cell used to optimize the thicknesses of the p -layers. | 177 |
| 5.9 | Structures used for p -type emitter trials over p - and n -type wafers. The front part (i -layer, p -emitter and ITO) was deposited in the UB. The rear passivating stacks were deposited in the UPC before the emitters. In the case of the n -wafer, the laser firing was performed after the last annealing process. | 180 |
| 5.10 | Measured carrier lifetimes for both p (top) and n (bottom) wafers with the p -type emitter and ITO deposited in the UB. Several curves at different stages after consecutive annealing or laser firing processes are shown. | 181 |
| 5.11 | Structure used for i -layer passivation trials. The depositions are symmetrical, so the layers on both sides are identical. The ITO is deposited at room temperature with the same conditions as in Sec. 5.4.1. | 184 |

List of Tables

| | | |
|------|---|-----|
| 2.1 | Precursor gases for the PECVD used in the reactor. Purity is written here as quality code, where the number before the dot represents the number of nines and the last number indicates the last decimal, <i>i.e.</i> 4.5 would mean a purity of 99.995 % | 35 |
| 2.2 | Targets used for depositing TCOs and metals used in the front and back contacts of the cells. | 37 |
| 3.1 | Criteria for 'device quality' amorphous silicon films [23]. | 67 |
| 3.2 | Deposition parameters for intrinsic silicon layers. The bold quantity in varying parameters is the one kept constant in the rest of the series. . . | 68 |
| 3.3 | Criteria for boron doped amorphous silicon films for its application in solar cells [23]. | 89 |
| 3.4 | Criteria for boron doped microcrystalline silicon films for its application in solar cells [23]. | 89 |
| 3.5 | Deposition parameters for boron doped amorphous silicon layers. | 90 |
| 3.6 | Deposition parameters for the optimized boron doped amorphous silicon layers. | 92 |
| 3.7 | Deposition parameters for boron doped microcrystalline silicon layers. The numbers next to the name of the series indicate the order. | 93 |
| 3.8 | Deposition parameters for the optimized boron doped microcrystalline silicon layers. | 96 |
| 3.9 | Deposition conditions for the TCO trials. All the samples were deposited at room temperature and with a power of 120 W. | 97 |
| 3.10 | Characteristic parameters of the best PIN solar cells. | 106 |
| 3.11 | Average of the characteristic parameters of the working PIN solar cells. | 106 |
| 3.12 | Characteristic parameters of the best NIP solar cells. | 108 |
| 3.13 | Average of the characteristic parameters of the working NIP solar cells. | 108 |
| 3.14 | Characteristic parameters of the best PIN solar cells with integrated current. | 110 |
| 3.15 | Characteristic parameters of the best NIP solar cells with integrated current. | 110 |
| 3.16 | Characteristic parameters of a standard solar cell (1 cm ²) currently implemented at UB (1 sun illumination). | 113 |
| 4.1 | Deposition parameters for the UB cells used in the thickness optimization experiment. The thickness of the <i>i</i> -layer is varied, having the four used samples 160, 200, 240 and 280 nm. | 121 |

List of Tables

| | | |
|------|---|-----|
| 4.2 | Initial and final values and relative losses of the parameters of UB cells of different thicknesses. | 124 |
| 4.3 | Evolution of J - V curve parameters in T -Solar samples. | 134 |
| 4.4 | Temperature coefficients for T -Solar samples ($^{\circ}\text{C}^{-1}$). | 135 |
| 4.5 | Evolution of J - V curve parameters in UB samples. | 138 |
| 4.6 | Values of relative parameters in UB samples arranged by degradation temperature. | 139 |
| 4.7 | Values and relative values of the short circuit (up) and open circuit (down) resistances in UB samples in the initial and annealed states. . . | 141 |
| 4.8 | Short circuit current values obtained from EQE curves integrations for UB cells. | 144 |
| 4.9 | Temperature coefficients for UB samples ($^{\circ}\text{C}^{-1}$). | 146 |
| 5.1 | Deposition parameters for intrinsic silicon layers and alumina layers used in passivation results. a-Si:H is deposited by PECVD and Al_2O_3 by sputtering. | 159 |
| 5.2 | Effective lifetime, implicit open circuit voltage and effective surface recombination velocity of the minority carriers for the annealed samples under one sun illumination. | 160 |
| 5.3 | Deposition parameters for indium tin oxide layers. The bold quantity in varying parameters is the one kept constant in the other series. | 165 |
| 5.4 | Summary of the results of the measured parameters in ITO series. The deposition times for p_{O_2} and temperature series are 30 min and 24 min respectively. | 167 |
| 5.5 | Summary of the results of the measured parameters in ITO over devices in the three stages of deposition (see Fig. 5.5). From top down: as the emitter is deposited, as the ITO is deposited over the emitter and after the thermal annealing (1 h at 160°C in air). The name of the sample refers itself to the quarter of the same wafer over which each ITO is deposited (the center and the temperature of deposition are detailed). . . | 170 |
| 5.6 | Values of the parameters of the best solar cells (1 cm^2) with different ITOs for each finger pitch. | 172 |
| 5.7 | Deposition parameters for p -doped a-Si:H and μc -Si:H layers in the temperature optimization. | 174 |
| 5.8 | Parameters obtained from the measurements of the p -doped layers over 1737 Corning glass. | 176 |
| 5.9 | Deposition times for both amorphous and microcrystalline p -layers, and its corresponding estimated thicknesses. The name references the deposition times (min) of the layers. | 177 |
| 5.10 | Characteristic parameters and integrated transmittance values of the a-Si:H solar cells with the varying thicknesses of the amorphous and microcrystalline p -layers in the stack. $\%EQE_{400-800}$ and $\%EQE_{400-550}$ correspond to the percentages of the areas integrated under the curves of the $EQEs$ in the specified range. | 178 |

5.11 Effective lifetime and implicit open circuit voltage after the successive annealings or LFC processes for both p (left) and n (right) wafers with the p -type emitter and ITO deposited at the UB. The annealings were performed at the UPC in a forming gas atmosphere. 182

5.12 Effective lifetime and implicit open circuit voltage after the successive annealing processes for the i a-Si:H and i a-SiC _{x} :H deposited at the UB (at 200°C). The thickness of both intrinsic layers (a-SiH and a-SiC _{x} :H) are about 33 nm. 184

5.13 Effective lifetime and implicit open circuit voltage in the i a-Si:H samples deposited at the UB at different temperatures (200, 250 and 300°C). The thickness of both intrinsic layers (a-SiH and a-SiC _{x} :H) are about 33 nm. 185

List of symbols, acronyms and abbreviations

List of symbols

Latin alphabet

| | |
|-------------|---|
| A | Absorptance($1-T-R$) |
| Bp | Background pressure |
| c | Speed of light |
| D | Depletion |
| d_e | Distance between electrodes (PECVD) or between substrate and electrode (Sputtering) |
| d | Thickness |
| E_a | Activation energy |
| E_g | Tauc optical band gap energy |
| f | Frequency |
| G | Conductance |
| G_0 | Global irradiance reference = 1000 W m^{-2} |
| H | Global irradiation in the array plane [Wh m^{-2}] |
| h | Planck's constant |

Symbols, acronyms and abbreviations

| | |
|---------------------------------|---|
| I | Electric current |
| I_{ph} | Photogenerated current |
| I_n | Relative intensity at $\lambda=n$ |
| $i-$ | intrinsic (not doped) |
| J | Current density |
| J_0 | Saturation current density |
| J_L | Photogenerated current density |
| J_m | Maximum power current density |
| J_{sc} | Short circuit current density |
| k | Boltzmann's constant |
| L, L_{bulk}, L_{sur} | Thickness of the i -layer and its regions (bulk and surface-affected) |
| l | Length |
| $Mtoe$ | Million Tones of Oil Equivalent |
| N_A | Number of atoms |
| N_a | Doping density |
| $Ndb, Ndb_{bulk}, Ndb_{sur}$.. | Defect density of the i -layer and its regions (bulk and surface-affected) |
| n | Carrier concentration, refractive index, number of electrons, ideality factor |
| $n - doped; n-$ | Negatively doped |
| q | Elemental charge |

| | |
|-----------------------|---|
| q_e | Electron charge |
| p | Pressure |
| P | Power |
| P_0 | Power of incident light (normally density [W/cm ²]) |
| P_n | Nominal power of the module [W] |
| $p - doped; p-$ | Positively doped |
| PR | Performance Ratio (plant) |
| PR_m | Performance Ratio (module) |
| R | Reflectance |
| R_d | Deposition rate |
| R_{oc} | (Area Normalized) Open circuit resistance [Ω cm ²] |
| R_p | (Area Normalized) Parallel resistance [Ω cm ²] |
| R_s | (Area Normalized) Series resistance [Ω cm ²] |
| R_{sc} | (Area Normalized) Short circuit resistance [Ω cm ²] |
| R_{sh} | Sheet resistance |
| S | Surface recombination velocity |
| S_{eff} | Effective surface recombination velocity |
| s | Substrate refractive index |
| T | Transmittance, Temperature |
| T_s | Substrate temperature |

Symbols, acronyms and abbreviations

| | |
|----------|------------------------|
| U | Recombination velocity |
| V | Voltage |
| V_{bi} | Built-in voltage |
| V_m | Maximum power voltage |
| V_{oc} | Open circuit voltage |
| V_T | Boltzmann potential |
| W | Wafer thickness |
| w | Width |
| Y_m | Module yield |
| Y_r | Radiation yield |

Greek alphabet

| | |
|--------------------------------------|---|
| α | Absorption coefficient, Temperature coefficient |
| χ_c | Raman crystalline fraction |
| $\Delta\sigma$ | Variation of the photoconductance |
| η | Energy conversion efficiency |
| Φ | Flow |
| λ | Wavelength |
| μ, μ_n, μ_p | Mobility (Electron mobility, Hole mobility) |
| $\mu\tau$ | Mobility-lifetime product |
| ρ | Resistivity |
| $\sigma, \sigma_{dark}, \sigma_{ph}$ | Conductivity(generic), Dark conductivity, Photoconductivity |
| σ_{DC}/σ_{OP} | Electrical to optical conductivity (Figure of merit) |
| τ, τ_{eff} | Carrier lifetime, Effective carrier lifetime |

List of acronyms

| | |
|--------------|---|
| <i>AC</i> | Altern Current |
| <i>AM1.5</i> | Solar spectrum at an Air Mass of 1.5 |
| <i>ARC</i> | Anti-Reflection Coating |
| <i>AZO</i> | Aluminum doped Zinc Oxide |
| <i>BR</i> | Back Reflector |
| <i>CIGS</i> | Cadmium Indium Gallium Selenide |
| <i>CVD</i> | Chemical Vapor Deposition |
| <i>DBs</i> | Dangling bonds |
| <i>DC</i> | Direct Current |
| <i>DPC</i> | Deposition Chamber |
| <i>EQE</i> | External Quantum Efficiency |
| <i>FF</i> | Fill Factor |
| <i>HIT</i> | Heterojunction with Intrinsic Thin layer |
| <i>HWCVD</i> | Hot Wire Chemical Vapor Deposition |
| <i>IBC</i> | Interdigitated back contact |
| <i>IQE</i> | Internal Quantum Efficiency |
| <i>ISO</i> | International Organization for Standardization |
| <i>ITO</i> | Indium Tin Oxide ($\text{In}_2\text{O}_3:\text{SnO}_2$) |
| <i>LED</i> | Light Emitting Diode |

Symbols, acronyms and abbreviations

| | | |
|--------------|-------|--|
| <i>LFC</i> | | Laser Fired Contact |
| <i>LID</i> | | Light Induced Degradation |
| <i>LL</i> | | LoadLock |
| <i>LPICM</i> | | Laboratoire des Interfaces et des Couches Minces |
| <i>MNT</i> | | Micro y NanoTecnología |
| <i>NIR</i> | | Near InfraRed |
| <i>PECVD</i> | | Plasma-Enhanced Chemical Vapor Deposition |
| <i>PMT</i> | | Photomultiplier Tube |
| <i>PERC</i> | | Passivated Emitter and Rear Cell |
| <i>PERL</i> | | Passivated Emitter Rear Locally diffused |
| <i>PLC</i> | | Programmable Logic Controller |
| <i>PLD</i> | | Pulsed Laser Deposition |
| <i>PV</i> | | Photovoltaic |
| <i>PVB</i> | | Polyvinyl butyral |
| <i>PVD</i> | | Physical Vapor Deposition |
| <i>QSPC</i> | | Quasi-Steady PhotoConductance |
| <i>RCA</i> | | Radio Corporation of America |
| <i>RF</i> | | Radio Frequency |
| <i>rpm</i> | | Revolutions per minute |
| <i>RT</i> | | Room Temperature |

| | |
|-------------------|--------------------------------------|
| <i>sccm</i> | Standard cubic centimeter per minute |
| <i>SHJ</i> | Silicon Hetero-Junction |
| <i>SR</i> | Spectral Response |
| <i>SRH</i> | Shockley-Read-Hall |
| <i>STC</i> | Standard Test Conditions |
| <i>SWE</i> | Staebler-Wronski Effect |
| <i>TCO</i> | Transparent Conducting Oxide |
| <i>TMB</i> | Trimethylborane ($B(CH_3)_3$) |
| <i>TF</i> | Thin Films |
| <i>UB</i> | Universitat de Barcelona |
| <i>UPC</i> | Universitat Politècnica de Catalunya |
| <i>UV</i> | UltraViolet |
| <i>VIS</i> | Visible |

Chemical species

| | |
|--|--------------------------------|
| <i>aSiO_x</i> | Amorphous silicon oxide |
| <i>a - Si : H</i> | Hydrogenated amorphous silicon |
| <i>Al₂O₃</i> | Alumina |
| <i>CdTe</i> | Cadmium Telluride |
| <i>CH₄</i> | Methane |
| <i>c - Si</i> | Crystalline silicon |

Symbols, acronyms and abbreviations

| | | |
|----------------|-------|---------------------------------------|
| $GaAs$ | | Gallium Arsenide |
| H_2O_2 | | Hydrogen peroxide |
| HCl | | Hydrochloric acid |
| HF | | Hydrofluoric acid |
| In_2O_3 | | Indium oxide |
| InP | | Indium phosphide |
| μSiO_x | | Microcrystalline silicon oxide |
| $\mu c-Si : H$ | | Hydrogenated microcrystalline silicon |
| NH_3 | | Ammonia |
| PbS | | Lead sulfide |
| PH_3 | | Phosphine |
| $p-Si$ | | Polycrystalline silicon |
| $pm-Si : H$ | | Hydrogenated polimorphous silicon |
| SiH_4 | | Silane |
| $SiC_x : H$ | | Hydrogenated silicon carbide |
| $SiN_x : H$ | | Hydrogenated silicon nitride |
| SiO_2 | | Silicon oxide |
| SnO_2 | | Tin oxide |
| $SnO_2 : F$ | | Fluorine doped Tin Oxide |
| ZnO | | Zinc oxide |
| $ZnO : Al$ | | Aluminum doped Zinc Oxide |
| $ZnO : Ga$ | | Gallium doped Zinc Oxide |

List of abbreviations

| | |
|------------------------|---|
| <i>Deg.</i> | Degradation |
| <i>diam.</i> | Diameter |
| <i>et al.</i> | From latin, <i>et alii</i> (and others) |
| <i>Eq.</i> | Equation |
| <i>Fig.</i> | Figure |
| <i>i.e.</i> | From latin, <i>id est</i> (that is) |
| <i>Sec.</i> | Section |
| <i>tech.rep.</i> | Technical report |
| <i>Th.</i> | Thickness |
| <i>vol.</i> | Volume |
| <i>wt.</i> | Weight |

Curriculum Vitae

Personal Data

Name: **Álvaro Caballero Lorenzo**
Date of Birth: April 2, 1987 (Valladolid, España)
Nationality: Spain
Cell Phone: (0034) 636 962 451
e-mail: alvarocablor@gmail.com

Academic Background

2011-2016 **Physics Ph.D.** (Solar Energy Group, Universitat de Barcelona): *Optimization of a-Si:H and other materials for different PV technologies.* Directed by Joan Bertomeu and José Miguel Asensi.
2010-2011 **Master's Degree in Instrumentation in Physics** (Universidad de Valladolid)
2005-2010 **BSC Physics** (Universidad de Valladolid).

Professional Background

2009-2010 Internship for collaboration at research tasks at Electronics Department of the Universidad de Valladolid.
2011-2015 Internship for training of research staff, Solar Energy Group, Universitat de Barcelona.

Experimental Skills

- Vacuum Technology: Working experience with Ultra-High Vacuum thin film deposition equipment in Clean Room environment (PECVD, sputtering, thermal evaporation).
- Optical and Structural Characterization: UV/VIS/NIR Spectrophotometer, RAMAN, Confocal microscopy.

Symbols, acronyms and abbreviations

- Electrical Characterization: Four point probe, solar cells characterization, thin film characterization.

Language Skills

- Spanish: Native language.
- English: Fluent.
- Catalan: Intermediate.
- French: Intermediate.

Scientific publications

- Intermediate amorphous silicon layer for crystalline silicon passivation with alumina Proceedings of 30th European Photovoltaic Solar Energy Conference and Exhibition (2015) 719 - 723. Jorge A. García-Valenzuela, Álvaro Caballero, José M. Asensi, Joan Bertomeu, Jordi Andreu, Luis G. Gerling-Sarabia, Anna B. Morales, Pablo Ortega, Cristóbal Voz.
- Light induced degradation and long term stability of a-Si:H solar cells and modules. Proceedings of 29th European Photovoltaic Solar Energy Conference and Exhibition (2014) 1638 - 1641. Álvaro Caballero, Luigi Morrone, Marta Llusà, José Miguel Asensi, Joan Bertomeu, Jordi Andreu.
- Growth differences of AZO on different glass textures and their application in thin film solar cells. Proceedings of 29th European Photovoltaic Solar Energy Conference and Exhibition (2014) 1912 -1916. M. Llusà, L. Morrone, A. Caballero, A. Antony, J.M. Asensi, J. Andreu, J. Bertomeu.
- Graded index at the TCO/p interface for silicon thin film solar cells using Nb doped TiO₂ Proceedings of the 29th European Photovoltaic Solar Energy Conference and Exhibition, (2014) 1941-1943.

A. Antony, M. Llusçà, F. Rojas Tarazona, L. Morrone, A. Caballero, J.M. Asensi, J. Andreu, J. Bertomeu.

Presentations at conferences

- EUPVSEC 30th European PV Solar Energy Conference and Exhibition Poster presentation: Intermediate amorphous silicon layer for crystalline silicon passivation with alumina Jorge A. García-Valenzuela, Álvaro Caballero, José M. Asensi, Joan Bertomeu, Jordi Andreu, Luis G. Gerling-Sarabia, Anna B. Morales, Pablo Ortega, Cristóbal Voz.
- EUPVSEC 29th European PV Solar Energy Conference and Exhibition Poster presentation: Light induced degradation and long term stability of a-Si:H solar cells and modules. Álvaro Caballero, Luigi Morrone, Marta Llusçà, José Miguel Asensi, Joan Bertomeu, Jordi Andreu.
- EUPVSEC 29th European PV Solar Energy Conference and Exhibition Poster presentation: Growth differences of AZO on different glass textures and their application in microcrystalline silicon solar cells. M. Llusçà, L. Morrone, A. Caballero, A. Antony, J.M. Asensi, J. Andreu, J. Bertomeu.
- EUPVSEC 29th European PV Solar Energy Conference and Exhibition Poster presentation: Growth differences of AZO on different glass textures and their application in microcrystalline silicon solar cells. M. Llusçà, L. Morrone, A. Caballero, A. Antony, J.M. Asensi, J. Andreu, J. Bertomeu.
- 1st School in Materials for Photonics Applications, (2012) Poster Presentation: Towards the Improvement of Thin Film Silicon Solar Cells through novel materials and techniques. A. Caballero, J.M. Asensi, P. Carreras, P. Frigeri, M. Llusçà, L. Morrone, R. Roldán, J. Bertomeu.

Acknowledgements

Finalmente, el camino iniciado hace más de cuatro años en la Universidad de Barcelona llega a su fin. Como todo en la vida, la realización de la tesis ha estado llena de altibajos, pero en el balance final, puedo decir que ha sido una experiencia vital enriquecedora durante la cual he disfrutado y aprendido mucho.

En primer lugar, mi más profundo y sincero agradecimiento a mis dos directores de tesis. Al Dr. Joan Bertomeu, gracias por haberme dado la oportunidad de formar parte del grupo, por tu confianza y tu disponibilidad y, sobre todo, por tu preocupación por ayudarme a llevar este trabajo a buen término. Y al Dr. José Miguel Asensi, por tu capacidad para enseñarme, tu dedicación y tu colaboración a la hora de realizar tantas medidas y experimentos. También quiero dar las gracias al Dr. Jordi Andreu, por haber ejercido como un director más, transmitiéndome conocimientos y proporcionándome ideas y proyectos que sin duda han mejorado la calidad de esta tesis. Muchísimas gracias por hacer posible todo esto.

No menos importantes son los compañeros del grupo, que me han permitido gozar de un ambiente inmejorable y también de grandes momentos fuera del trabajo, desde cenas hasta bodas, pasando por conciertos... ¡pero sobre todo cafés! En especial, gracias a Marta, que ha estado en este viaje de principio a fin y es con quien he compartido más buenos y malos momentos. Ya eres mi amiga que vive más lejos, y desde luego que te lo mereces. Gracias también a Luigi y a Paolo, el equipo de guerra contra la rebelión del PECVD y la evaporadora, y a Oriol y a Paz, por guiarme en mis primeros pasos en el departamento. Por supuesto también al resto de compañeros del grupo y del departamento que han sido parte de esta experiencia: Jofre, Jorge, Laura, Jerson y tantos otros. Y por último gracias al resto de profesores del departamento y al personal de

secretaría, siempre dispuesto a ayudar.

Agradecer también a las personas de otros centros que han colaborado en la realización esta tesis. Al LPICM de Palaiseau, donde realicé mi estancia y aprendí mucho. En especial al Dr. Pere Roca, por permitirme trabajar en su excelente grupo y ayudarme a ampliar mis conocimientos; y al Dr. Federico Ventosinos por ser de tanta ayuda durante mi tiempo allí. Y por otro lado, al Dr. Cristóbal Voz y el grupo MNT de la UPC por su colaboración en el trabajo con obleas de silicio. En especial, gracias a Anna: no sólo he aprendido mucho trabajando contigo, sino que ha sido un placer. No quiero olvidarme de los doctores Salvador Dueñas, Helena Castán y Luis Bailón, del departamento de Electrónica de la Universidad de Valladolid. No sólo fuisteis los primeros en confiar en mí para la investigación, sino que además conseguisteis que de verdad me gustase y quisiese seguir. Por ello os estoy verdaderamente agradecido.

Fuera del ámbito científico, quiero dar las gracias a mis amigos, tanto a los que nos conocemos desde el colegio e instituto como a los que tuve la suerte de conocer en la carrera. Es fantástico poder contar con todos vosotros y que, por muy desperdigados que estemos, cada vez que nos encontramos es como si nada hubiera cambiado. Muchas gracias también a mis tíos Nina, Isidro y Puri, mis primos Erika, Noemí y Daniel, a mi abuela Dolores y en general a toda mi familia, por siempre creer en mí. Especialmente gracias a mi hermano Alex, con quien disfruto cada vez que nos juntamos; a mi madre, preocupada constantemente por mi bienestar; y a mi padre, que siempre me escucha con interés y aconseja con sabiduría. Tened presente que si he logrado llegar hasta aquí es gracias a vosotros. Y por supuesto, muchas gracias a ti, Lucía, que has hecho mucho más que la portada de esta tesis. La aventura que empezamos viniendo juntos a Barcelona hubiera sido tan diferente sin ti que ni puedo ni quiero imaginarlo. Mil gracias por tu compañía, tu apoyo y tu paciencia conmigo.

Finalmente, quiero acabar dedicando esta tesis a mi abuelo Martín, al que echo mucho de menos y que para mí siempre fue un ejemplo y siempre lo será.